

ANALYSIS OF SCANNING IN DUAL OFFSET REFLECTOR
ANTENNAS AND THE BIFOCAL SYSTEM

by

Carey Milford Rappaport

SUBMITTED IN PARTIAL FULFILLMENT
OF THE REQUIREMENTS FOR THE
DEGREES OF

BACHELOR OF SCIENCE

MASTER OF SCIENCE

and

ELECTRICAL ENGINEER

at the

MASSACHUSETTS INSTITUTE OF TECHNOLOGY

June 1982

© Carey Milford Rappaport 1982

The author hereby grants M.I.T. permission to reproduce and to
distribute copies of this thesis document in whole or in part.

Signature of Author

~~Department of Electrical Engineering
and Computer Science~~ May 10, 1982

Certified by

Jin Au Kong
Thesis Supervisor (Academic)

Certified by

Robert M. Sorbello
Company Supervisor (COMSAT Laboratories)

Accepted by

Arthur C. Smith
Chairman, Departmental Committee
on Graduate Students

Archives
MASSACHUSETTS INSTITUTE
OF TECHNOLOGY

OCT 20 1982

LIBRARIES

Analysis of Scanning in Dual Offset Reflector Antennas
and the Bifocal System

by

CAREY MILFORD RAPPAPORT

Submitted to the Department of Electrical Engineering
and Computer Science on May 10, 1982, in
Partial Fulfillment of the Requirements for the
Degrees of Bachelor of Science and
Master of Science in Electrical Engineering

ABSTRACT

Geosynchronous satellite antenna systems capable of producing narrow, well-formed beams which can scan across the entire 18° field of view of the earth are becoming increasingly important. The demand for small coverage spot beams and shaped contour beams necessitates particularly low sidelobes. Reflector antennas offer many advantages over other systems, such as lenses and phased arrays, in that they are lightweight, frequency independent, and use a minimum of electronic components. Dual offset reflectors are the most optically flexible and compact type of reflector antenna. Having an offset configuration minimizes sidelobe levels by eliminating subreflector blockage. The extra degree of freedom afforded by two reflectors permits the shaping of their surfaces to optimize scanning performance.

To scan a beam, the antenna's feed is transversely displaced about the system axis. Several techniques have been used to shape reflectors to improve scanning performance. This shaping alters the focal region characteristics to promote ray collimation for beams received from various angles. These designs are discussed, and a new antenna system, the offset bifocal, is formulated and examined. Based on the symmetric bifocal, the offset design focuses rays from two aperture inclinations to two distinct focal points. Unlike the previous designs, however, the offset bifocal does not suffer from blockage and hence has far superior sidelobe performance. Computer simulated comparisons and experimental test results are included.

Thesis Supervisors: Dr. Jin Au Kong
Professor of Electrical Engineering

Dr. Robert M. Sorbello
Manager, Satellite Antenna Department,
COMSAT Laboratories

Biographical Sketch

Carey Rappaport is a second year graduate student, pursuing a master's degree and beginning his doctoral research at the Massachusetts Institute of Technology. As a student in the electromagnetics area of electrical engineering, his current interests are in plasma fusion engineering and laser physics.

Research for his master's thesis took place at the Antenna Lab at COMSAT Laboratories, where Carey has worked as a cooperative student since 1978. His work at COMSAT included computer antenna pattern simulation and optimization, microwave measurements, RF circuit construction, and automated antenna range system design.

With the approval of his thesis, Carey expects to receive four degrees from M.I.T., including a bachelor's in mathematics. He has been employed by M.I.T. as a tutor for the math department; a research consultant with the Ralph Parsons hydrodynamics laboratory; and as both a teaching assistant and a research assistant for the EECS department.

As the son of an American diplomat, Carey's background includes a considerable amount of travel. He was born and lived the first five years of his life in Tokyo, Japan. He also lived in Washington, D.C., and Rome, Italy. Carey has won awards of first place in the Mid-Atlantic Mathematics Competition and the Foreign Service Merit Scholarship. He is a member of the IEEE and Sigma Xi, and is an Eagle Scout.

Carey is an active member of the M.I.T. community. He is a Graduate Resident at one of the undergraduate dorms, and also works with the admissions office as an interviewer.

Acknowledgments

I would like to thank many people who contributed, both directly and indirectly, to this thesis. I am deeply indebted to my parents, Paul and Evelyn Rappaport, for providing me with unceasing support, inspiration, direction and understanding.

I also appreciate the efforts of Laura MacGinitie to assuage aggravations and help me maintain motivation.

More directly, I wish to express thanks to the Management as well as to many employees of COMSAT Labs. The entire Antenna Lab contributed greatly and in particular Dan DiFonzo, Bob Sorbello, and Bryan Lee helped enormously with technical discussions and advice. Ken Pease's model design and experimental help made a tedious measurement program smooth and successful. The help of members of the model shop and computer center is also appreciated. I am grateful to Professor Kong, my thesis supervisor, and his electrodynamics group at M.I.T. for providing an academic flavor to my research.

Finally, I would like to thank COMSAT's Technical Publications and Word Processing groups; and especially Blanche Reid for producing so elegant a manuscript.

Table of Contents

	<u>Page No.</u>
I. INTRODUCTION	1
A. Background	1
B. Scanning and Optical Aberrations	3
C. Applications of Scanning Reflectors in Satellite Communications	8
D. Reflector Design Fundamentals	16
E. Reflectors Designed for Scanning	23
II. SCHWARZSCHILD ANTENNA	33
A. Optical Considerations and Capabilities of the Schwarzschild Antenna	33
B. Graphical Solution to the Schwarzschild Equations	37
C. Analytic Solution of the Schwarzschild and Comparison to the Cassegrain	39
D. Alternative Schwarzschild Design	46
APPENDIX II.1. DERIVATION OF THE SCHWARZ- SCHILD REFLECTOR ANTENNA PROFILE EQUATIONS	50
APPENDIX II.2. SPEAKEASY COMPUTER PROGRAM TO GENERATE AND PLOT SCHWARZSCHILD PROFILES	57

Table of Contents (Continued)

	<u>Page No.</u>
III. DERIVATION OF FORMULAS	59
A. The Bifocal Principle	59
B. Point Generation Methodology	70
C. Transmit Ray Analysis	75
D. Receive Ray Analysis	78
E. Surface Generation	82
APPENDIX III.1. CALCULATION OF \bar{R}_{3k}	96
APPENDIX III.2. COMPUTER PROGRAM PLOT	
LISTING (IN SPEAKEASY)	99
IV. ANALYTIC RESULTS	100
A. Description of Geometry and Surface	
Approximation	100
B. Analytic Tools	109
C. Computed Performance	113
D. Comparative Cases	122
APPENDIX IV. COMPUTER PROGRAM FEEDA LISTING	
AND SAMPLE RUN	168

Table of Contents (Continued)

	<u>Page No.</u>
V. MODEL FABRICATION	170
A. Support Structure	170
B. Reflector Fabrication	173
APPENDIX V. PL 1 PROGRAMS TO GENERATE NUMER- ICALLY CONTROLLED MILLING MACHINE INPUT TAPES, AND SAMPLE RUN	192
VI. TEST MEASUREMENTS	201
A. Experimental Setup	201
B. Experimental Results	203
VII. SUMMARY AND CONCLUSIONS	251
APPENDIX VIII. DESCRIPTION AND PROGRAM LISTING OF THE BIFOCAL GENERATING PROGRAM	258
APPENDIX IX. PARAMETER STUDY	293
REFERENCES	315

List of Illustrations

<u>Figure No.</u>	<u>Title</u>	<u>Page No.</u>
1	The Five Primary Optical Aberrations at the Antenna Aperture: a) Linear, b) Quadratic, c) Coma, d) Astigmatism, e) Spherical Aberration	5
2	The Earth Viewed From Geosynchronous Orbit	9
3	Comparison of Conventional Global Beam Coverage to Earth Station Density	10
4	The Three Basic Types of Reflector Antennas	13
5	Limitations of the Equivalent Parabola Concept Applied to Scanning in a Cassegrain Antenna	15
6	The Degrading Effects of Subreflector Blockage and Spillover on the Radiation Pattern	20
7	Offset Dual Reflector Derived from the Symmetric Parent Dual Reflector	22
8	Optical Focal Loci for an Offset Cassegrain	25

List of Illustrations (Continued)

<u>Figure No.</u>	<u>Title</u>	<u>Page No.</u>
9	Ray Paths for a Scanning Dual Reflector	27
10	Torus Geometry	29
11	Comparison of Scanned Gain Reduction for Various Reflector Antennas	30
12	Comparison of Scanned First Sidelobe Level for Various Reflector Antennas ...	31
13	Geometry of the Schwarzschild Dual Reflector	34
14	Comparison of Coma Aberration for Three Reflector Antennas: a) Paraboloid, b) Cassegrain, and c) Schwarzschild ...	36
15	Graphical Method of Generating Schwarzschild Profiles	38
16	Right Half of a Symmetric Schwarzschild Profile	41
17	The Far-Field Radiation Pattern of a Symmetric Schwarzschild Antenna	43
18	Scanning Performance of Cassegrain Antenna vs Schwarzschild Antenna	44

List of Illustrations (Continued)

<u>Figure No.</u>	<u>Title</u>	<u>Page No.</u>
19	Gregorian Schwarzschild Profile	47
20	Radiation Pattern for the Offset Gregorian Schwarzschild Configuration: On-Axis Beam Configuration	48
21	Radiation Pattern for the Offset Gregorian Schwarzschild Configuration: 5.5° Scanned Beam	49
22	Comparison of Symmetric Bifocal and Corresponding Cassegrain Profiles	62
23	Extension of 2-Dimensional Bifocal Profile to 3 Dimensions by Rotation About the Axis	63
24	Nonideal Nature of the Symmetric Bi- focal a) Oblique View, b) Projection on x-z Plane	65
25	Geometry of Scanned Aperture Phase Planes	67
26	Aperture Phase Plane Intersection Line	69
27	Transmit Point Generation Procedure	71
28	Receive Point Generation Procedure	72

List of Illustrations (Continued)

<u>Figure No.</u>	<u>Title</u>	<u>Page No.</u>
29	Generation of the Kth Pair of Offset Bifocal Points	73
30	A Set of Subreflector Points and Normals Which Cannot be Joined with a Smooth, Well Behaved Curve	83
31	Subreflector Realizability Check	85
32	Extension of 2-Dimensional Profile to 3 Dimensions Using a Specified Trans- verse Polynomial	87
33	Progression of Projections of Space Curves onto the x-y Plane	89
34	Progression of Projections of Space Curves onto the y-z Plane	90
35	Sample Computer Output for Five Separate Transverse Starting Points $\Delta y = 0.011$..	91
36	Illumination Efficiency of the Main Re- flector Profile for Totally Illuminated Subreflector for Three Scanned Positions	93
37	Actual Ray Paths for Offset Bifocal Profile at -8° and $+8^\circ$	95

List of Illustrations (Continued)

<u>Figure No.</u>	<u>Title</u>	<u>Page No.</u>
III.1-1	Geometry of Tilted Aperture Phase Plane Vector Analysis	97
38	Difference in Wavelengths Between the Bifocal Main Reflector and its Best Fitting Paraboloid	101
39	Procedure for Finding the Best Fit Off- set Cassegrain to the Offset Bifocal ...	104
40	Illuminated Spots on the Main Reflector Projection for Three Feed Positions	107
41	Reduction in Aperture Phase Error for Axial Refocusing of Central Feed in a Symmetric Bifocal [76]	110
42	Numerical Specification of Geometry Analyzed Including: Focal Points, Reflector Profile Segment Limits and Projected Reflector Centers (scale 1:0.00104 λ)	114
43	Radiation Contour Patterns of a 130 λ Offset Bifocal Feed with Optimized Circular Waveguides for -8°, 0°, and +8° in Elevation	116

List of Illustrations (Continued)

<u>Figure No.</u>	<u>Title</u>	<u>Page No.</u>
44	Contour Pattern for 0° Scan Without Refocusing	118
45	Radiation Patterns in the Elevation Plane for the Optimized Bifocal at -8°, 0°, and +8°	119
46	3-Dimensional Plot of Beams Scanned at -8°, 0°, and +8°	121
47	Elevation Cut Patterns for the Bifocal with a Widened Subreflector	123
48	The Equivalent Paraboloid of the Offset Bifocal Analyzed	124
49	Contour Patterns for Largest Offset Paraboloid Contained Within the Bifocal Volume Limits: -8°, 0°, and +8°	126
50	Elevation Patterns for Offset Paraboloid: -8°, 0°, and +8°	127
51	Scanned Beams for Offset Paraboloids Proposed in INTELSAT VI	129

List of Illustrations (Continued)

<u>Figure No.</u>	<u>Title</u>	<u>Page No.</u>
52	High Frequency Contour Patterns (half-power beamwidth at 0.25° or ± 32 beamwidths of scan for -8° , 0° , and $+8^\circ$) ...	130
53	Elevation Patterns for ± 120 Beamwidths of Scan for -8° , 0° , and $+8^\circ$	131
54	Offset Paraboloid Scanned the Equivalent of 120 0.065° Beamwidths	132
55	Plot of Scan Loss vs Aperture Diameter for 8° Scanning of an Offset Paraboloid	133
56	Offset Bifocal and the Corresponding Cassegrain with Common Main Reflector	136
57	Difference Between the Bifocal and Cassegrain Subreflector Profiles	137
58	Comparison of Type a and b Cassegrains, Indicating Inefficiently Illuminated Section a-b	138
59	Type c Cassegrain with Main Reflector Positioned at Extreme Rear of the Limiting Volume	140

List of Illustrations (Continued)

<u>Figure No.</u>	<u>Title</u>	<u>Page No.</u>
60	Contour Patterns for Type a Cassegrain: -8°, 0°, and +8°	142
61	Elevation Scan Patterns for the Bifocal with 7λ Circular Feeds	144
62	Elevation Scan Patterns for the Type a Cassegrain with 7λ Circular Feeds	145
63	Contour Patterns for the Bifocal with 7λ Circular Feeds	148
64	Contour Patterns for Type a Cassegrain with 7λ Circular Feeds	149
65	High Frequency Elevation Scan Comparison (heavy line: bifocal, light line: type a Cassegrain)	150
66	Contour Patterns for Type b Cassegrain with 7λ Circular Feed	151
67	Scan Performance for Type b Cassegrain: 7λ Feed	152
68	Scan Performance for Bifocal: 7λ Feed	154

List of Illustrations (Continued)

<u>Figure No.</u>	<u>Title</u>	<u>Page No.</u>
69	Elevation Scan Patterns for Type c Cassegrain: 7λ Feed	155
70	Differing Focusing Characteristics for High and Low Magnification (and curvature) Subreflectors	157
71	Contour Plots for Entire Field of View	159
72	Beams Scanned in Both Azimuth and Elevation for Bifocal with Optimized Feeds	161
73	Type a Cassegrain Scanned in Both Azimuth and Elevation	162
74	Feed Angle Variation for a) Elevation Scanning and b) Azimuth Scanning	164
75	High Frequency Azimuth and Elevation Scanning: $\pm 32 \times \pm 32$ Beamwidths	165
76	Detail of High Frequency Azimuth and Elevation Scanning	166
77	Limits of Scanning with Offset Bifocal: 13 One Degree Beamwidths	167

List of Illustrations (Continued)

<u>Figure No.</u>	<u>Title</u>	<u>Page No.</u>
78	Support Framework for Experimental Model	171
79	Intersection of the Limiting Cube and Subreflector Plane Yielding the Largest Inscribed Circle	175
80	View of the Subreflector in the Double Primed Coordinate System: a) Pro- jection onto Hexagon, b) and c) Orthogonal Views	176
81	Geometry of Coordinate Rotation	179
82	View of Subreflector Positioned Inside 12 in. Cube: Side Edge and Top Views	180
83	Left Half Mill Paths	184
84	Right Half Mill Path	185
85	Error Between Cut Paths of a Ball End Mill	186
86	Error Between an Arc and a Straight Line	188
87	Prime Focus Configuration Test	205

List of Illustrations (Continued)

<u>Figure No.</u>	<u>Title</u>	<u>Page No.</u>
88	The Offset Bifocal Antenna--View 1	207
89	The Offset Bifocal Antenna--View 2	208
90	Author Making Adjustments on Test Antenna	209
91	Computed Elevation Scan Patterns for 7λ Pyramidal Horn Feed	210
92	Detail of Unscanned Beam Using 7λ Pyramidal Horn	211
93	Measured Unscanned Beam, 7λ Pyramidal Horn	212
94	7λ Pyramidal Horn at (-0.2°, -8.6°)	213
95	7λ Pyramidal Horn (0.3°, 7.8°)	214
96	Computed versus Measured Performance with 7λ Pyramidal Horn: -8°, 0°, and +8°	215
97	7λ Pyramidal Horn (-0.3°, -5.5°)	216
98	Subreflector Spillover Pattern Before Recoating	217
99	Subreflector Spillover (with Mylar covering)	218

List of Illustrations (Continued)

<u>Figure No.</u>	<u>Title</u>	<u>Page No.</u>
100	Subreflector Spillover After Recoating	219
101	7λ Pyramidal Horn Unscanned Beam After Subreflector Recoating (0° , 0.3°)	220
102	7λ Pyramidal Horn (-5° , 0.2°)	221
103	7λ Pyramidal Horn (-5.2° , 8.1°)	222
104	7λ Pyramidal Horn (-5.1° , -8.5°)	223
105	7λ Pyramidal Horn (-5.2° , -5.2°)	224
106	7λ Pyramidal Horn (4.9° , 0°)	225
107	7λ Pyramidal Horn (5.6° , 7.8°)	226
108	7λ Pyramidal Horn (4.2° , -8.5°)	227
109	7λ Pyramidal Horn (4.5° , -5.3°)	228
110	7λ Pyramidal Horn, Extended Scan (-0.4° , 11.8°)	229
111	7λ Pyramidal Horn, Extended Scan (-4.9° , 11.6°)	230
112	7λ Pyramidal Horn, Extended Scan (5.6° , 11.5°)	231
113	7λ Pyramidal Horn, Wide Azimuth Scan (-8.6° , 0.7°)	232

List of Illustrations (Continued)

<u>Figure No.</u>	<u>Title</u>	<u>Page No.</u>
114	7 λ Pyramidal Horn, Wide Azimuth Scan (-9.0°, 8.6°)	233
115	7 λ Pyramidal Horn, Wide Azimuth Scan (8.7°, 4.6°)	234
116	Typical Measured Contour Pattern (0.3°, 7.8°)	235
117	Optimized Horn Feed (0°, -0.5°)	236
118	Optimized Horn Feed (0°, -9.2°)	237
119	Optimized Horn Feed (0°, 7°)	238
120	Optimized Horn Feed (-5.0°, -0.5°)	239
121	Optimized Horn Feed (-5.5°, 8.8°)	240
122	Optimized Horn Feed (-5.0°, 7.0°)	241
123	Optimized Horn Feed (5.0°, -0.5°)	242
124	Optimized Horn Feed (5.5°, -8.8°)	243
125	Optimized Horn Feed (5.0°, 1.0°)	244
126	Scan Angle Study 1°	294
127	Scan Angle Study 2°	295
128	Scan Angle Study 4°	296
129	Scan Angle Study 6°	297
130	Scan Angle Study 6.6°	298

List of Illustrations (Continued)

<u>Figure No.</u>	<u>Title</u>	<u>Page No.</u>
131	Scan Angle Study 7°	299
132	Scan Angle Study 8°	300
133	Scan Angle Study 12°	301
134	Subreflector Vertex Study	302
135	Path Length Study	304
136	Aperture Center Location Study	305
137	Aperture Position Study $C_1 = 0$	306
138	Aperture Position Study $C_1 = 0.1$	307
139	Aperture Position Study $C_1 = 0.2$	308
140	Aperture Position Study $C_1 = 0.3$	309
141	Aperture Position Study $C_1 = 0.4$	310
142	Aperture Position Study $C_1 = 0.5$	311
143	First Subreflector Normal Study \hat{n}_{S_1} = (0,0,-1)	312
144	First Subreflector Normal Study \hat{n}_{S_1} = (0.1,0,-1).....	313
145	First Subreflector Normal Study \hat{n}_{S_1} = (0.2,0,-1)	314

List of Tables

<u>Table No.</u>	<u>Title</u>	<u>Page No.</u>
1	List of Variables	74
2	Spillover Past Reflectors	146

I. INTRODUCTION

A. Background

Perhaps the most critical component in a high performance microwave communications system is its antenna. The antenna serves to concentrate radiated power in a prescribed manner. For satellite applications, this means providing an angular region of high intensity in the direction of the earth, with a minimum amount of power wasted in other directions.

The key measure of an antenna's performance, its gain, is directly dependent on the area of its effective aperture. Reflectors, lenses, and phased arrays are the primary devices used to magnify the source aperture and increase gain. The first two increase the effective aperture area by a purely geometric transformation, whereas the phased array electrically transforms the aperture. The lens antenna is a heavy, complex structure which, like the phased array, is very frequency dependent. There is no blockage with a lens aperture since the feed array is behind it. Its axial symmetry provides good cross polarization performance. However, surface impedance matching requirements, dissipative losses, as well as weight and bandwidth limitations make lenses inferior to reflectors in most satellite applications. The reflector

antenna is the simplest, cheapest, and lightest alternative, and has been the primary means of providing high gain microwave beams.

In the far field, or Fraunhofer region, the spatial power distribution pattern is independent of radius from the source. It is proportional to the Fourier transform of the aperture phase and amplitude distribution [1]-[5]. The antenna's pattern is very sensitive to the phase distribution at its aperture. Beam direction, maximum gain, and the power outside the main lobe and associated sidelobe levels are strongly dependent on the aperture phase function [6],[7].

For a given well-behaved amplitude distribution, maximum forward gain will be realized with a constant phase distribution. A linear variation of phase steers or scans the beam in the direction perpendicular to the tilted plane of constant phase. Any quadratic or higher order phase variations across the aperture are considered aberrations and lead to beam degradation. It is essential to understand the effects of phase aberrations when designing an antenna system [8].

For single fixed beam antennas, the aperture conditions are dependent only on the reflector surface placement and geometry. There is only one source input, with fixed position

and orientation. However, a scanning antenna must be able to produce a variable linear phase distribution depending on varying source conditions. Maintaining a flexible linear phase function while minimizing higher-order aberration terms is generally difficult. A phased array antenna can do this fairly simply, by applying the required phase shifts to successive elements. Given enough elements, a linear variation can be approached.

B. Scanning and Optical Aberrations

For reflectors and lenses, scanning is accomplished by transversely displacing the feed from the antenna's focus (its unscanned aberration-free source position). For systems with a single perfect focal point, this displacement always produces higher order phase terms. The absence of higher order terms at any other position would imply the existence of a second perfect focal point there.

The phase at each point of the antenna's aperture is proportional to the path length of the ray which emanates from the source and is traced through the system to that point. With the source at the focus of a paraboloid, for instance, all rays emerge parallel to the axis and trace the same distance to any plane perpendicular to this axis.

For a circular aperture, the primary aberrations are expressed by the first Siedal sum and have five terms [9],[10]:

- (1) the linear term

$$\phi_1 = Axr \cos \phi,$$

- (2) the quadratic, or field curvature term

$$\phi_2 = Br^2,$$

- (3) the cubic, or primary coma term

$$\phi_3 = Cxr^3 \cos \phi,$$

- (4) the astigmatic term

$$\phi_4 = Dx^2r^2 \cos 2\phi,$$

- (5) the spherical aberration term

$$\phi_5 = Er^4,$$

where the aperture has coordinates (r, ϕ) and x is the feed displacement from the focus. These aperture phase functions and their effects on the far-field pattern are illustrated in three dimensions in Figure 1.

The symmetric even order terms--the quadratic and spherical aberration terms--are independent of transverse feed displacement. These are minimized by axial refocusing of the feed. Spherical aberration is present in systems lacking a perfect focal point (a spherical reflector, for example). Line feeds or subreflector correctors are sometimes used to eliminate this effect.

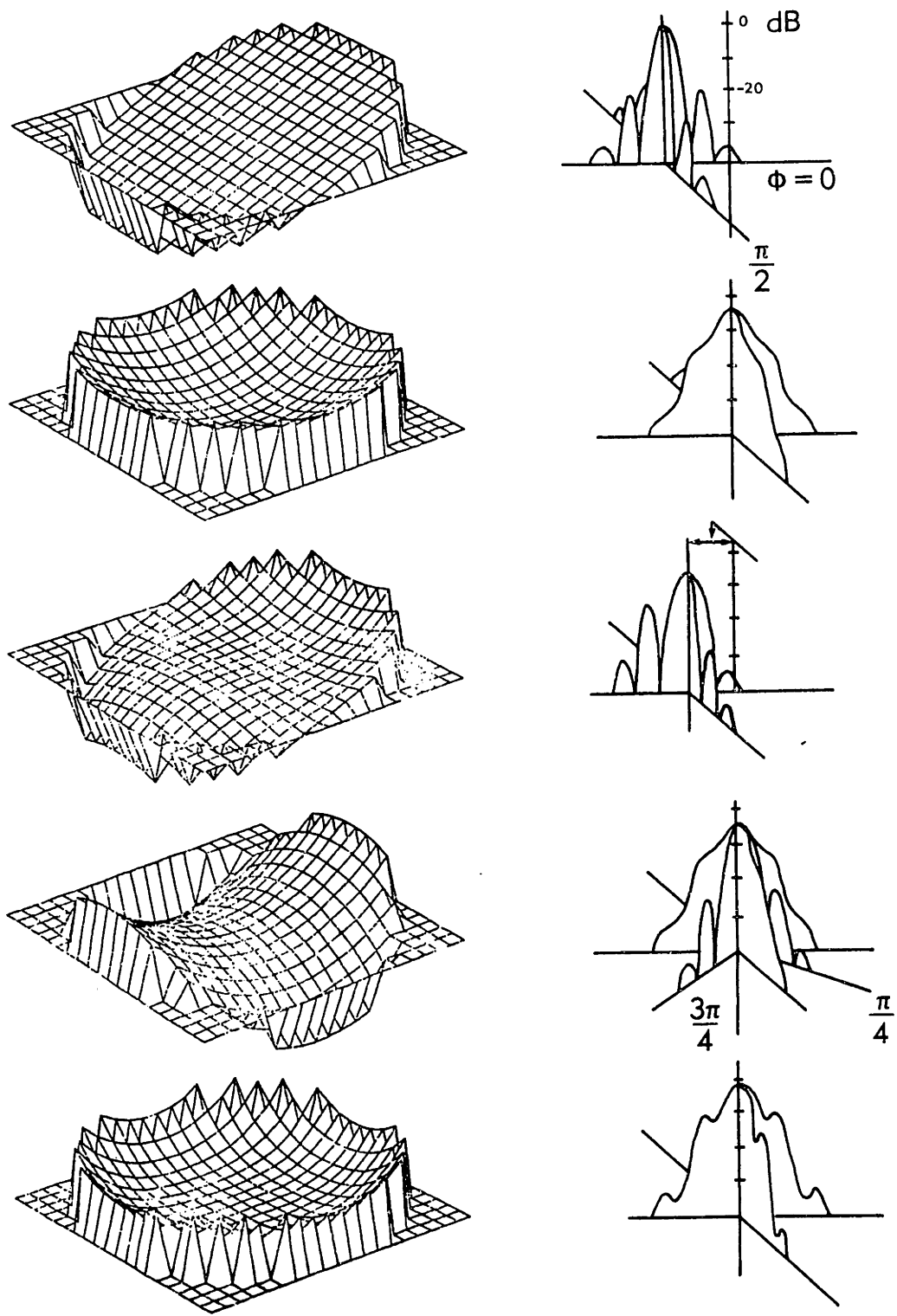


Figure 1. The Five Primary Optical Aberrations at the Antenna Aperture: a) Linear, b) Quadratic, c) Coma, d) Astigmatism, e) Spherical Aberration

The coma term is an odd order aberration, so it causes an asymmetric effect in the plane of scan. The beam broadens, the first null in the scanned direction fills, and the first sidelobe on the axial side--the coma lobe--rises. Also, the beam peak is shifted, but by only a small amount compared to the linear shifting. Coma has no effect in the plane perpendicular to the scanned plane. Because of its linear dependence on feed displacement x , coma tends to be the dominant aberration for small displacements. The effects of astigmatism [11] are greatest in the principal planes of the beam pattern. It is zero on the diagonal planes. As with quadratic aberration, refocusing improves the pattern in one of the principal planes, but worsens it in the other. Thus, there are different optimal focal points for the tangential (plane of scan) and sagittal (normal to plane of scan) planes. The distances between these points is a measure of the astigmatism of the system.

Several authors have dealt with the problem of finding the best focal locus of a paraboloidal antenna [12]-[15]. The most general solution appears to be given by Balling, et al. [16] which considers an offset geometry with focal length f , focus to aperture center distance d_1 , and feed displacement along the offset focal surface--the plane with

normal $(d_1, 0, -f)$ --by a vector $[x, 0, x(d_1/f)]$. On this focal surface, the symmetric terms are zero. The results for the above constants are:

$$A = \frac{2k(d/2f)^2 \sqrt{1 + (d_1/f)^2}}{f} \frac{1}{[1 + (d_1/2f)^2]^2} ,$$

$$B = 0 ,$$

$$C = \frac{-k\sqrt{1 + (d_1/f)^2}}{4f^3} \frac{1}{[1 + (d_1/2f)^2]^2} ,$$

$$D = \frac{-kd_1\sqrt{1 + (d_1/f)^2}}{4f^3} \frac{1}{[1 + (d_1/2f)^2]^2} ,$$

$$E = 0 ,$$

$$k = 2\pi/\lambda .$$

Scanning is of great concern for antennas used in satellite applications. When high resolution is important, as is the case with point-to-point networking and direct broadcast communications, the antenna must provide a large number of high gain, well-formed spot beams over its entire field of view. Well-formed beams are also required in multibeam antennas. High efficiency shaped coverage contours are useful for illuminating specific geographic regions. Since they are produced by coherently combining component beams, each beam must have low sidelobes and well defined nulls to prevent undesirable interference.

C. Applications of Scanning Reflectors in Satellite Communications

Viewed from geostationary orbit, the earth subtends an angle of 17.4° (Figure 2). This specifies the amount of scanning required of a satellite antenna. Figure 3a illustrates the power distribution of a conventional global coverage beam pointing toward the earth's center. The density decreases for increasing angle as a result of both tapering of the beam and the greater surface area illuminated per unit solid angle transmitted. Figure 3b displays the number of earth stations for each one-half degree field of view. Notice the preponderance of earth stations at the edges of the earth. This follows from the fact that satellites are usually situated over the oceans, so they can communicate from one continent to another. Also, the total angular area varies as the field angle squared, so the larger angles represent a greater amount of surface area. It should be emphasized that having a single antenna scan $\pm 8^\circ$ is preferable to two antennas of lower performance. Aside from the obvious advantage of greater efficiency with one, being able to include all areas of coverage, including areas between the scan limits, with one antenna provides a high degree of flexibility.

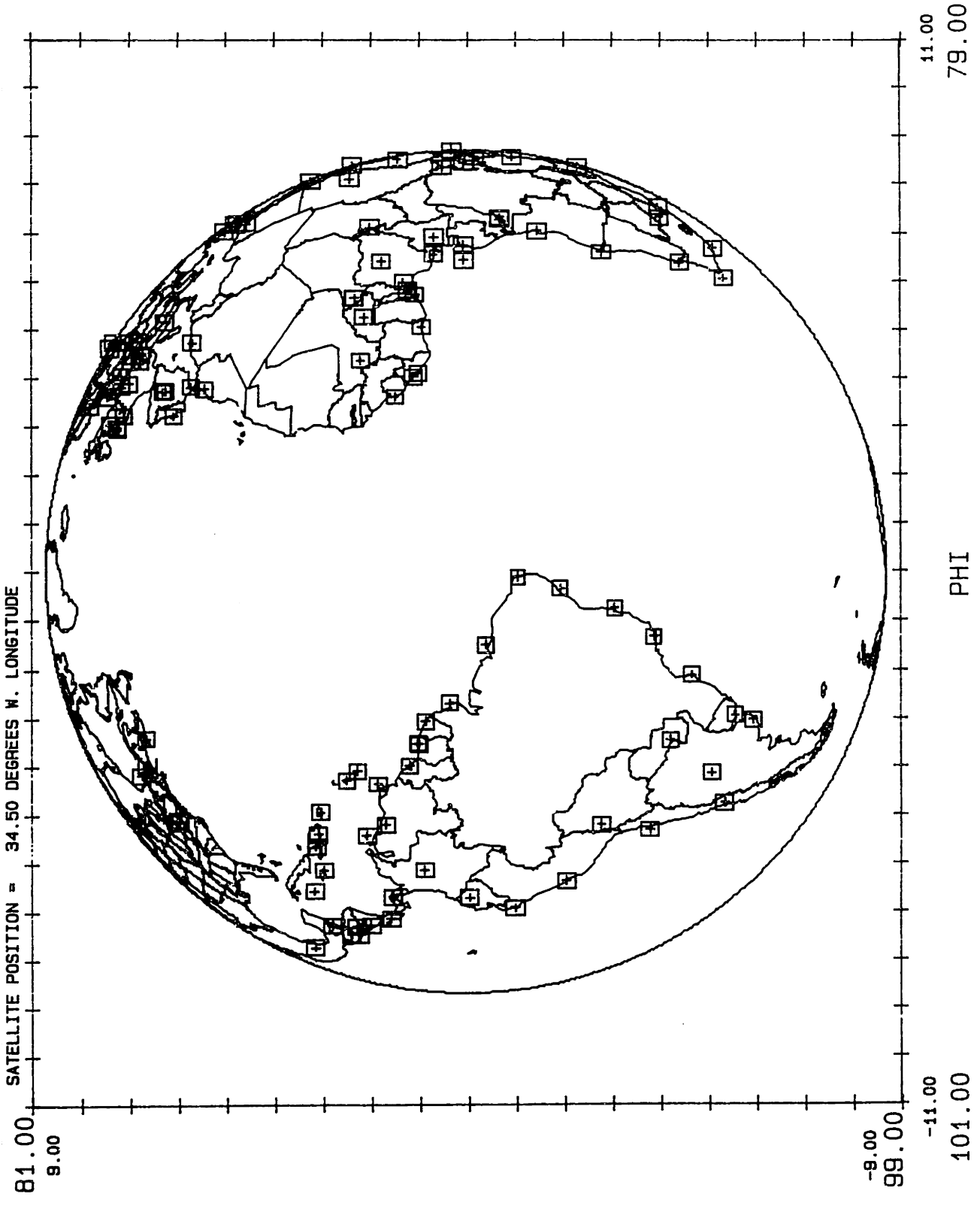


Figure 2. The Earth Viewed From Geosynchronous Orbit

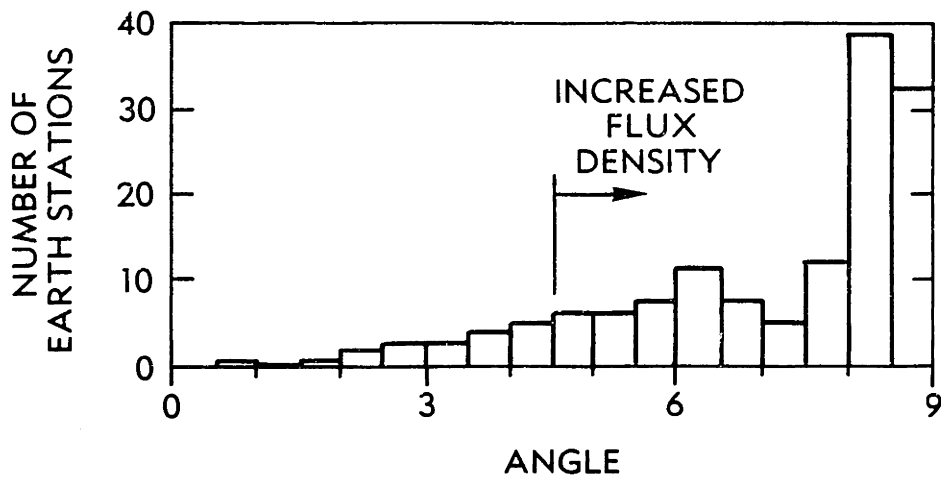
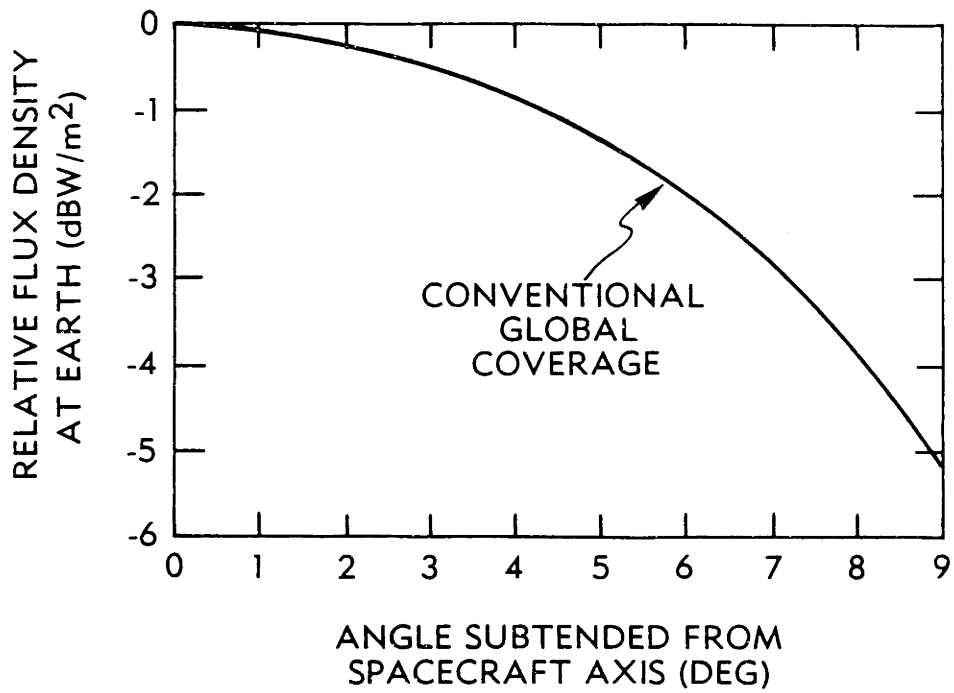


Figure 3. Comparison of Conventional Global Beam Coverage to Earth Station Density

Single reflectors, because of their simplicity, are used most often in satellites. They do have certain disadvantages, including long focal lengths, inconvenient feed placement, and lack of design flexibility. The paraboloid of revolution is the only single surface which will collimate the rays from a received plane wave. The scanning characteristics are well known, as indicated above.

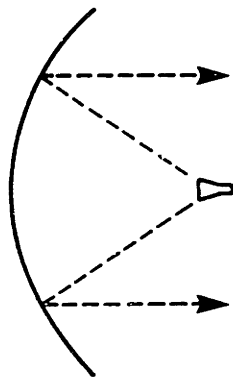
Dual reflector systems are an improvement over paraboloids in both packaging efficiency and design flexibility. Since the secondary reflector, the subreflector, redirects rays back to the main reflector, the actual system focal length is much less than its equivalent focal length. Also, the feed may now be positioned near or behind the main reflector, shortening feed lines and simplifying the placement of the associated electronics. Servicing and maintenance of the feed is simplified as well. Another mechanical advantage is the ease of supporting a relatively lightweight subreflector.

There are several disadvantages to the dual-reflectors. The subreflector blocks the center of the aperture--usually where radiation intensity is greatest--and thereby reduces efficiency. Gain suffers and sidelobe levels increase. The fact that two surfaces must intercept rays also introduces the problem of minimizing power missing the surfaces (spillover) while keeping the illumination efficiency high. Alignment is

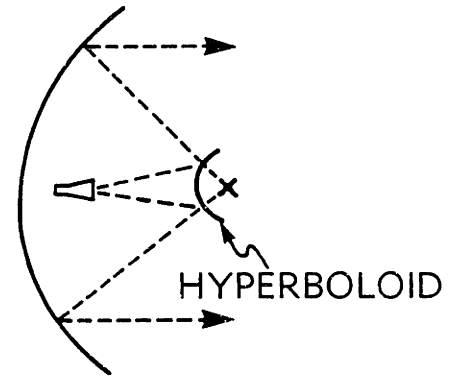
crucial in dual reflectors. Unlike single reflectors, where the feed concentrates power over the wide angle subtended by the main reflector, the dual-reflector feed must illuminate a much smaller subreflector. Thus larger feed horns are required and their placement must be precise [17]. Larger feed horns are less preferable for multibeam antennas, since their size may prevent their phase centers from being close enough to generate adjacent component beams.

Dual reflectors are of two major types; the Cassegrain and the Gregorian. Based on the optical telescope designs first introduced in 1672, they consist of a parabolic main reflector, and, respectively, either a hyperbolic or elliptical subreflector [18]. One of the two subreflector focal points coincides with the paraboloid focus, while the source is placed at the other focal point. Figure 4 shows the arrangement of these common antenna systems. A spherical wave leaving the source is transformed by the subreflector into a spherical wave emanating from the virtual focus of the paraboloid.

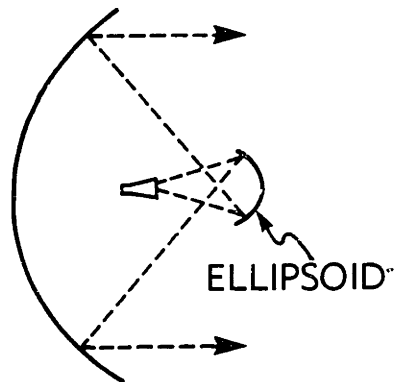
Several methods are used for analyzing Cassegrain antennas. One very powerful technique is that of defining the equivalent parabola, which has the same aperture and feed illumination angle as the Cassegrain [19]. The equivalent focal length f_e is equal to mf , where f is the main reflector focal



FOCAL POINT FED PARABOLOID



CASSEGRAIN ANTENNA



GREGORIAN ANTENNA

Figure 4. The Three Basic Types of Reflector Antennas

length and magnification $m = f_1/f_2$ is the ratio of the distances to the subreflector from each focus. For small scan angles, the equivalent parabola concept is very useful [20]. However, for larger feed displacements and scan angles, Figure 5, spillover prevents acceptable modeling of the dual reflector as a paraboloid. Note the reduced size of the scanned equivalent parabola in relation to the illuminated section of the main reflector.

Scattering theory and geometric theory of diffraction [21]-[26] have been used for a more detailed analysis. The mathematics is tedious and numerical methods are often required. Results are preferable to the equivalent paraboloid method since with the latter, the number of beamwidths of scan is the key parameter, whereas with dual reflectors the geometrical angle of scan is more important. Dual reflectors have less frequency dependence because of their relatively long effective focal length for the given packaging volume. Also, illumination efficiency is directly dependent on the system's geometry, and this tends to have the dominant effect in scanning. The scanning tradeoffs in dual reflectors are much more sophisticated than for paraboloids. The effective focal length increases as subreflector curvature increases. This implies, however, that the subreflector is smaller and spillover is of greater concern. On the other hand, if a

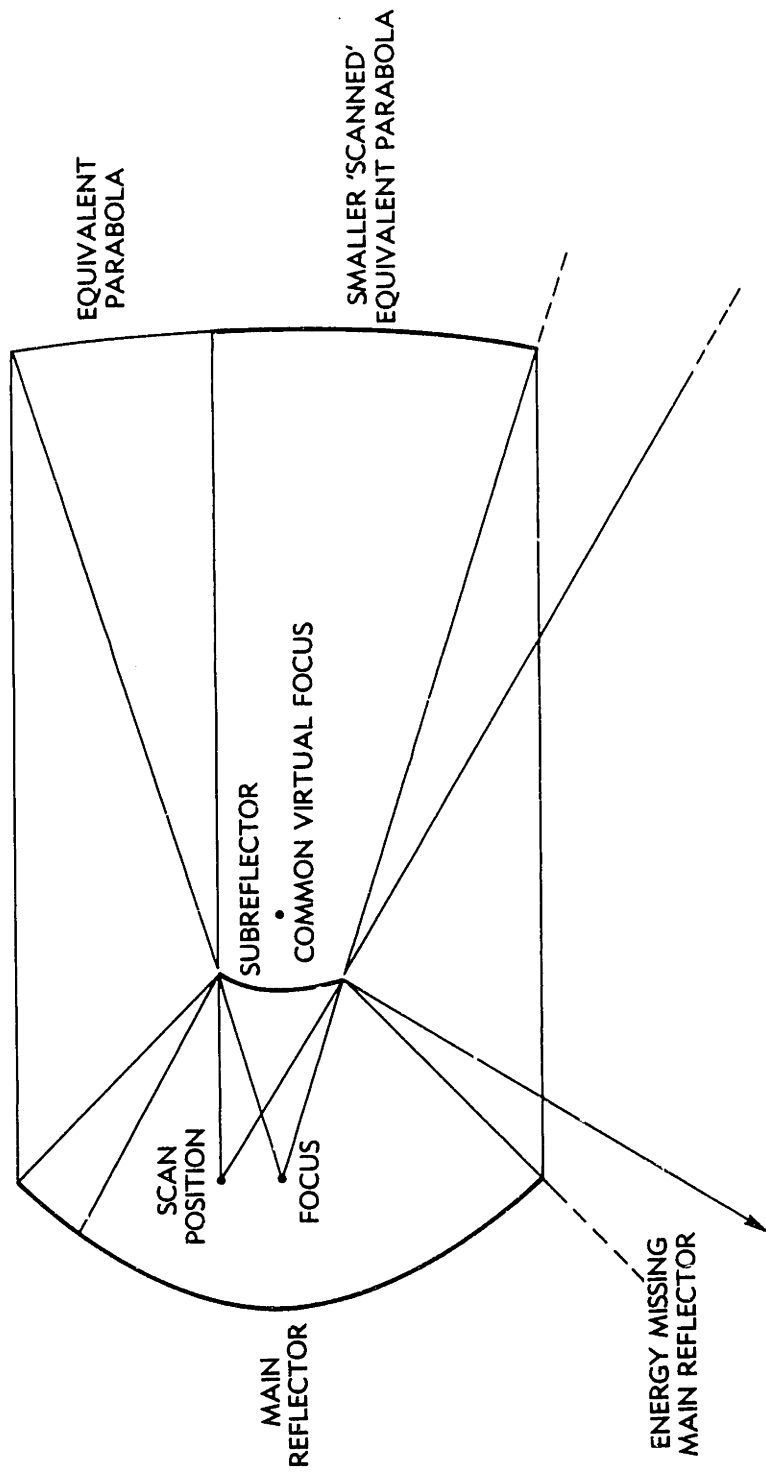


Figure 5. Limitations of the Equivalent Parabola Concept Applied to Scanning in a Cassegrain Antenna

flatter subreflector is used, its required area for efficient main reflector illumination is large and blockage becomes significant.

D. Reflector Design Fundamentals

Many attempts have been made to increase the performance of dual reflectors. Unlike with the single reflector, there are an infinite number of pairs of surfaces which produce a plane wave output for spherical wave input at the focus. Although it is possible to generate a dual reflector with an arbitrary phase and amplitude distribution at the aperture [27],[28] most efforts have been directed to simply improving the main reflector illumination efficiency.

With very few exceptions [29],[30], dual reflectors with "shaped" surfaces are synthesized using geometric optics [31]-[36]. This principle involves viewing propagation as a point-to-point correlation from wavefront to wavefront. A ray can be assigned to each point, pointing in the direction of the normal to the wavefront. This ray can then be traced through the reflector system. For homogeneous media, the Eikonal equation of optics states that all ray paths are straight lines. Electromagnetic radiation exactly follows the rays, with E and H fields aligned perpendicularly to each ray.

The geometric optics analysis of assuming zero wavelength must be viewed as an approximation when considering interaction with finite conductors. Diffraction effects are not present since edges only block rays, but cannot cause them to bend. Thus geometrical optics cannot be used to find the far-field radiation pattern of a well-formed beam, since it is entirely determined by diffraction.

Snell's law of reflection--that incident and reflected rays are coplanar, and that the angle of incidence equals the angle of reflection--can be directly applied to waves. Also useful is the theorem of Malus. It states that providing the rays are normal to one given wavefront, they are normal to every wavefront, despite any finite number of reflections or refractions. Thus the family of rays forms a normal rectilinear congruence with every wavefront. This is the basis for the principle of equal path length along any ray between two wavefronts.

One particularly useful aspect of the geometric optics analysis is the assumption that each ray represents a constant differential power flow. The power within a bundle of rays must remain constant throughout the optical system. Thus power density on any two wavefronts is inversely proportional to the ratio of areas bounded by a given set of rays. This

property of conservation of energy is useful in many synthesis applications.

Geometrical optics provides three sets of constraints for the synthesis of reflector antennas: Snell's law; the theorem of Malus (path length constancy); and conservation of energy. Other optical conditions are used for specialized systems. Specifically, the Abbé sine condition is used for scanning systems.

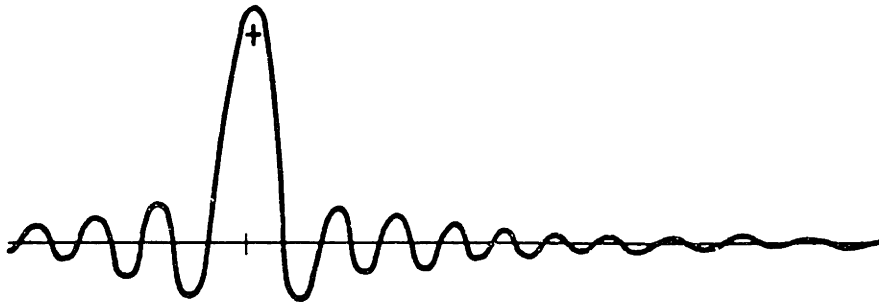
Two constraints--path length constancy and Snell's law--were used in deriving the parabola, which was rotated to form the single reflector surface. For a dual reflector, four constraints must be specified to generate the specific 2-dimensional profile. For symmetric systems, these are rotated as with the paraboloid.

Additional parameters must be specified if the conservation of energy constraint is imposed. This constraint merely describes how the feed phase and amplitude distribution are transformed to an aperture distribution. Thus it is necessary to specify the input and output distributions. In most cases the input is tapered feed pattern with amplitude of the form $\cos^n \theta$ and with a spherical phase distribution. The wave at the aperture is most often a uniformly illuminated plane wave.

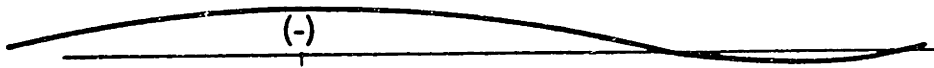
Several authors have introduced shaped Cassegrain antennas using this complete synthesis procedure [27],[28],[37],[38]. Solutions to the derived equations require numerical methods. The resulting surfaces are generally both transcendental functions which are difficult to fabricate and analyze.

A great deal of effort has been spent on dual reflector designs which keep one of the standard Cassegrain surfaces fixed (usually the main reflector) and shape the other. Green [39] first showed that by shaping the subreflector, and then making small alterations to the main reflector to preserve the planar phase front, uniform illumination could be attained. The beam is not exactly focused, but the improvement in performance is appreciable. Other systems [40]-[47] consider correcting for main reflector deformations or errors, or generating particular aperture distributions and polarizations.

The difficulty of subreflector blockage has come up many times in the preceding description. Figure 6 illustrates the deleterious effects of blockage and spillover. Since the Fourier transform is a linear operation, these numerous individual effects can be added together. The subreflector blockage can be thought of as the removal of a circle of uniform, constant amplitude power from the center of the



a) Diffraction pattern of aperture



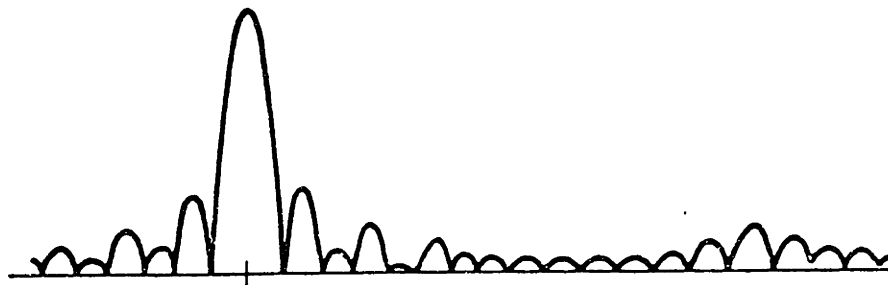
b) Subreflector blockage



c) Spar blockage (spar perpendicular to scan plane)



d) Subreflector spillover



Resulting radiation pattern

Figure 6. The Degrading Effects of Subreflector Blockage and Spillover on the Radiation Pattern

aperture. Thus one subtracts a much wider $\sin x/x$ pattern from the original far-field pattern. Also consider the small effect of spars, which lowers gain evenly across the field of view. These effects lower the main lobe power level, and simultaneously increase the first and third sidelobe dip. The result is lower gain and higher sidelobe magnitude. Power spilling past the subreflector is sufficiently large and close to the axis to also become apparent on the combined pattern. With single reflectors, the spillover is almost 150° away from the axis, so it is negligible. Methods of making the subreflector less obstructive have been proposed [18],[24] such as serrating or perforating the surface; or fabricating it from a linearly polarized material, illuminating it with radiation of the orthogonal polarization, and using a twist reflection material for the main reflector. A much more feasible concept is the offset configuration. This consists of a section (usually circular) of the main reflector and the corresponding section of the subreflector of a symmetric dual reflector (Figure 7). Blockage is eliminated and the VSWR of the feed is reduced, but the focal-length-to-diameter ratio (f/D) has increased by the ratio of the parent main reflector diameter to the offset section diameter. The lack of symmetry also tends to increase cross polarization and make analysis much more difficult.

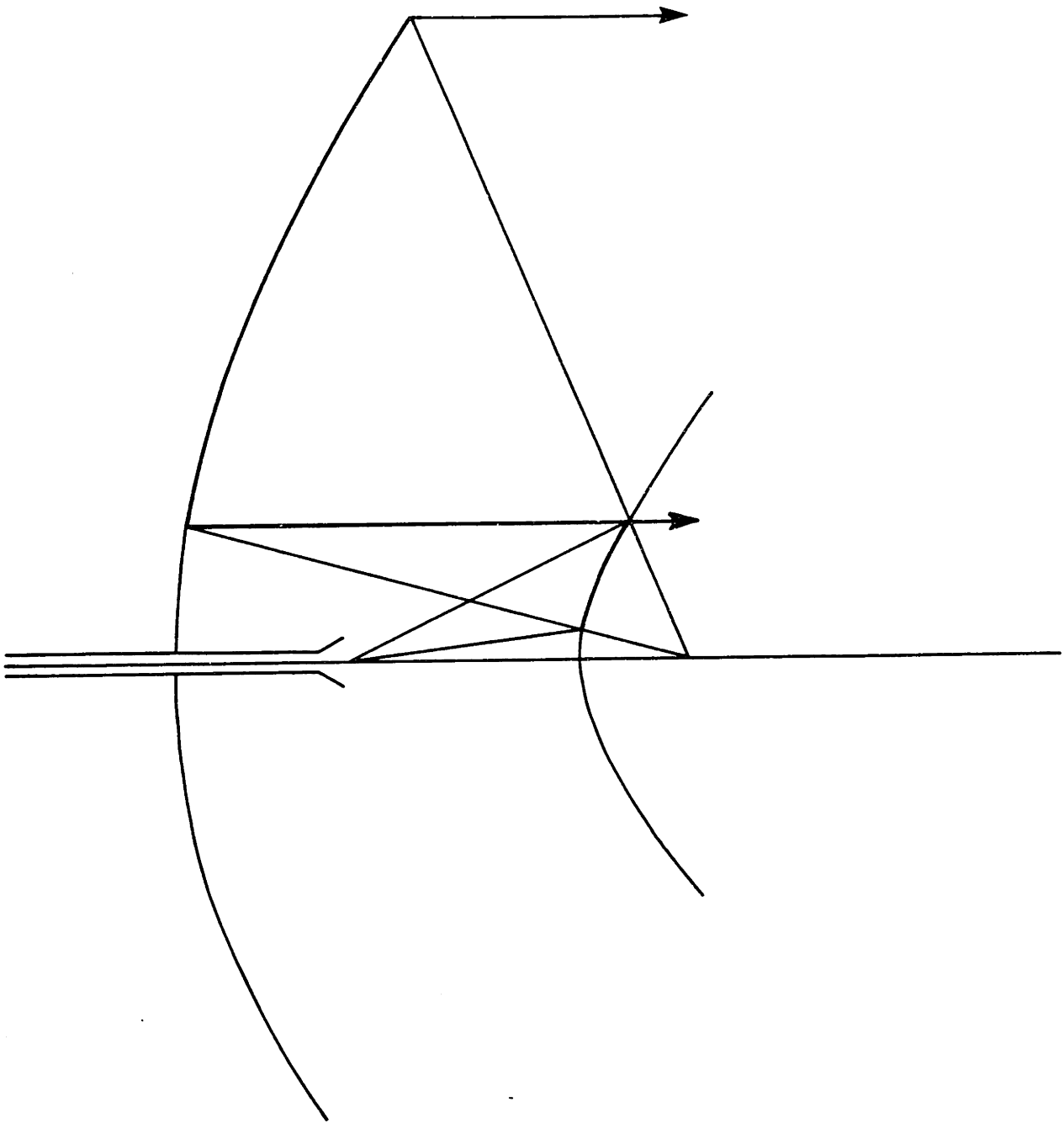


Figure 7. Offset Dual Reflector Derived from the Symmetric Parent Dual Reflector

Offset designs often make use of the Gregorian configuration. In the symmetric case, having a concave subreflector increases the reflector separation without much improvement in performance. Since the Gregorian subreflector inverts the reflected image, it can be placed entirely below the antenna axis and illuminate the main reflector anywhere above the axis. Blockage is avoided while still using a large offset section of the main reflector. With special geometrical restrictions, cross polarization can be eliminated [48]-[50] with the Gregorian configuration.

Simultaneous shaping of both surfaces of dual offset reflectors has been explored [51]-[55]. The problem involves solving a pair of partial nonlinear differential equations. These simplify to ordinary differential equations when the offset is eliminated and the system becomes symmetric. Approximate methods of solving the equations show reasonable analytic results [51], but the processes involve considerable trial and error and significant amounts of numerical computation.

E. Reflectors Designed for Scanning

Scanning with an offset system is slightly different from the symmetric case. The optimum focal locus is no longer symmetrically disposed about the antenna axis. Instead, the

best focal positions for scanned beams, to the first approximation, are on the plane perpendicular to the offset axis [56]-[59]. The precise feed position depends on spillover and illumination efficiency as well as path length and phase error considerations.

Dual offset reflectors have also been used in scanning applications [60]-[64]. However, the principle of an inclined focal locus was not introduced until recently [65] by Krichevsky. For considerable amounts of beam scanning, the equivalent parabola concept must be discarded. Thus, this problem of choosing the optimum focal point for a particular scan angle while keeping spillover in mind is very difficult. The choice is strongly dependent on the particular Cassegrain geometry. Changing either surface curvature will greatly change the position of the focal surface. Figure 8 indicates a typical result found by Krichevsky. Lines of constant scan angle are indicated, as well as the optimum positions along these lines. It should be noted that both the linear and second order approximations differ considerably from the optimal focal line predicted by the equivalent parabola model.

The tilted optimal focal locus indicates an additional level of flexibility in the design of scanning antenna systems. There is also an increase in complexity associated with

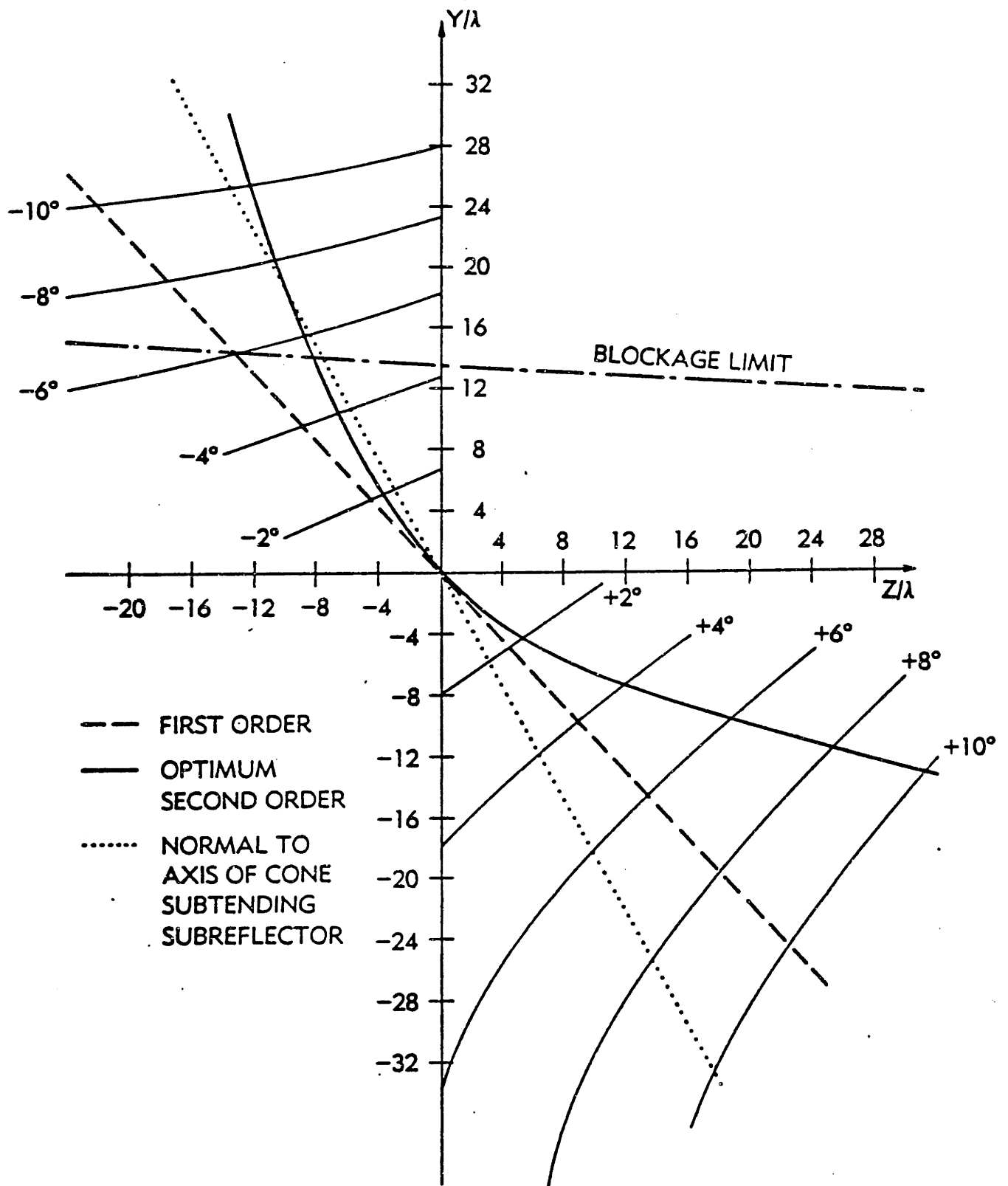


Figure 8. Optimal Focal Loci for an Offset Cassegrain

offset systems. This is the primary reason why scanning systems are almost always symmetric designs. Figure 9 depicts ray tracing in an offset dual reflector scanning system along with ray paths for $\pm 9^\circ$ of scan.

Several antennas have been developed to deal specifically with scanning. The spherical cap [66] is the simplest scanning antenna. With a source positioned approximately halfway between the sphere and its center, the surface resembles a paraboloid over a limited angular region. In fact, if the parabola's curvature value at its vertex is inverted and used as the radius of the osculating circle at that vertex, this circle corresponds to the profile of the spherical cap.

Since it is not a perfect paraboloid, the cap suffers from spherical aberration. This aberration increases with larger angular illumination from the feed or with higher frequencies. The sphere's symmetry would produce identical patterns for all scan orientations as long as there is no spill-over. This would imply the entire reflector is underilluminated. Usually a compromise is made between scanning perfection and reflector inefficiency.

Subreflector correctors have been designed [67] which eliminate the spherical aberration in the cap. Usually of the Gregorian type, they make use of the sphere's caustic to collimate all incoming rays. Unfortunately, the corrector

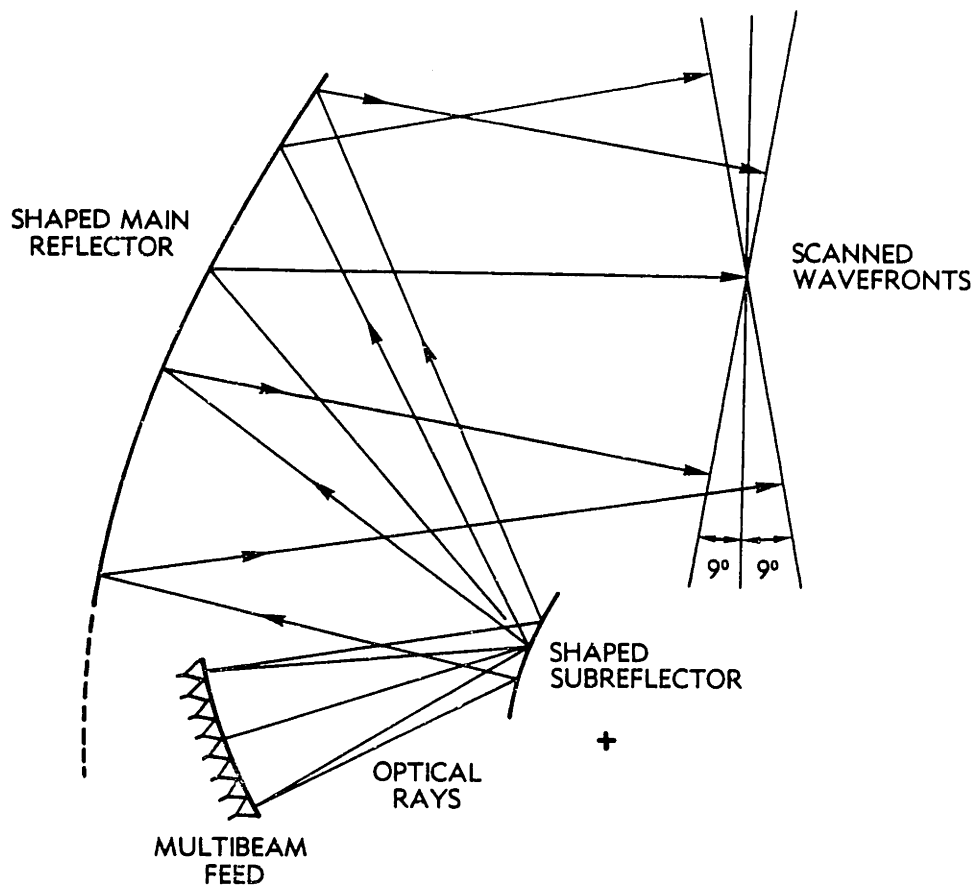


Figure 9. Ray Paths for a Scanning Dual Reflector

only works for one particular scan direction, and must be moved mechanically if the beam is to be redirected. This characteristic makes scanning arrays impractical and shaped beams impossible for corrected spherical caps.

Some possible improvements to the basic spherical cap are the torus and the spheraboloid [68]. The latter attempts to reduce spherical aberration at the expense of scanning performance by choosing the surface which is the locus of points midway between the sphere and the closest paraboloid. The torus is a doubly curved surface with a circular profile in the plane of scan and a parabolic profile in the orthogonal plane (Figure 10). Thus the torus is capable of scanning in one plane only.

These circular systems, the Cassegrain, and the bifocal--which will be discussed in the following chapters--are compared in Figures 11 and 12.* As expected, the gain is high and uniform across several degrees for the spherical cap. The less circular antennas have an increasing amount of scan loss. The bifocal is the worst on axis but improves for its design scanning position of 5°. Observing sidelobe values, Figure 12, one sees the defocusing effects of spherical

*The torus reflector is not included because it is usually rectangular, while the above antennas have circular apertures.

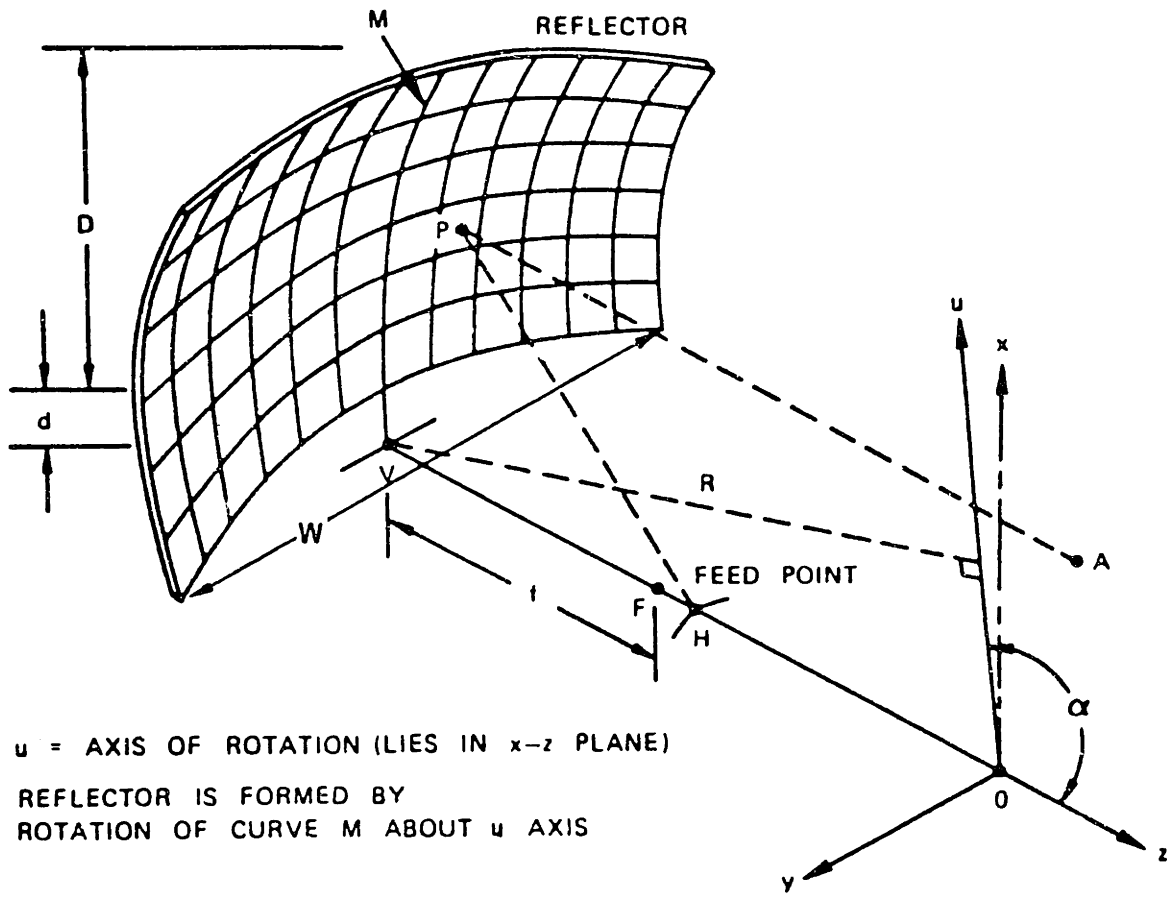


Figure 10. Torus Geometry

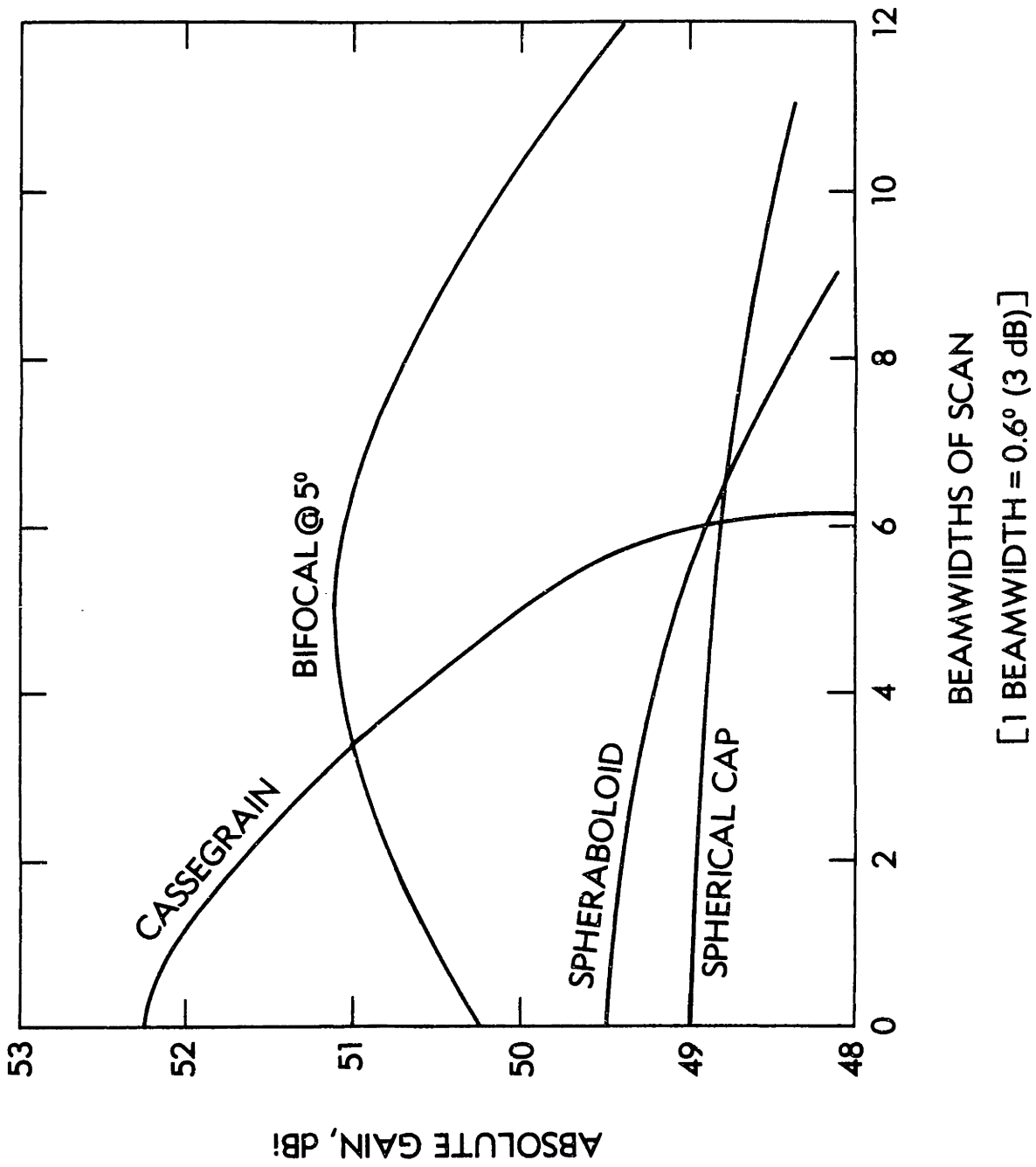


Figure 11. Comparison of Scanned Gain Reduction for Various Reflector Antennas [1 BEAMWIDTH = 0.6° (3 dB)]

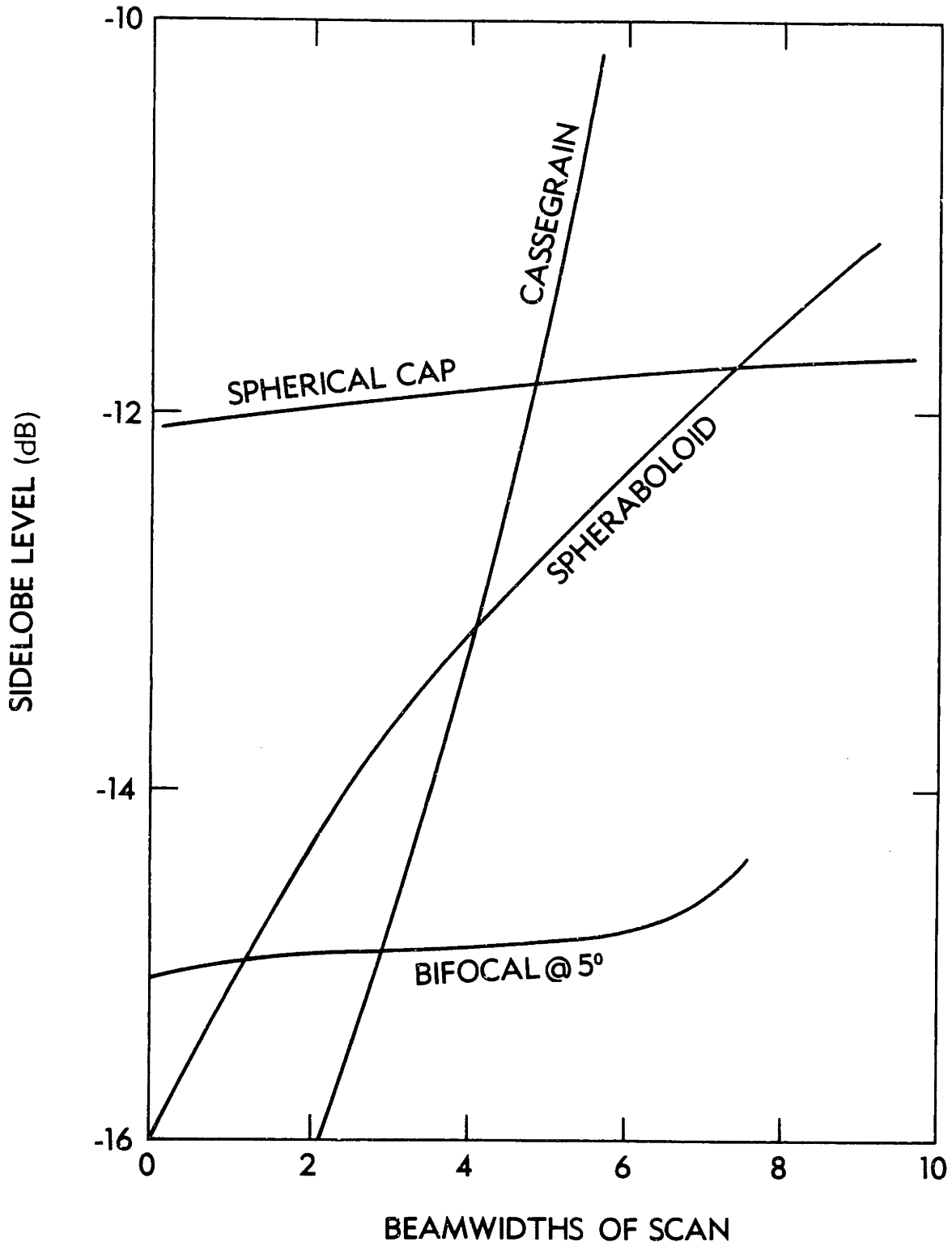


Figure 12. Comparison of Scanned First Sidelobe Level for Various Reflector Antennas

aberration. As with the above trend, the closer to spherical the surface, the higher and less scan dependent the sidelobe level. If sidelobe level is critical, the bifocal appears to be the best overall choice.

Two other designs have been discussed in the literature. The confocal paraboloid [59],[69] has a feed array in the near field of a small offset parabolic subreflector with focal point coinciding with the main reflector's. This type of antenna has been shown to scan effectively up to 3° . The final scanning dual reflector is the Schwarzschild antenna. This system is described in the next chapter.

II. SCHWARZSCHILD ANTENNA

A. Optical Considerations and Capabilities of the Schwarzschild Antenna

One of the very limited number of antenna designs which specifically addresses the wide angle scanning problem is the Schwarzschild system. Although Schwarzschild's work concerned optical telescopes, his ideas have been readily transferred to antenna design [70]-[75]. Unlike the spherical cap or torus, this dual reflector has a perfect focus for the unscanned beam, and thus more closely resembles the Cassegrain antenna.

The Schwarzschild's distinguishing characteristic is its aplanatism. This is the optical principle, used in lens design, to ensure optimum collimation of paraxial rays [9]. A system is said to be aplanatic if axial points form a stigmatic image of each other, and if their conjugate rays satisfy the "Abbé sine condition." The first condition implies a perfect point focus for axial rays originating at infinity (that is, a plane wave).

The Abbé sine condition is illustrated in Figure 13. Briefly, it states that for a ray leaving the focus with an angle α , and emerging from the system at a height y , that

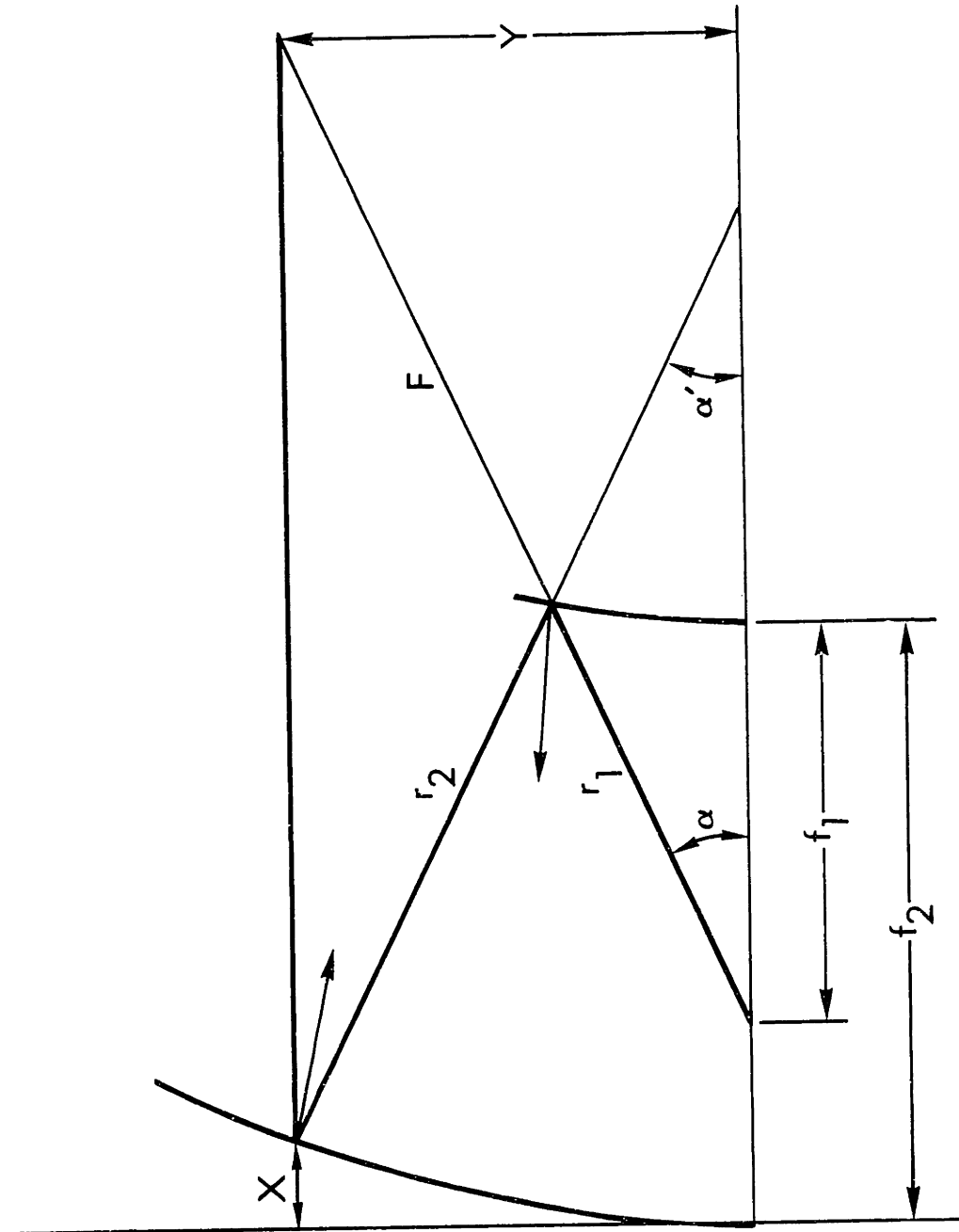


Figure 13. Geometry of the Schwarzschild Dual Reflector

$y/\sin \alpha$ is a constant F . Fulfilling this geometrical condition eliminates the first order coma term. Thus, the Schwarzschild has a coma coefficient which approaches zero at the focus with zero slope (Figure 14). The higher order coma terms are not eliminated by the sine condition, so although the Schwarzschild is superior to the Cassegrain for all angles, it is only for paraxial rays that there is a particular advantage in using it.

The geometrical design of the Schwarzschild is similar to the Cassegrain. Since two reflector surfaces are to be specified, four constraints can be imposed. The first, the Abbé sine condition, replaces the Cassegrain's conservation of energy of a ray bundle traced through the system. The remaining three: the theorem of Malus, that a wavefront is perpendicular to all rays at points which have the same path length from the focus, and Snell's law applied to each surface, are common to both antennas.

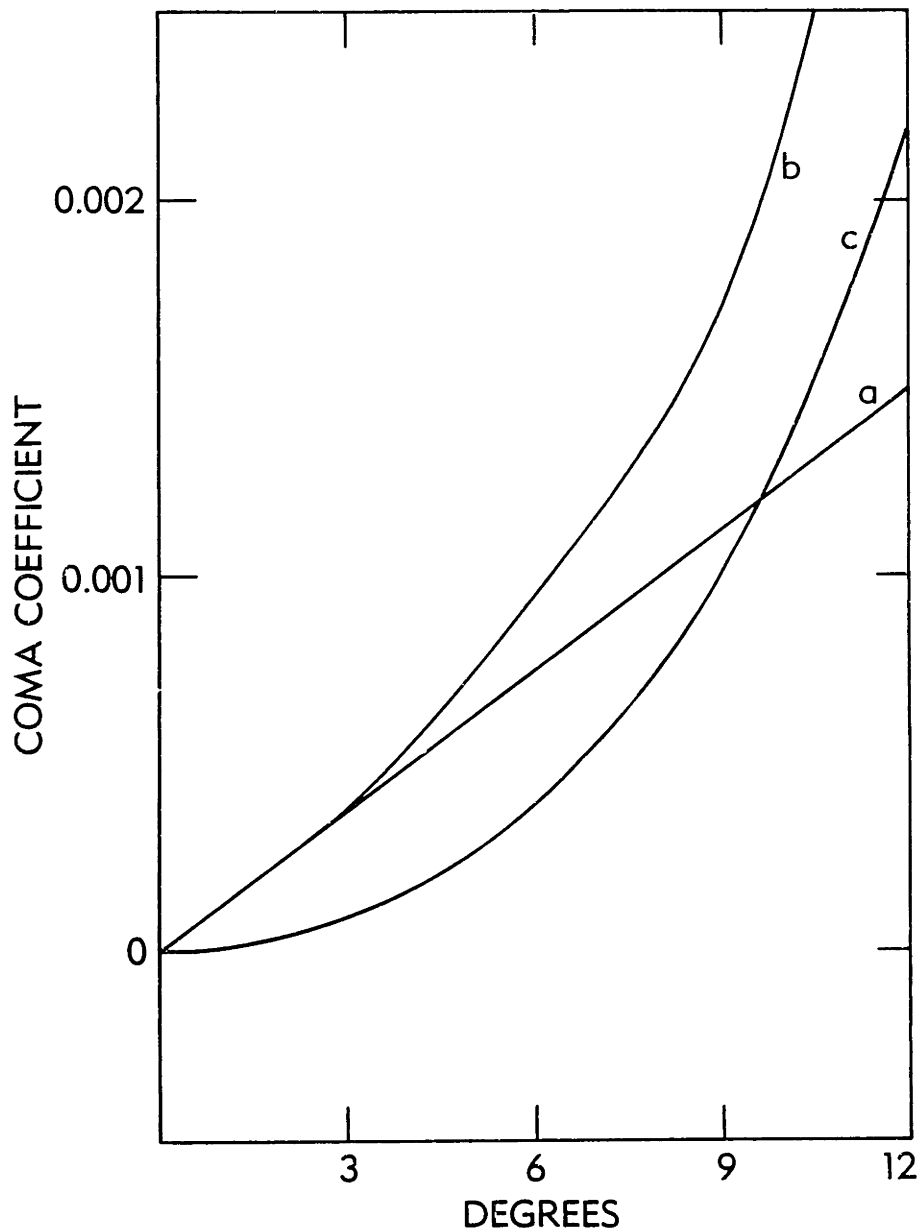
These constraints can be stated mathematically as:

$$(1) \quad y = F \sin \alpha$$

$$(2) \quad r_1 + r_2 = f_1 + f_2 + x$$

$$(3) \quad \frac{1}{r_1} \frac{dr_1}{d\alpha} = \tan \left(\frac{\alpha + \alpha'}{2} \right)$$

$$(4) \quad \begin{cases} r_1 \cos \alpha - r_2 \cos \alpha' = f_1 - f_2 + x \\ r_1 \sin \alpha + r_2 \cos \alpha' = y . \end{cases}$$



a-PARABOLOID
 b-CASSEGRAIN
 c-SCHWARZSCHILD

Figure 14. Comparison of Coma Aberration for Three Reflector Antennas: a) Paraboloid, b) Cassegrain, and c) Schwarzschild

Note that Snell's law at the main reflector is implied from condition (1) and the geometrical relations (4).

B. Graphical Solution to the Schwarzschild Equations

Solutions to these constraints can be found analytically or graphically. Ponomarev [72] devised an iterative graphical method of generating Schwarzschild profiles. His approach ignores the path length constraint and explicitly applies Snell's law at the main reflector. The essence of his argument is that for the Abbé sine condition to hold, every ray traced through the reflector system intersects the ray projected through the subreflector, at a distance F . Thus, by drawing a circle of radius F about the focus, choosing points on this circle, connecting the points to the focus to define rays and simultaneously drawing horizontal rays back from these points, and determining the paths between the two reflectors, the system can be defined (Figure 15). The final step of determining the actual connecting paths between reflectors is accomplished by first choosing a pair of arbitrary starting points for each reflector. These two must be on two rays which intersect at the circle. Then using Snell's law, the normals to the reflector curves at these points are found by bisecting the angles formed by the connecting ray and the

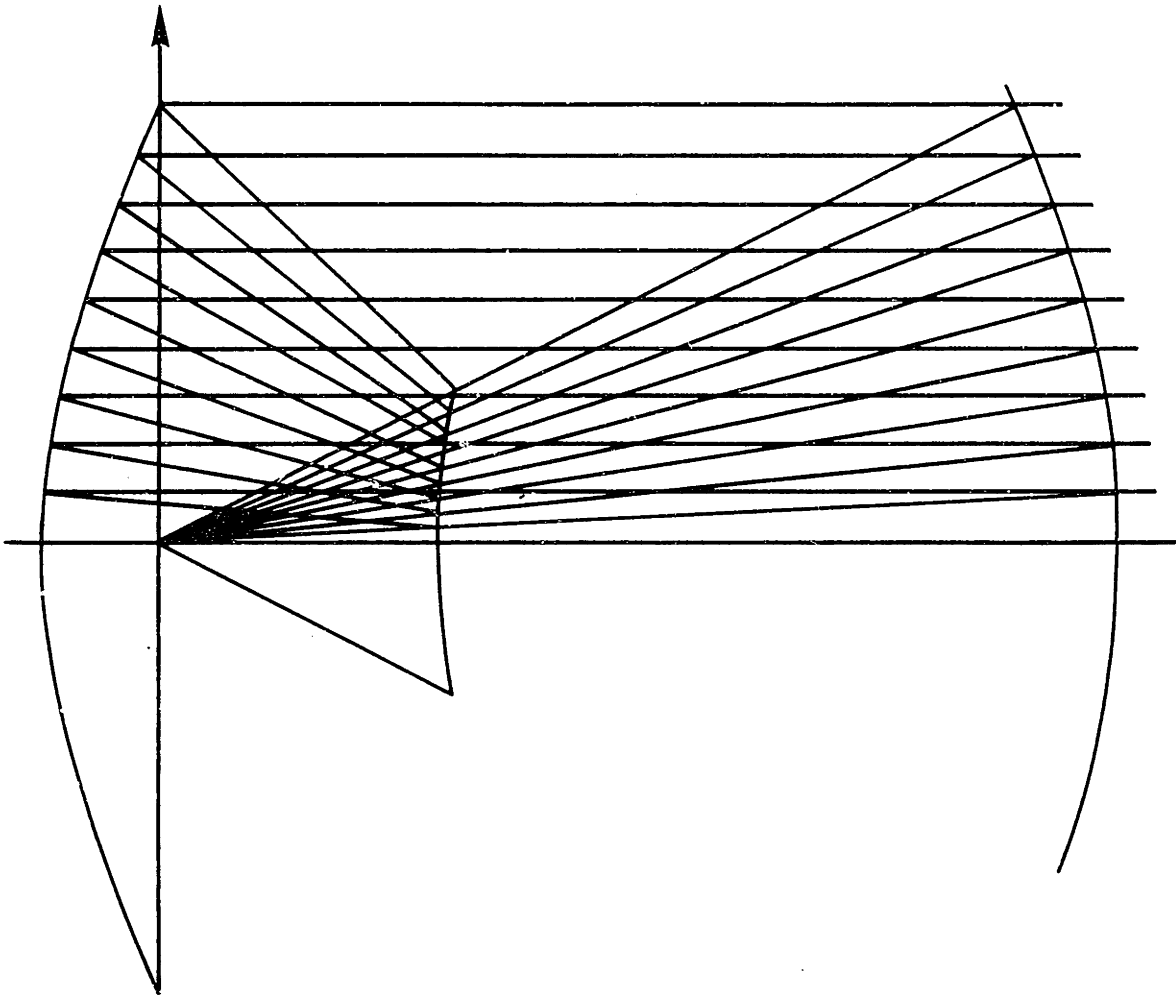


Figure 15. Graphical Method of Generating Schwarzschild Profiles

radial or horizontal rays. Once the normals are known, tangential rays through the point are extended until they intersect the next radial or horizontal ray. This defines the next pair of reflector points. This procedure is then repeated until a sufficient number of points has been generated. The points can then be connected with straight lines, cubic splines, or best fit to polynomial curves using least squares, or Lagrangian interpolation.

Unfortunately, the choice of the arbitrary starting points is crucial in the design of the profiles. Unless great care is taken in their selection, the following iterations may produce normals which vary so greatly that an unreasonable geometry may result. Furthermore, it is very difficult to determine the final reflector diameters, separation, and illumination requirements before beginning the iterations.

C. Analytic Solution of the Schwarzschild and Comparison to the Cassegrain

A more useful solution to the Schwarzschild is the analytic one [70]-[71]. Details of the derivation of this solution are presented in this chapter's first appendix (Appendix II.1). The parametric results (for input parameters F , f_1 , f_2 , and variable α) for the subreflector are:

$$x_s = r_1 \cos \alpha - (f_1 - f_2),$$

$$y_s = r_1 \sin \alpha,$$

with

$$r_1 = \frac{1}{\frac{s}{f_2} + \frac{1}{f_1} \left(1 - \frac{sF}{f_2}\right)^{f/(F-f_2)} (1-s)^{-f_2/(F-f_2)}}$$

with $s = \sin^2 \alpha/2$, and the main reflector:

$$x_m = -f_1 + \frac{(1-s)[sF^2 + r_1(f_2 - 2sF)]}{f_2 - r_1 s}$$

$$y_m = 2F\sqrt{s(1-s)} .$$

A computer program, written in SPEAKEASY, was used to calculate and plot solutions to the profile equations. A listing is provided in Appendix II.2. One of the cases examined, for the solution to $F = 5$, $f_1 = f_2 = 1$, is shown in Figure 16 (for the right half only). The best fitting fourth order polynomials for the subreflector, PS, and main reflector, PM, are included. It is noted that the entire reflector system closely resembles a Cassegrain. Furthermore, the equation of the main reflector varies from a perfect parabola by not more than 1.1 percent over its full range. The difference between the two reflectors is apparent in the subreflector. For a Cassegrain with the similar parabolic main reflector and some initial subreflector point $y = 1$, this hyperboloid would have the form

$$y = 0.625 + 0.375 \sqrt{1 + \left(\frac{x}{0.5}\right)^2} .$$

```

T2 = 1
FOCUS = 0
PH (A 5 COMPONENT ARRAY)
-5.4146E-5 -5.4642E-15 .2002 1.6752E-15 -3.3696E-4
PS (A 5 COMPONENT ARRAY)
1.0013 2.0591E-14 .68237 -5.7779E-14 -.33528

```

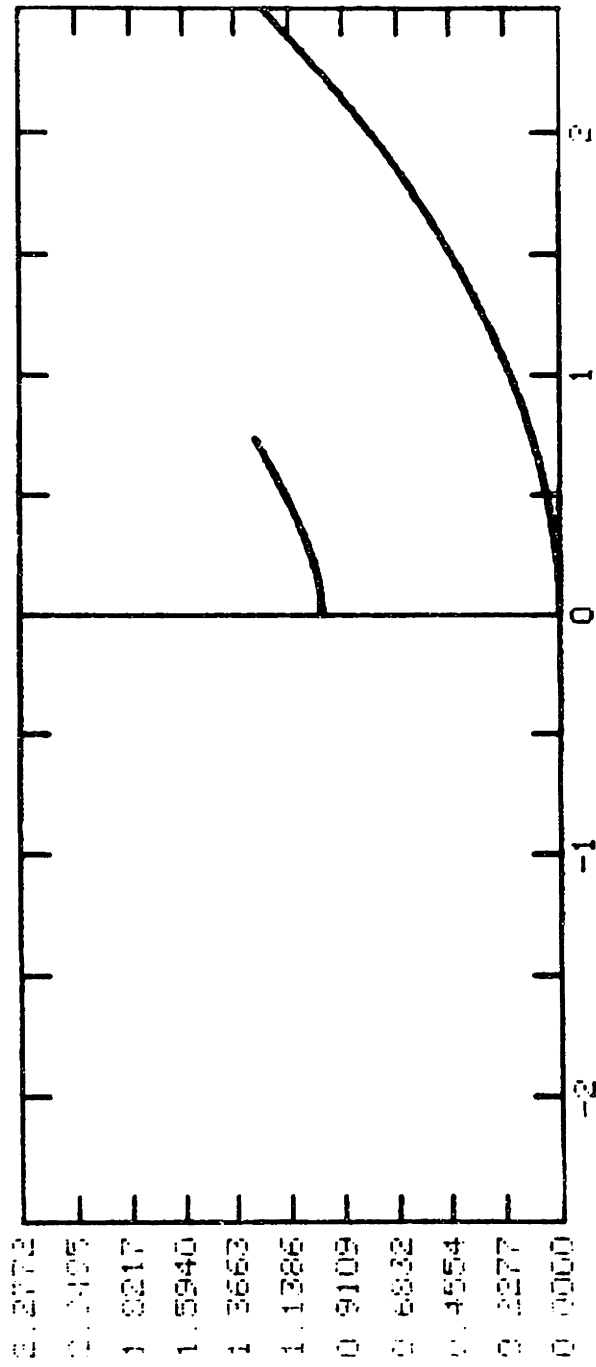


Figure 16. Right Half of a Symmetric Schwarzschild Profile

This is approximated to fourth order by

$$y = 1 + 0.75x^2 - 0.75x^4 .$$

This equation appears to differ from the Schwarzschild subreflector a great deal. In fact, the differences are hardly visible graphically. There is slightly more curvature near the axis, and less farther away. Electrically, the differences are more noticeable. Figure 17 shows a computed radiation pattern. The sidelobes are higher than normal, and the first nulls have filled in considerably. These effects may be due to approximation errors or to inefficient illumination of the main reflector.

The scanning performance of the Schwarzschild is illustrated in Figure 18, which was calculated by White and DeSize [70]. It depicts the normalized path errors across the aperture for both types of antennas. The Schwarzschild is always better, although it appears to be primarily effective for less than 5°.

It is noticed that Schwarzschilds, with a large value for F , increasingly resemble Cassegrains. This is based on the first-order equivalence of F and F_{eq} --the Cassegrain equivalent focal length. For a given height off the axis, an increase in F increases the radius of the circle of radial and horizontal ray intersection until it can be approximated as a parabola. This corresponds to the equivalent parabola of a

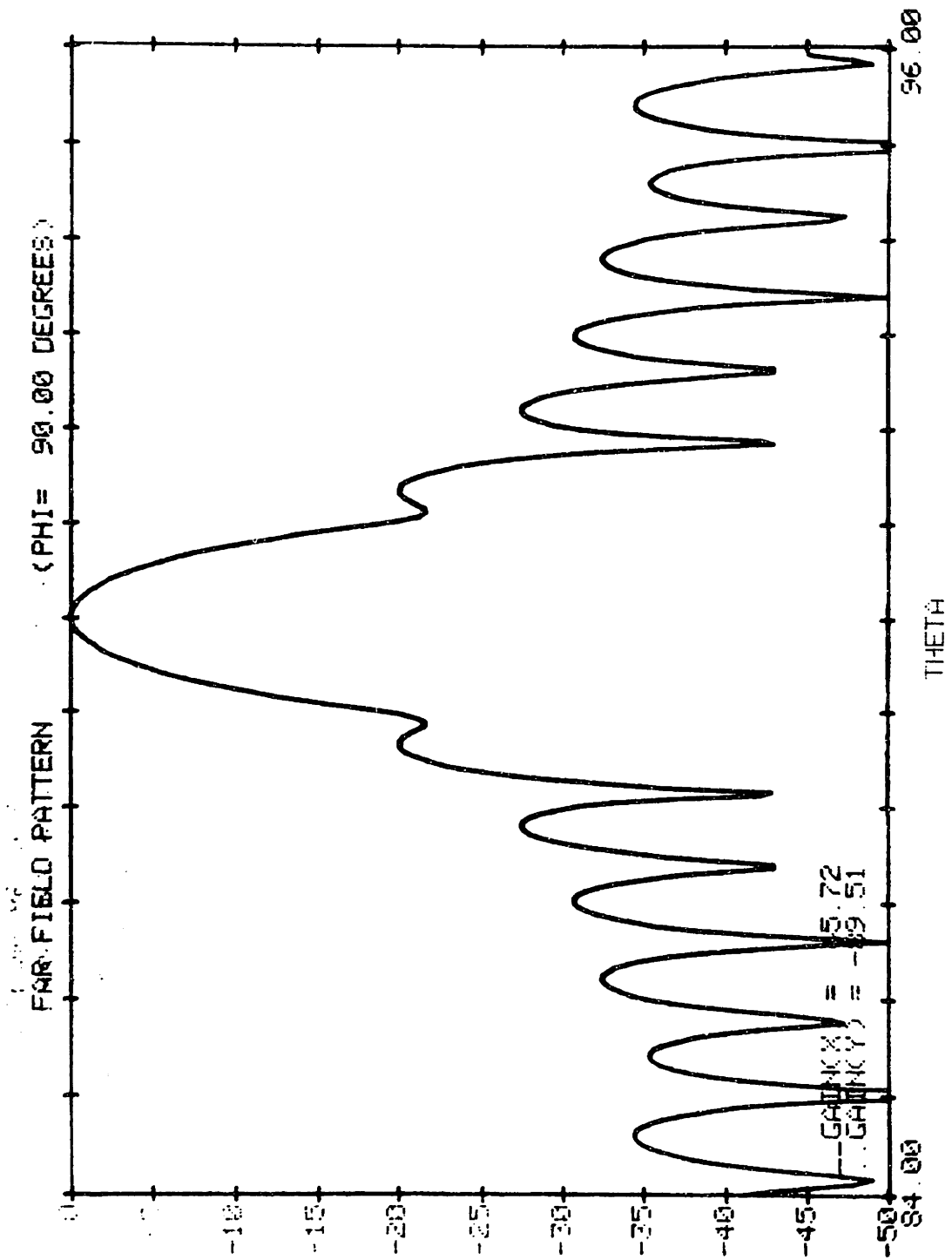


Figure 17. The Far-Field Radiation Pattern of a Symmetric Schwarzschild Antenna

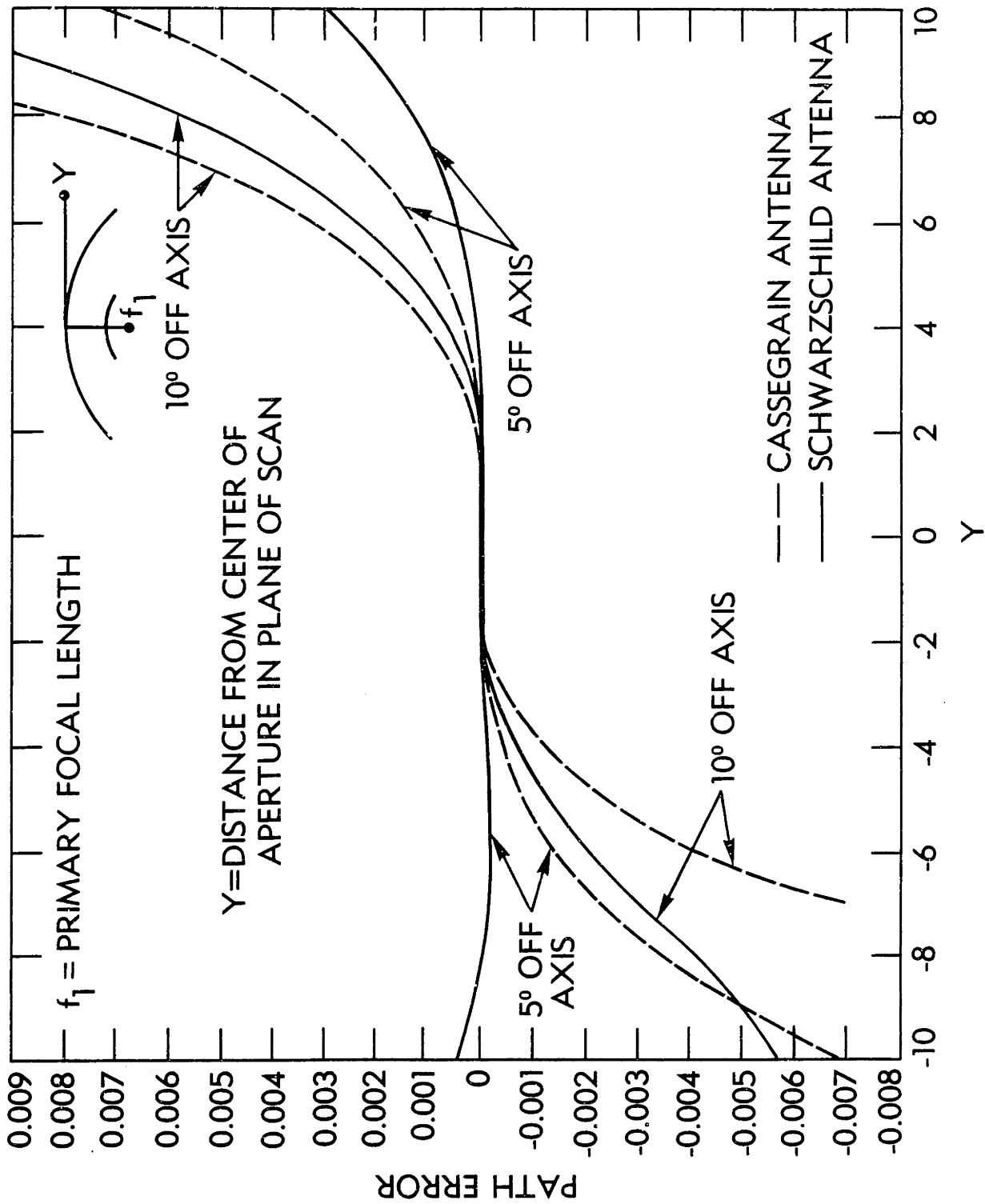


Figure 18. Scanning Performance of Cassegrain Antenna vs Schwarzschild Antenna

Cassegrain system. To fully specify the Cassegrain, the only additional necessary parameter is its magnification, which identifies the relative separation of the reflectors. In terms of Schwarzschild parameters,

$$m = \frac{f_1}{F_p - f_2} \quad (\text{II-1})$$

and

$$m = \frac{F_{eq}}{f_1} \quad (\text{II-2})$$

where F_p is the focal length of the parabolic main reflector.

This formula predicts a magnification of 4.0 for the case previously examined. However, if the value of F and F_{eq} are both chosen to be 5, the magnification from formula (II-2) becomes 5, and F_p becomes 1.2. This makes the coefficient of the parabola's quadratic term 0.2083, up from 0.2002. On the other hand, the relative spacing can be altered to keep the same parabolic main reflector. In this case, $f_1 = f_2 = 1.035$. Finally, the main reflector and reflector spacing could be kept constant, and the focal point could be moved. This makes $f_2 = 1.05$, a 5-percent increase.

In all of the comparative cases, it is seen that the Schwarzschild's feed illumination angle is larger. This is reasonable, since it is necessary to minimize the effects of transverse feed displacements. This fact does, however, lead to a serious subreflector blockage problem.

D. Alternative Schwarzschild Design

One method of minimizing blockage effects is to use a Gregorian Schwarzschild configuration. Figure 19 shows an example of this geometry. The only modification necessary to the above formulation is to choose a negative F . Optically, this implies having rays cross and invert between the two reflectors. Blockage is eliminated, although the packaging size has increased. Since the conservation of energy constraint is not used in the formulation of the profile equations, the crossing of rays does not cause any mathematical problems. This design offers excellent scanning possibilities without the overwhelming blockage problems of standard Schwarzschilds. Figure 20 shows the far-field pattern for this offset Gregorian configuration. It was found that the pattern is very sensitive to subreflector perturbations. A fourth-order least-squares polynomial was used to approximate the profiles, but sizeable errors for the subreflector were still present. This may explain the unusual hump near the beam peak.

The scanning performance for this antenna is shown in Figure 21. With the feed moved from the focal point $(0,0,-0.5)$ to the scan position $(-0.4,0,-0.5)$, the beam scans 5.3° . The gain loss is 3 dB.


```

PM (A 5 COMPONENT ARRAY)
-2.6835E-6  4.4378E-14  .32501  -1.0813E-14  3.6863E-4
PS (A 5 COMPONENT ARRAY)
.9962  -1.3508E-13  -1.0505  6.2337E-13  -2.2229

```

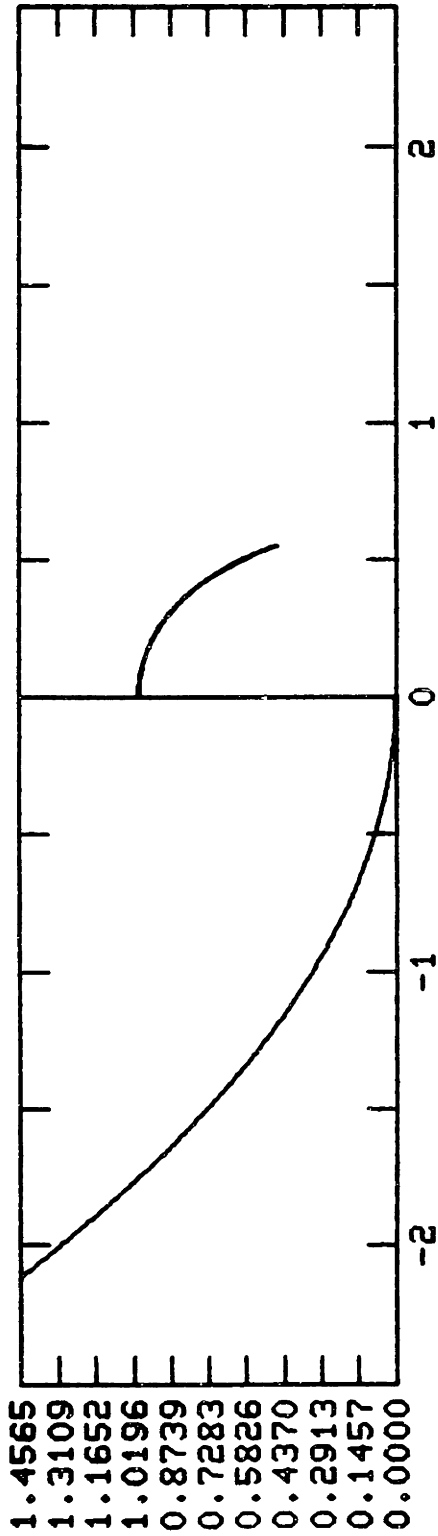


Figure 19. Gregorian Schwarzschild Profile

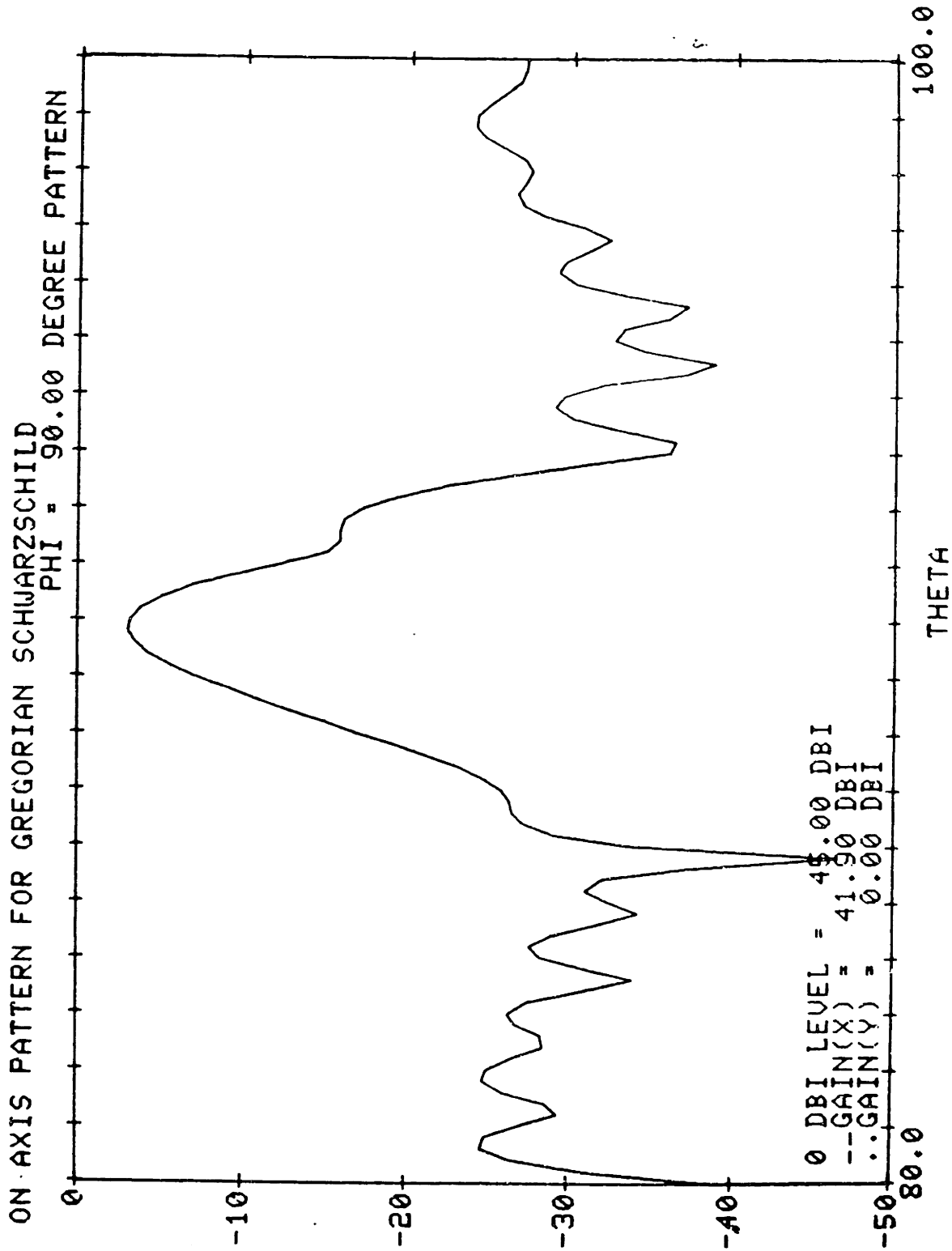


Figure 20. Radiation Pattern for the Offset Gregorian Schwarzschild Configuration: On-Axis Beam Configuration

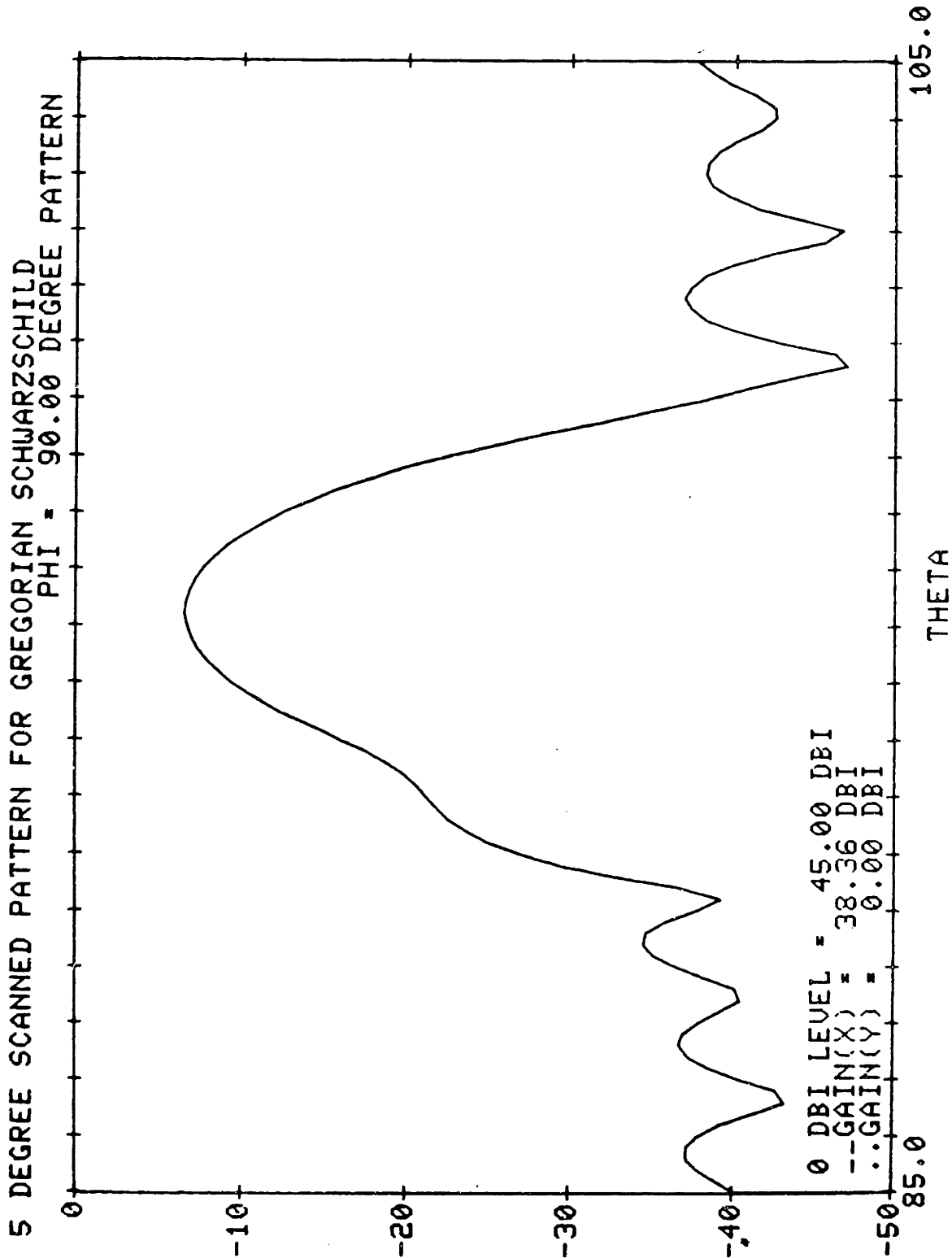


Figure 21. Radiation Pattern for the Offset Gregorian Schwarzschild Configuration: 5.5° Scanned Beam

APPENDIX II.1. DERIVATION OF THE SCHWARZSCHILD
REFLECTOR ANTENNA PROFILE EQUATIONS

Referring to Figure 13 and using the five constraining equations:

$$y = F \sin \alpha \quad (\text{II.1-1})$$

$$r_1 + r_2 = f_1 + f_2 + x \quad (\text{II.1-2})$$

$$\frac{1}{r_1} \frac{dr_1}{d\alpha} = \tan \left(\frac{\alpha + \alpha'}{2} \right) \quad (\text{II.1-3})$$

$$r_1 \cos \alpha - r_2 \cos \alpha' = f_1 - f_2 + x \quad (\text{II.1-4})$$

$$r_1 \sin \alpha + r_2 \sin \alpha' = y \quad (\text{II.1-5})$$

the subreflector and main reflector equations are derived.

Starting with the subreflector, f_1 and x are eliminated from equation (II.1-4) using equation (II.1-2):

$$-r_2 \cos \alpha' = (r_1 + r_2 - f_2) - f_2 - r_1 \cos \alpha$$

or

$$r_2(1 + \cos \alpha') = 2f_2 + r_1(\cos \alpha - 1) \quad (\text{II.1-6})$$

Next, r_2 is eliminated using equations (II.1-1) and (II.1-5),

$$\frac{(F - r_1) \sin \alpha}{\sin \alpha'} (\cos \alpha' + 1) = 2f_2 + r_1(\cos \alpha - 1) .$$

Isolating α' ,

$$\frac{\cos \alpha' + 1}{\sin \alpha'} = \frac{2f_2 + r_1(\cos \alpha - 1)}{(F - r_1) \sin \alpha} \quad (\text{II.1-7})$$

Recall the trigonometric identities

$$\sin \alpha = 2 \sin \frac{\alpha}{2} \cos \frac{\alpha}{2} ,$$

$$\tan \frac{\alpha}{2} = \frac{\sin \alpha}{1 + \cos \alpha} ,$$

$$\sin^2 \frac{\alpha}{2} = \frac{1 - \cos \alpha}{2} .$$

Using these, equation (II.1-7) becomes

$$\tan \frac{\alpha'}{2} = \frac{(F - r_1) 2 \sin \frac{\alpha}{2} \cos \frac{\alpha}{2}}{2f_2 - 2r_1 \sin^2 \frac{\alpha}{2}} \quad (\text{II.1-8})$$

Let $s = \sin^2 \alpha/2$, so that $\cos^2 \alpha/2 = 1 - s$.

Using equation (II.1-2),

$$\frac{1}{r_1} \frac{dr_1}{d\alpha} = \frac{\tan \frac{\alpha}{2} + \tan \frac{\alpha'}{2}}{1 - \tan \frac{\alpha}{2} \tan \frac{\alpha'}{2}} \quad (\text{II.1-9})$$

$$\frac{1}{r_1} \frac{dr_1}{d\alpha} = \frac{\frac{\sin \alpha/2}{\cos \alpha/2} + \frac{2(F - r_1) \sin (\alpha/2) \cos (\alpha/2)}{2f_2 - 2r_1 s}}{1 - \frac{\sin \alpha/2}{\cos \alpha/2} \frac{2(F - r_1) \sin (\alpha/2) \cos (\alpha/2)}{2f_2 - 2r_1 s}} \quad (\text{II.1-10})$$

$$\frac{1}{r_1} \frac{dr_1}{d\alpha} = \left(\frac{\sin \alpha/2}{\cos \alpha/2} \right) \left[\frac{f_2 - r_1 s + (F - r_1)(1 - s)}{f_2 - r_1 s - (F - r_1) s} \right] \quad (\text{II.1-11})$$

$$\frac{1}{r_1} \frac{dr_1}{d\alpha} = \frac{\sin (\alpha/2) \cos (\alpha/2)}{1 - s} \frac{f_2 + F - r_1 - Fs}{(f_2 - Fs)} \quad (\text{II.1-12})$$

Noting that

$$\frac{ds}{d\alpha} = \frac{d}{d\alpha} \left(\sin^2 \frac{\alpha}{2} \right) = \sin \frac{\alpha}{2} \cos \frac{\alpha}{2} ,$$

$$\frac{dr_1}{d\alpha} = \frac{dr_1}{ds} \sin \frac{\alpha}{2} \cos \frac{\alpha}{2} .$$

Thus, equation (II.1-12) becomes

$$\frac{1}{r_1} \frac{dr_1}{ds} = - \frac{r_1 + F_s - F - f_2}{(1-s)(f_2 - F_s)} \quad (\text{II.1-13})$$

This differential equation is solved by first substituting $\rho = 1/r_1$.

$$\frac{1}{r_1} \frac{dr_1}{ds} = \rho \left(- \frac{1}{\rho^2} \right) \frac{d\rho}{ds} \quad (\text{II.1-14})$$

Equation (II.1-13) can be written

$$\frac{d\rho}{ds} = \frac{1}{(1-s)(f_2 - F_s)} + \rho \frac{F_s - F - f_2}{(1-s)(f_2 - F_s)} \quad (\text{II.1-15})$$

which is a first-order linear differential equation of the form

$$\rho' + f(s)\rho = g(s) \quad ,$$

with
$$f(s) = - \frac{F_s - F - f_2}{(1-s)(f_2 - F_s)} \quad ,$$

and
$$g(s) = \frac{1}{(1-s)(f_2 - F_s)} \quad .$$

The integrating factor is $e^{\int f(x)dx}$. The integral is solved using partial fractions. $f(s)$ is of the form

$$\frac{A + Bs}{(1-s)(C-s)} = \frac{(A + BC)/(1-C)}{C-s} + \frac{(A+B)/(C-1)}{1-s} \quad .$$

So $\int f(s)ds = [-(A + BC)/(1-C)] \ln(C-s) - [(A+B)/(C-1)] \ln(1-s)$, and

$$\begin{aligned} \exp[\int f(s)ds] &= (C-s)(A+BC)/(C-1) \\ &\cdot (1-s)(A+B)/(1-C) \quad . \end{aligned} \quad (\text{II.1-16})$$

Now

$$A = \frac{F + f_2}{F}$$

$$B = \frac{-F}{F}$$

$$= -1$$

$$C = \frac{f_2}{F} .$$

Thus, the integrating factor is

$$(IF) = \left(\frac{f_2}{F} - s\right)^{F/(f_2-F)} (1-s)^{f_2/(F-f_2)} , \quad (II.1-17)$$

and equation (II.1-15), multiplied by the integrating factor, is

$$\frac{d}{ds} [\rho(IF)] = (IF) \frac{1}{(1-s)(f_2-Fs)} . \quad (II.1-18)$$

Multiplying by ds and integrating

$$\begin{aligned} & \rho \left(\frac{f_2}{F} - s\right)^{F/(f_2-F)} (1-s)^{f_2/(F-f_2)} \\ &= \int \frac{\left(\frac{f_2}{F} - s\right)^{F/(f_2-F)} (1-s)^{f_2/(F-f_2)}}{(1-s)(f_2-Fs)} ds \\ &= \int (1-s)^{(2f_2-F)/(F-f_2)} \\ & \quad \cdot \left(\frac{f_2}{F} - s\right)^{(2F-f_2)/(f_2-F)} \left(\frac{1}{F}\right) ds \end{aligned} \quad (II.1-19)$$

Let $x = f_2/(F - f)$, $y = -F/(F - f)$. Equation (II.1-19) can be written

$$\rho(C - s)^Y (1 - s)^X = \frac{1}{F} \int (C - s)^{Y-1} (1 - s)^{X-1} ds . \quad (II.1-20)$$

Since $x + y = -1$,

$$\rho(C - s)^Y(1 - s)^X = \frac{1}{F} \left[(C - s)^Y(1 - s)^X s \frac{1}{C} \right] + K \quad (\text{II.1-21})$$

where K is the constant of integration.

Solving equation (II.1-21),

$$\rho = \frac{s}{FC} + K(C - s)^{-Y} (1 - s)^{-X}$$

$$\frac{1}{r_1} = \frac{s}{f_2} + K \frac{f_2}{F} - s^{F/(F-f_2)} (1 - s)^{-f_2/(F-f_2)} \quad (\text{II.1-22})$$

To find the value of K , substitute $s = 0$, which corresponds to $\alpha = 0$ where $r_1 = f_1$, into equation (II.1-22)

$$\frac{1}{f_1} = K \left(\frac{f_2}{F} \right)^{F/(F-f_2)},$$

or

$$K = \frac{1}{f_1} \left(\frac{F}{f_2} \right)^{F/(F-f_2)}. \quad (\text{II.1-23})$$

The final form of equation (II.1-22) is

$$\frac{1}{r_1} = \frac{s}{f_2} + \frac{1}{f_1} \left(1 - \frac{Fs}{f_2} \right)^{F/(F-f_2)} (1 - s)^{-f_2/(F-f_2)}, \quad (\text{II.1-24})$$

and the subreflector points in Cartesian Coordinates, (x_s, y_s) are obtainable from the polar representation (r_1, α) with origin at $x = f_2 - f_1$:

$$(x_s, y_s) = (f_2 - f_1 + r_1 \cos \alpha, r_1 \sin \alpha).$$

The main reflector equations are obtained from equations (II.1-1), (II.1-2), (II.1-4), (II.1-5), and (II.1-24). Equations (II.1-4) and (II.1-5) can be rewritten

$$-r_2 \cos \alpha' = f_1 - f_2 + x - r_1 \cos \alpha \quad (\text{II.1-25})$$

$$r_2 \sin \alpha' = y - r_1 \sin \alpha . \quad (\text{II.1-26})$$

Squaring and adding these yields

$$\begin{aligned} r_2^2 &= r_1^2 - 2r_1 \cos \alpha (f_1 - f_2 + x) \\ &\quad + (f_1 - f_2 + x)^2 + (F - 2Fr_1) \sin^2 \alpha \end{aligned} \quad (\text{II.1-27})$$

where y was substituted according to equation (II.1-1).

Equation (II.1-2), with $x = x_m$, is:

$$r_2 = (f_1 + f_2 - r_1) + x_m \quad (\text{II.1-28})$$

Using this value for r_2 in equation (II.1-27)

$$\begin{aligned} &(f_1 + f_2 - r_1)^2 + 2x_m(f_1 + f_2 - r_1) + x_m^2 \\ &= r_1^2 - 2r_1 \cos \alpha (f_1 - f_2 + x_m) + (f_1 - f_2)^2 \\ &\quad + 2x_m(f_1 - f_2) + x_m^2 + (F - 2Fr_1) \sin^2 \alpha \end{aligned} \quad (\text{II.1-29})$$

which simplifies to

$$\begin{aligned} &x_m(2r_1 \cos \alpha + 4f_2 - 2r_1) \\ &= -(f_1 + f_2)^2 + 2r_1(f_1 + f_2) - 2r_1(f_1 - f_2) \cos \alpha \\ &\quad + (f_1 - f_2)^2 + (F^2 - 2Fr_1) \sin^2 \alpha . \end{aligned} \quad (\text{II.1-30})$$

Since $s = \sin^2 \alpha/2$, $\sin \alpha = 2\sqrt{s(1-s)}$, and $\cos \alpha = 1 - 2s$.

Substituting these values and solving equation (II.1-30) for x yields

$$\begin{aligned}
x_m &= \frac{-4f_1f_2 + 2r_1[(f_1 + f_2) - (f_1 - f_2)(1 - 2s)] + (F^2 - 2Fr_1) 4s(1 - s)}{4f_2 - 2r_1 + 2r_1(1 - 2s)} \\
&= \frac{-2f_1f_2 + r_1[2f_2 + (f_1 - f_2)(2s)] + 2(F^2 - 2Fr_1)s(1 - s)}{2f_2 - 2r_1s} \\
&= \frac{(1 - s)[s(F^2 - 2Fr_1) + f_2r_1] - f_1f_2 + r_1f_1s}{f_2 - r_1s} \\
&= \frac{1 - s}{f_2 - r_1s} [s(F^2 - 2Fr_1) + f_2r_1] - f_1 . \tag{II.1-31}
\end{aligned}$$

Rewriting equation (II.1-1) in terms of s yields the equation for y_m :

$$y_m = 2F\sqrt{s(1 - s)} \tag{II.1-32}$$

APPENDIX II.2. SPEAKEASY COMPUTER PROGRAM TO
GENERATE AND PLOT SCHWARZSCHILD PROFILES

Given the focal length, F ; and the initial main reflector/
subreflector separation, T_1 ; this program generates a series
of Schwarzschild profiles for varying focal lengths T_2 . In
addition, the least squares fitted sixth order polynomial for
each reflector is found. All four curves are plotted on axes
with the same scale. The coefficients, for terms of increasing
order of the two sixth order polynomials are also displayed.

EDITING SCHW

```

1 PROGRAM
2 GRAPHICS(TEK+010)
3 T1=1
4 F=-5
5 FOR T2=1,3,.5
6 FOCUS=T2-T1
7 THET=INTEGERS(0,300)/10*(3.14159/180)
8 S=(SIN(THET/2))**2
9 FT1=F-T1
10 R=S/T1+(1-S*F/T1)**(F/(FT1))/T2*(1-S)**(-T1/(FT1))
11 RHO=1/R
12 Y=2*F*(S*(1-S))**.5
13 X=-T2+(1-S)*(F*F*S+RHO*(T1-2*F*S))/(T1-RHO*S)
14 YMAX=Y(301)
15 XS=RHO*COS(THET)-(T2-T1)
16 FOCUS=XS(1)-T2
17 YS=RHO*SIN(THET)
18 TP=MAX(T1,(T1+XS(301)),X(301))
19 TD=0
20 TDIF=TP-TD
21 YDIF=2*YMAX
22 SCA=YDIF/TDIF
23 SETYSCALE(FROM:TD,TO:TP)
24 SETXSCALE(FROM:-YMAX,TO:YMAX)
25 LX=6/ABS(SCA)
26 SETYAXIS(LENGTH=LX)
27 SETXAXIS(LENGTH=6)
28 XAX=99999099*(X-X(1))
29 XF=X,X
30 YF=Y,-Y
31 XSF=XS,XS
32 YSF=YS,-YS
33 PM=LSQPDL(YF,XF,4)
34 PS=LSQPDL(YSF,XSF,4)
35 XFM=PM(1)+PM(3)*Y*Y+PM(5)*Y**4
36 XFS=PS(1)+PS(3)*YS*YS+PS(5)*YS**4
37 GRAPH(XAX,X,XFM:Y)
38 T2
39 FOCUS
40 F
41 PM
42 PS
43 ADDGRAPH(XAX,XS,XFS:YS)
44 NEXT T2
*45 NEXT F

```

III. DERIVATION OF FORMULAS

A. The Bifocal Principle

The design procedure for a bifocal dual reflector system involves tracing ideal rays through the system from a source to an arbitrary aperture plane. This assumption of the high frequency limit is valid for microwave reflectors with diameters much larger than the wavelength, and is the basis for geometrical optics. Using ideal rays reduces the derivation to solving a geometrical problem.

The basic constraints of the problem are: Snell's law of reflection, which must be applied on each of the two reflector surfaces; and two path length conditions, one for each of the two focal points. For a well-focused beam, rays leaving the reflector must be parallel and have the same phase. These two conditions define a planar phase front at an arbitrary aperture plane. The necessity of a planar phase front is obvious if the antenna is viewed as a receiver of spherical waves emitted at an infinite distance. To guarantee uniform phase across the wave front, the physical distance traversed by each ray must be identical. This path length, then, is a constant for all rays leaving one focus, and emerging perpendicular to its respective scanned aperture plane. Unlike certain previously derived design methods [28],[37]-[39], the law of

conservation of energy for an arbitrary ray bundle is not used in this derivation.

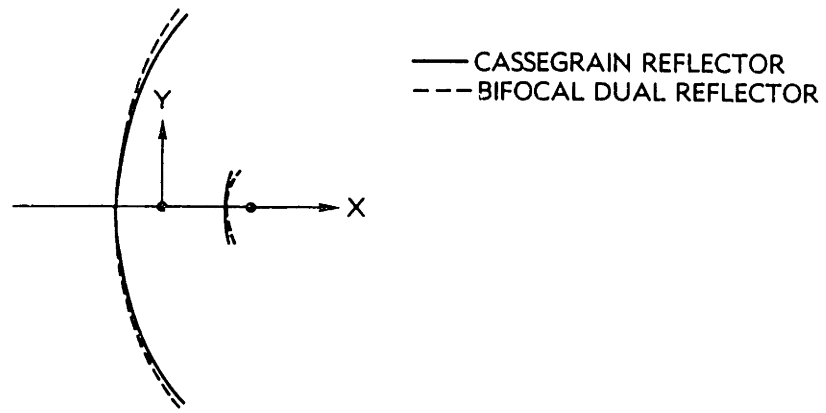
Using Snell's law introduces differentials which are brought about from representing a surface normal. Requiring total generality in design, as with the case of nonsymmetrical systems, these differentials must be considered partials. Since Snell's law must be used twice, it becomes necessary to solve a second order partial differential equation, which cannot, in general, be solved exactly [51].

This dilemma is solved by using an iterative algebraic method. Rao [76],[77], and Kumazawa and Karikomi [78],[79], solved the 2-dimensional, symmetric bifocal problem by alternately considering transmitted and received rays. The method, based on ideas used first in lens design [80],[81], involves the notion that every point on each reflector surface must reflect two rays--one from each focus--to each particular emerging scan direction. Thus, each main reflector point reflects the two rays which originated at the foci and were bounced off two particular subreflector points.

Similarly, each subreflector point must reflect two rays, one from each focus. These then strike the main reflector at two separate points. Each ray of the pair corresponds to one scan direction or the other.

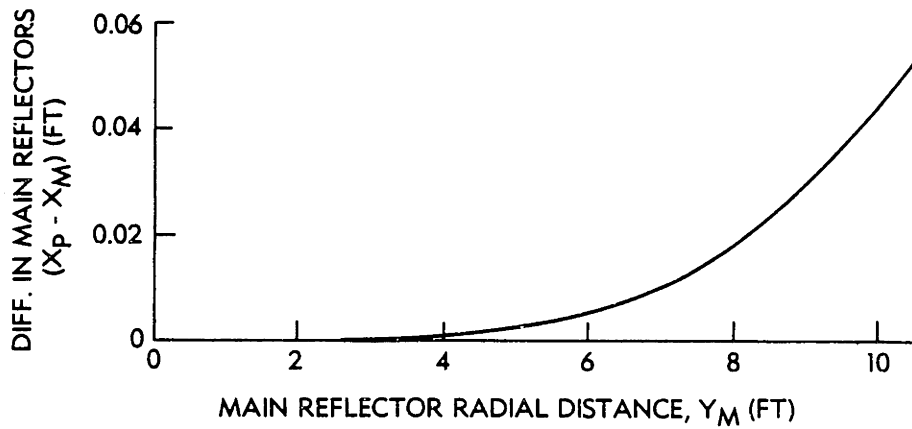
Two sets of points are determined, one set for the main reflector, and one for the subreflector. The best fitting curves to each set are then found. Generally, a polynomial least-squares method is used. Since Rao's design is symmetric, an even order polynomial is obtained. If the number of points for each curve is small enough, an interpolation method or cubic spline technique can be used. Since the derived points are exact solutions, the later methods of curve-fitting--which find curves passing through these points--is preferable. Figure 22, from Rao's paper, shows the difference between the symmetric bifocal and the closest Cassegrain.

The two curves represent planar slices of the subreflector and the main reflector. To generate actual surfaces, the curves are rotated about the axis of symmetry (z-axis). Figure 23 shows the results of this design. It is noticed that the two focal points in the planar solution become a ring in the 3-dimensional case. Every planar cut which includes the axis of symmetry is a perfect 2-dimensional solution to the bifocal problem, as long as the two foci are included in the plane. Obviously, there is no focus on the axis; indeed, points on the axis are the most defocused ones in the focal region.

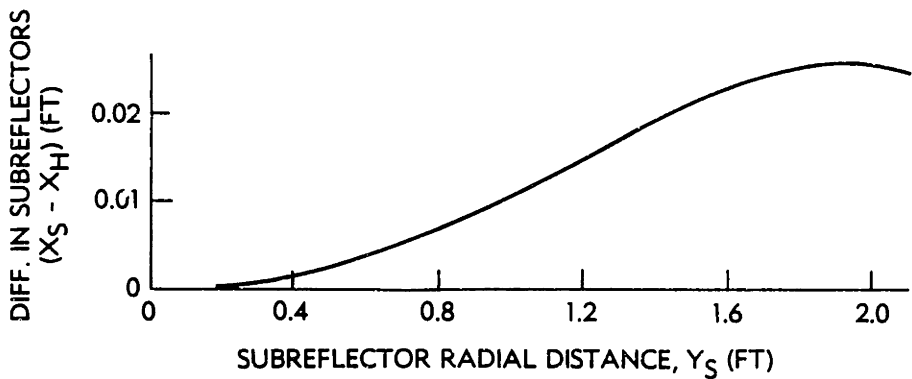


— CASSEGRAIN REFLECTOR
 --- BIFOCAL DUAL REFLECTOR

a. Antenna Configuration



b. Main Reflector Comparison



c. Subreflector Comparison

Figure 22. Comparison of Symmetric Bifocal and Corresponding Cassegrain Profiles

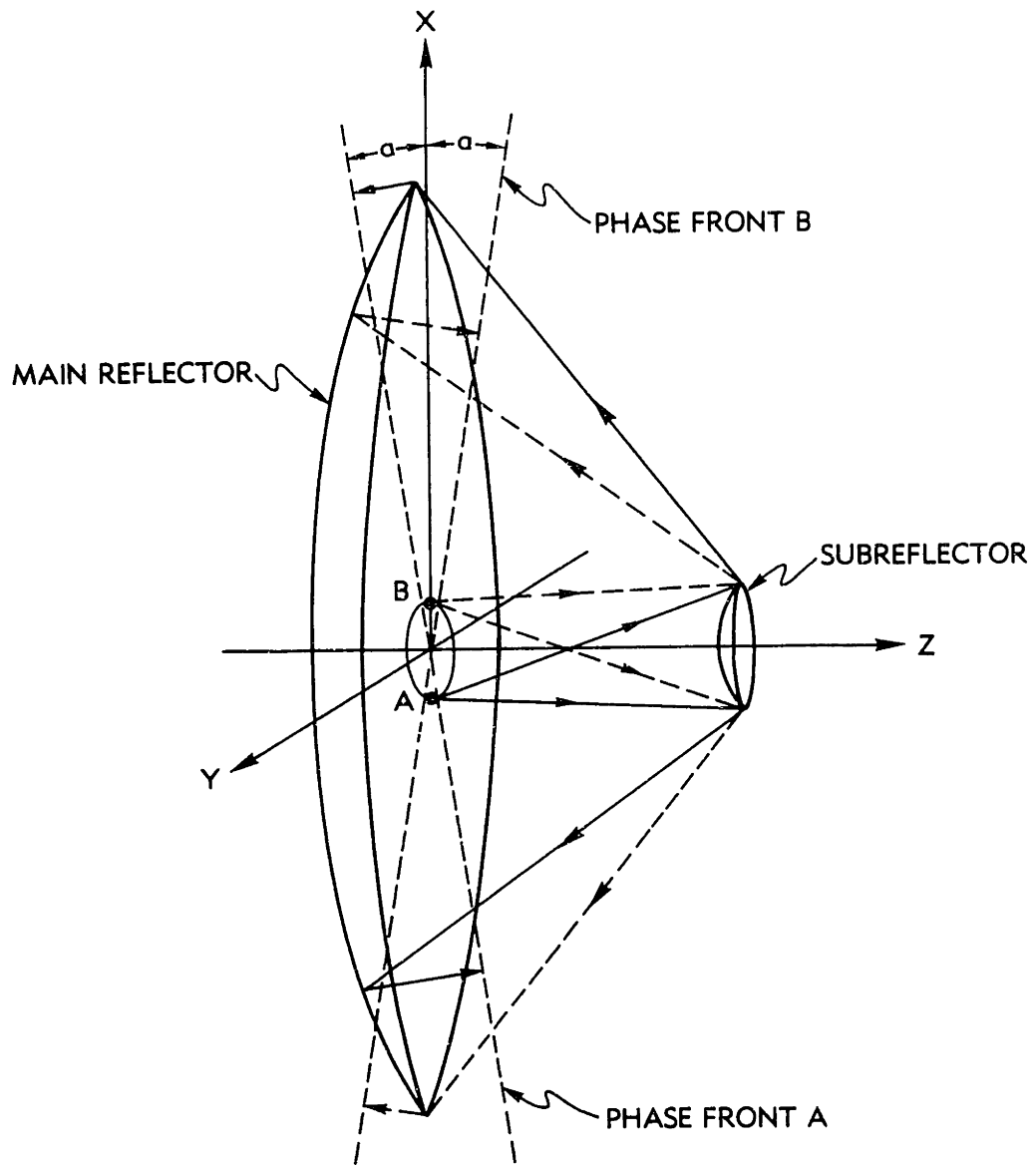


Figure 23. Extension of 2-Dimensional Bifocal Profile to 3 Dimensions by Rotation About the Axis

This method does not, however, provide an exact solution for surfaces in 3 dimensions. The difficulty arises from the fact that rays originating at either focus which leave the plane of symmetry do not emerge from the system as desired. In fact, a ray incident on the subreflector at a point in a transverse plane ($x-z$) perpendicular to the plane of its focus ($y-z$) (Figure 24a) performs almost as a ray in the 2-dimensional case originating at a point halfway between foci. This can be seen by examining the projection of the ray onto the $x-z$ plane (Figure 24b). Thus, Rao's design is only approximately a bifocal solution. The foci are only "perfect foci" for rays contained in planes of symmetry. Several authors have suggested that the bifocal has the best wide-angle scanning performance of all dual reflector antennas [68],[82]. An offset bifocal has been proposed [83], where circular sections of each surface are chosen for the antenna. However, since large sacrifices were made for the sake of the simplifying symmetry, applying an asymmetric condition appears to cancel the particular advantage.

The use of vectors provides more flexibility than Rao's planar approach. Additional degrees of freedom include allowing asymmetric foci location, and the specification of an arbitrary aperture center. The increased flexibility requires the determination and specification of several parameters.

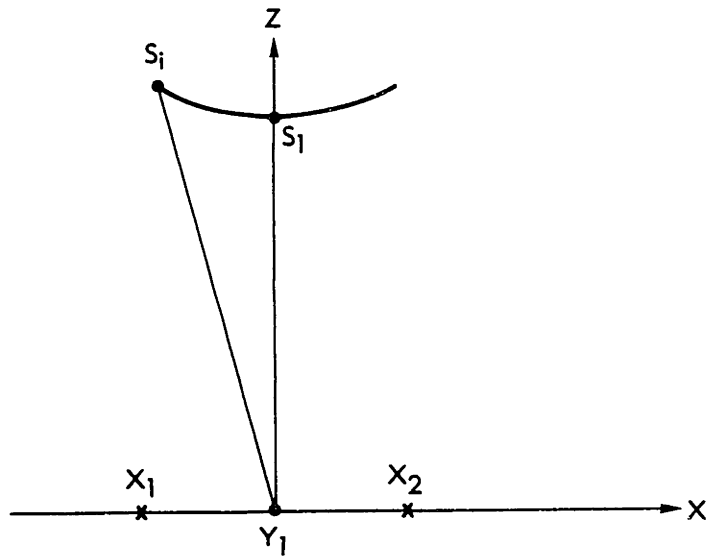
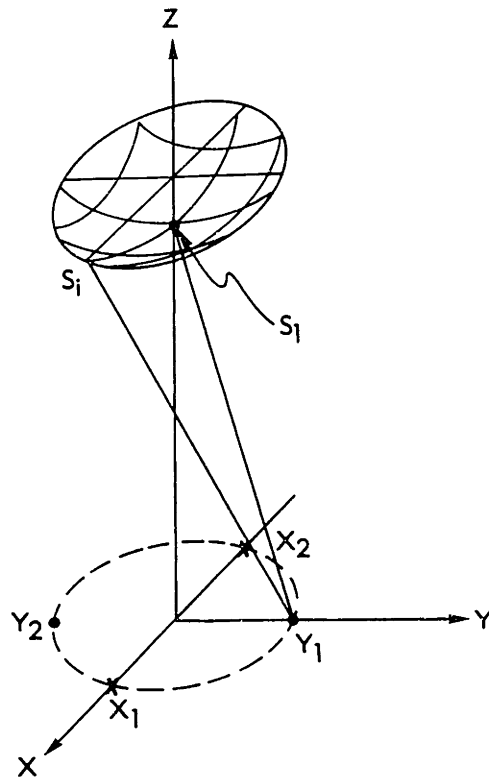


Figure 24. Nonideal Nature of the Symmetric Bifocal
 a) Oblique View, b) Projection on x-z Plane

The two focal points and their respective scanning directions, the path lengths from both foci, the final aperture center, the constant path length, and an initial subreflector point and its normal, make up the collection of input parameters. The scanning direction is specified by the angles α and β , measured counterclockwise from the x-axis and counterclockwise from the y-axis, respectively (Figure 25).

The path length from each focus is specified for rays traveling to the two scanned aperture planes. For a circularly symmetric reflector system, the path length for each focus is the same. However, in the design of an offset system, the boresight axis is parallel to the feed axis, but does not coincide with it. Instead, it is translated so as to avoid blockage by the subreflector. A path length difference between rays leaving one focus and emerging at its aperture plane, and rays leaving the other focus emerging at the other aperture plane can be used to vertically translate the boresight axis. To specify the difference, the two aperture planes are made to intersect at line ℓ which does not intersect the feed axis. This happens if ℓ is not in the plane containing the boresight (z) axis. That is, if rays are scanned symmetrically about the z-axis in an offset system, the scanned aperture planes would intersect at a line in the

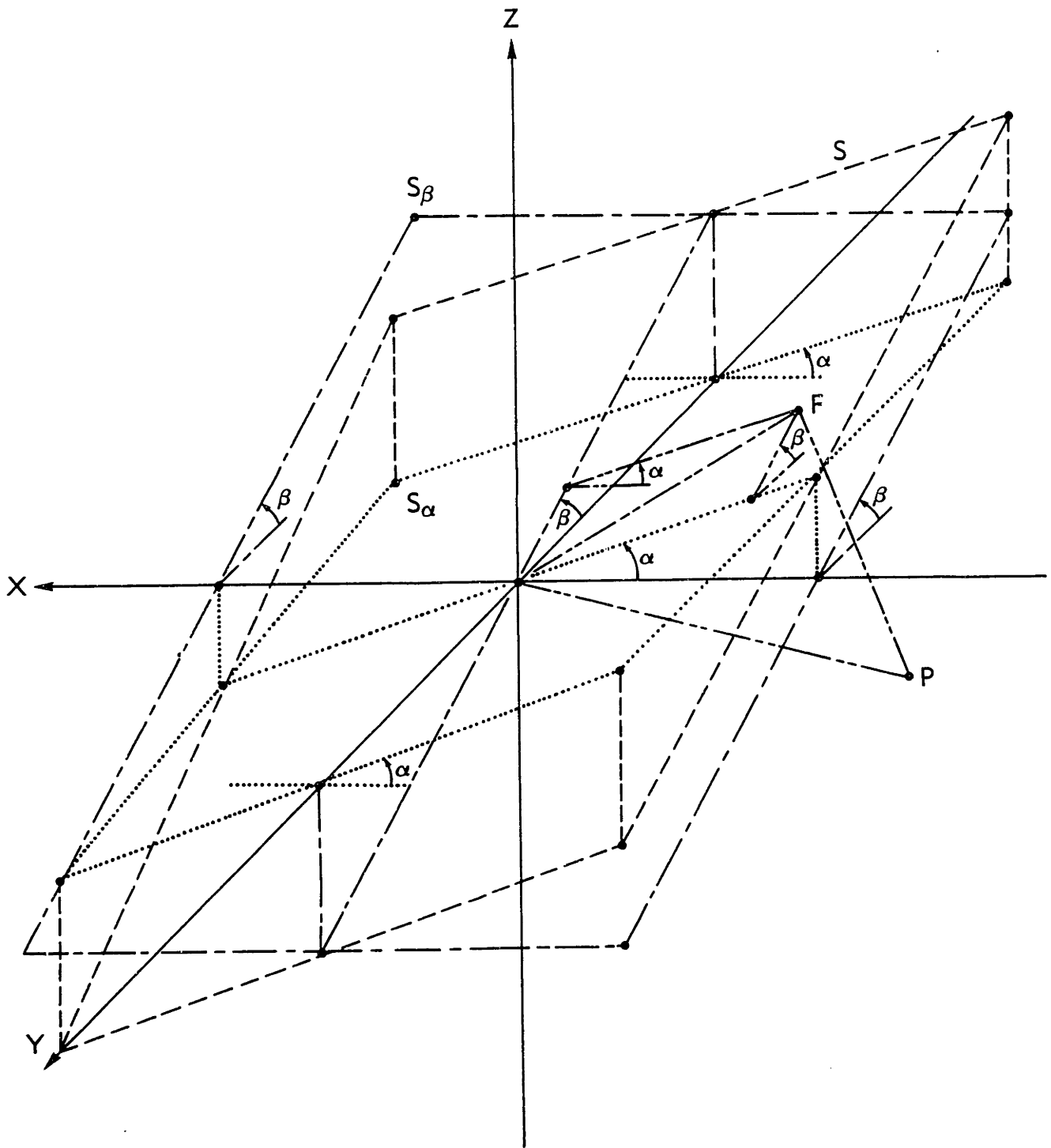


Figure 25. Geometry of Scanned Aperture Phase Planes

x-y plane, which does not include the origin. It is shown in the next section that if the focal points are axially displaced about the origin, but not symmetrically with respect to the z-axis (Figure 26), that the optimum intersection line of the aperture planes does not intersect the z-axis. This concept is essential in the design of an offset system, since the boresight axis is parallel to the aperture center line, but is translated so as to avoid blockage by the subreflector. Thus, the intersection line of the aperture planes defines a new boresight axis, and in doing so, specifies a separate path length for each focal point. In effect, adjusting this "aperture center" adds a constant phase shift term to the phase function at the aperture.

The point (C_1, C_2) is the input parameter which locates the intersection line which lies on the x-y plane. These are the coordinates of the point on the intersection line closest to the origin. If the x- or y-components of the foci are zero, then scanning occurs about the x-axis or the y-axis, the intersection line is parallel to the x-axis or the y-axis, and C_1 or C_2 is zero, respectively.

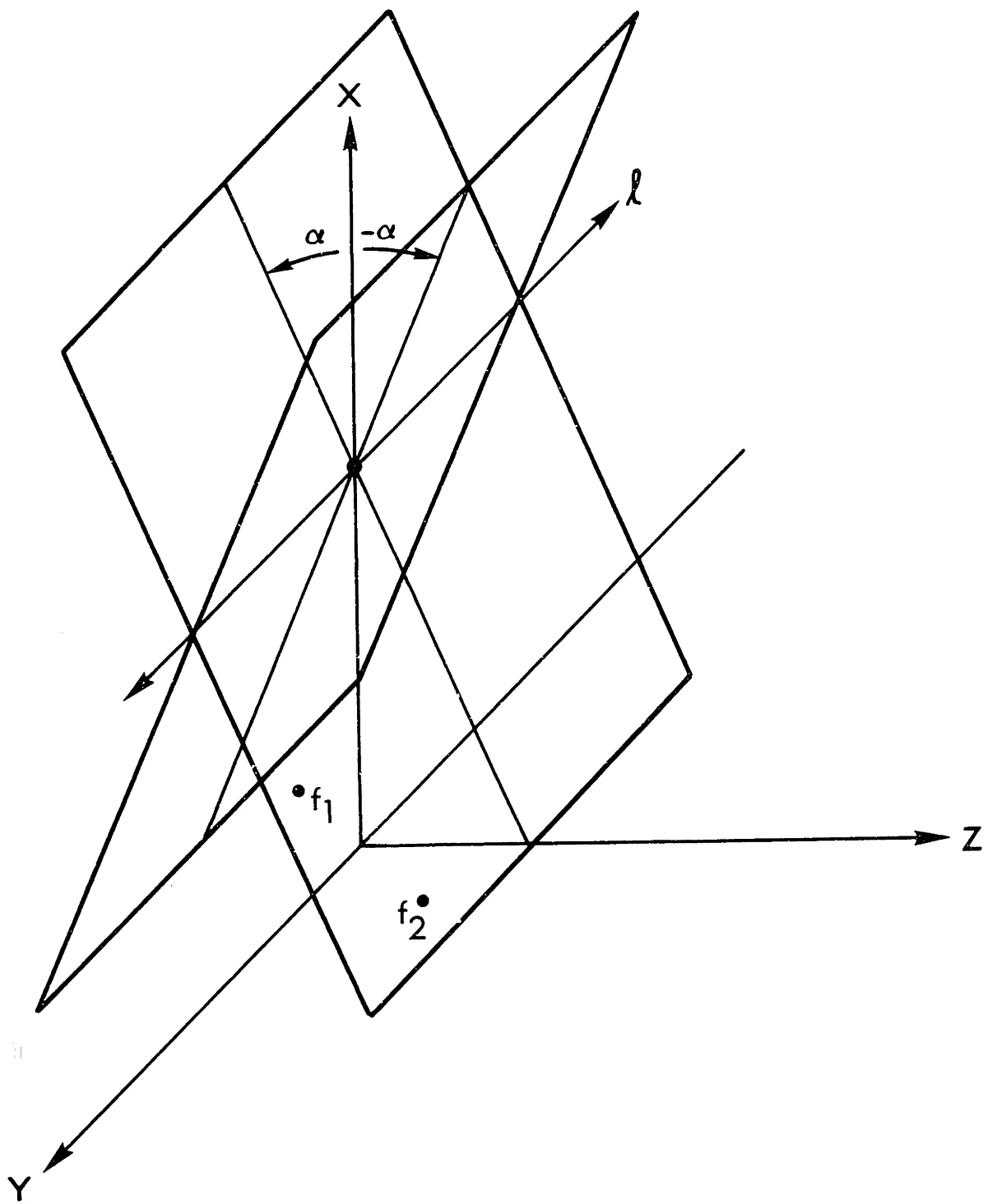


Figure 26. Aperture Phase Plane Intersection Line

B. Point Generation Methodology

Once the starting parameters have been determined, a ray, \bar{R}_1 , is traced from one focal point F_1 to the first subreflector point S_1 . Since the surface normal, \hat{n}_{S_1} , to the subreflector at this point has been specified as an input parameter, the reflected ray, \bar{R}_2 , is found. This reflected vector, the output vector, \bar{R}_3 , (which is computed from the scan angles and the aperture center $(C,0,0)$, and the path length, L , are used to derive the first main reflector point M_1 and its normal \hat{n}_{M_1} (Figure 27).

Now the system is viewed in the receive mode. A ray, \bar{R}_3' , traced from the other scanned aperture to the previously determined main reflector point M_1 . Again, since the normal n_{M_1} has also just been determined, the reflector ray \bar{R}_2' is found. This ray will be different from the corresponding transmit mode ray. Since after reflection off the subreflector, the ray \bar{R}_1' must intersect the second focal point F_2 , and since the total path length is known, the next subreflector point S_2 and its normal \hat{n}_{S_2} are determined (Figure 28).

The process is then repeated, starting with the new subreflector point. Figure 29 illustrates the generation of the K th pair of points.

Table 1 contains the definition of variables used in the following mathematical discussion.

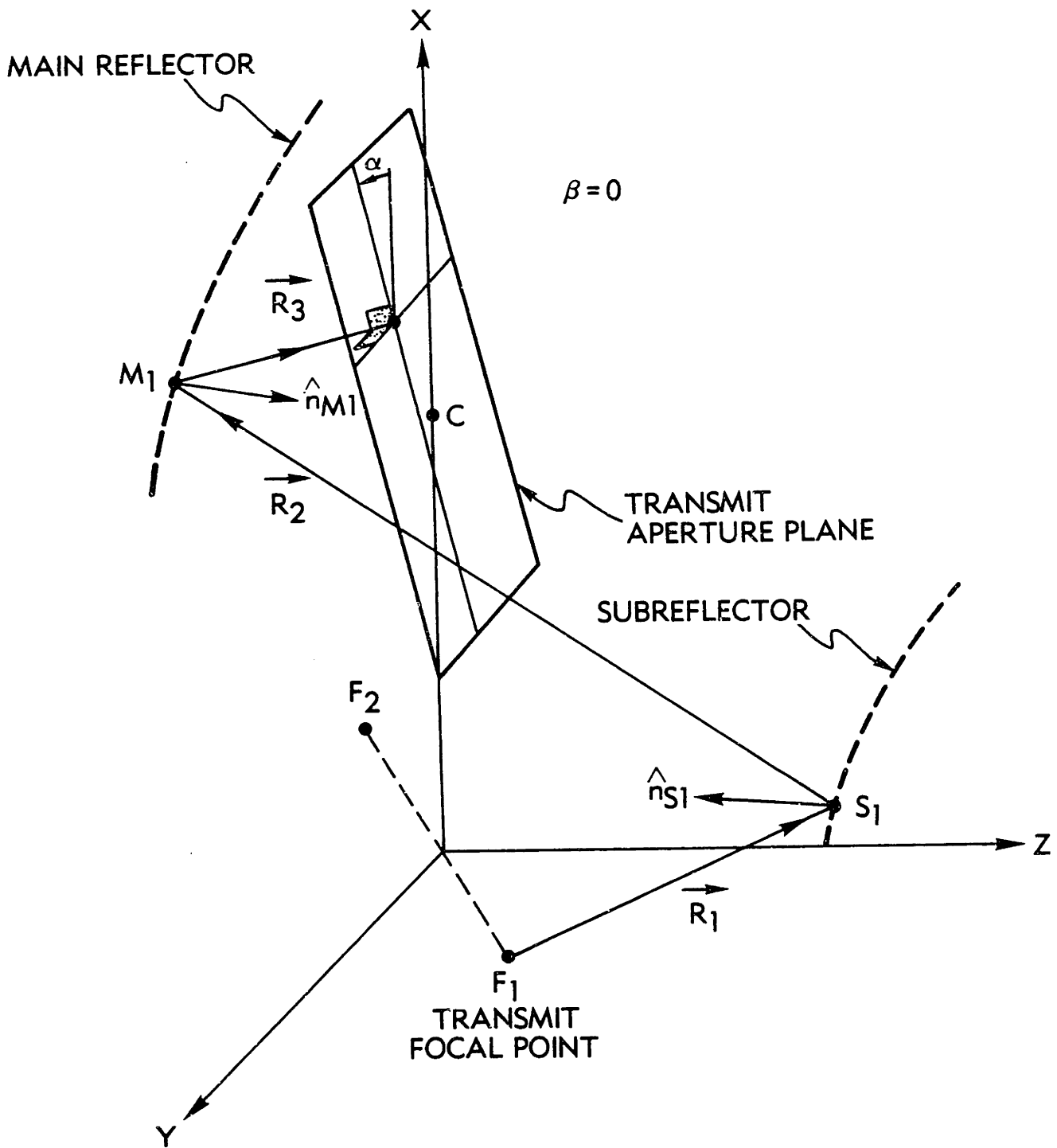


Figure 27. Transmit Point Generation Procedure

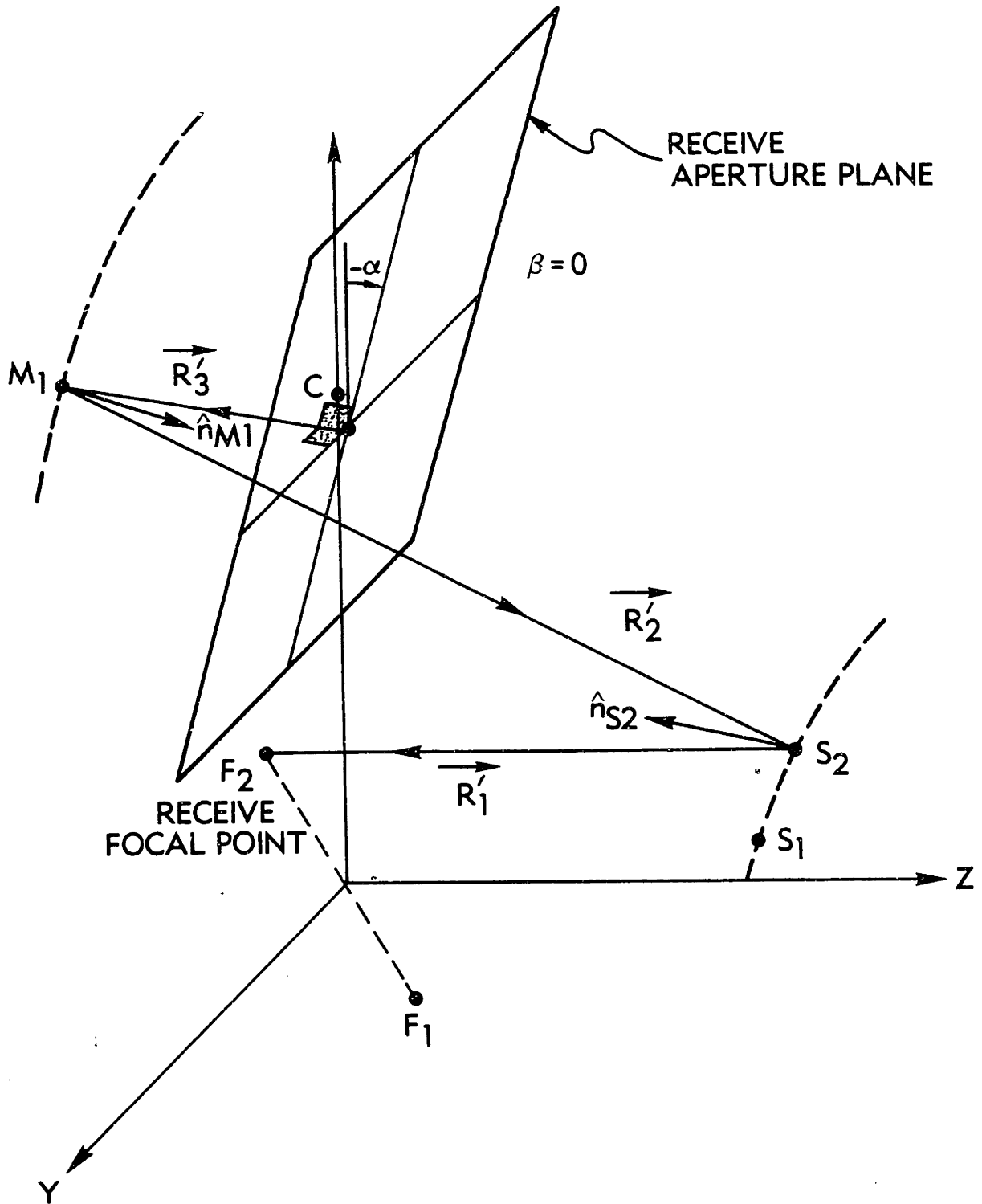


Figure 28. Receive Point Generation Procedure

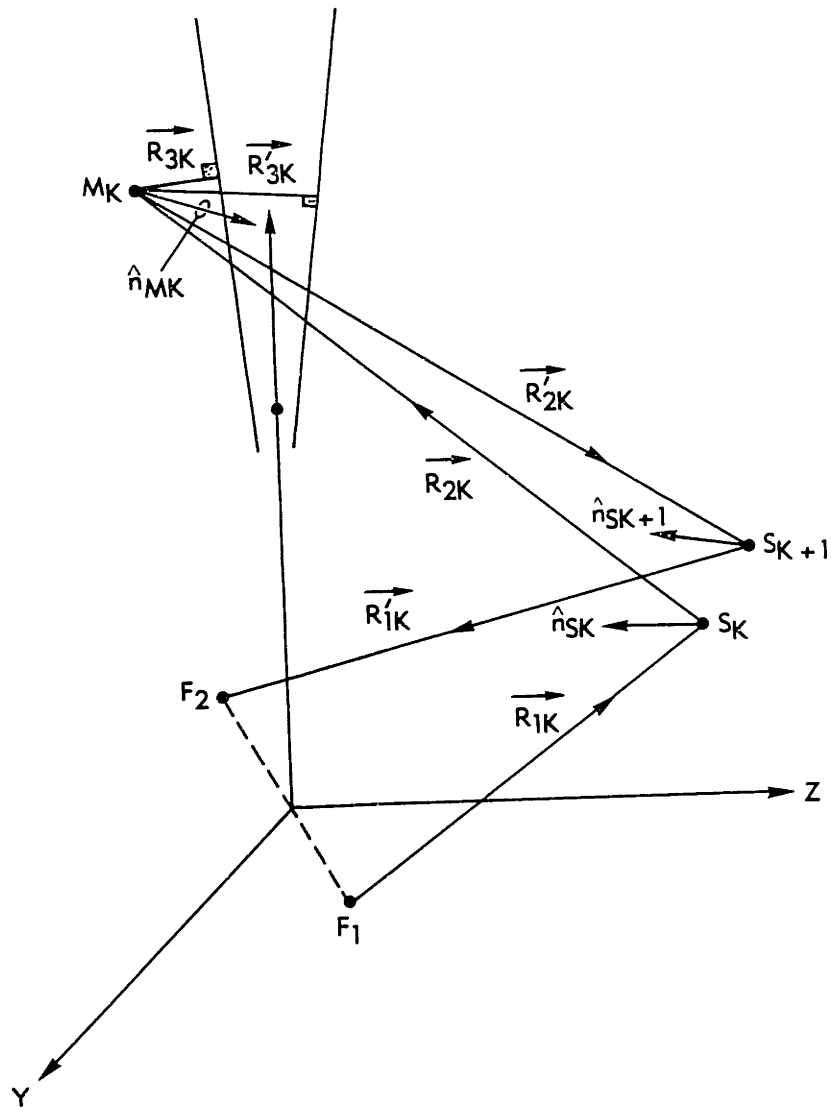


Figure 29. Generation of the \$K\$th Pair of Offset Bifocal Points

Table 1. List of Variables

α_i	angle of scan in x-y plane $i = \begin{matrix} 1 & \text{transmit mode} \\ 2 & \text{receive mode} \end{matrix}$
β_i	angle of scan in y-z plane $i = \begin{matrix} 1 & \text{transmit mode} \\ 2 & \text{receive mode} \end{matrix}$
\bar{F}_i	position vector of focal point $i = \begin{matrix} 1 & \text{transmit mode} \\ 2 & \text{receive mode} \end{matrix}$
\bar{S}_k	position vector of the kth point on the subreflector
\bar{M}_k	position vector of the kth point on the main reflector
\hat{n}_{Sk}	unit normal of the kth point on the subreflector
\hat{n}_{Mk}	unit normal of the kth point on the main reflector
\bar{R}_{1k}	$= \bar{S}_k - \bar{F}_1$, original transmit ray
\bar{R}_{2k}	$= \bar{M}_k - \bar{S}_k$, first reflected transmit ray
\bar{R}_{3k}	vector from \bar{M}_k to the first (transmit) aperture plane, normal to this plane; i.e., second reflected transmit ray
\bar{R}'_{1k}	$= \bar{F}_2 - \bar{S}_{k+1}$, first receive ray
\bar{R}'_{2k}	$= \bar{S}_{k+1} - \bar{M}_k$, first reflected receive ray
\bar{R}'_{3k}	vector from second (receive) aperture plane to \bar{M}_k , normal to the plane; i.e., second reflected receive ray
\hat{r}_{jk}	$= \bar{R}_{jk} / \bar{R}_{jk} $, $j = 1, 2, 3$
\hat{r}'_{jk}	$= \bar{R}'_{jk} / \bar{R}'_{jk} $, $j = 1, 2, 3$
C_1	x-component of the point on the aperture plane intersection line nearest the origin
C_2	y-component of above
L	path length from each focal point to its respective aperture plane

C. Transmit Ray Analysis

The four system constraints are: Snell's law, for a transmit ray;

$$\hat{r}_{2k} = \hat{r}_{1k} - 2(\hat{n}_{SK} \cdot \hat{r}_{1k}) \hat{n}_{SK} \quad (\text{III-1})$$

at the subreflector, and for the main reflector:

$$\hat{r}_{3k} = \hat{r}_{2k} - 2(\hat{n}_{MK} \cdot \hat{r}_{2k}) \hat{n}_{MK} \quad (\text{III-2})$$

Snell's law for received rays:

$$\hat{r}'_{2k} = \hat{r}'_{3k} - 2(\hat{n}_{MK} \cdot \hat{r}'_{3k}) \hat{n}_{MK} \quad (\text{III-3})$$

at the main reflector, and

$$\hat{r}'_{1k} = \hat{r}'_{2k} - 2(\hat{n}_{Sk+1} \cdot \hat{r}'_{2k}) \hat{n}_{Sk+1} \quad (\text{III-4})$$

at the subreflector. Note in equation (III-4) the term \hat{n}_{Sk+1} indicates the normal at the newly generated subreflector point. The path length conditions are the sum of the magnitudes of the three traced rays:

$$L = |\bar{R}_{1k}| + |\bar{R}_{2k}| + |\bar{R}_{3k}| \quad (\text{III-5})$$

$$L = |\bar{R}'_{1k}| + |\bar{R}'_{2k}| + |\bar{R}'_{3k}| \quad (\text{III-6})$$

From the definition of \bar{R}_{1k}

$$|\bar{R}_{1k}| = \sqrt{(S_{k_x} - F_{1_x})^2 + (S_{k_y} - F_{1_y})^2 + (S_{k_z} - F_{1_z})^2} \quad (\text{III-7})$$

$$|\bar{R}_{1k}| = \sqrt{(S_{k+1_x} - F_{2_x})^2 + (S_{k+1_y} - F_{2_y})^2 + (S_{k+1_z} - F_{2_z})^2} \quad (\text{III-8})$$

The ray, \bar{R}_{3k} , is derived from the vector formula for the distance between a point and a plane (see Appendix III).

$$|\bar{R}_{3k}| = \frac{(C_1 - M_{k_x}) \sin \alpha_1 \cos \beta_1 + (C_2 - M_{k_y}) \cos \alpha_1 \sin \beta_1 - M_{k_z} \cos \alpha_1 \cos \beta_1}{\sqrt{1 - \sin^2 \alpha_1 \sin^2 \beta_1}} \quad (\text{III-9})$$

For the received ray, the only changes are the angles α_2 and β_2 .

$$|\bar{R}'_{3k}| = \frac{(C_1 - M_{k_x}) \sin \alpha_2 \cos \beta_2 + (C_2 - M_{k_y}) \cos \alpha_2 \sin \beta_2 - M_{k_z} \cos \alpha_2 \cos \beta_2}{\sqrt{1 - \sin^2 \alpha_2 \sin^2 \beta_2}} \quad (\text{III-10})$$

Proceeding with the transmit analysis,

$$\bar{M}_k = \bar{S}_k + \bar{R}_{2k} \quad (\text{III-11})$$

by definition; hence,

$$\bar{M}_k = \bar{S}_k + |\bar{R}_{2k}| \hat{r}_{2k} \quad (\text{III-12})$$

Rewriting equation (III-9) using equation (III-12),

$$\begin{aligned} |\bar{R}_{3k}| = & \left\{ \left[C_1 - (S_{k_x} + |\bar{R}_{2k}| \hat{r}_{2k_x}) \right] \sin \alpha_1 \cos \beta_1 \right. \\ & + \left[C_2 - (S_{k_y} + |\bar{R}_{2k}| \hat{r}_{2k_y}) \right] \cos \alpha_1 \sin \beta_1 \\ & \left. + \left[-S_{k_z} + |\bar{R}_{2k}| \hat{r}_{2k_z} \right] \cos \alpha_1 \cos \beta_1 \right\} / (1 - \sin^2 \alpha_1 \sin^2 \beta_1)^{1/2} \quad (\text{III-13}) \end{aligned}$$

Combining equations (III-5) and (III-13) and performing the necessary algebra, we have:

$$L = |\bar{R}_{1k}| + |\bar{R}_{2k}| P + Q, \quad (\text{III-14})$$

where

$$P = 1 - \frac{r_{2k_x} \sin \alpha_1 \cos \beta_1 + r_{2k_y} \cos \alpha_1 \sin \beta_1 + r_{2k_z} \cos \alpha_1 \cos \beta_1}{\sqrt{1 - \sin^2 \alpha_1 \sin^2 \beta_1}}$$

$$Q = \frac{(C_1 - S_{k_x}) \sin \alpha_1 \cos \beta_1 + (C_2 - S_{k_y}) \cos \alpha_1 \sin \beta_1 + (-S_{k_z}) \cos \alpha_1 \cos \beta_1}{\sqrt{1 - \sin^2 \alpha_1 \sin^2 \beta_1}}$$

Solving equation (III-14) for $|\bar{R}_{2k}|^*$

$$|\bar{R}_{2k}| = \frac{(L - |\bar{R}_{1k}| - Q)}{P} \quad (\text{III-15})$$

The three components of \bar{M}_k are then found by substituting equation (III-15) into equation (III-12).

$$M_{k\ell} = S_{k\ell} + \frac{r_{2k\ell} (L - |\bar{R}_{1k}| - Q)}{P}, \quad \ell = x, y, z \quad (\text{III-16})$$

To find the value of the normal at this main reflector point, we need,

$$\hat{r}_{1k} = \frac{(\bar{S}_k - \bar{F}_1)}{|\bar{S}_k - \bar{F}_1|} \quad (\text{III-17})$$

by definition, and so, using equation (III-1),

$$\hat{r}_{2k} = \frac{(\bar{S}_k - \bar{F}_1)}{|\bar{S}_k - \bar{F}_1|} - 2 [\hat{n}_{Sk} \cdot (\bar{S}_k - \bar{F}_1)] \frac{(\bar{S}_k - \bar{F}_1)}{|\bar{S}_k - \bar{F}_1|} \hat{n}_{Sk} \quad (\text{III-18})$$

also from Appendix III

$$\hat{r}_{3k} = \frac{(\sin \alpha_1 \cos \beta_1) \hat{i} + (\cos \alpha_1 \sin \beta_1) \hat{j} + (\cos \alpha_1 \cos \beta_1) \hat{k}}{\sqrt{1 - \sin^2 \alpha_1 \sin^2 \beta_1}} \quad (\text{III-19})$$

*Notice that $P = 1 - \hat{r}_{2k} \cdot \hat{r}_{3k}$, and $Q = (\bar{C} - \bar{S}_k) \cdot \hat{r}_{3k}$, where $\bar{C} = (C_1, C_2)$. Thus

$$|\bar{R}_{2k}| (1 - \hat{r}_{2k} \cdot \hat{r}_{3k}) = L - |\bar{R}_{1k}| - (\bar{C} - \bar{S}_k) \cdot \hat{r}_{3k}$$

or

$$L = |\bar{R}_{1k}| + |\bar{R}_{2k}| + \hat{r}_{3k} \cdot (-\bar{R}_{2k} + (\bar{C} - \bar{S}_k))$$

Now, since $\bar{R}_{2k} + \bar{S}_k = \bar{M}_k$, and referring to Appendix III:

$$L = |\bar{R}_{1k}| + |\bar{R}_{2k}| + |\bar{R}_{3k}|,$$

which checks.

Now, rearranging equation (III-2) and normalizing, the main reflector surface normal at point k is:

$$\hat{n}_{MK} = \frac{(\hat{r}_{3k} - \hat{r}_{2k})}{|\hat{r}_{3k} - \hat{r}_{2k}|} \quad (\text{III-20})$$

Thus, equations (III-16) and (III-17) completely specify the kth main reflector point.

D. Receive Ray Analysis

For the receive analysis, \bar{M}_k is known and \bar{S}_{k+1} is desired. By definition,

$$\bar{S}_{k+1} = \bar{M}_k + \bar{R}'_{2k} \quad (\text{III-21})$$

or

$$\bar{S}_{k+1} = \bar{M}_k + |\bar{R}'_{2k}| \hat{r}'_{2k} \quad (\text{III-22})$$

Using equation (III-21) in equation (III-8), and substituting the result into equation (III-6), the path length is

$$L = \left[(F_{2x} - M_{kx} - |\bar{R}'_{2k}| r'_{2kx})^2 + (F_{2y} - M_{ky} - |\bar{R}'_{2k}| r'_{2ky})^2 + (F_{2z} - M_{kz} - |\bar{R}'_{2k}| r'_{2kz})^2 \right]^{1/2} + |\bar{R}'_{2k}| + |\bar{R}'_{3k}| \quad (\text{III-23})$$

Now letting

$$\begin{aligned} A &= L - |\bar{R}'_{3k}| \\ a &= F_{2x} - M_{kx} \\ b &= F_{2y} - M_{jy} \\ c &= F_{2z} - M_{kz} \end{aligned}$$

equation (III-23) becomes

$$\begin{aligned} \left(A - |\bar{R}'_{2k}| \right)^2 &= \left(a + \hat{r}'_{2k_x} |\bar{R}'_{2k}| \right)^2 + \left(b + \hat{r}'_{2k_y} |\bar{R}'_{2k}| \right)^2 \\ &\quad + \left(c + \hat{r}'_{2k_z} |\bar{R}'_{2k}| \right)^2 \end{aligned} \quad (\text{III-24})$$

Expanding equation (III-24) yields

$$\begin{aligned} &A^2 - 2A |\bar{R}'_{2k}| + |\bar{R}'_{2k}|^2 \\ &= a^2 + b^2 + c^2 + 2 |\bar{R}'_{2k}| \left(a\hat{r}'_{2k_x} + b\hat{r}'_{2k_y} + c\hat{r}'_{2k_z} \right) \\ &\quad + \left[\left(\hat{r}'_{2k_x} \right)^2 + \left(\hat{r}'_{2k_y} \right)^2 + \left(\hat{r}'_{2k_z} \right)^2 \right] |\bar{R}'_{2k}|^2 \end{aligned} \quad (\text{III-25})$$

But \hat{r}'_{2k} is a unit vector, therefore:

$$A^2 - 2A |\bar{R}'_{2k}| = B^2 + 2C |\bar{R}'_{2k}| \quad (\text{III-26})$$

where

$$B^2 = a^2 + b^2 + c^2$$

$$C = a\hat{r}'_{2k_x} + b\hat{r}'_{2k_y} + c\hat{r}'_{2k_z}$$

Solving equation (III-26) for $|\bar{R}'_{2k}|$

$$|\bar{R}'_{2k}| = \frac{1}{2} \frac{(A^2 - B^2)}{(A + C)} \quad (\text{III-27})$$

and the three components of \bar{S}_{k+1} are found by substituting equation (III-27) into equation (III-22).

$$S_{k+1\ell} = M_{k\ell} + \frac{1}{2} \frac{(A^2 - B^2)}{(A + C)}, \quad \ell = x, y, z \quad (\text{III-28})$$

Again, as a check, notice

$$|\bar{R}'_{2k}| = \frac{1}{2} \frac{(L - \bar{R}'_{3k})^2 - |\bar{F}_2 - \bar{M}_k|^2}{(L - \bar{R}'_{3k}) + (\bar{F}_2 - \bar{M}_k) \cdot \hat{r}'_{2k}}$$

or

$$\begin{aligned} & 2 |\bar{R}'_{2k}| L - |\bar{R}'_{3k}| + 2 |\bar{R}'_{2k}| \hat{r}'_{2k} \cdot (\bar{F}_2 - \bar{M}_k) \\ &= (L - |\bar{R}'_{3k}|)^2 - (\bar{F}_2 - \bar{M}_k) \cdot (\bar{F}_2 - \bar{M}_k) \end{aligned}$$

and since

$$|\bar{R}'_{2k}| \hat{r}'_{2k} = \bar{R}'_{2k} ,$$

$$\begin{aligned} & (L - |\bar{R}'_{3k}|)^2 - 2(L - |\bar{R}'_{3k}|) |\bar{R}'_{2k}| \\ &+ (\bar{F}_2 - \bar{M}_k) \cdot (-2\bar{R}'_{2k} - \bar{F}_2 + \bar{M}_k) = 0 \end{aligned}$$

recalling that $\bar{R}'_{1k} + \bar{R}'_{2k} = \bar{M}_k - \bar{F}_2$, we have

$$\begin{aligned} & (L - |\bar{R}'_{3k}|)^2 - 2(L - |\bar{R}'_{3k}|) |\bar{R}'_{2k}| \\ &- (\bar{R}'_{1k} + \bar{R}'_{2k}) + (\bar{R}'_{1k} - \bar{R}'_{2k}) = 0 \end{aligned}$$

simplifying and using the quadratic formula

$$L - |\bar{R}'_{3k}| = \frac{1}{2} \left(2|\bar{R}'_{2k}| \pm \sqrt{4|\bar{R}'_{2k}|^2 + 4(|\bar{R}'_{1k}|^2 - |\bar{R}'_{2k}|^2)} \right)$$

finally,

$$L = |\bar{R}'_{2k}| + |\bar{R}'_{1k}| + |\bar{R}'_{3k}|$$

Now it remains to find the surface normal at this sub-reflector point. From Appendix III,

$$\hat{r}'_{3k} = \frac{(\sin \alpha_2 \cos \beta_2)\hat{i} + (\cos \alpha_2 \sin \beta_2)\hat{j} + (\cos \alpha_2 \cos \beta_2)\hat{k}}{\sqrt{1 - \sin^2 \alpha_2 \sin^2 \beta_2}} \quad (\text{III-29})$$

Substituting this into equation (III-3) yields

$$\hat{r}'_{2k} = \frac{(\sin \alpha_2 \cos \beta_2)\hat{i} + (\cos \alpha_2 \sin \beta_2)\hat{j} + (\cos \alpha_2 \cos \beta_2)\hat{k}}{\sqrt{1 - \sin^2 \alpha_2 \sin^2 \beta_2}} - \frac{2\hat{n}_{MK} \cdot [(\sin \alpha_2 \cos \beta_2)\hat{i} + (\cos \alpha_2 \sin \beta_2)\hat{j} + (\cos \alpha_2 \cos \beta_2)\hat{k}] \hat{n}_{MK}}{\sqrt{1 - \sin^2 \alpha_2 \sin^2 \beta_2}} \quad (\text{III-30})$$

Also by definition,

$$\hat{r}'_{1k} = \frac{\bar{S}_{k+1} - \bar{F}_2}{|\bar{S}_{k+1} - \bar{F}_2|} \quad (\text{III-31})$$

Using equation (III-4), this subreflector normal is

$$\hat{n}_{S_{k+1}} = - \frac{\hat{r}'_{2k} - \hat{r}'_{1k}}{|\hat{r}'_{2k} - \hat{r}'_{1k}|} \quad (\text{III-32})$$

Thus, cycling through the above formulas iteratively generates two sets of points. The spacing of points depends on the input parameters and cannot be reduced without affecting the scanning characteristics of the system. The points are joined using LaGrange interpolation or least squares curve fitting. Several mathematical texts were particularly useful for this analysis [84]-[88].

E. Surface Generation

Unlike the planar symmetrical case, there is no guarantee that the points determined iteratively in the offset case can be joined to form a continuous curve. Since each iteration specifies a pair of both points and their normals, simply finding the best-fit polynomial through the points does not suffice. Figure 30 illustrates this problem. Four points and their normals are specified. If these points are connected with a smooth curve, the normals specified at the points disagree with the normals to the curve at these points.

This problem can be solved by adjusting the aperture center parameters C_1 or C_2 , or the first subreflector normal \hat{n}_{S1} , which are not present in the symmetric case. It has been noticed, though not rigorously proved, that if the best-fit curve agrees with the normal at one of the points, it approximately agrees with the normals of the other points defining that curve. Also, if the subreflector curve agrees with its specified normals, so will the main reflector curve.

To verify that the best-fit functions truly represent the desired curves, a test was devised. If the curve is indeed a correct solution, every point on it can be used as an initial point for the iterative generation process. Keeping the other parameters fixed, the initial point is picked at random from the curve, the normal to the curve at that point

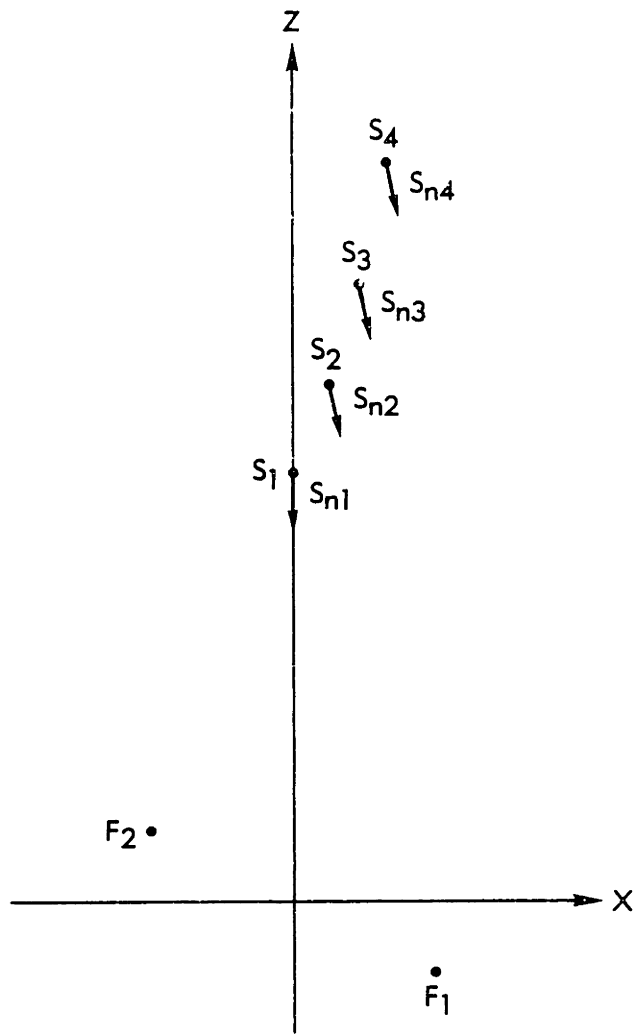


Figure 30. A Set of Subreflector Points and Normals Which Cannot be Joined with a Smooth, Well Behaved Curve

is calculated, and a new iterative generation is performed. The best-fit polynomial for the subreflector curve is found from the new set of subreflector points, and the result is compared to the original best-fit function. If there are only small discrepancies between the two over the desired domain, the original curve is a good solution. Figure 31 displays the results of this verification by indicating the differences between the original and perturbed curves for case of $\pm 8^\circ$ focusing with $L = 0.65$, $\bar{F}_1 = (-0.1, 0, -0.2)$, $\bar{F}_2 = (0.1, 0, -0.3)$, $\bar{S}_1 = (0, 0, 0.7)$, and $\hat{n}_{S1} = (0, 0, -1)$. The random point on the original curve is $(0.01, 0, 0.72)$.

More complex than joining planar points with a curve is the problem of joining points in space to arrive at a surface. The vector iteration techniques can generate an infinite sequence of points in space, each of which is an exact solution to the system with given parameters but independent of all but a few preceding and succeeding points.

The procedure used to form a surface is basically a trial and error formulation. First, a "reasonable" 2-dimensional offset solution is found. For simplicity, assume this 2-dimensional profile and the focal points are in the x-z plane. This curve is tested to verify its correspondence to the required normals. Then an even order polynomial is chosen in the transverse (y-z) plane that will be the locus

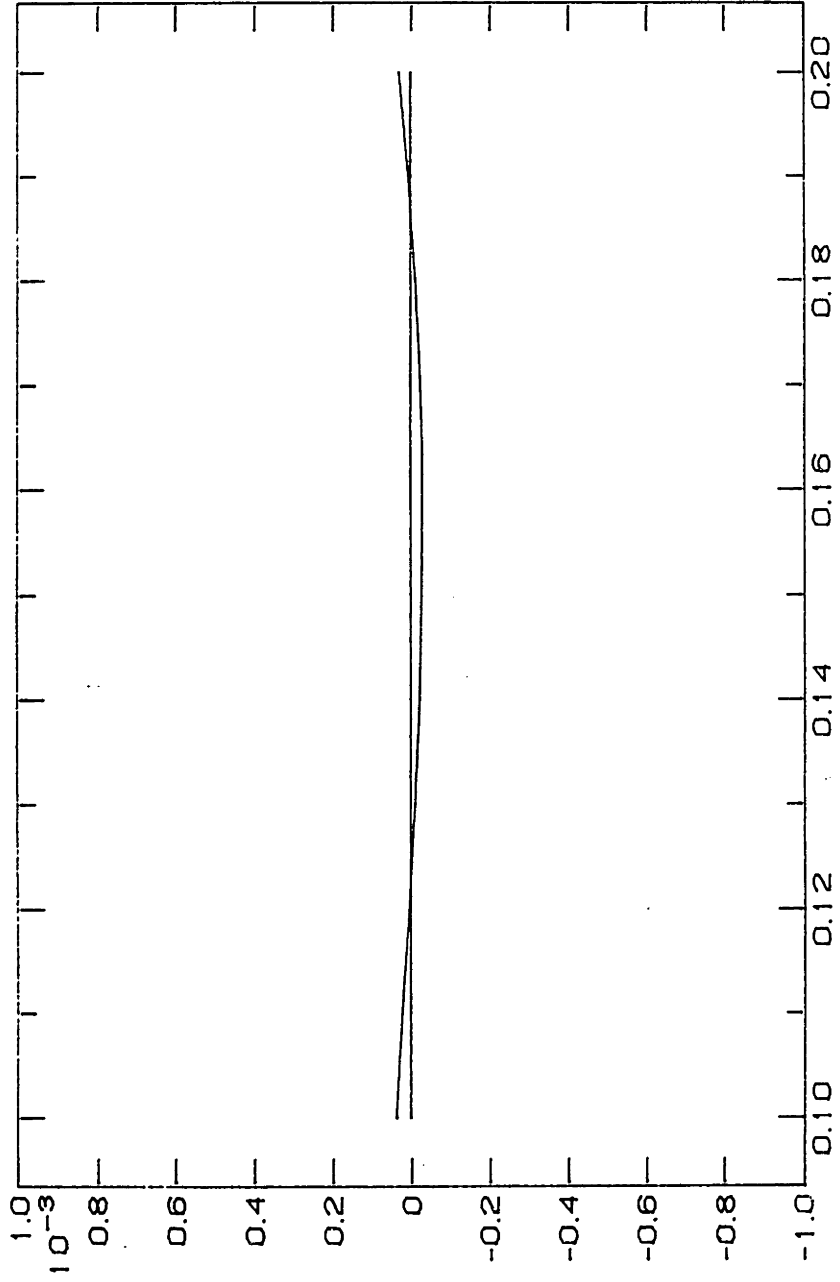


Figure 31. Subreflector Realizability Check

of subreflector starting points (\vec{S}_{1i}). This transverse polynomial determines the shape of the reflectors in 3 dimensions. A small increment in the transverse direction (Δy) is chosen to determine the \bar{S}_{1i} (refer to Figure 32). The starting point of the i th iteration is thus:

$$\bar{S}_{1i} = [x_0, y_0 + i\Delta y, z_0 + P(i\Delta y)]$$

where (x_0, y_0, z_0) is the point where the transverse starting polynomial intersects the original 2-dimensional offset curve, and $P(y)$ is the transverse polynomial. The starting normals are also found from the polynomial:

$$\hat{n}_{S1i} = \frac{\left(n_{S1x}, \left. \frac{dP}{dy} \right|_{i\Delta y}, n_{S1z} \right)}{\sqrt{(n_{S1x})^2 + \left(\left. \frac{dP}{dy} \right|_{i\Delta y} \right)^2 + (n_{S1z})^2}}$$

Now, if the transverse polynomial is carefully chosen, each new sequence of subreflector points will fit on a space curve resembling the original 2-dimensional curve. The algorithm for choosing the transverse polynomial for the particular case tested is presented in the next chapter. A surface is constructible if the following three conditions are met.

a. The progression of projections of the space curves onto the x - z plane must vary continuously and monotonically from the original curve (in the x - z plane).

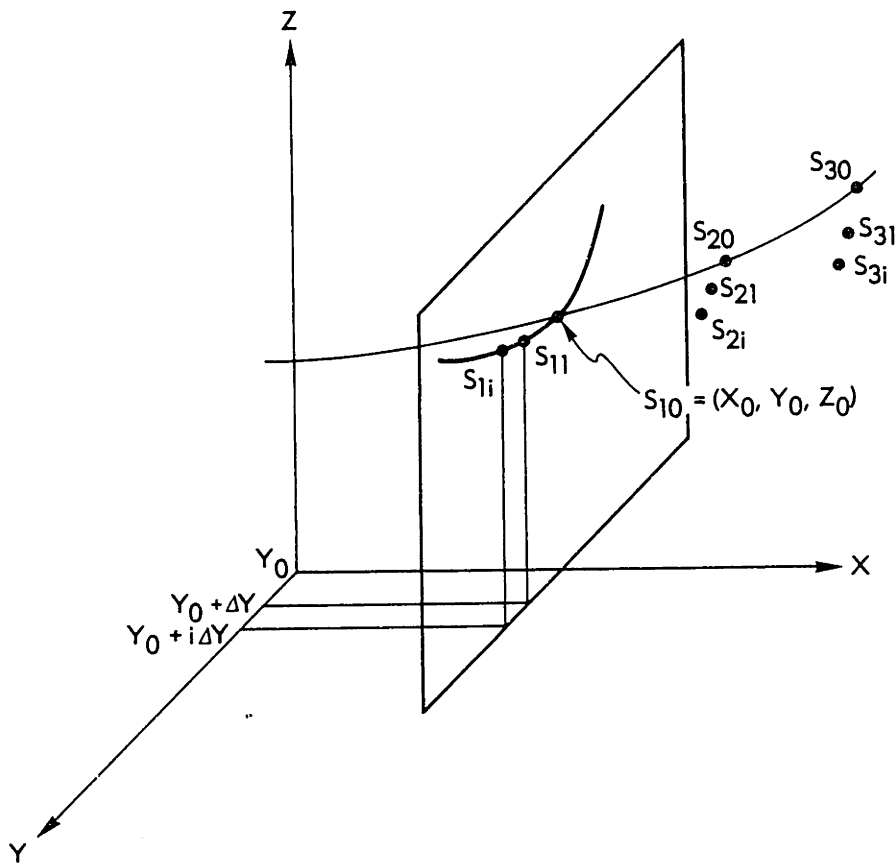


Figure 32. Extension of 2-Dimensional Profile to 3 Dimensions Using a Specified Transverse Polynomial

b. The displacement of each curve in the y -direction must remain fairly constant over the domain of x -values.

c. The y -components of the normals at each of the points on a given curve must remain fairly constant over the domain of x -values.

Thus, there should be no jumps in y or the normals along any path in the transverse direction, and every curve differs from the previous one in the same way as the one before it. This guarantees that the surface has no cusps and does not fold into itself, and that the normals at the derived points are the normals to the surface at these points.

Figure 33 shows the progression of projections of the space curves onto the x - y plane. It is apparent that there are no overlappings or large gaps. The progression of projections of the same space curves (which continue past the reflector boundaries) onto the y - z plane is shown in Figure 34. This demonstrates a gradual, predominantly linear deviation from the original curve. Note that the original curve projects directly onto the axis. The deviations become more apparent for curves farther from the x -axis. Again, there are no overlappings or large gaps. The computer printout data which were used to generate these plots are shown in Figure 35. It is observed that the y -component of the subreflector normals increases slightly from the starting point. This

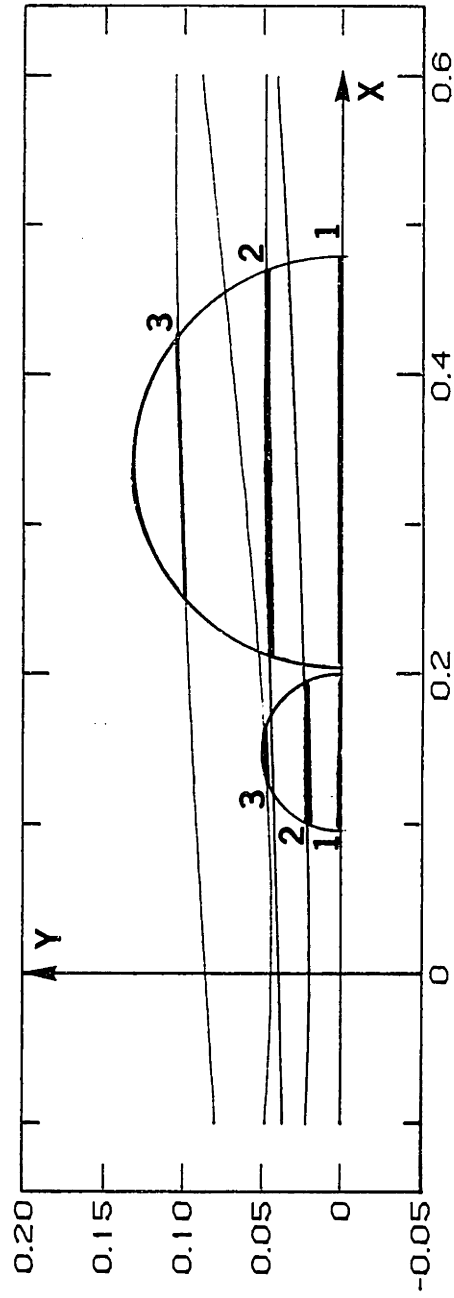


Figure 33. Progression of Projections of Space Curves onto the x-y Plane

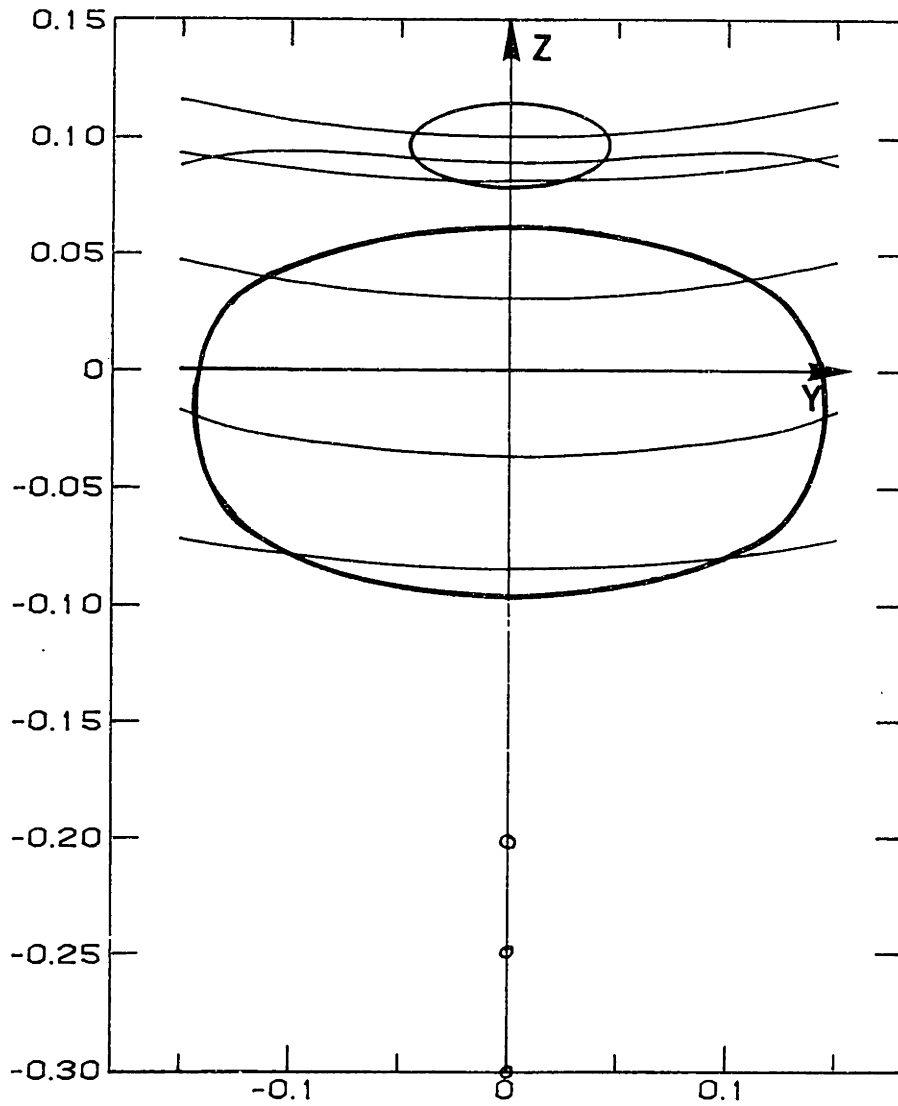


Figure 34. Progression of Projections of Space Curves onto the y-z Plane

Portions of the text on the
following page(s) are not legible
in the original.

```

INITIAL PCINTS = 10000 0.0 -20000 0.10000 0.0 -30000
1ST SUBREFLECTOR PCINT 0.05000 0.0 0.07228
1ST SUBREFLECTOR NORMAL 0.05054 0.0 -0.94589
ALPHA1 ALPHA2 BETA1 BETA2 L C1 C2
H.CC -H.CC 0.0 0.0 0.650 0.252 0.0

```

1

SUBREFLECTOR POINTS			SUBREFLECTOR NORMAL			MAIN REFLECTOR POINTS			MAIN REFLECTOR NORMAL		
0.050	0.0	0.072	0.091	0.0	-0.996	0.189	0.0	-0.098	-0.269	0.0	0.963
0.112	0.0	0.081	0.186	0.0	-0.983	0.322	0.0	-0.048	-0.426	0.0	0.905
0.188	0.0	0.099	0.259	0.0	-0.966	0.449	0.0	0.024	-0.544	0.0	0.839
0.284	0.0	0.127	0.298	0.0	-0.955	0.555	0.0	0.100	-0.617	0.0	0.787
0.397	0.0	0.163	0.305	0.0	-0.952	0.629	0.0	0.160	-0.652	0.0	0.758

COEFFICIENTS FOR THE POLYNOMIAL OF ORDER 4 ARE
0.07066 -0.02648 1.28116 -2.09789 1.28589

COEFFICIENTS FOR THE POLYNOMIAL OF ORDER 4 ARE
-0.12854 0.05630 0.48560 0.49150 -0.38942

2

SUBREFLECTOR POINTS			SUBREFLECTOR NORMAL			MAIN REFLECTOR POINTS			MAIN REFLECTOR NORMAL		
0.075	0.011	0.075	0.132	0.015	-0.991	0.245	0.024	-0.080	-0.339	-0.032	0.940
0.142	0.012	0.087	0.220	0.018	-0.975	0.377	0.025	-0.019	-0.481	-0.033	0.876
0.226	0.013	0.109	0.275	0.018	-0.960	0.497	0.026	0.057	-0.580	-0.032	0.814
0.331	0.015	0.142	0.304	0.018	-0.953	0.590	0.026	0.128	-0.635	-0.030	0.772
0.445	0.018	0.178	0.302	0.017	-0.953	0.651	0.026	0.180	-0.658	-0.029	0.752

COEFFICIENTS FOR THE POLYNOMIAL OF ORDER 4 ARE
0.07094 -0.03112 1.31356 -2.18166 1.35712

COEFFICIENTS FOR THE POLYNOMIAL OF ORDER 4 ARE
-0.13703 0.14311 0.17845 0.96118 -0.65147

3

SUBREFLECTOR POINTS			SUBREFLECTOR NORMAL			MAIN REFLECTOR POINTS			MAIN REFLECTOR NORMAL		
0.075	0.022	0.075	0.132	0.031	-0.991	0.245	0.048	-0.078	-0.339	-0.065	0.939
0.142	0.023	0.088	0.220	0.035	-0.975	0.377	0.051	-0.018	-0.480	-0.065	0.875
0.226	0.026	0.110	0.279	0.037	-0.960	0.497	0.052	0.058	-0.579	-0.063	0.813
0.331	0.031	0.142	0.303	0.036	-0.952	0.589	0.052	0.129	-0.634	-0.060	0.771
0.445	0.036	0.179	0.301	0.035	-0.953	0.650	0.051	0.180	-0.657	-0.057	0.752

COEFFICIENTS FOR THE POLYNOMIAL OF ORDER 4 ARE
0.07109 -0.02951 1.30900 -2.17209 1.34914

COEFFICIENTS FOR THE POLYNOMIAL OF ORDER 4 ARE
-0.13631 0.14609 0.17377 0.96851 -0.65773

4

SUBREFLECTOR POINTS			SUBREFLECTOR NORMAL			MAIN REFLECTOR POINTS			MAIN REFLECTOR NORMAL		
0.075	0.033	0.076	0.132	0.046	-0.990	0.245	0.072	-0.076	-0.338	-0.097	0.936
0.142	0.035	0.088	0.219	0.053	-0.974	0.376	0.076	-0.016	-0.479	-0.098	0.873
0.227	0.039	0.111	0.277	0.055	-0.959	0.496	0.077	0.060	-0.577	-0.095	0.811
0.331	0.046	0.143	0.301	0.054	-0.952	0.588	0.077	0.130	-0.632	-0.090	0.770
0.445	0.054	0.179	0.299	0.052	-0.953	0.648	0.077	0.181	-0.655	-0.086	0.751

COEFFICIENTS FOR THE POLYNOMIAL OF ORDER 4 ARE
0.07136 -0.02688 1.30165 -2.15714 1.33717

COEFFICIENTS FOR THE POLYNOMIAL OF ORDER 4 ARE
-0.13495 0.14961 0.17059 0.97314 -0.66380

5

SUBREFLECTOR POINTS			SUBREFLECTOR NORMAL			MAIN REFLECTOR POINTS			MAIN REFLECTOR NORMAL		
0.075	0.044	0.076	0.132	0.062	-0.989	0.244	0.099	-0.074	-0.336	-0.129	0.933
0.142	0.047	0.089	0.218	0.070	-0.973	0.376	0.101	-0.013	-0.476	-0.130	0.870
0.227	0.052	0.111	0.276	0.073	-0.958	0.495	0.103	0.062	-0.574	-0.126	0.809
0.331	0.061	0.144	0.299	0.072	-0.952	0.586	0.103	0.132	-0.628	-0.119	0.769
0.445	0.072	0.180	0.297	0.070	-0.952	0.649	0.102	0.183	-0.651	-0.114	0.750

COEFFICIENTS FOR THE POLYNOMIAL OF ORDER 4 ARE
0.07172 -0.02324 1.29166 -2.13673 1.32076

COEFFICIENTS FOR THE POLYNOMIAL OF ORDER 4 ARE
-0.13306 0.15431 0.16692 0.97729 -0.67155

Figure 35. Sample Computer Output for Five Separate Transverse Starting Points
 $\Delta y = 0.011$

is partly due to the slightly increasing y-component of the space curve. Also, the y-component of the normals increases with a consistent pattern for each curve generation. Thus, this example produces good results.

Choosing the proper sections of the generated surfaces for the sub- and main reflectors is a difficult task. As with the torus, only part of the reflector is used for any particular scan direction. It is impossible for rays reflecting off every point on the main reflector from a variety of angles to intercept the subreflector. Thus, efficiency is fairly low for both the torus and the bifocal. Figure 36 displays this problem. Notice the small amount of overlap of the illuminated segments on the main reflector.

It is possible to increase the efficiency of the main reflector, but at the expense of underilluminating the subreflector. If, instead of fixing the angle of illumination of the subreflector by the feeds, the main reflector is assumed to be fully illuminated, the subreflector becomes oversized. Tracing the rays which hit the extreme edges of the main reflector to the subreflector and then to the feed, the maximum size of the subreflector is determined. However, for this case, the subreflector becomes as large as the main reflector and blockage, alignment, and packaging problems rule out this configuration.

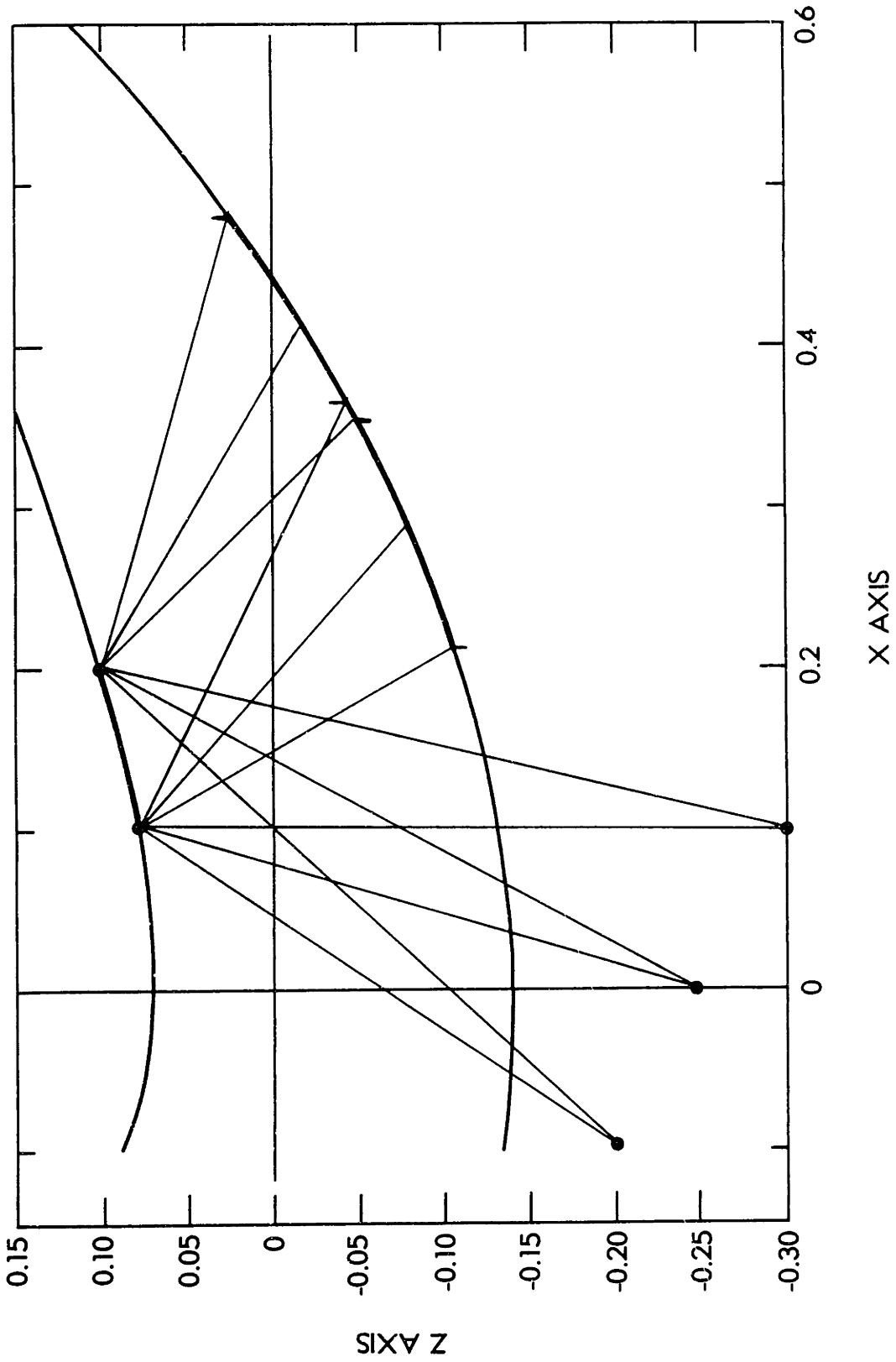


Figure 36. Illumination Efficiency of the Main Reflector Profile for Totally Illuminated Subreflector for Three Scanned Positions

An offset design was computed and tested. The geometry of the system is shown in Figure 37. This offset design has no blockage and uses feeds which are displaced asymmetrically about the z-axis. Notice the narrow feed angle. Even with a large subreflector (one third the diameter of the main reflector) and its accompanying low magnification factor, a small feed angle is required to eliminate spillover past the subreflector. The feeds are positioned behind the main reflector, which detracts from the packaging advantage, but is necessary to provide adequate feed displacement about the z-axis.

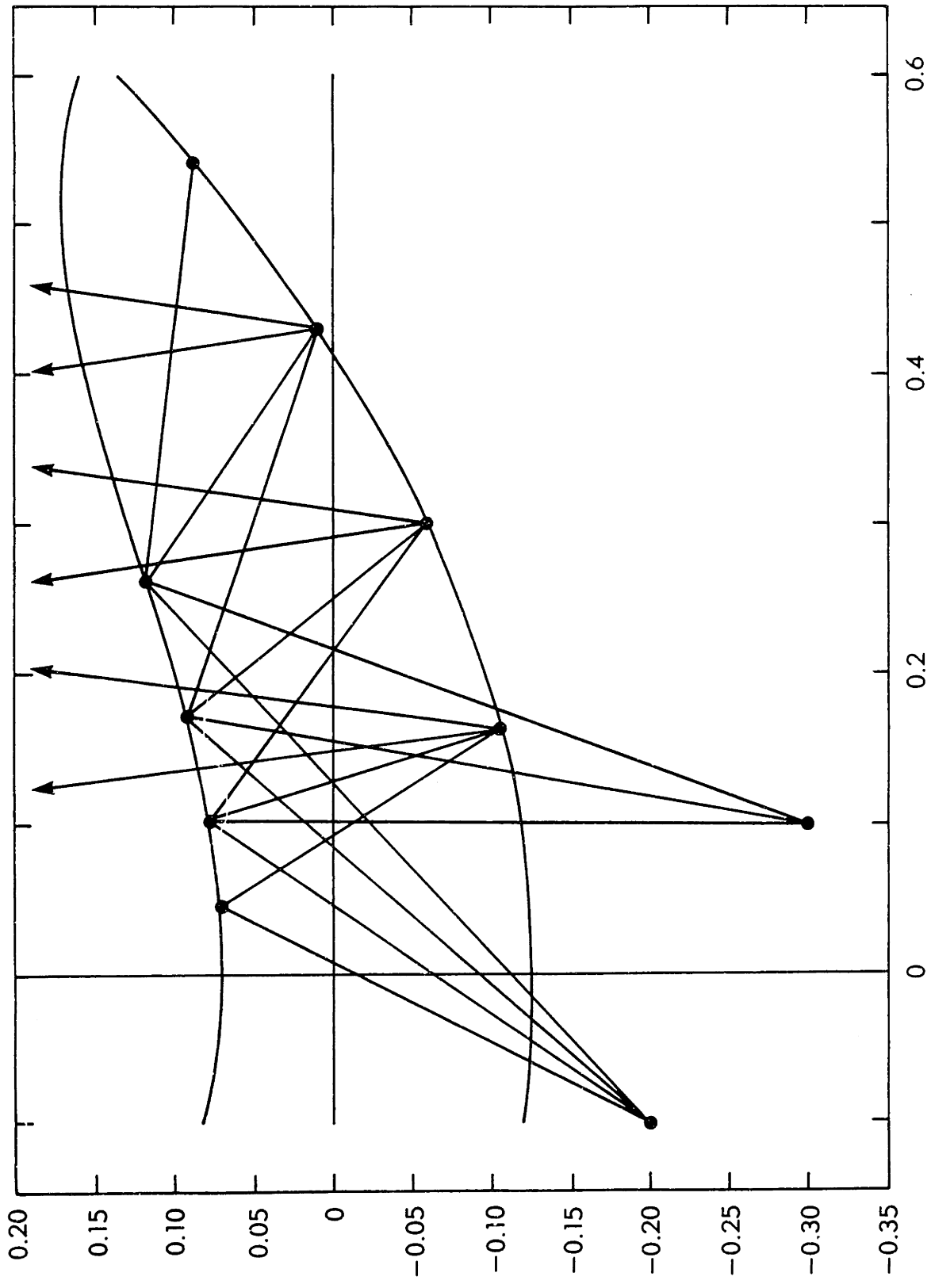


Figure 37. Actual Ray Paths for Offset Bifocal Profile at -8° and $+8^\circ$

APPENDIX III.1. CALCULATION OF \bar{R}_{3k}

The second reflected rays \bar{R}_{3k} , \bar{R}'_{3k} must originate at the point \bar{M}_k , and be normal to the scanned aperture planes. Thus, it is necessary to derive the normals to the aperture planes and also the perpendicular distances between them and \bar{M}_k .

Referring to Figure III.1-1,

$$\bar{CM} + \bar{MP} + \bar{PC} = 0$$

\bar{MP} is normal to Σ_1 and hence is normal to all vectors lying in Σ_1 .

$$\bar{PC} \in \Sigma_1$$

so

$$\bar{MP} \cdot (\bar{CM} + \bar{MP} + \bar{PC}) = 0$$

$$\bar{MP} \cdot \bar{CM} + |\bar{MP}|^2 = 0$$

or

$$|\bar{MP}| = - \frac{\bar{MP} \cdot \bar{CM}}{|\bar{MP}|} = -\bar{CM} \cdot \frac{\bar{MP}}{|\bar{MP}|}$$

Define

$$\bar{MP} = \bar{p} \times \bar{q} \quad ; \quad \bar{p}, \bar{q} \in \Sigma_1$$

So \bar{mp} is a normal to Σ_1 .

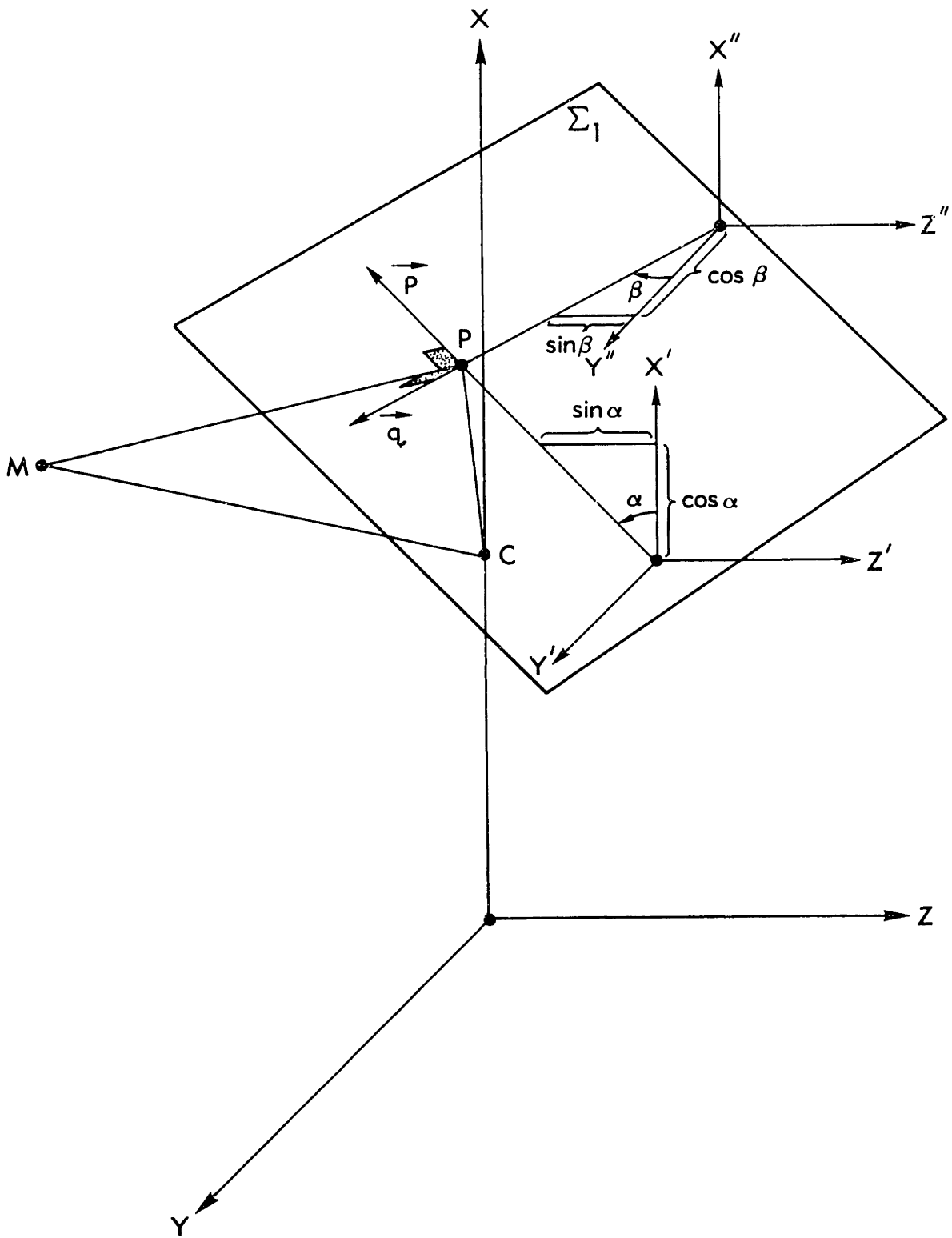


Figure III.1-1. Geometry of Tilted Aperture Phase Plane Vector Analysis

From the definition of the scan angle, let

$$\bar{p} = \cos \alpha_i \hat{i} - \sin \alpha_i \hat{k} \quad i = 1, 2$$

$$\bar{q} = \cos \beta_i \hat{j} - \sin \beta_i \hat{k} \quad i = 1, 2$$

$$\overline{mp} = (\sin \alpha_i \cos \beta_i) \hat{i} + (\cos \alpha_i \sin \beta_i) \hat{j} + (\cos \alpha_i \cos \beta_i) \hat{k},$$

$i = 1, 2$

$$\begin{aligned} |\overline{mp}|^2 &= \sin^2 \alpha_i \cos^2 \beta_i + \cos^2 \alpha_i \sin^2 \beta_i + \cos^2 \alpha_i \cos^2 \beta_i \\ &= \sin^2 \alpha_i \cos^2 \beta_i + \cos^2 \alpha_i \\ &= 1 - \sin^2 \alpha_i \sin^2 \beta_i, \end{aligned} \quad i = 1, 2$$

Also, since

$$\overline{CM} = (M_x - C_1) \hat{i} + (M_y - C_2) \hat{j} + (M_z) \hat{k}$$

$$\frac{\overline{MP}}{|\overline{MP}|} = \frac{\overline{mp}}{|\overline{mp}|} = \hat{r}_3 = \frac{(\sin \alpha_i \cos \beta_i) \hat{i} + (\cos \alpha_i \sin \beta_i) \hat{j} + (\cos \alpha_i \cos \beta_i) \hat{k}}{\sqrt{1 - \sin^2 \alpha_i \sin^2 \beta_i}}$$

$$\frac{\overline{MP}}{|\overline{MP}|} = \frac{(C_1 - M_x) \sin \alpha_i \cos \beta_i + (C_2 - M_y) \cos \alpha_i \sin \beta_i - M_z \cos \alpha_i \cos \beta_i}{\sqrt{1 - \sin^2 \alpha_i \sin^2 \beta_i}}$$

APPENDIX III.2. COMPUTER PROGRAM PLOT
LISTING (IN SPEAKEASY)

EDITING PLOT

```

1 PROGRAM
2 GRAPHICS(TEK4014)
3 YMIN=-1
4 XMIN=-.1
5 XMAX=1
6 YBEST=1
7 A, B, YMIN, XMIN, XMAX, YBEST "INPUT NEW VALUES IF DESIRED"
8 PAUSE
9 X=INTEGERS(-100,100)/100
10 YH=0*X
11 YAXIS=99999999*X
12 Y=A(1)+A(2)*X+A(3)*X*X+A(4)*X**3
13 Y=Y+A(5)*X**4+A(6)*X**5+A(7)*X**6
14 YP=(A(1)+A(2)*X+A(3)*X*X)*YBEST
15 Y1=B(1)+B(2)*X+B(3)*X*X+B(4)*X**3+B(5)*X**4+B(6)*X**5+B(7)*X**6
16 YMA=B(1)*1.2+.2
17 YMAX=ROUNDED(YMA,1)
18 F=1/(4*A(3))
19 AA=B(1)+.5*(-A(1)-F)
20 EE=(F+A(1))/(2*B(1)-F-A(1))
21 IF (EF*EF .LE. 1 .OR. YBEST .EQ. 0) GO TO A
22 BB=AA*(EE*EE-1)**.5
23 XH=X/BE
24 YH=B(1)+AA*((1+YH*XH)**.5-1)
25 A: XAXIS=0
26 LENGY=(YMAX-YMIN)*1.04333
27 LENGX=(XMAX-XMIN)
28 CHOOS=MAX(LENGY,LENGX)
29 LENGX=LENGX/CHOOS*6
30 LENGY=LENGY/CHOOS*6
31 SETXAXIS(LENGTH=LENGX)
32 SETYAXIS(LENGTH=LENGY)
33 SETYSCALE(FROM:YMIN,TO:YMAX)
34 SETXSCALE(FROM:XMIN,TO:XMAX)
*35 GRAPH(Y,Y1,YP,YH,XAXIS,YAXIS:X)

```

IV. ANALYTIC RESULTS

A. Description of Geometry and Surface Approximation

The offset bifocal antenna system is generated on a point-by-point basis. Polynomial representations can approximate the surfaces, but unless they are of low order, they are hard to analyze and very difficult to fabricate.

The most practical bifocal design would be one which has a surface geometry that is close to existing quadric reflector shapes. Minimizing the departure of the main reflector surface from that of a paraboloid simplifies many aspects of the study of the offset bifocal. If a bifocal can be found such that its main reflector can be replaced by a paraboloid, then we have, in fact, found a wide angle scan correcting sub-reflector for this particular paraboloid.

To pursue this paraboloid approximation, first it is noticed that the variation of the 2-dimensional profile of the offset bifocal derived in the previous chapter from a true displaced parabola is at most only 0.055 wavelengths (Figure 38). It is reasonable to use this second order approximation, namely:

$$f(x) = 0.6858x^2 + 0.0155x - 0.13594 .$$

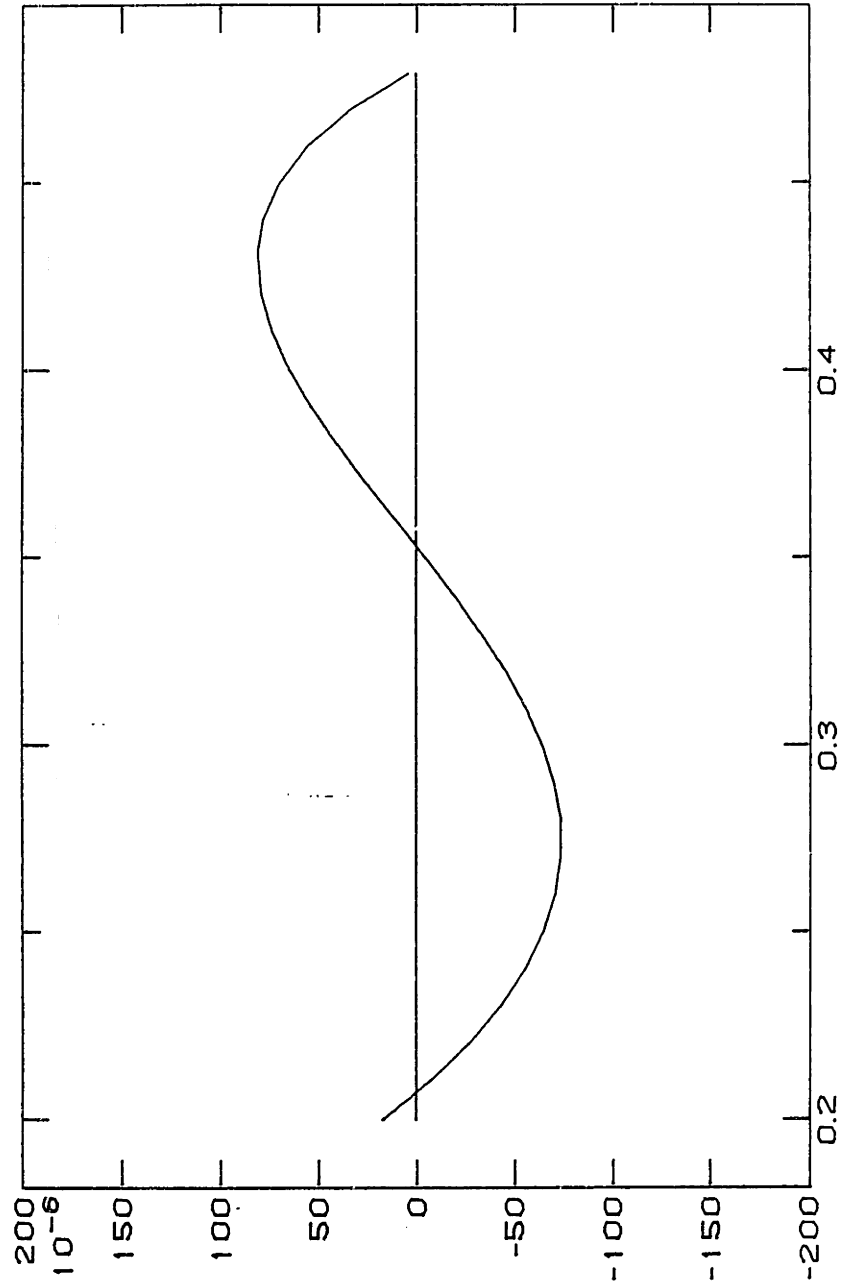


Figure 38. Difference in Wavelengths Between the Bifocal Main Reflector and its Best Fitting Paraboloid

A paraboloid of revolution is represented as the sum of two independent second-order functions of x and y , with the same quadratic coefficient. Thus, since it is assumed that the surfaces are symmetric about the offset plane, the equation of the paraboloid is:

$$z = 0.6858(x^2 + y^2) + 0.0155x - 0.13594 .$$

This paraboloid has a focal length of 0.3645 and a vertex at (0.01130, 0, -0.13594).

It is now necessary to find the corresponding offset bifocal subreflector (if possible). Starting with its 2-dimensional profile, a transverse function is sought. In the case of the offset Cassegrain reflector system, both surfaces are represented by a sum of independent functions of x and y . Using a particular Cassegrain subreflector's transverse function $[g(y)]$ to extend the bifocal profile to a surface appears to be a promising method. This Cassegrain must be one which has 2-dimensional profiles which best fit those of the bifocal. Once the 2-dimensional correspondence is found, the transverse function is duplicated.

The Cassegrain geometry which best fits the bifocal profile curves is difficult to define. Although the main reflectors will coincide, choosing an on-axis focal point for the bifocal or determining what part of its subreflector fits

the hyperbola is somewhat arbitrary. Using a simple approximation, the point on the line connecting the two bifocal foci $(-0.1, 0, -0.2)$ and $(0.1, 0, -0.3)$, having the same x value as the parabola's vertex: $(0.01130, 0, -0.25565)$ is used as the coinciding focus. The point on the subreflector profile $(0.01130, 0, 0.07053)$ is chosen to be common with the Cassegrain's hyperboloid.

Now, referring to Figure 39, the equations of the parabola and hyperbola

$$z_p = \frac{1}{4f} (x - x_0)^2 + z_0$$

and

$$z_H = a \sqrt{1 + \left(\frac{x - x_0'}{b}\right)^2} + z_0' - a$$

can be derived. It is apparent that

$$2c = z_0 + f - (-0.25565) ,$$

$$c - a = z_0 + f - z_0' .$$

$$b = \sqrt{c^2 - a^2}$$

Also, knowing the coefficient of the quadratic term of the parabola is 0.6858, the equations are

$$z_p = 0.6858(x - 0.0113)^2 - 0.13594$$

$$z_H = 0.08406 \sqrt{1 + \left(\frac{x - 0.0113}{0.22707}\right)^2} - 0.01353 .$$

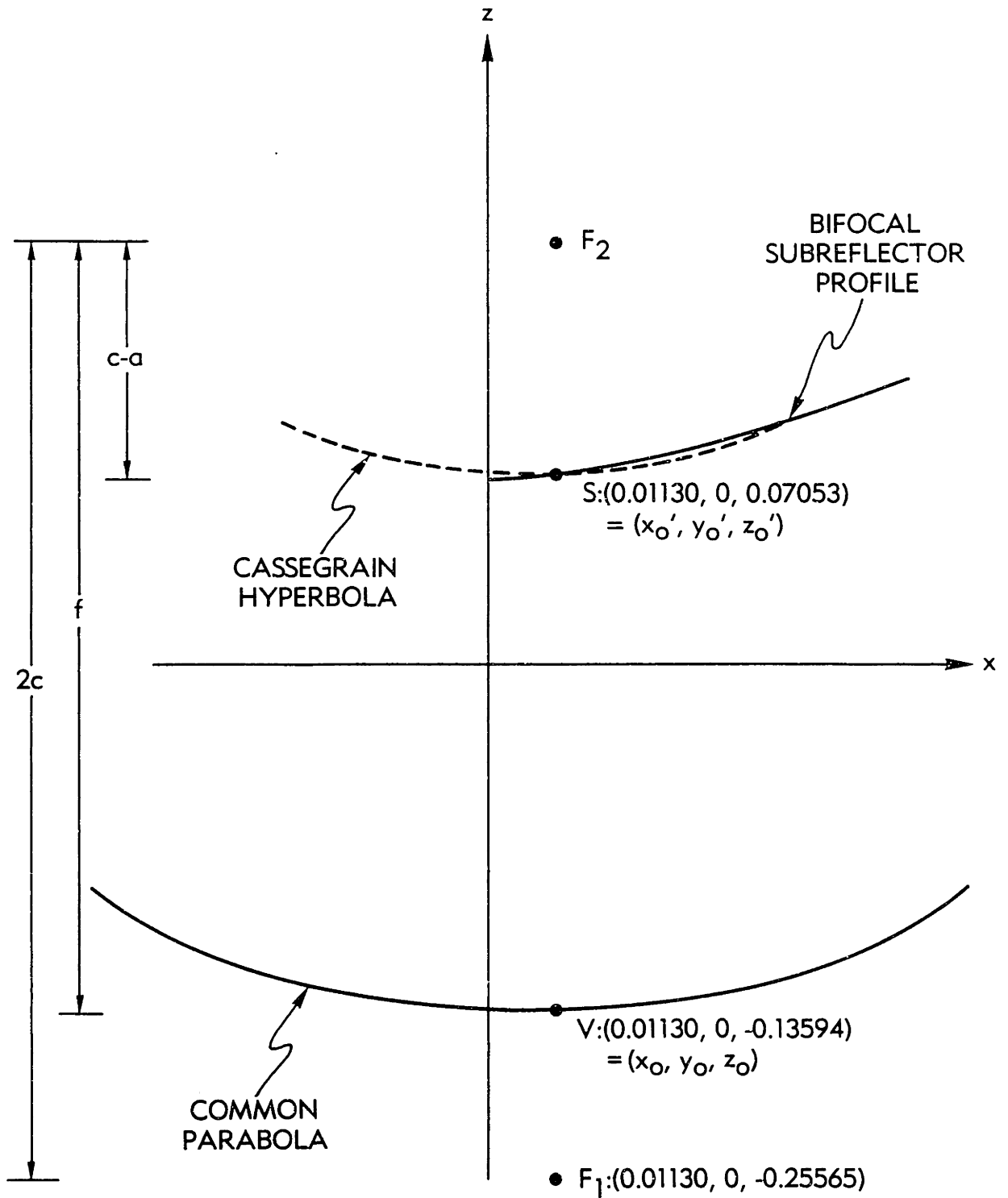


Figure 39. Procedure for Finding the Best Fit Offset Cassegrain to the Offset Bifocal

The hyperbola can be expanded as a power series:

$$z_H = z_0 + \frac{a}{2b^2} (x - x_0)^2 + - \frac{a}{8b^2} (x - x_0)^4 + \dots,$$

or entering particular values:

$$z_H = z_0' + 0.8152(x - 0.0113)^2 - 3.953(x - 0.0113)^4 + \dots$$

Having found the best fitting Cassegrainian hyperbola, an extension to the full hyperboloid follows:

$$z_H = z_0' + 0.8152[(x - 0.0113)^2 + y^2] - 3.953[(x - 0.0113)^4 + y^4] + \dots,$$

and so the transverse function is taken to be

$$g(y) = 0.8152y^2 - 3.953y^4 .$$

Analysis will proceed using this type of subreflector with a paraboloidal main reflector. Special fabrication is needed only for the subreflector.

Although the above procedure ends with the specification of the transverse polynomial instead of beginning with it, it nevertheless determines a surface with an offset bifocal profile using a simple main reflector. Of course, this newly derived transverse polynomial can be used to generate a "true" bifocal. This was done, and the resulting main reflector closely resembles a paraboloid. However, the differences in the surface geometry and the resulting electrical performance do not warrant the more complex design.

Since different sections of the main and subreflector's surfaces are illuminated for different scan positions, at least one of the surfaces must be oversized. Because of size limitations of the fabrication machinery, it is desirable to minimize the subreflector diameter. Thus, the section of the infinite surface which comprises the subreflector would be efficiently illuminated, sacrificing efficiency on the main reflector. Choosing the optimum sections of each surface is a very complex task. One must attempt to maximize area on both surfaces, yet minimize the separation between regions on the main reflector illuminated by different feeds. The amount of beam overlap on the main reflector determines the overall efficiency of the system. Of course, in choosing the optimal sections, subreflector blockage must be avoided. The problem of finding an algorithm to select the best sections is not addressed here. Tracing rays through the 2-dimensional profiles provides a trial and error method for selecting these sections. Figure 35 shows a typical progression of trial points, and the optimum segment choice.

Extending these segment limits to surface regions is accomplished by taking sections which have circular projections on an aperture plane perpendicular to the z-axis, with top and bottom limits coinciding with the profile segment limits (see Figure 40). The three highlighted circles on the

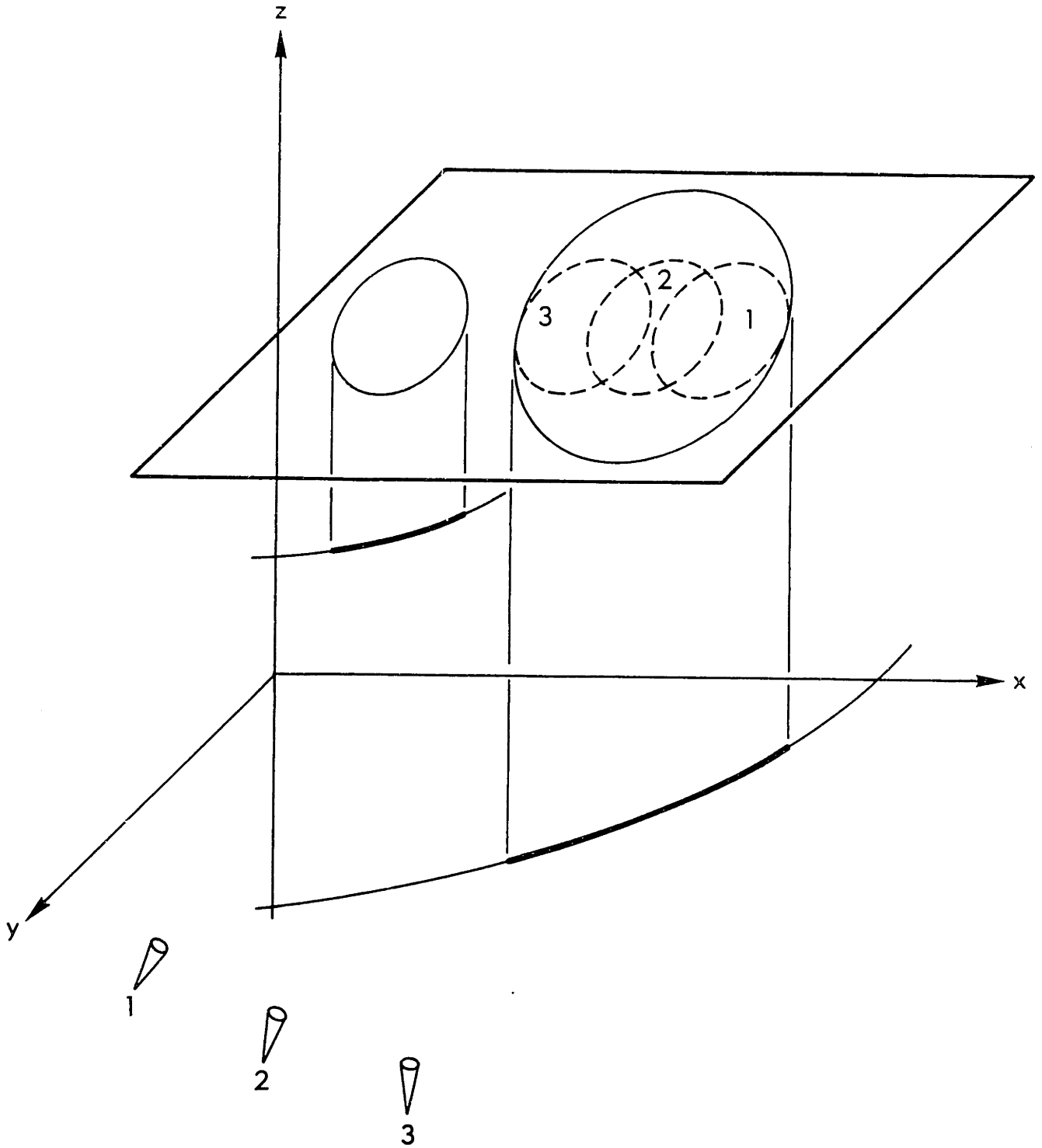


Figure 40. Illuminated Spots on the Main Reflector
Projection for Three Feed Positions

main reflector projection indicate the spots illuminated by the subreflector for three feed positions. It is noticed that for scanning in the elevation plane, a large part of the main reflector is unilluminated. This can partially be compensated for by widening the subreflector, or increasing the curvature in the transverse direction.

Choosing the proper illumination function for the subreflector is the next critical step in the antenna design. Since the subtended angle from the three feeds vary, different size source apertures are required. For simplicity, the primary radiators are modeled by circular waveguides. A tradeoff analysis must be made to minimize spillover, while maintaining an efficient (as near uniform as possible) illumination on the subreflector.

A FORTRAN program FEEDA was written to determine the subreflector subtended angle and the direction of the vector which is its bisector (see Appendix IV). Specifying a feed point, the reflector center, and projected radius, FEEDA provides the correct size and orientation of the feed.

The final step in the bifocal antenna design is the derivation of the optimum feed locus. As demonstrated for offset paraboloids [12] and Cassegrains [65], the locus is not a plane, but rather curved away from the first reflector. Rao [76],[77] also showed that the quadratic and astigmatic

phase errors could be significantly reduced if the on-axis feed in the symmetric bifocal is refocused backward (Figure 41). This result is predictable from optical aberrations theory where even order errors are minimized by axial refocusing.

The on-axis performance of the offset bifocal is optimized at the point $(-0.010, 0, -0.291)$. It has been discovered, however, that for smaller feed apertures and low frequencies, the phase aberration losses become less significant than spillover losses. So, for smaller feeds, the optimum position is closer to the subreflector.

B. Analytic Tools

COMSAT Laboratories' general antenna program (GAP) is a general purpose tool for the analysis of reflecting antenna systems [89]. Specifying reflector and feed geometries and orientations, GAP can provide near- and far-field power distributions, and supply spillover and polarization information. Surfaces can be entered as polynomials of up to fourth-order, or--using a finite element routine--as an array of surface points and normals. A large variety of feed types are available, modeling both ideal sources and real waveguide structures.

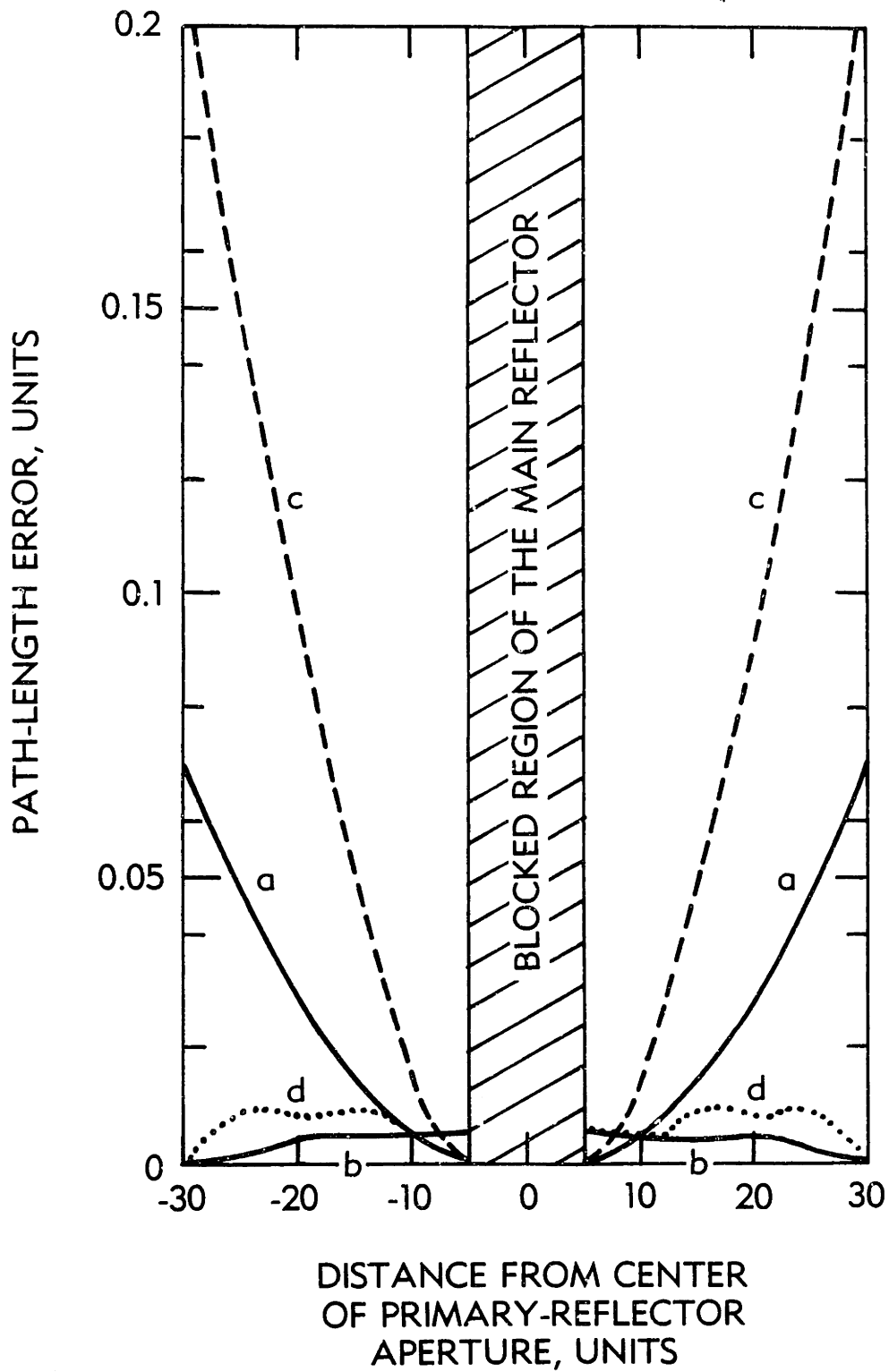


Figure 41. Reduction in Aperture Phase Error for Axial Refocusing of Central Feed in a Symmetric Bifocal [76] (2° scan: a. at halfway point; b. refocused. 4° scan: c. at halfway point; d. refocused.)

The program approximates the field scattering using both geometrical and physical optics. The former is used to trace through all reflectors from the feed to the final (main) reflector. The physical optics approximation is then used at the final reflector to provide the required far-field pattern. Since the source field must be discretized, the geometrical optics method is extremely suitable. Of course, a large number of sample rays must be used to specify the field, but reflections off secondary reflectors follow quickly by applying Snell's Law to each individual ray. Once rays have been traced to the main reflector, the induced surface current at the intersection point is found using

$$\vec{J}_s = 2 \sqrt{\frac{\epsilon}{\mu}} \hat{n} \times (\hat{S}_i \times \vec{E}) ,$$

where \hat{n} is the unit normal, \hat{S}_i is the incident unit vector, and \vec{E} is the incident electric field.

Proceeding with the physical optics approximation, Huygen principle,* and the far-field approximated dyadic Green's function are used to arrive at the equation of the E-field in the far field:

*That the field solution within a region V' is completely determined by boundary conditions on the surface S' enclosing V' . For a detailed derivation, see Silver or Kong.

$$\bar{E}_S = - \frac{j\omega\mu}{2\pi R} e^{-jkR} \int_{S'} ds e^{jk \cdot \bar{R}'} \cdot \left\{ (\bar{I} - \hat{R}\hat{R}) \cdot \bar{J}_S(\bar{R}') - \frac{1}{\eta} \bar{R} \times \bar{M}_S(\bar{R}') \right\}$$

where integration is taken over primed coordinates, and unprimed coordinates are the observation points, and \bar{I} is the identity dyadic. Since there are no magnetic currents on the surface of a perfect conductor,

$$\bar{M}_S(\bar{R}') = 0 .$$

The far-field pattern, within a constant factor of proportionality, is thus:

$$\bar{F}(\theta, \phi) = \int_{S'} ds e^{jk \cdot \bar{R}'} (\bar{I} - \hat{R}\hat{R}) \bar{J}_S(\hat{R}')$$

Digitizing the integral in order to numerically solve for \bar{F} yields:

$$F(\theta, \phi) = \sum_{i=1}^n a_i [e^{jk \cdot \bar{R}'} (\bar{I} - \hat{R}\hat{R}) \bar{J}_S(\hat{R}')],$$

where a_i is a small element of area.

Although GAP does not take diffraction at the edges of the reflectors into account, excellent agreement exists between computed and experimental performance.

The primary output from GAP is graphical far-field pattern information. Standard cut patterns provide gain, beamwidth, and sidelobe information for one dimension.

More useful, however, are 2-dimensional contour plots. These indicate the beam shape and the existence of sidelobes not on the principle azimuth and elevation planes. Contour plots are indispensable for shaped beam analysis. Contributions from several feeds can be superposed to analyze multi-beam array feed systems. Another useful characteristic of contour plotting is the clear representation of beams scanned in both azimuth and elevation in relation to one another.

The final form of far-field output makes use of 3-dimensional graphics. It combines the 2-dimensional contour pattern with the height (intensity) information available in cut plots. Appropriate shadowing yields perspective. Three-dimension graphics is limited to qualitative illustration, however, because of the inherent difficulty in indicating gain levels.

C. Computed Performance

Using GAP, a wide variety of test cases for the offset bifocal, and a battery of comparative analyses were performed. First, consider the bifocal. Figure 42 illustrates the geometry employed. In most of the following patterns, the main reflector has a diameter of 130λ , and a subreflector diameter 47.5λ . The feed to subreflector distance varies from 139.7λ to 188.0λ . The subtended illumination angles are 9° , 12.5° ,

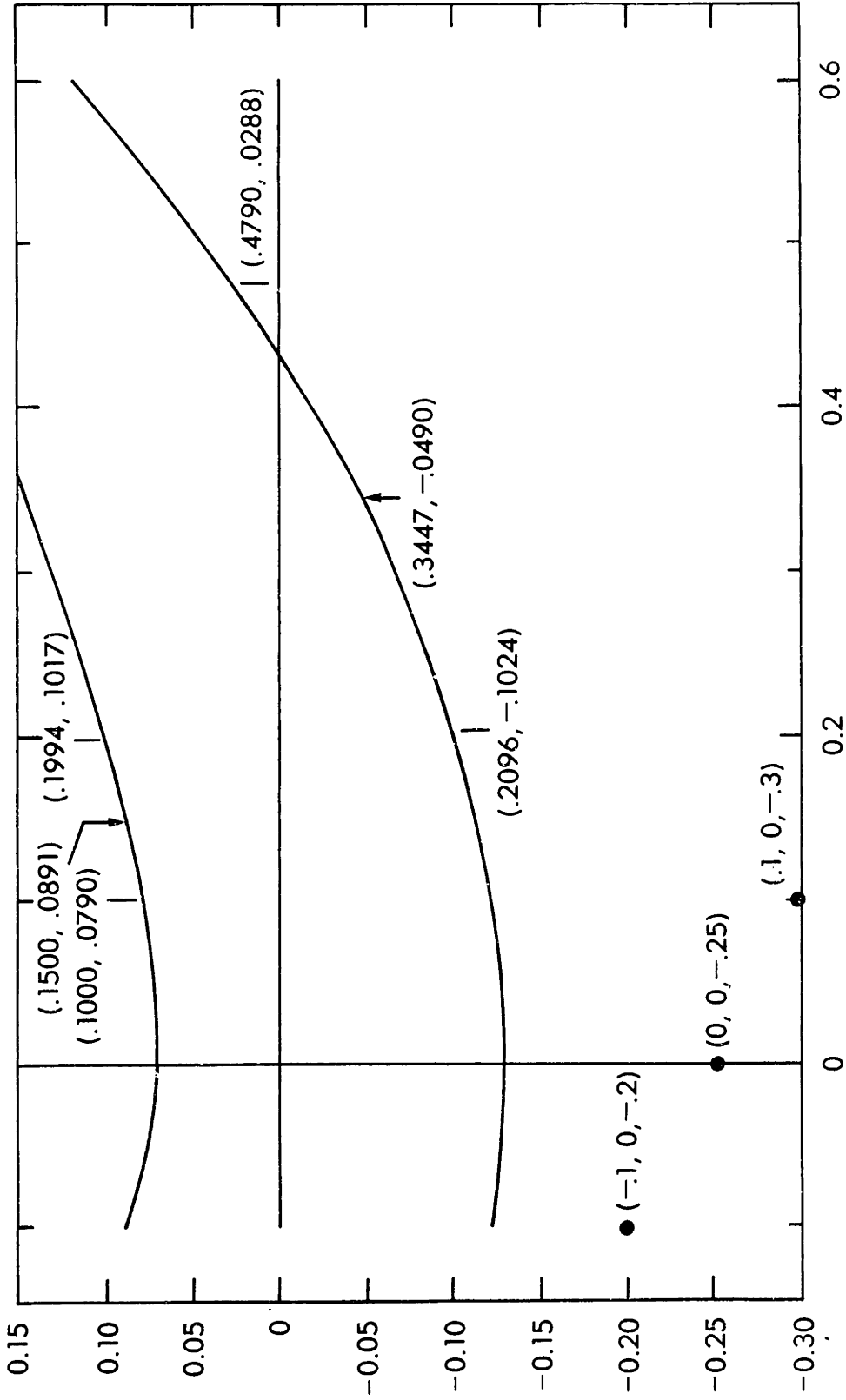


Figure 42. Numerical Specification of Geometry Analyzed Including:
 Focal Points, Reflector Profile Segment Limits and Projected
 Reflector Centers (scale 1:0.00104λ)

and 13.8° . The equivalent aperture illuminated at 100 percent efficiency has a peak gain of $10 \log_{10} (\pi D/\lambda)^2 = 52.2$ dB and a 3-dB beamwidth of 0.54° .

Several feed types were tested. The optimum arrangement, which correctly balances the tradeoff between maximum (uniform) efficiency and minimum spillover, and simultaneously minimizes feed area, consists of circular waveguides with aperture diameters of 12, 9.6, and 11.2 wavelengths for -8° , 0° , and $+8^\circ$, respectively. Note that the on-axis feed has the smallest aperture. This is due to the fact that the central section of the main reflector is illuminated by this feed, so it is more advantageous to provide a gradually tapered power distribution than restrict subreflector spillover. For the other feed positions, the top and bottom edges of the main reflector are illuminated, necessitating a more tapered distribution across both main and subreflectors.

Figure 43 shows the power contour patterns formed for the two scanned and the on-axis positions. The contour levels, similar to topographic map representations, correspond to equi-gain contours. Relative to the peak gain, the levels in dB are -1, -3, -6, -10, -15, -20, -30 (with an additional level at -25 dB for the on-axis case to enhance sidelobe clarity). The vertical scale identifies the beam elevation angle, the horizontal being the azimuth angle, with $(90^\circ, 90^\circ)$ being

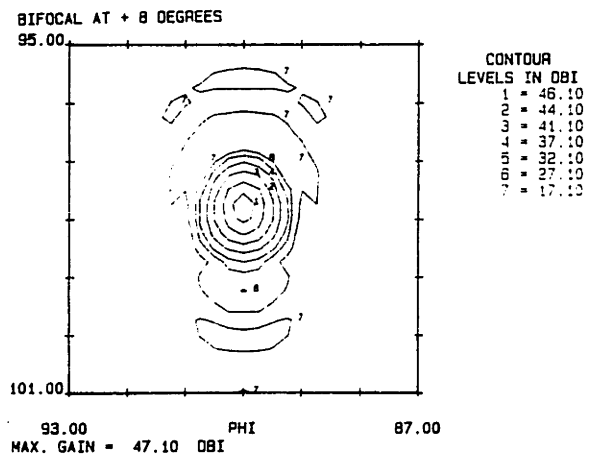
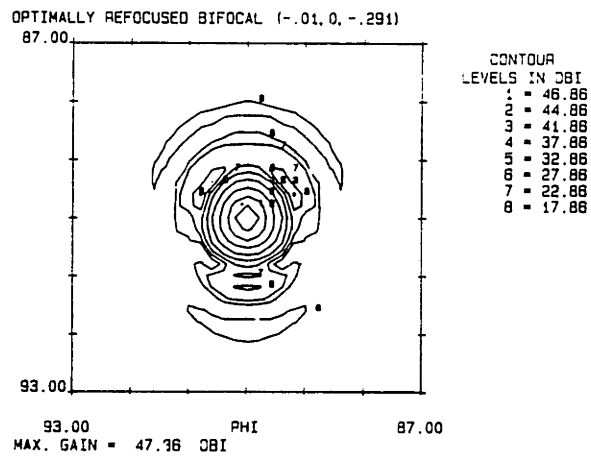
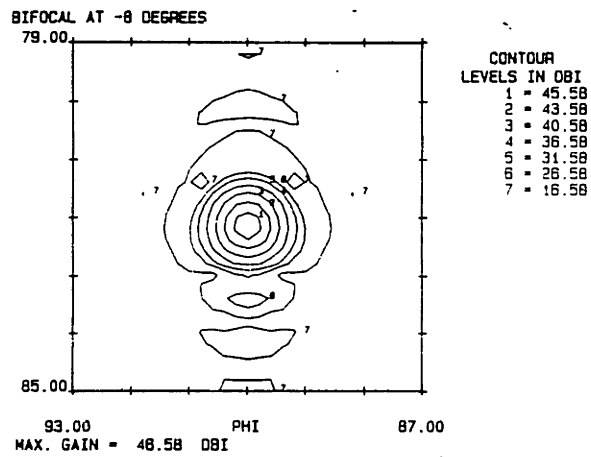
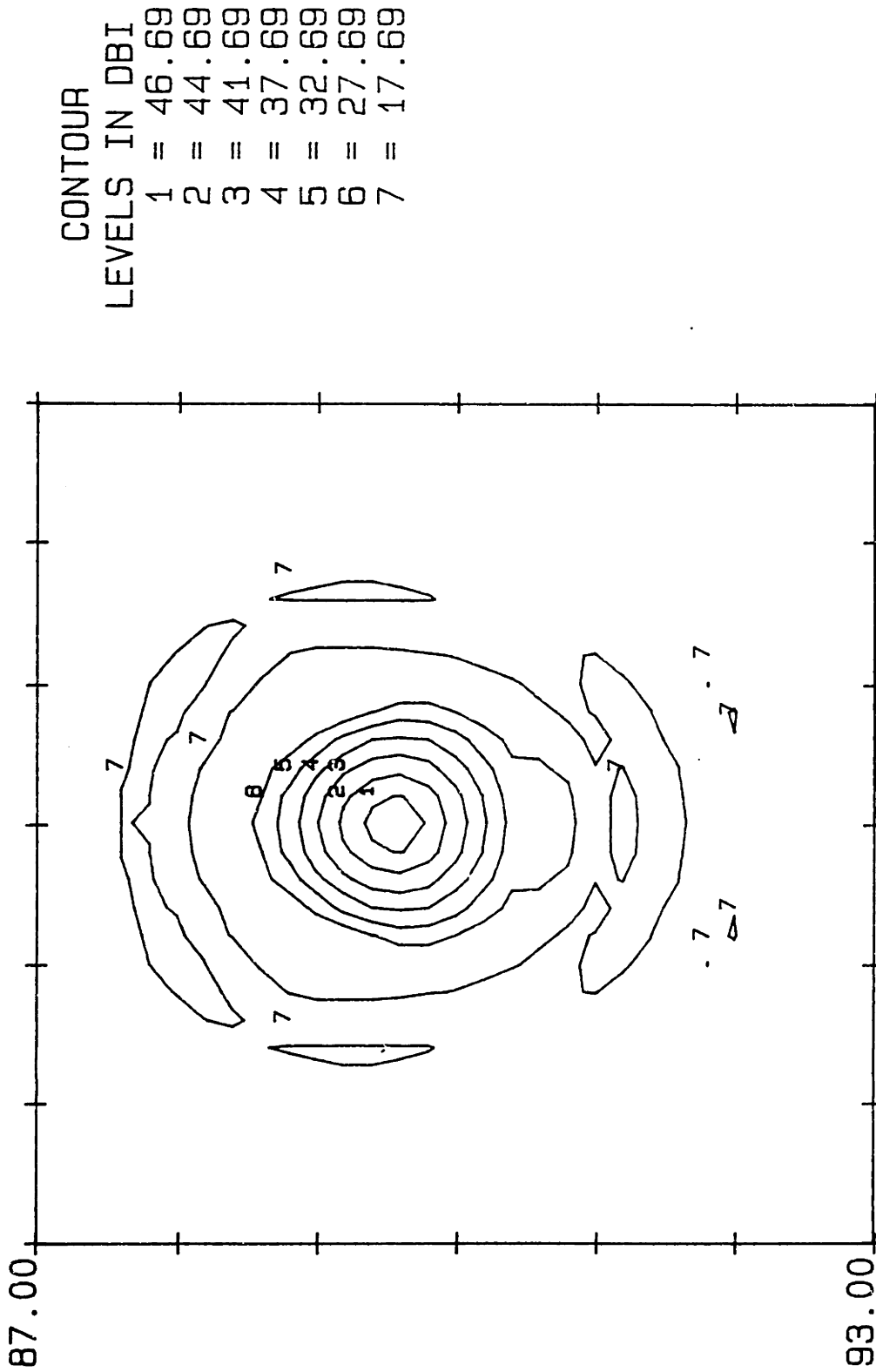


Figure 43. Radiation Contour Patterns of a 130λ Offset Bifocal Feed with Optimized Circular Waveguides for -8° , 0° , and $+8^\circ$ in Elevation

directly on-axis. Thus, with the beam centers located at 82°, 90°, and 98° in elevation, ±8° of scanning is demonstrated.

The best pattern, apparently, is for the on-axis case. Its superiority over the two design positions is the result of a combination of effects. Probably most importantly, the more efficient illumination of the center of the main reflector--which is inherently underilluminated--overcomes phase error aberrations. Also, the feed generating this beam has been optimally refocused. Figure 44 is the on-axis pattern before refocusing. The maximum gain is noticeably lower and the first sidelobes are higher. The improvement resulting from refocusing does not require any sacrifices or produce any asymmetries. This confirms the claim that the primary aberrations for beams located between the two design scan positions are of even order: quadratic phase error and astigmatism. Thus, the offset bifocal minimizes coma over the entire scanned field of view, a characteristic that is absent in all other antennas with single perfect focal points. The coma is not completely absent at the two design scan positions. The elevation cut patterns, Figure 45, indicate a slight asymmetry and clearly identify the sidelobe levels. However, the beams are circular with first sidelobe level 20-25 dB below the peak gain level.

BIFOCAL ON AXIS WITHOUT REFOCUSING



93.00 PHI 87.00

MAX. GAIN = 47.69 DBI

Figure 44. Contour Pattern for 0° Scan Without Refocusing

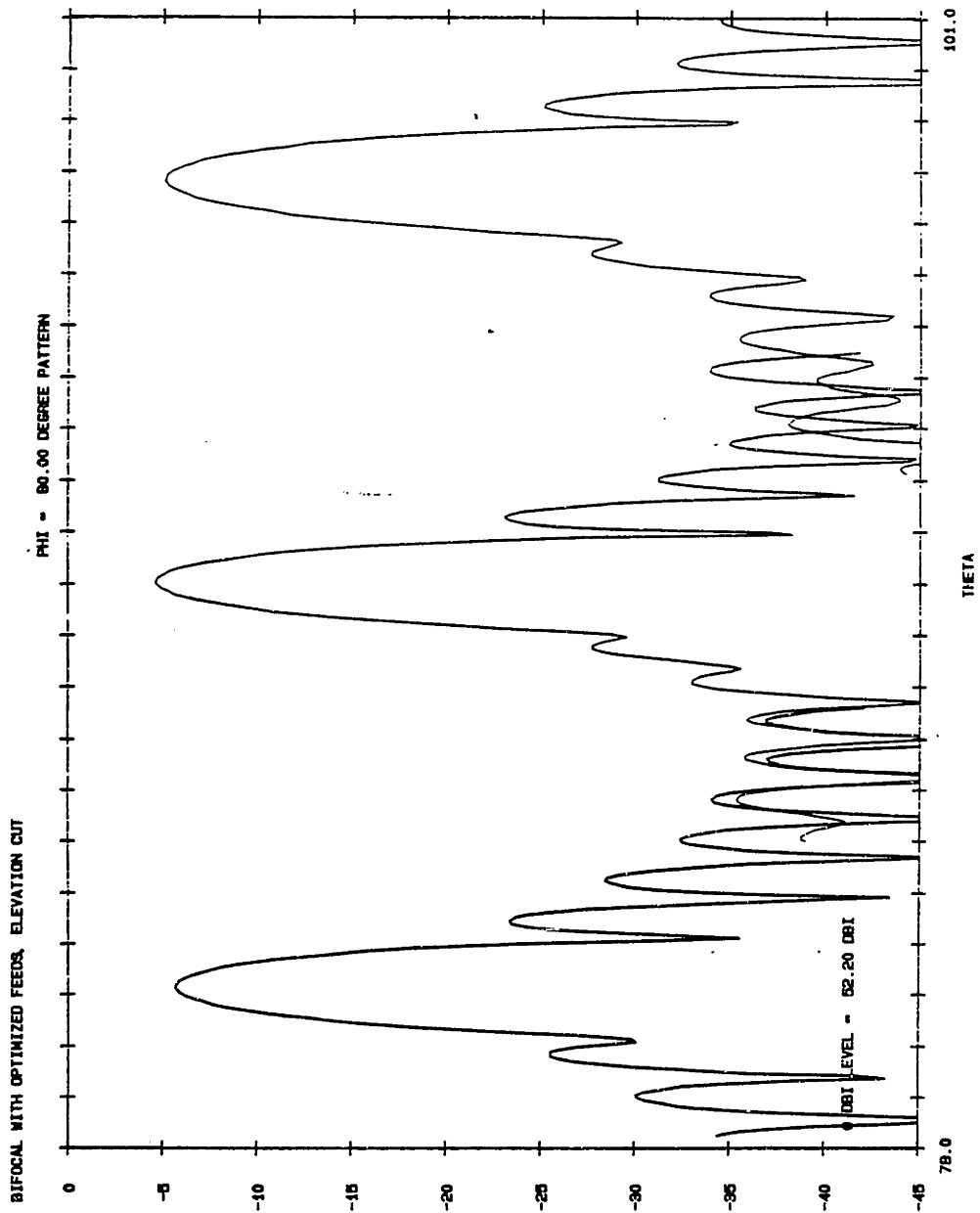


Figure 45. Radiation Patterns in the Elevation Plane for the Optimized Bifocal at -8° , 0° , and $+8^\circ$

The worst beam, which scans -8° , has 0.5 dB lower peak gain and 1.5 dB higher first sidelobe level than the $+8^\circ$ scanned beam.

This is due primarily to the very narrow subreflector subtended angle for this feed position (only 9.0° , which is 0.66 that of the other scanning feed's angle). Also, since both surfaces are at best approximations of a true bifocal pair, neither feed position is a perfect focus.

Figure 46a, b, and c presents the three radiation patterns in three dimensions.

To compare these results with Rao's [76],[77], it is noticed that the on-axis gain for the symmetric bifocal is lower than the scanned beam gain. One possible additional explanation for this is the presence of subreflector blockage in the symmetric case. It has been shown that different sections of the main reflector are illuminated for the varying scan positions. Subreflector blockage occurs primarily across the central portion of the main reflector--where the on-axis beam illumination is concentrated. The offset bifocal, of course, does not suffer from this problem. Thus, it improves on-axis performance over the symmetric case, but does not degrade scan performance.

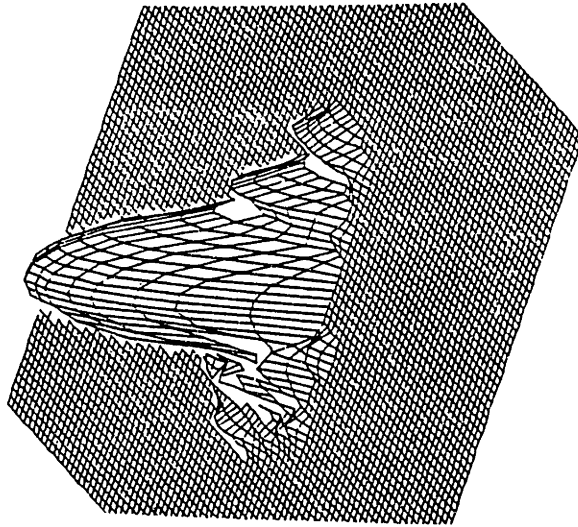
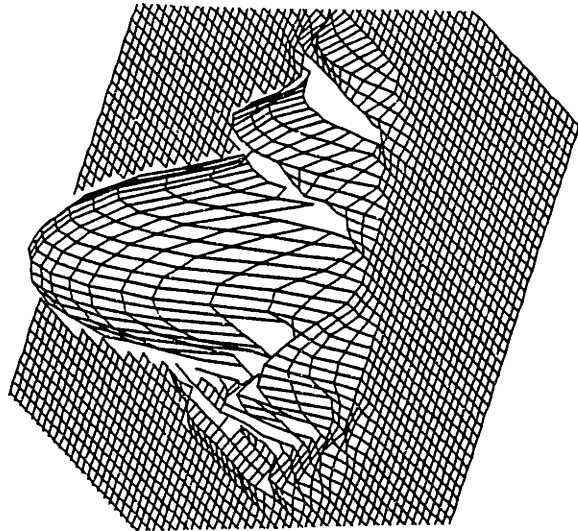
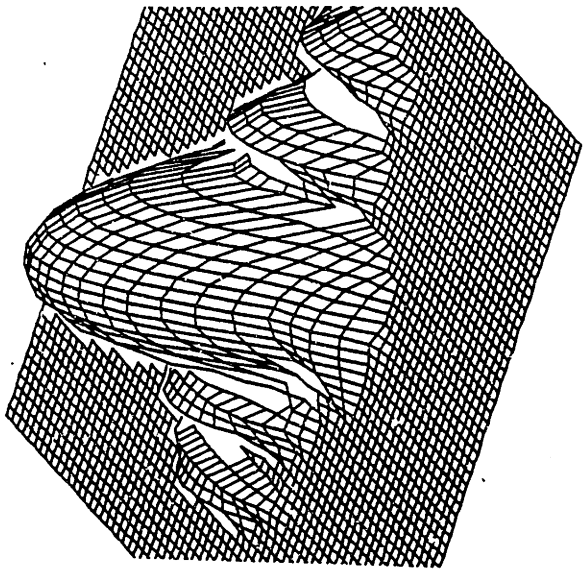


Figure 46. 3-Dimensional Plot of Beams
Scanned at -8° , 0° , and $+8^\circ$

One of the ways the poor illumination of the main reflector in this bifocal design can be alleviated is by widening the subreflector. Doing so allows reflected rays to hit the side edges of the main reflector. Figure 47 displays the resulting improvements. The peak gains have increased to 46.53, 48.76, and 47.48 dB for -8° , 0° , and $+8^\circ$ cases, respectively. The on-axis position improved the most, since its beam is formed from the central section of the main reflector, and there is more area on the side edges near the elevation center. There is no increase in blockage since the subreflector is increased in width, but not height.

Figure 48 attempts to define the equivalent parabola for the offset bifocal. Duplicating the offset profile across the symmetry axis, tracing rays from the feed to the specified edges of the subreflector, and extending rays from the specified edges of the main reflector to meet them defines the equivalent focal length of the bifocal. From this, the magnification is determined by dividing by the main reflector focal length.

D. Comparative Cases

As a comparison, an offset, prime focus paraboloid, having a focal length equal to the maximum length of the bifocal, was analyzed. For consistency, the projected diameter

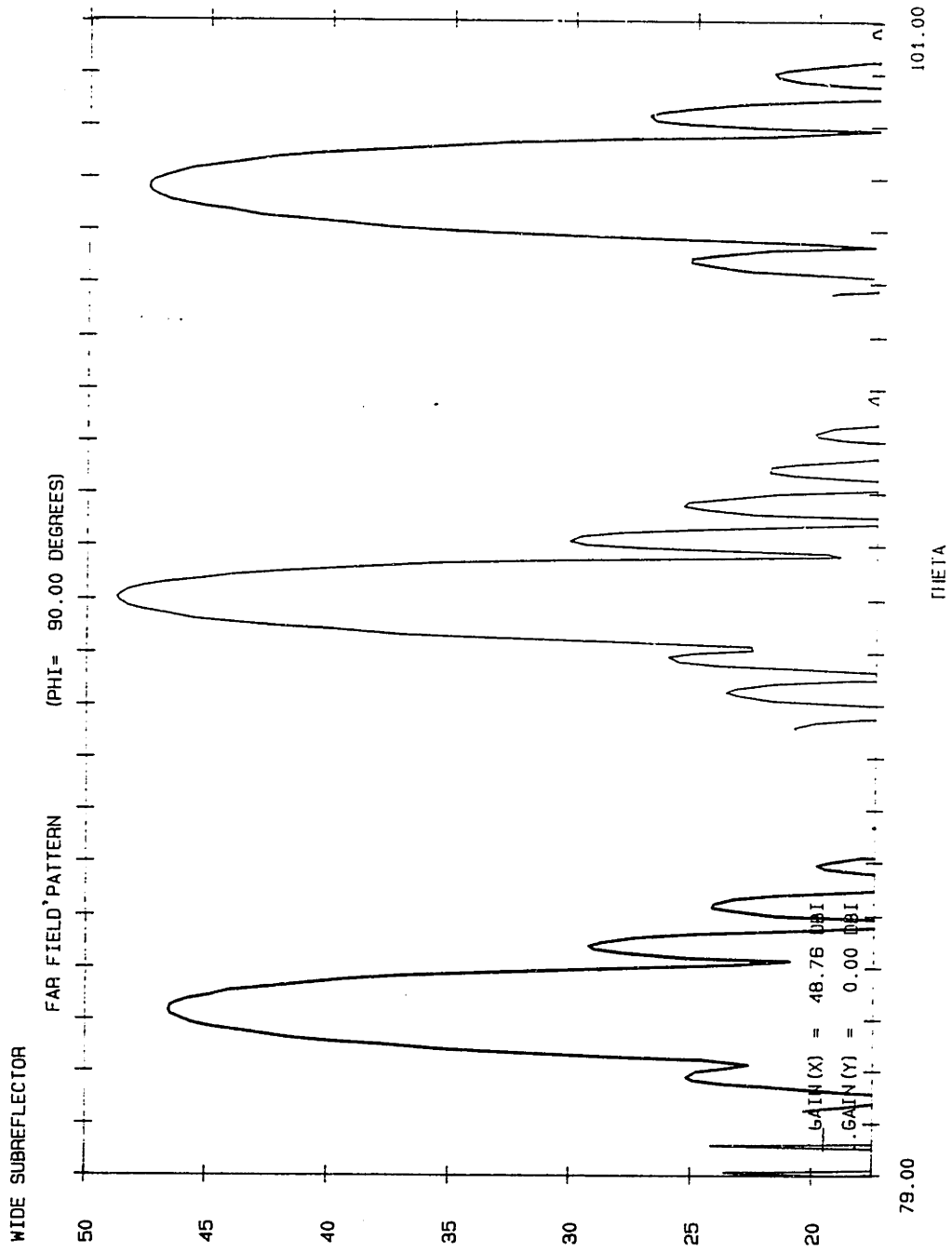


Figure 47. Elevation Cut Patterns for the Bifocal with a Widened Subreflector

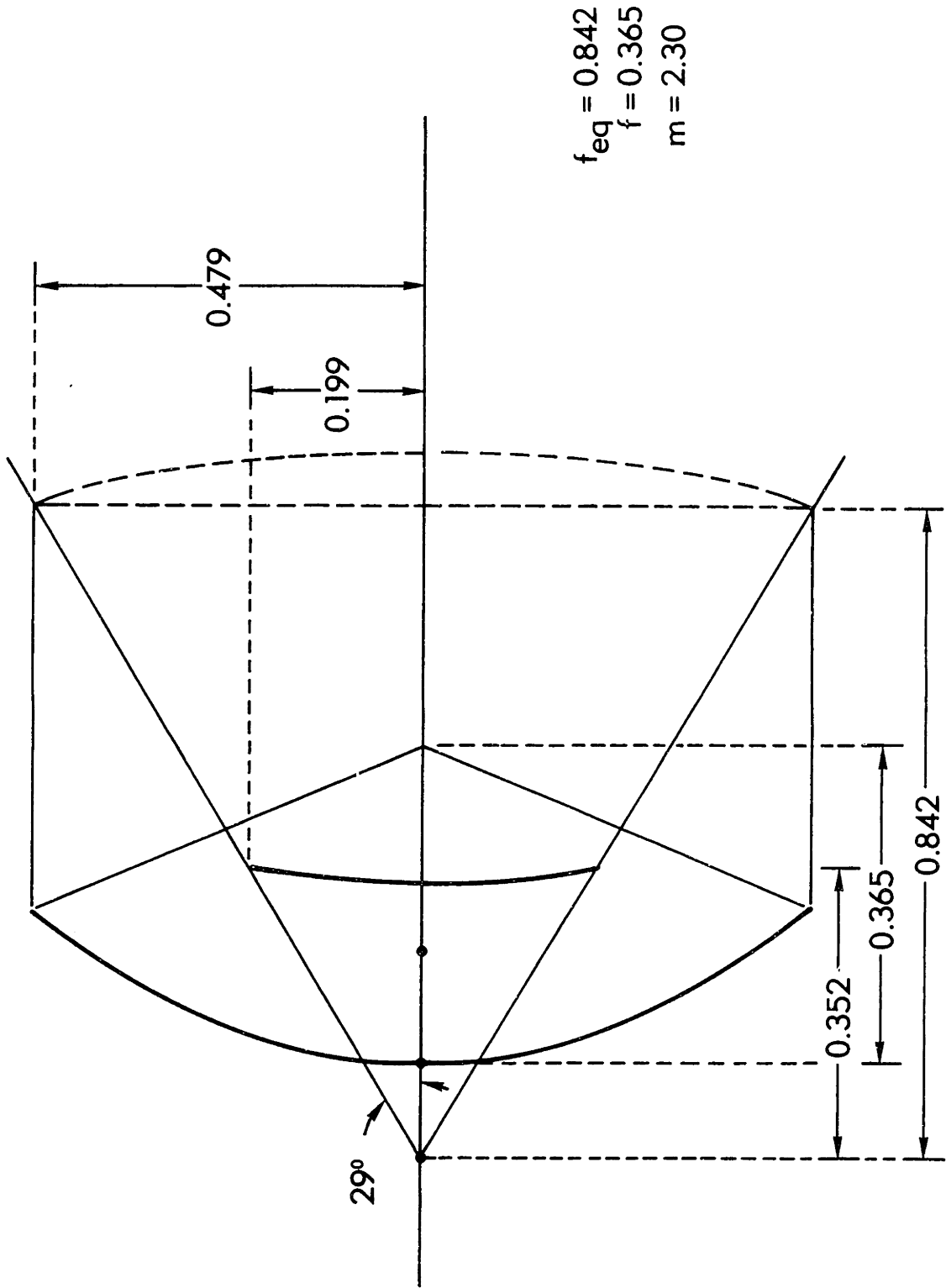


Figure 48. The Equivalent Paraboloid of the Offset Bifocal Analyzed

of this single reflector is the same as the bifocal's main reflector. Thus, it has the largest F/D ratio for any single reflector system totally contained within the boundaries specified by the bifocal. Figure 49 demonstrates the effect of scanning and the increasing coma aberration. The on-axis pattern is symmetrical, with much higher gain than any bifocal beam. The large F/D_{parent} ratio (0.3653) allows very efficient reflector illumination; indicated by the peak gain level at 51.49 dB, only 0.7 dB below the theoretical maximum. This corresponds to 85-percent efficiency.

The beams scanned $\pm 8^\circ$, however, are obviously distorted. The peak gain has dropped 7 and 8 dB, the beamwidth has more than doubled, and the sidelobe structure is smeared, unsymmetric, and much higher than in the on-axis case. This is more clearly visible in Figure 50, which shows the elevation cut pattern for each of the three locations. The large coma lobe is clearly visible in each of the scanned cases.

For both the $+8^\circ$ and -8° , the feed positions have been optimized for minimum path length variance over the reflector aperture using the work of Mrstik [90]. Additional refocusing proved to indicate that these feed locations provided the maximum gain and circularity.

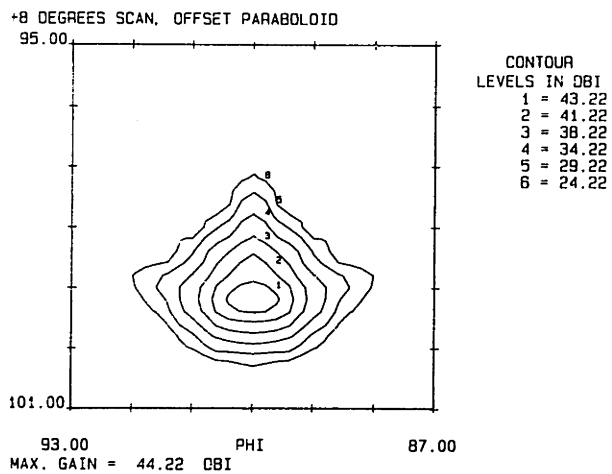
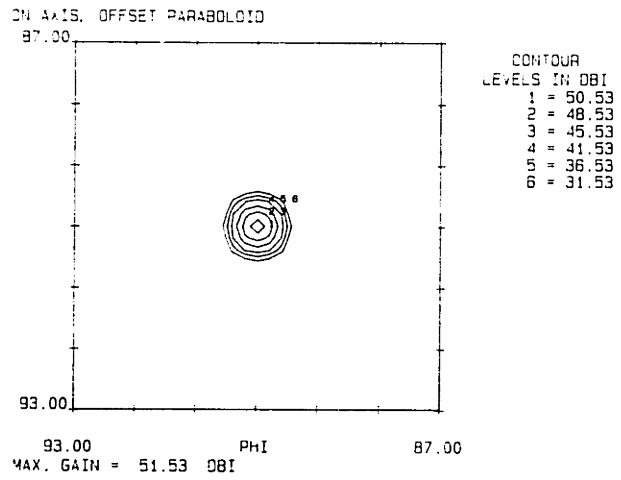
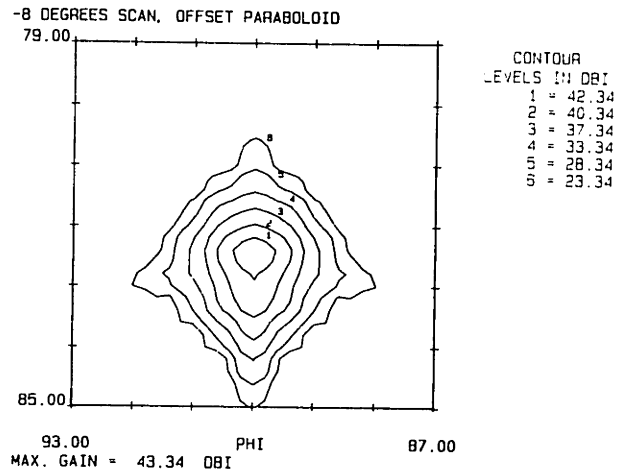


Figure 49. Contour Patterns for Largest Offset Paraboloid Contained Within the Bifocal Volume Limits: -8°, 0°, and +8°

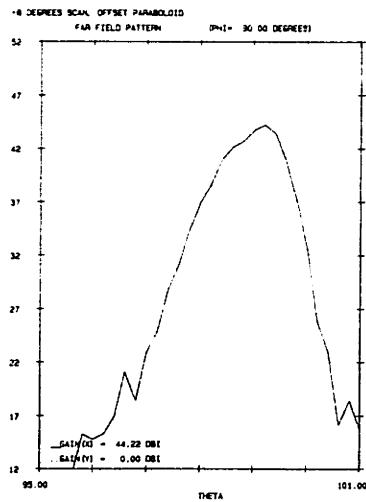
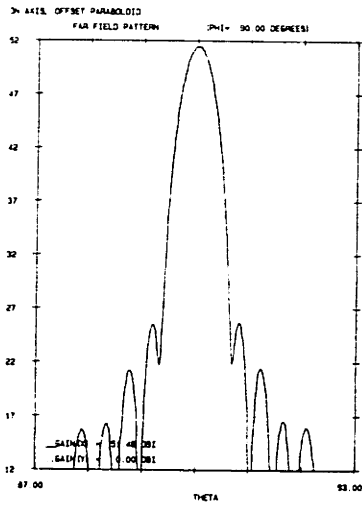
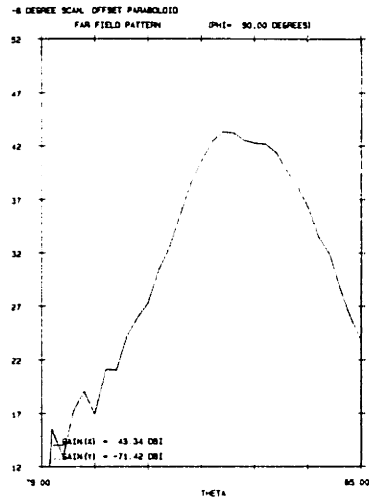


Figure 50. Elevation Patterns for Offset Paraboloid: -8° , 0° , and $+8^\circ$

According to the formula derived in the above paper, the 1-dB scan loss point for this parabolic system should be 1.8° . In order to maintain a 1-dB loss at an angle comparable to the bifocal, the F/D ratio must be greater than one--a threefold increase.

Figure 51 shows the scanning performance of offset paraboloids to be used in future satellites. These 4-dB contours show degradation at 8° even for an F/D of 1.4 (four times that which is possible with the bifocal volume). The scan loss for beam number 6 is 2.3 dB for the first case, and 0.9 dB for the second.

The frequency independence of the bifocal is exhibited in Figure 52 for a 4-fold increase to a 520λ diameter main reflector which results in a ± 32 beamwidth scan at the constant $\pm 8^\circ$; and in Figure 53 for a 16-fold increase to 2080λ . For each such increase, the maximum gain should increase by 12 dB. For the first set, peak gains have increased 10, 11.2, and 11.3 dB for very good agreement. The second set indicates additional increases of 5.3, 7.1, and 7.5 dB, with much higher sidelobes. However, even for such a large diameter system, the antenna patterns are recognizable as such. To compare with a similar offset paraboloid, for instance, Figure 54 shows an unrecognizable beam with 34 dB of scan loss. Figure 55 shows computed scan loss versus aperture size for a

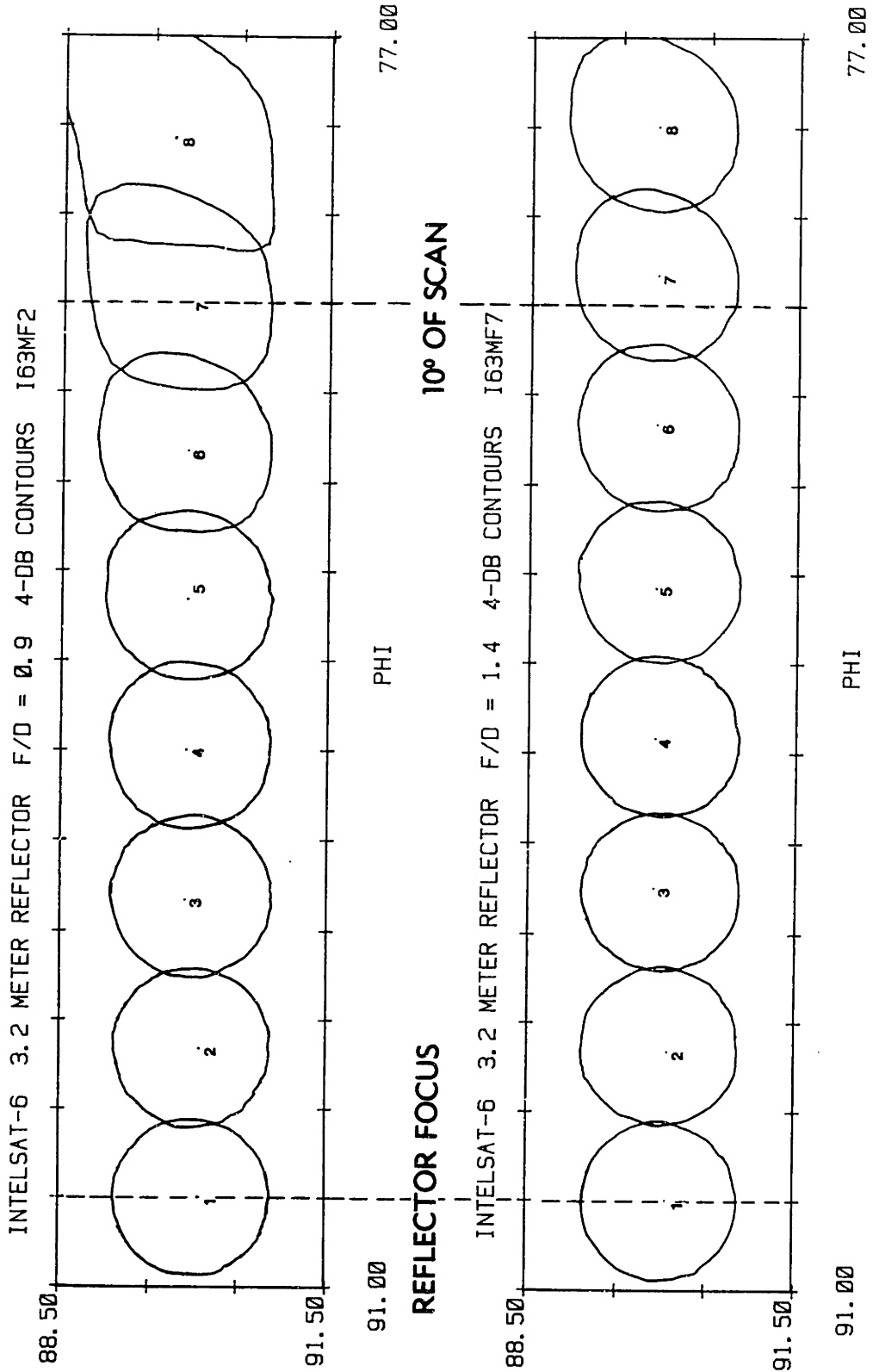


Figure 51: Scanned Beams for Offset Paraboloids Proposed in INTELSAT VI

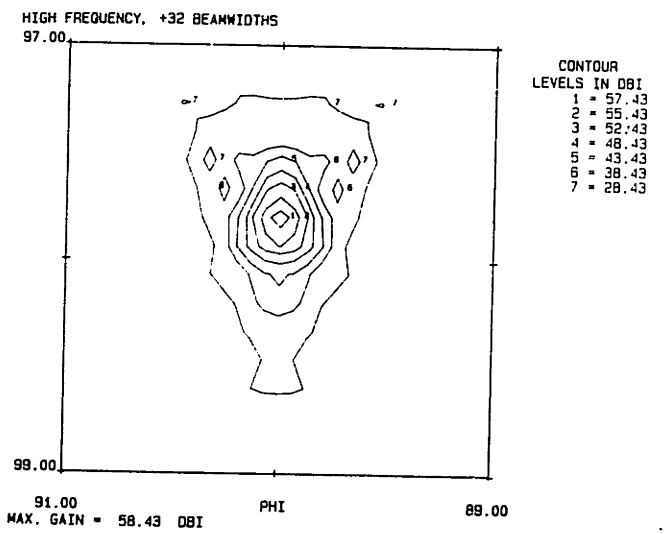
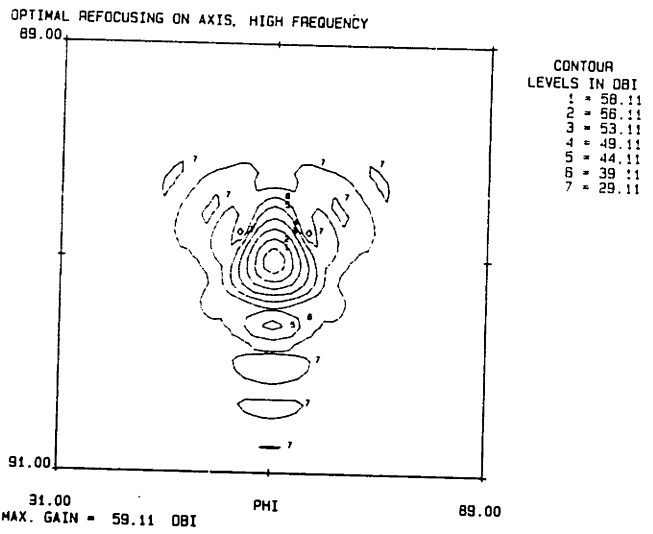
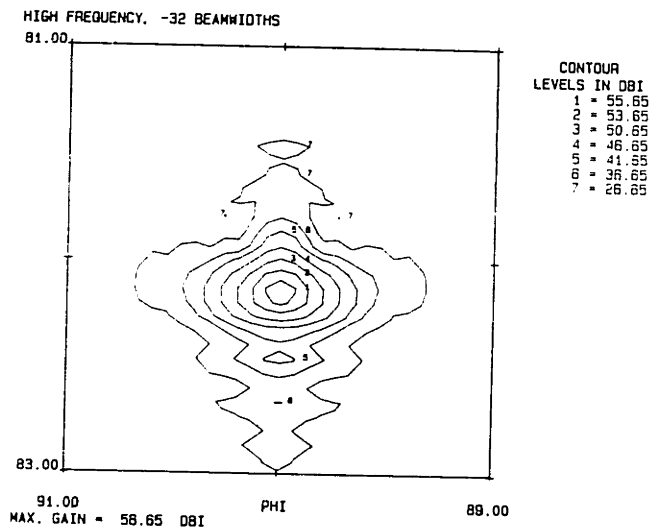


Figure 52. High Frequency Contour Patterns (half-power beamwidth at 0.25° or ± 32 beamwidths of scan for -8° , 0° , and $+8^\circ$)

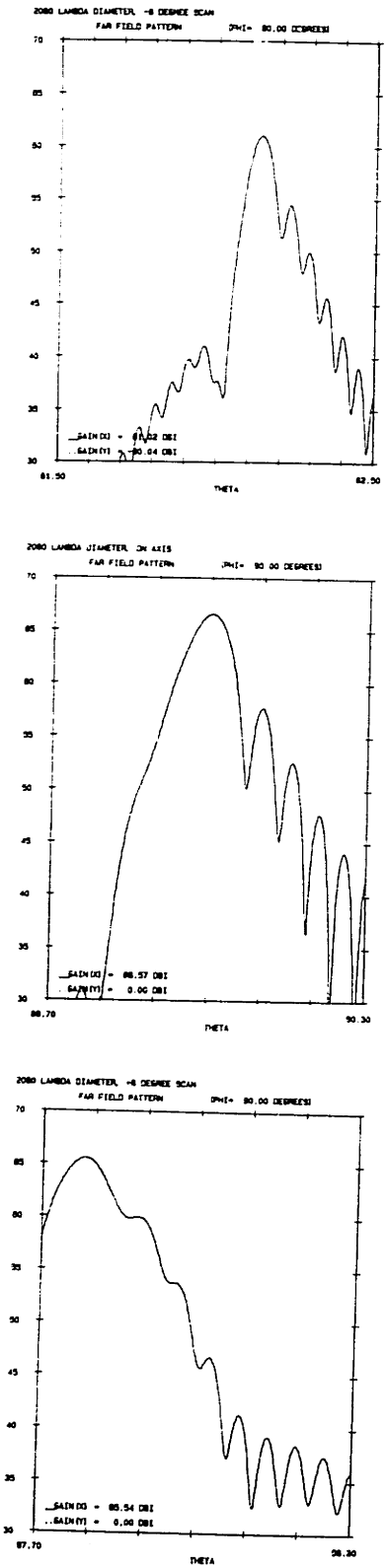


Figure 53. Elevation Patterns for ± 120 Beamwidths of Scan for -8° , 0° , and $+8^\circ$

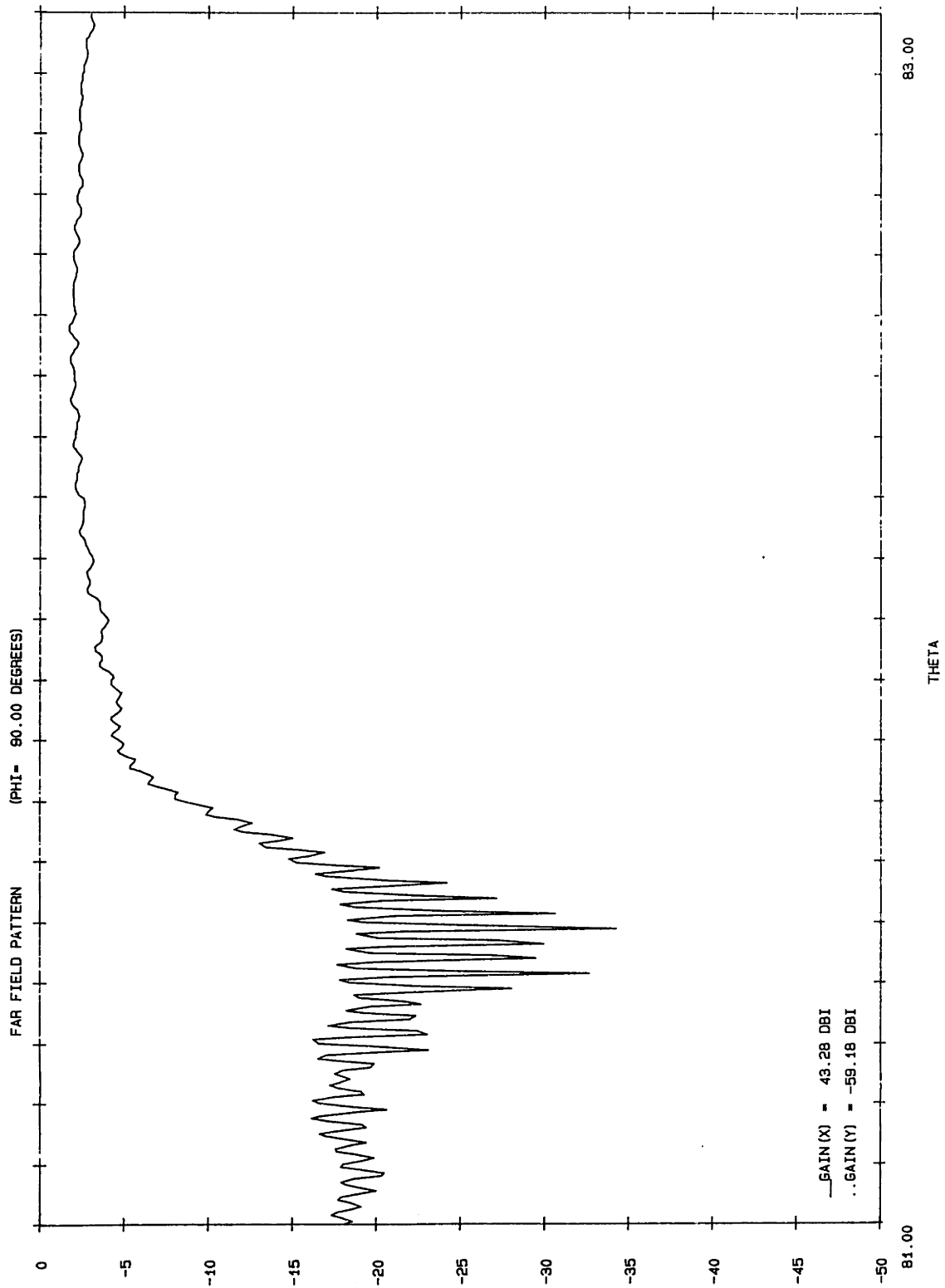


Figure 54. Offset Paraboloid Scanned the Equivalent
 of 120 0.065° Beamwidths

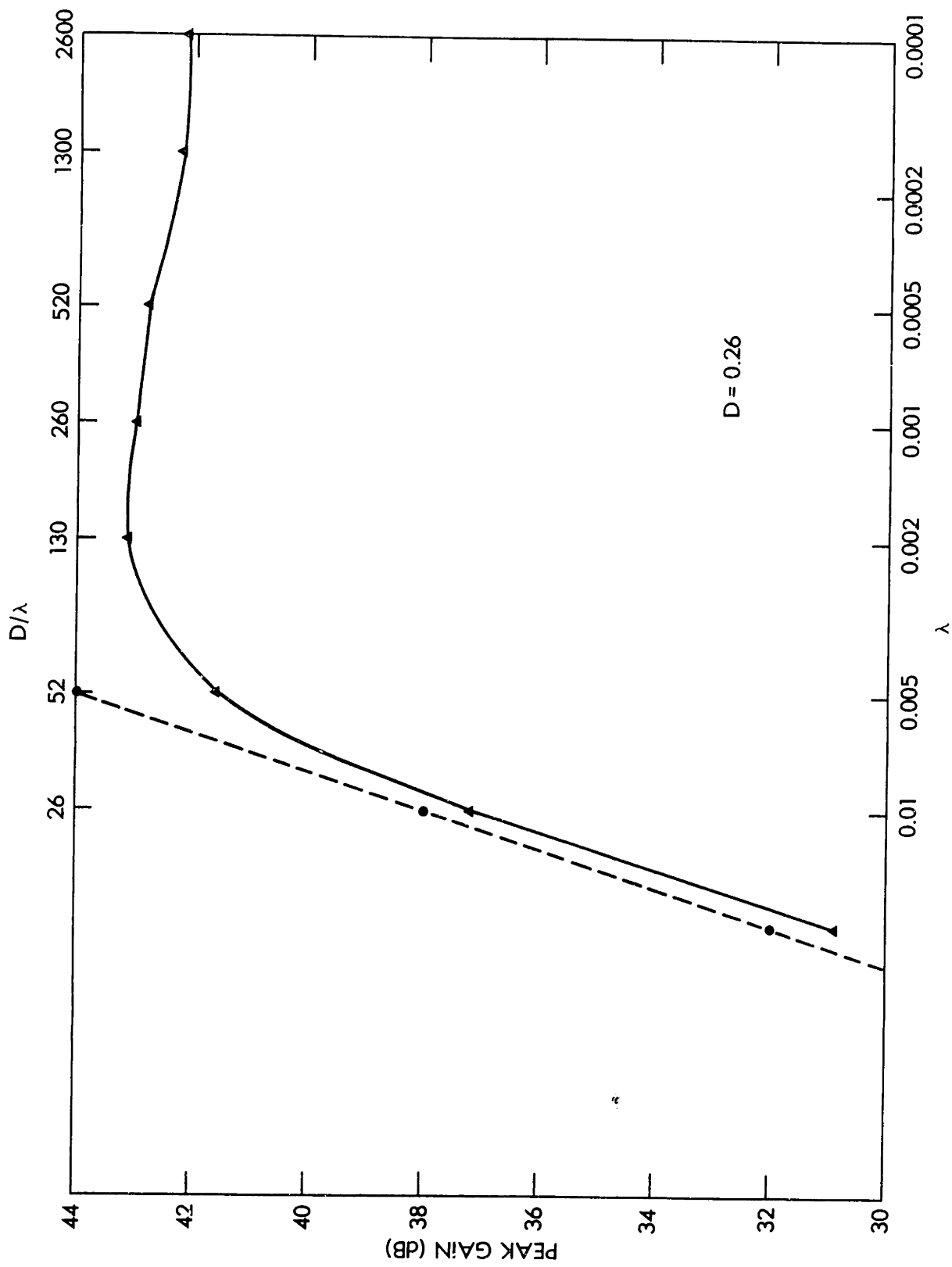


Figure 55. Plot of Scan Loss vs Aperture Diameter for 8° Scanning of an Offset Paraboloid

paraboloid. This high frequency example corresponds to 128 beamwidths of scanning. It is intended primarily for comparison and practical application seems unlikely.

A more insightful comparison is with an offset Cassegrain with similar dimensions. The determination of the "correct" configuration is more difficult than for the offset parabola. For gain comparisons, it is important to keep the main reflector diameter the same as for the bifocal. Also, since the primary advantage of Cassegrainian systems over single reflectors is its inherent packaging efficiency, it would seem reasonable to specify a limit on the overall volumes of the comparative cases. Even with these limitations, a great deal of flexibility remains.

Three comparative cases, each guided by the above criteria, have been considered:

- a. The Cassegrain with the same paraboloid for a main reflector, and a circular hyperboloid with foci coinciding with the paraboloid's focus and the on-axis bifocal feed location, with the same projected diameter as the bifocal subreflector. This antenna uses roughly the same amount of metal as the bifocal, and as such is a direct material cost or weight comparison. The main difference between the two antennas is in their subreflector profiles. The bifocal's

transverse polynomial was derived from this Cassegrain, but its profile is quite different. The relative profiles are shown in Figure 56. Figure 57 shows the difference between them. The Cassegrain consists of the indicated circular offset sections of the rotated plane curves. It is apparent that the bifocal subreflector has a greater degree of curvature, and hence spreads the reflected energy more fully over the main reflector. In fact, much of the Cassegrain main reflector is unilluminated from reflections off this flatter subreflector. To accomplish this more efficient illumination, a second design is analyzed.

b. The same paraboloid-hyperboloid combination, but with the subreflector extended considerably toward the negative x direction. A more efficient illumination could be realized by extension in the positive x direction, but this would cause blockage and defeat the offset goal. The upper section of the main reflector is eliminated by choosing a smaller diameter aperture which still just barely clears the top of the subreflector (see Figure 58). The previous type of Cassegrain had a main reflector extending to a , while the subreflector limit was at c . The present type only extends to b , eliminating the poorly illuminated region $a-b$. Unfortunately, this violates the constant aperture size requirement. Scaling the entire system in frequency restores the main reflector to

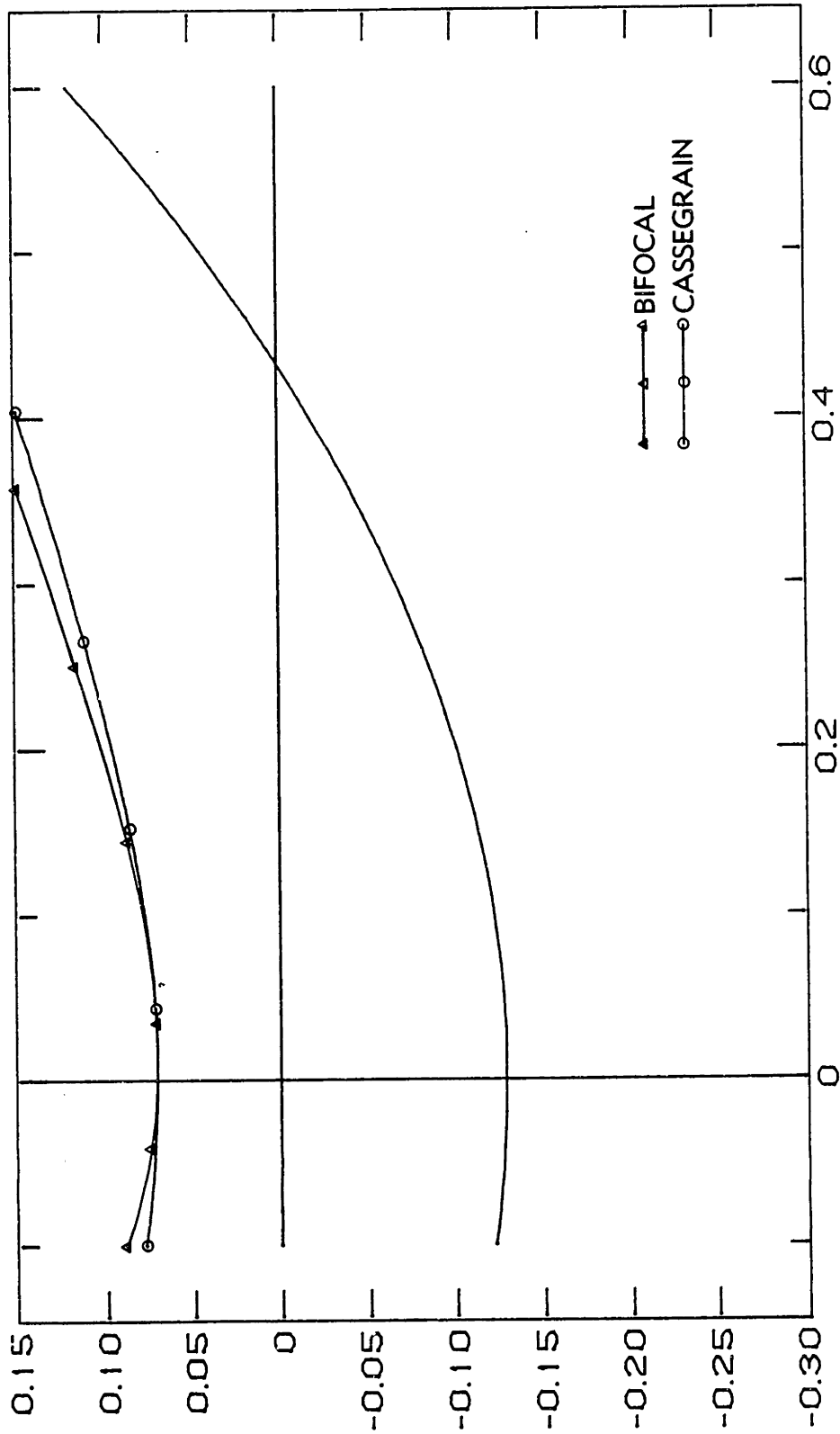


Figure 56. Offset Bifocal and the Corresponding Cassegrain with Common Main Reflector

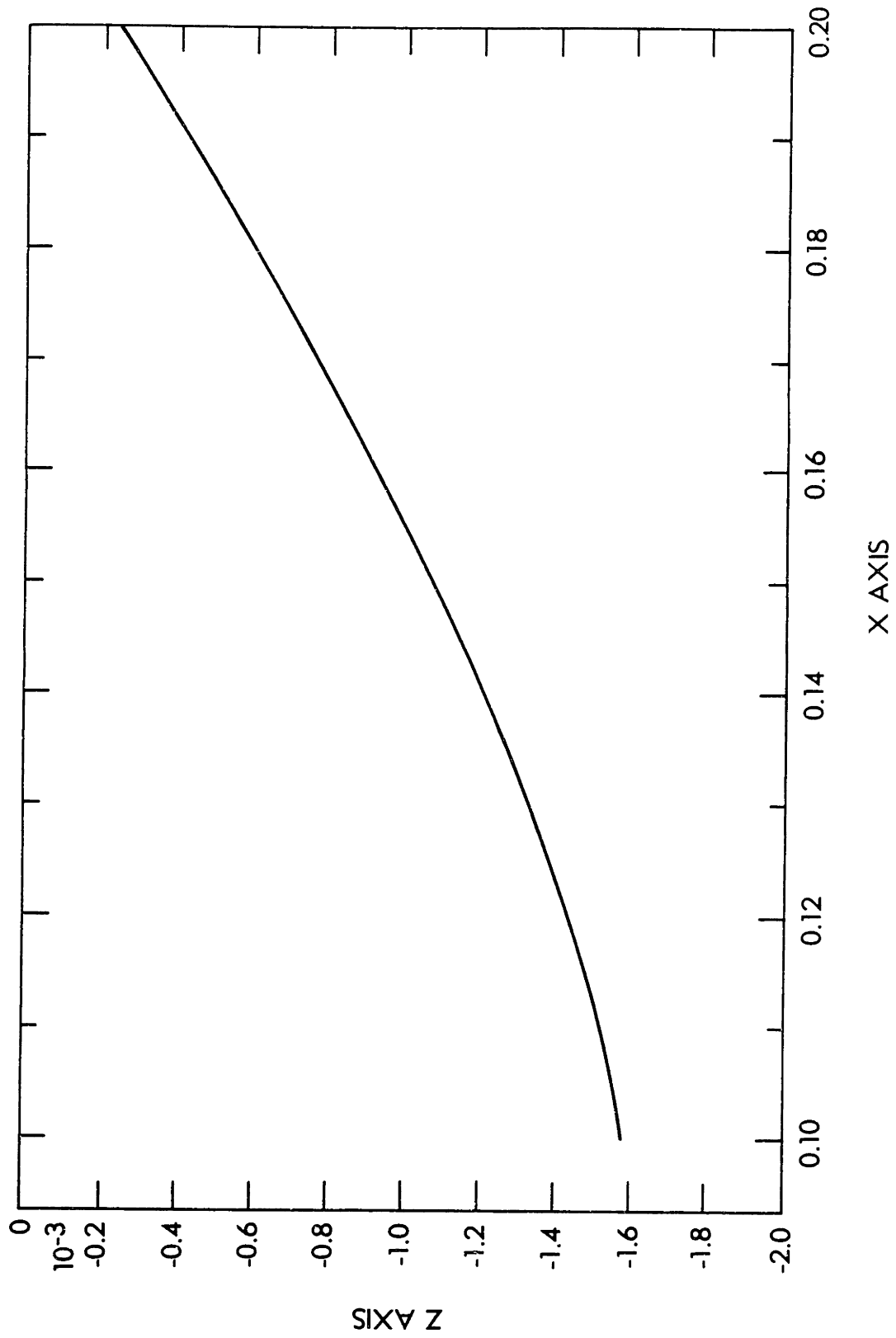


Figure 57. Difference Between the Bifocal and Cassegrain Subreflector Profiles

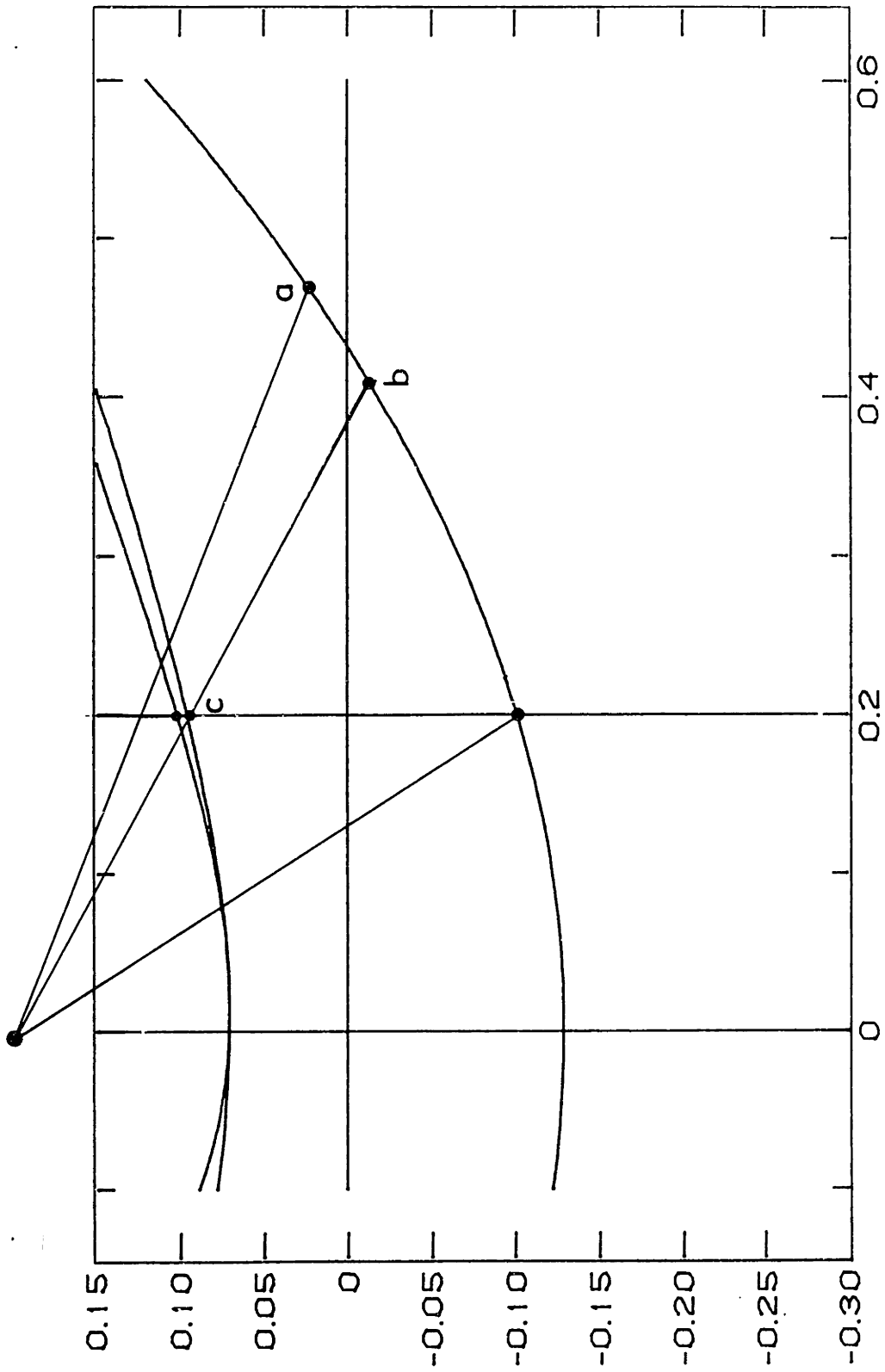


Figure 58. Comparison of Type a and b Cassegrains, Indicating Inefficiently Illuminated Section a-b

its correct diameter, but the focal length is larger than before. A comparison was made anyway to illustrate the performance of the "best" offset Cassegrain approximating an offset bifocal. The focal length and total height is 1.5 times that of the bifocal, and the subreflector is 1.82 times as large as its counterpart. Subreflector spillover, as well as main reflector illumination inefficiency, is minimized; so the predominant factor affecting gain and pattern clarity are phase errors. Thus, this case compares the actual surface geometries, but disregards the practical packaging comparison of focal length.

c. This third Cassegrainian case attempts to increase main reflector illumination without greatly exceeding the limiting volume. The hyperboloid used in the previous cases is once again used as the subreflector surface. The main reflector is a paraboloid with a coinciding focal point with the hyperboloid and with the longest focal length still allowing it to fit inside the limiting volume. This paraboloid touches the extreme rear limit and has a focal length approximately double that of the offset paraboloid analyzed earlier: 0.637 (as opposed to 0.35). The hyperboloid still touches the front limit (see Figure 59). Again, this reflector is oversized to minimize spillover. It is 2.03 times as large as that of the bifocal.

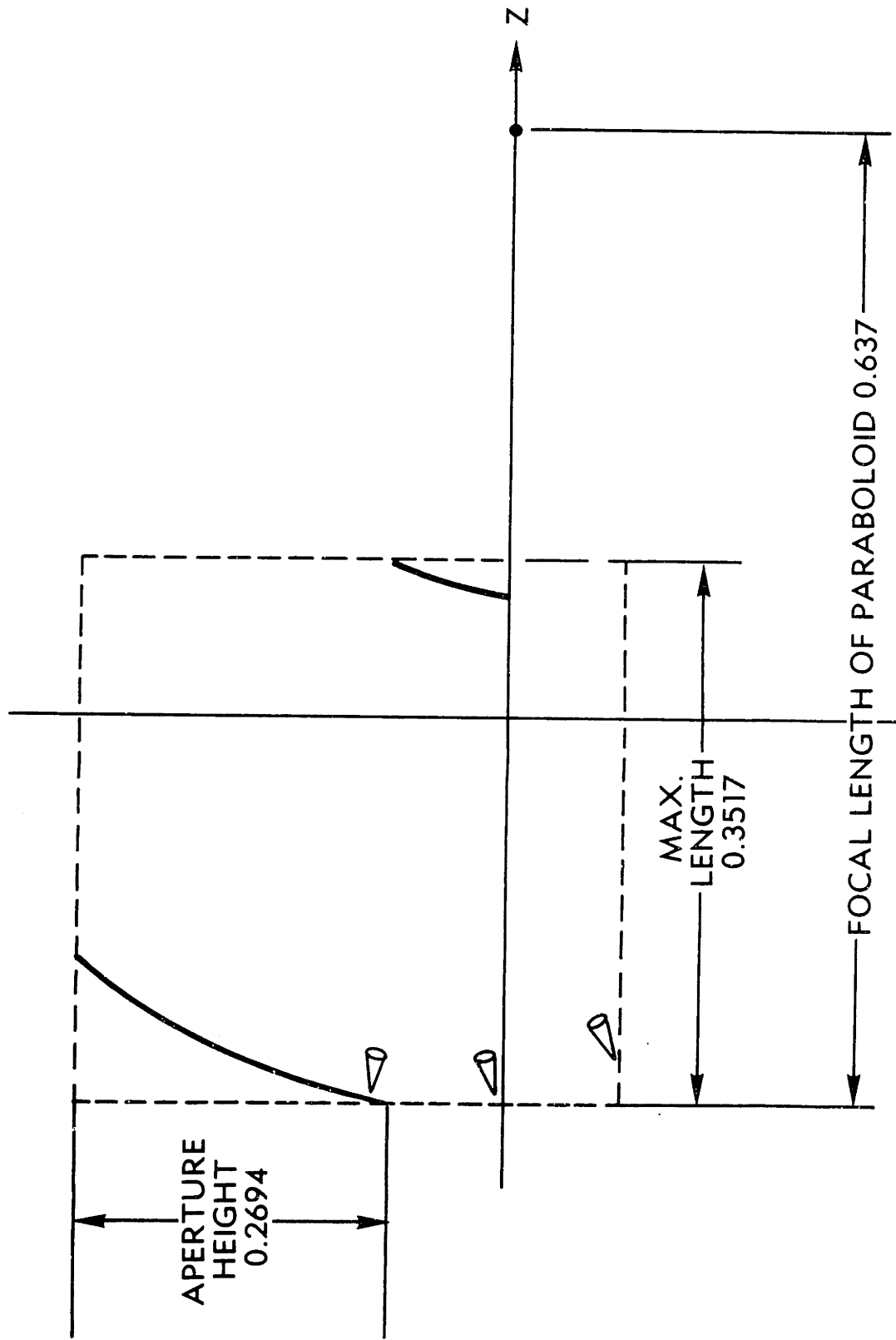


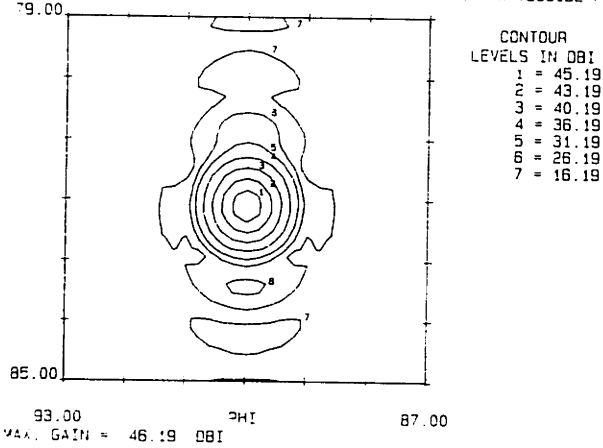
Figure 59. Type c Cassegrain with Main Reflector Positioned at Extreme Rear of the Limiting Volume

Thus, this system has the largest possible focal length, yet still maintains a subreflector wide enough to intercept scanned incoming rays. White and DeSize [70] have shown that scanning is best accomplished in Cassegrains with large effective focal lengths, but with low magnification configurations. This arrangement is thus nearly the optimum based on previously established design principles.

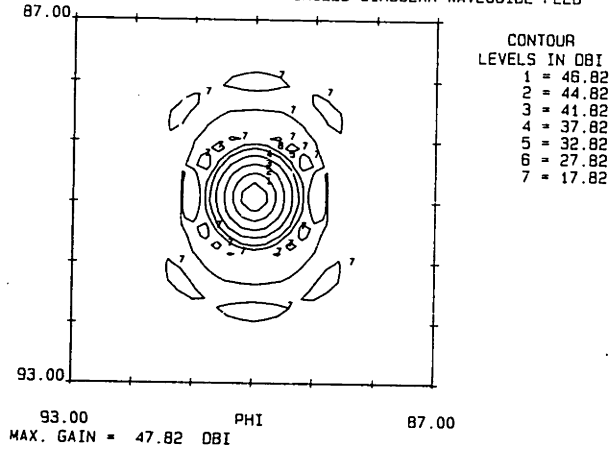
The results of the three Cassegrain cases are as follows.

Using the same size feed waveguides as used with the bifocal analysis, contour patterns are generated as shown in Figure 60. As expected, the on-axis contour is perfectly symmetrical, with peak gain almost equal to the bifocal's, but with better sidelobe structure. The -8° scan contour is similar to its counterpart, but careful inspection reveals the characteristic beam broadening and null filling opposite the coma lobe present at a much higher level on the Cassegrain plot. Lack of illumination (spillover) of the main reflector is the primary cause for the large scan gain loss for the beam scanned $+8^\circ$. Although its pattern is symmetrical with very low sidelobes, its gain is almost 1.5 dB lower than for the bifocal.

CASSEGRAIN: -8 DEG. SCAN, WITH OPTIMIZED CIRCULAR WAVEGUIDE FEED



CASSEGRAIN: ON AXIS, WITH OPTIMIZED CIRCULAR WAVEGUIDE FEED



CASSEGRAIN: +8 DEG. SCAN, WITH OPTIMIZED CIRCULAR WAVEGUIDE FEED

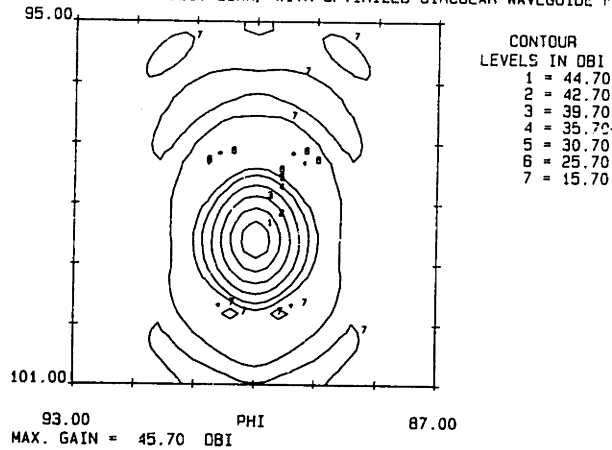


Figure 60. Contour Patterns for Type a Cassegrain: -8° , 0° , and $+8^\circ$

For a closer examination of the scanning comparison between the offset bifocal and its best fit Cassegrain, a standardized feed aperture for all scanned beams was chosen.

The beam deviation factor of the bifocal is somewhat difficult to define, since a central focal point does not exist. However, choosing the midpoint of the two foci and the center of the subreflector as the reference points provides a basis for calculation. The two foci are separated by 108.0 wavelengths and produce beams scanning a total of 16° . Thus, to ensure one 1° beam per scanned degree--which is of use in multibeam applications--each feed is allowed a diameter of 6.75λ . The distance from the subreflector to the foci midpoint is 185.4λ . Thus, with the feed displaced 2.08° , the beam scans 1.0° ; for a BDF of 0.48 . This value is very low compared to single reflectors [91].

The standardized circular waveguide feed diameter was selected to be 7λ . Figures 61 and 62 each show seven scanned beams--one for every 2 degrees. The peak gains for on-axis beams are 0.5 dB lower and the peaks fall much more rapidly than for the optimized feed case. This is due to the increased spillover past the subreflector. Table 2 lists the spillover for each reflector for the bifocal and Cassegrain. Notice the large main reflector spillover at $+8^\circ$ for the Cassegrain: indicative of the excessively narrow reflected

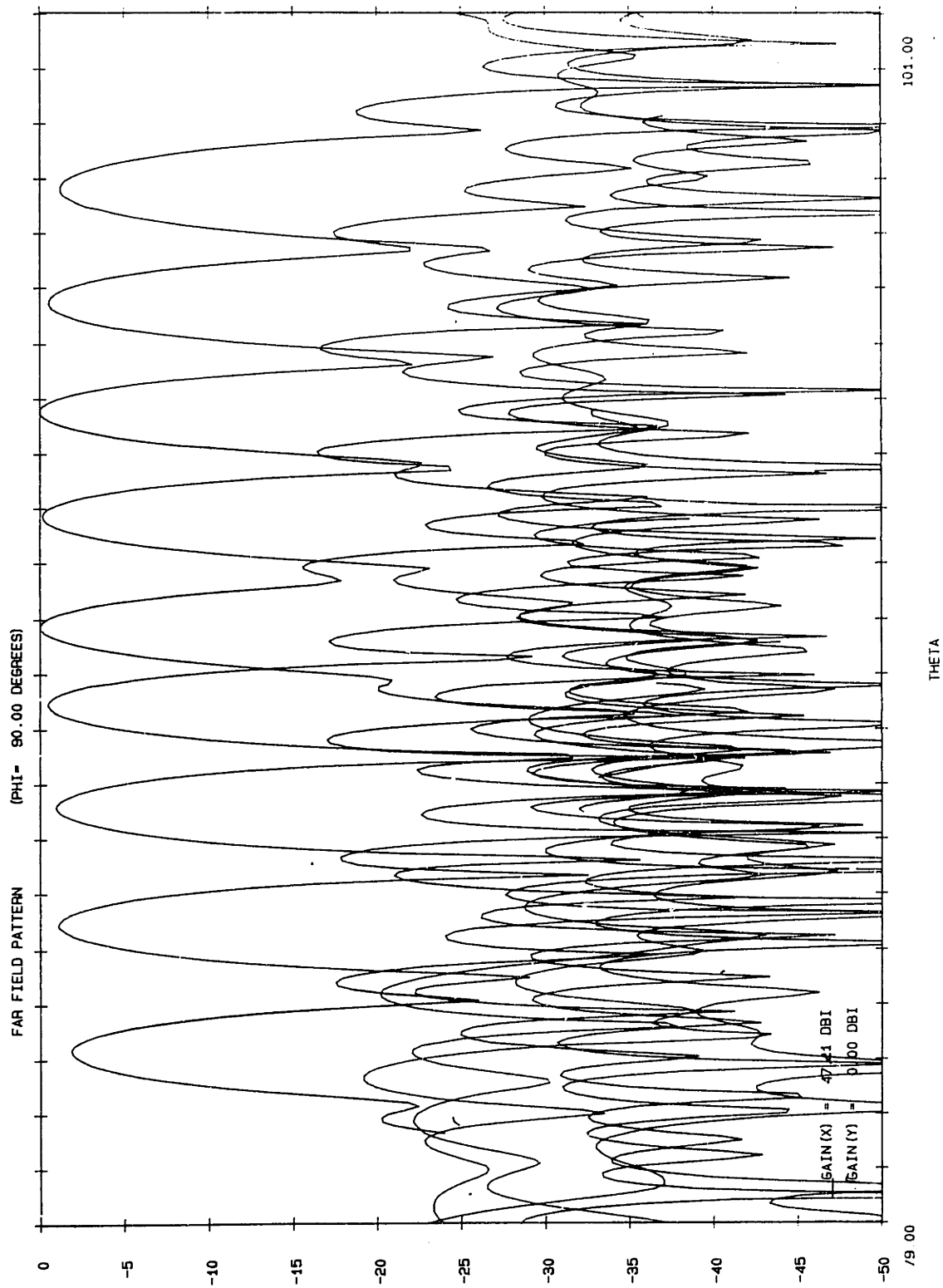


Figure 61. Elevation Scan Patterns for the Bifocal with 7λ Circular Feeds

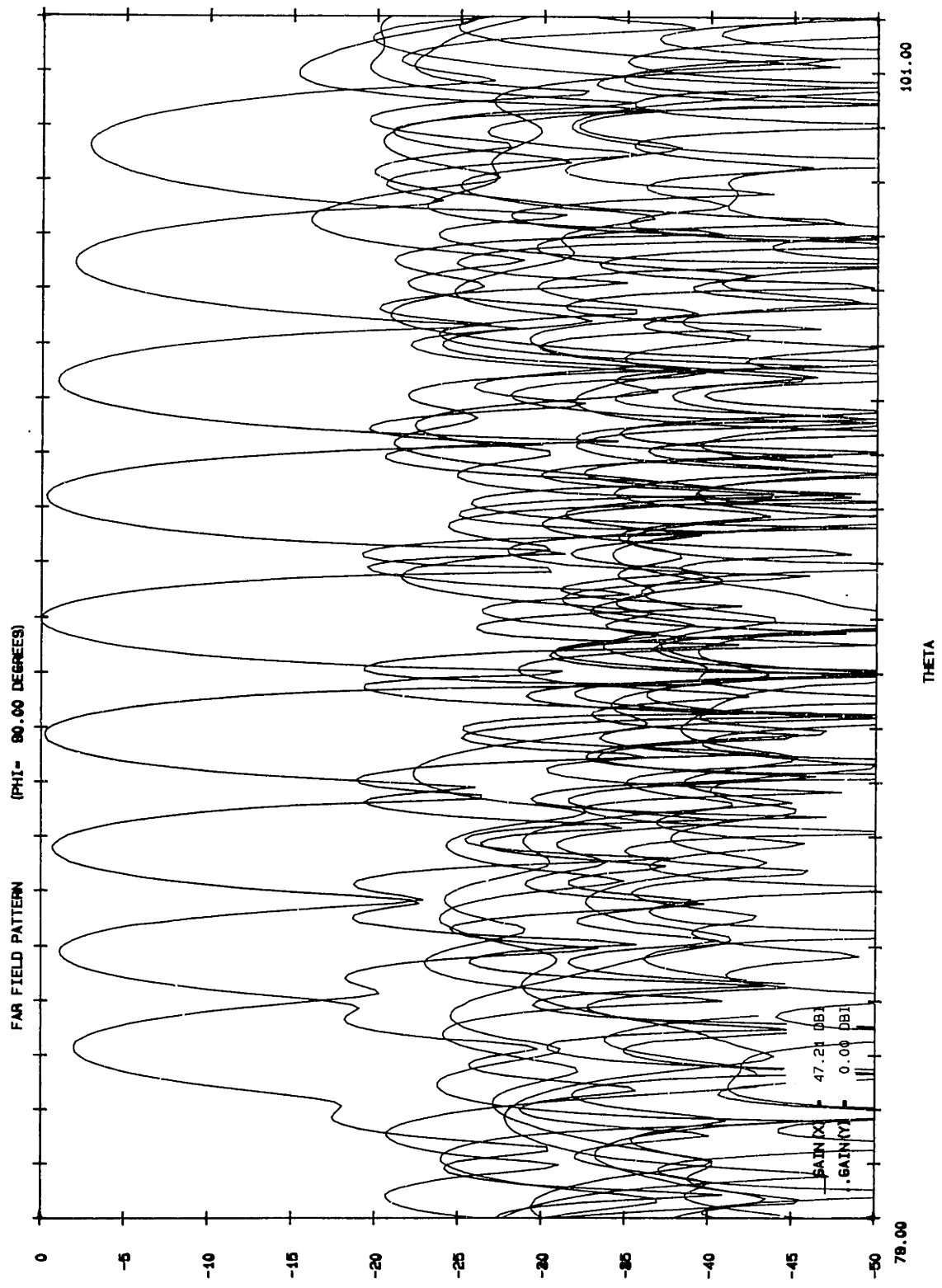


Figure 62. Elevation Scan Patterns for the Type a Cassegrain with 7λ Circular Feeds

region from its subreflector. The subreflector spillover is greater for the bifocal for all cases. This is due to the greater curvature of the bifocal. For a given projected reflector circle, a greater curvature causes a reflector to bend away from the rays, and thus intercept fewer. The gain differences are most noticeable at $+8^\circ$ (98°), as it was with optimized feeds. Observing the first sidelobe levels, however, indicates the real superiority of the bifocal. With the Cassegrain, they rise almost 3 dB from the on-axis beam to the scanned beams. Sidelobes of the bifocal actually fall 2 dB as beams are scanned.

Table 2. Spillover Past Reflectors

Beam	Subreflector		Main Reflector	
	Bifocal	Cassegrain	Bifocal	Cassegrain
-8°	2.36	2.20	0	0
-7°	2.09	2.01	0	0
-6°	1.98	1.82	0	0
-5°	1.84	1.75	0	0
-4°	1.66	1.62	0	0
-3°	1.60	1.48	0	0
-2°	1.55	1.41	0	0
-1°	1.44	1.37	0	0
0°	1.37	1.29	0	0
1°	1.34	1.26	0	0.07
2°	1.33	1.22	0	0.19
3°	1.28	1.16	0.02	0.29
4°	1.34	1.23	0.07	0.41
5°	1.38	1.31	0.11	0.53
6°	1.27	1.20	0.29	0.85
7°	1.35	1.27	0.25	0.97
8°	1.59	1.30	0.36	1.10

Contour patterns for the on-axis and extreme-scan beams for both antennas are shown in Figures 63 and 64.

The bifocal's frequency independence is again illustrated in Figure 65, which compares the two antennas at four times the frequency. The bifocal suffers much less from the electrical enlargement, maintaining well-focused beams without much peak gain loss. Cassegrains are, in general, less frequency dependent than offset paraboloids. White and DeSize [70] state that dual reflector scanning is determined primarily by its physical geometry. However, the equivalent parabola technique [20] is often employed in Cassegrainian analysis. Thus, electrical size is an important consideration for Cassegrains. The offset bifocal's geometrical scanning design provides superior high frequency performance because phase errors are always minimized at the $\pm 8^\circ$ scan positions.

The second comparative Cassegrain case--that of a system with 1.5 times the feed/subreflector spacing--was analyzed using the standard 7λ diameter waveguide. Results for the on-axis and $\pm 8^\circ$ scan positions are shown in Figure 66. This on-axis contour pattern is surpassed in quality only by the perfectly focused paraboloid. Peak gain is 3.37 dB higher than the similar bifocal beam, yet gain falls off 5 dB for -3° of scan to 45.7 dBI, to a level comparable to the corresponding bifocal. Figure 67 shows peak gain and first sidelobe

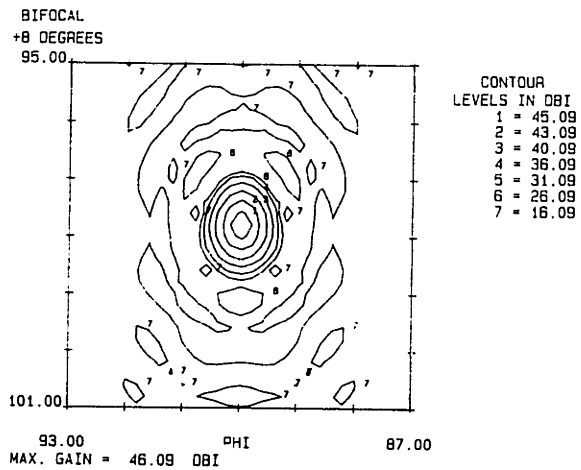
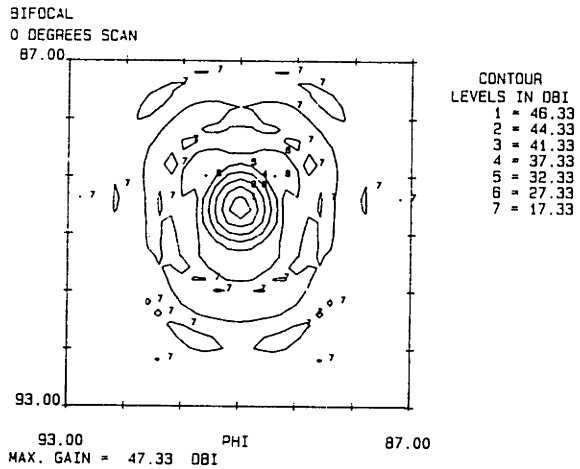
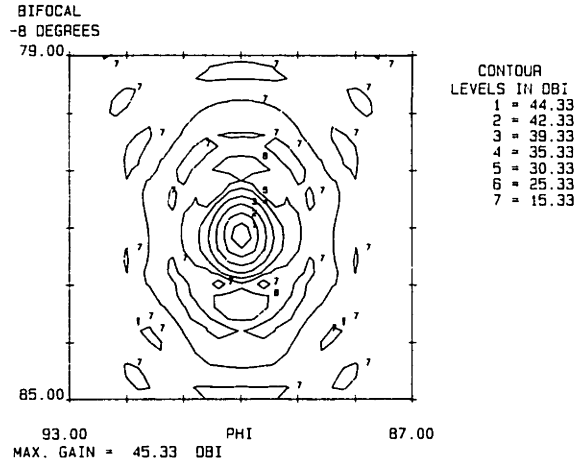
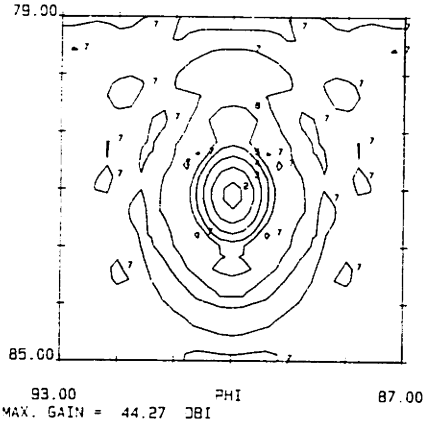


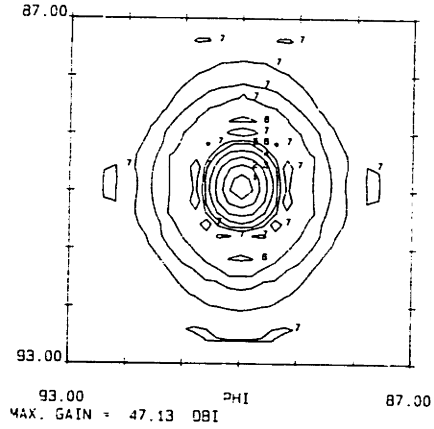
Figure 63. Contour Patterns for the Bifocal with 7λ Circular Feeds

CASSEGRAIN: -8 DEGREE SCAN

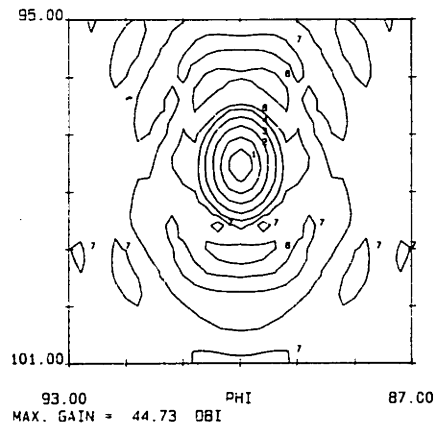


CONTOUR
LEVELS IN DBI
1 = 43.27
2 = 41.27
3 = 38.27
4 = 34.27
5 = 29.27
6 = 24.27
7 = 14.27

CASSEGRAIN: ON AXIS



CONTOUR
LEVELS IN DBI
1 = 46.13
2 = 44.13
3 = 41.13
4 = 37.13
5 = 32.13
6 = 27.13
7 = 17.13



CONTOUR
LEVELS IN DBI
1 = 43.73
2 = 41.73
3 = 38.73
4 = 34.73
5 = 29.73
6 = 24.73
7 = 14.73

Figure 64. Contour Patterns for Type a Cassegrain with 7λ Circular Feeds

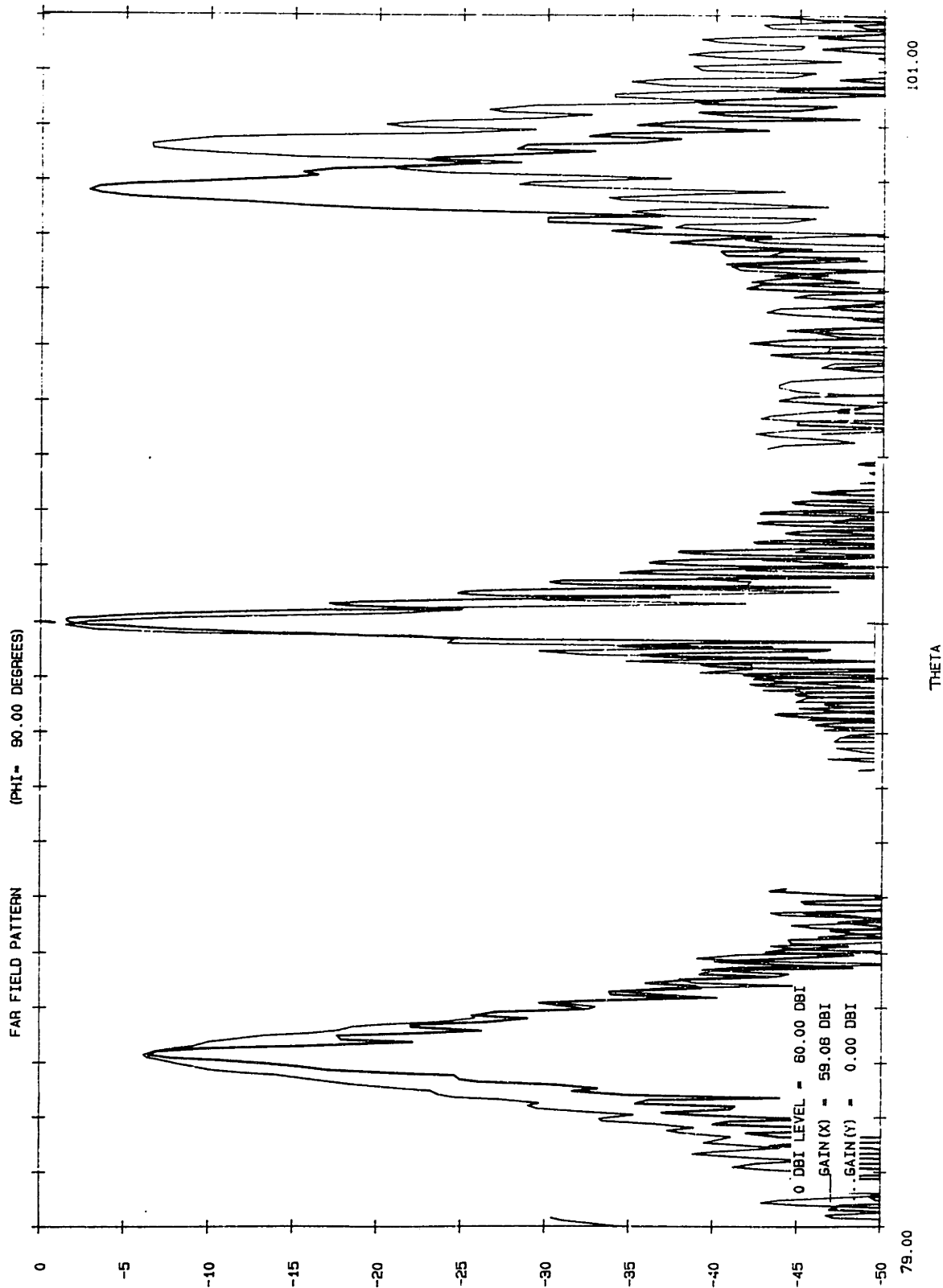


Figure 65. High Frequency Elevator Scan Comparison (heavy line: bifocal, light line: type a Cassegrain)

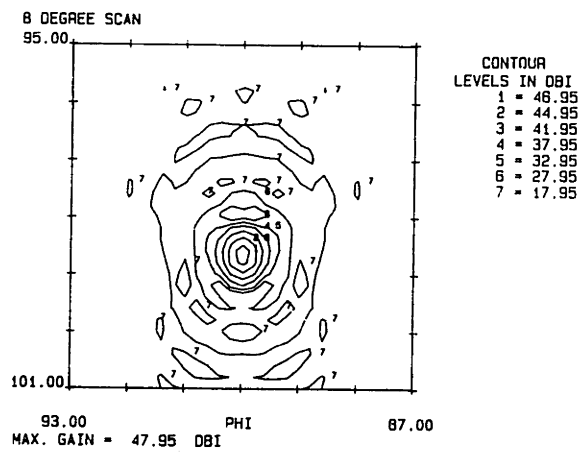
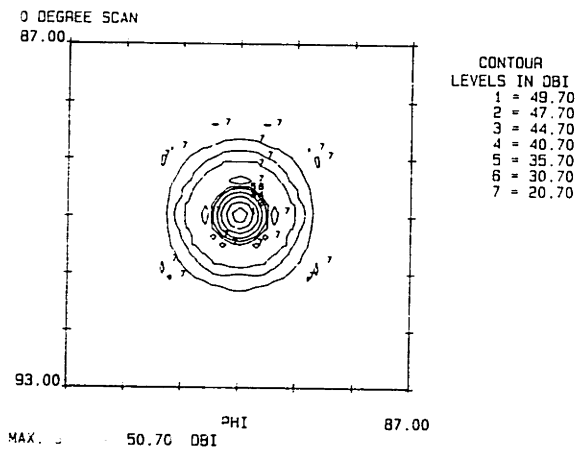
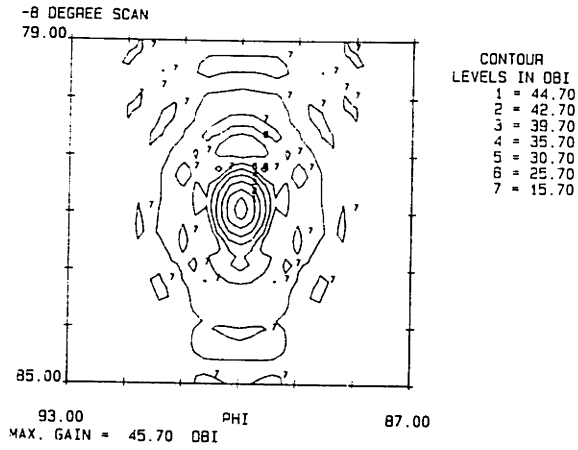


Figure 66. Contour Patterns for Type b Cassegrain with 7λ Circular Feed

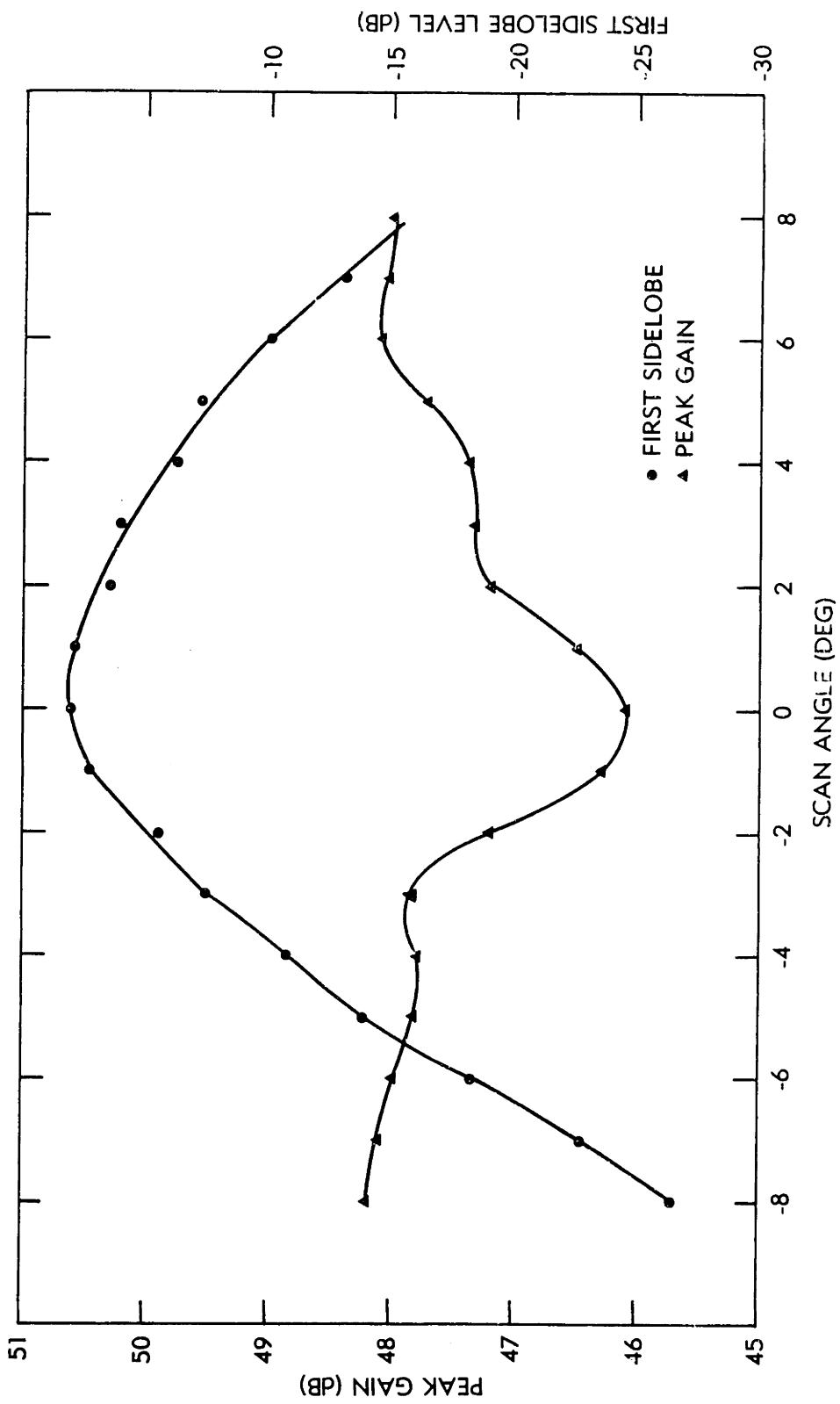


Figure 67. Scan Performance for Type b Cassegrain: 7λ Feed

levels for 1° increments of scan up to $\pm 8^\circ$. Compare with the similar plot for the bifocal, Figure 68. Since the subreflector is almost four times the area of the bifocal's subreflector, spillover past it is limited to a fairly constant 1.1 dB. Spillover past the main reflector, however, increases from 0.3 to 2.4 dB at -8° . As expected, adjusting the geometry to maximize illumination for the on-axis beam has deleterious effects on scanned beams.

To account for the 5-dB scan loss, an additional 3 dB of phase error effects must be present. Observing the high first sidelobes, which rise much faster than spillover, it is clear that defocusing degrades the beam significantly.

It should be made clear that to keep overall volume consistent, this Cassegrain could be scaled down electrically by adjusting the frequency by a factor of 1.5. This would reduce the gain for all scan positions by approximately 3 dB, making on-axis gain comparable, but scanned beams gains down 3 and 1 dB below the bifocal.

For the third Cassegrainian case, full advantage is taken of the limited volume. Again, a 7λ circular waveguide feed is used for all beams. As before, the on-axis performance is superior to the bifocal (Figure 69) with a peak gain of 49.6 dB. This is not as high as for the previous case, even though its main reflector is efficiently illuminated.

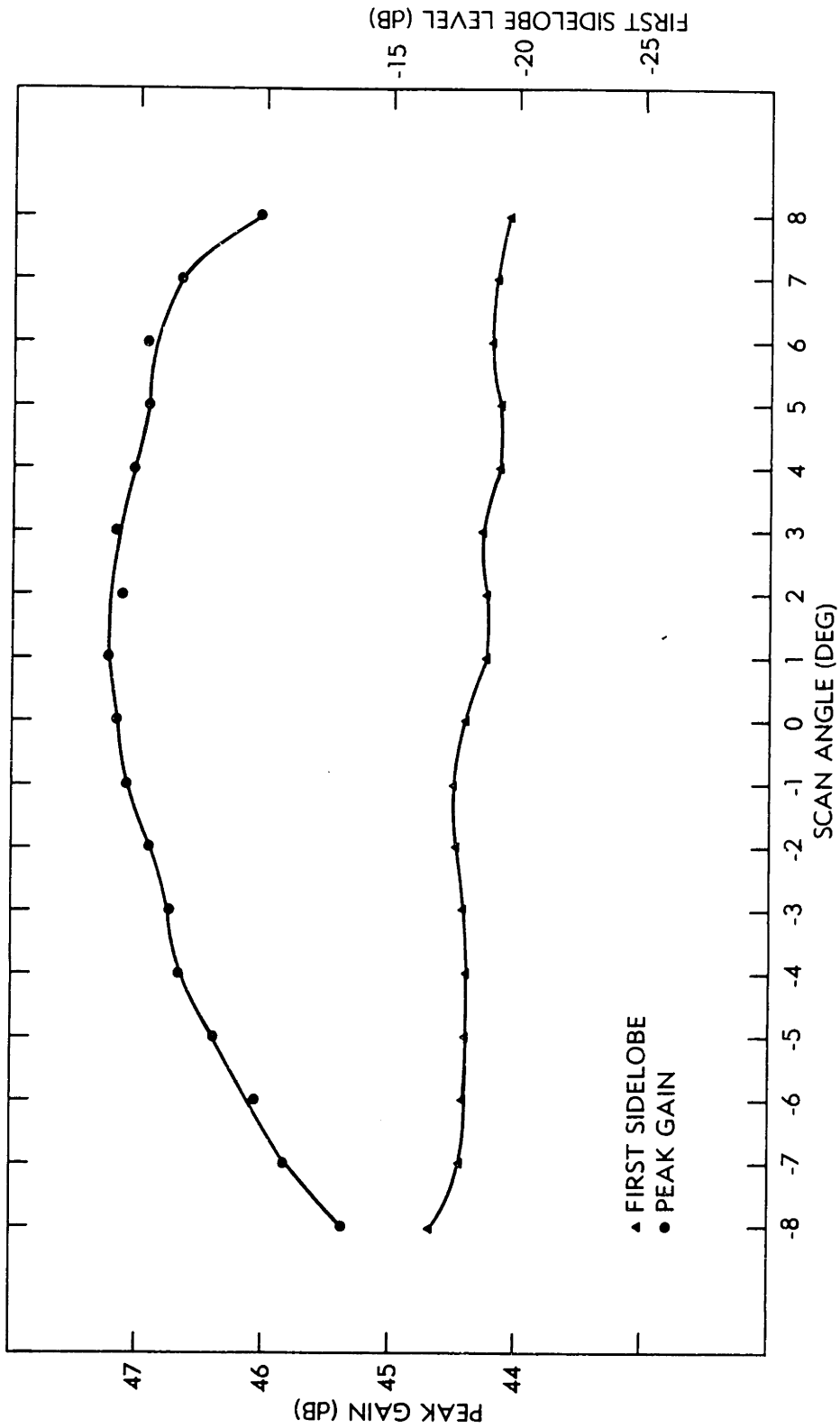


Figure 68. Scan Performance for Bifocal: 7λ Feed

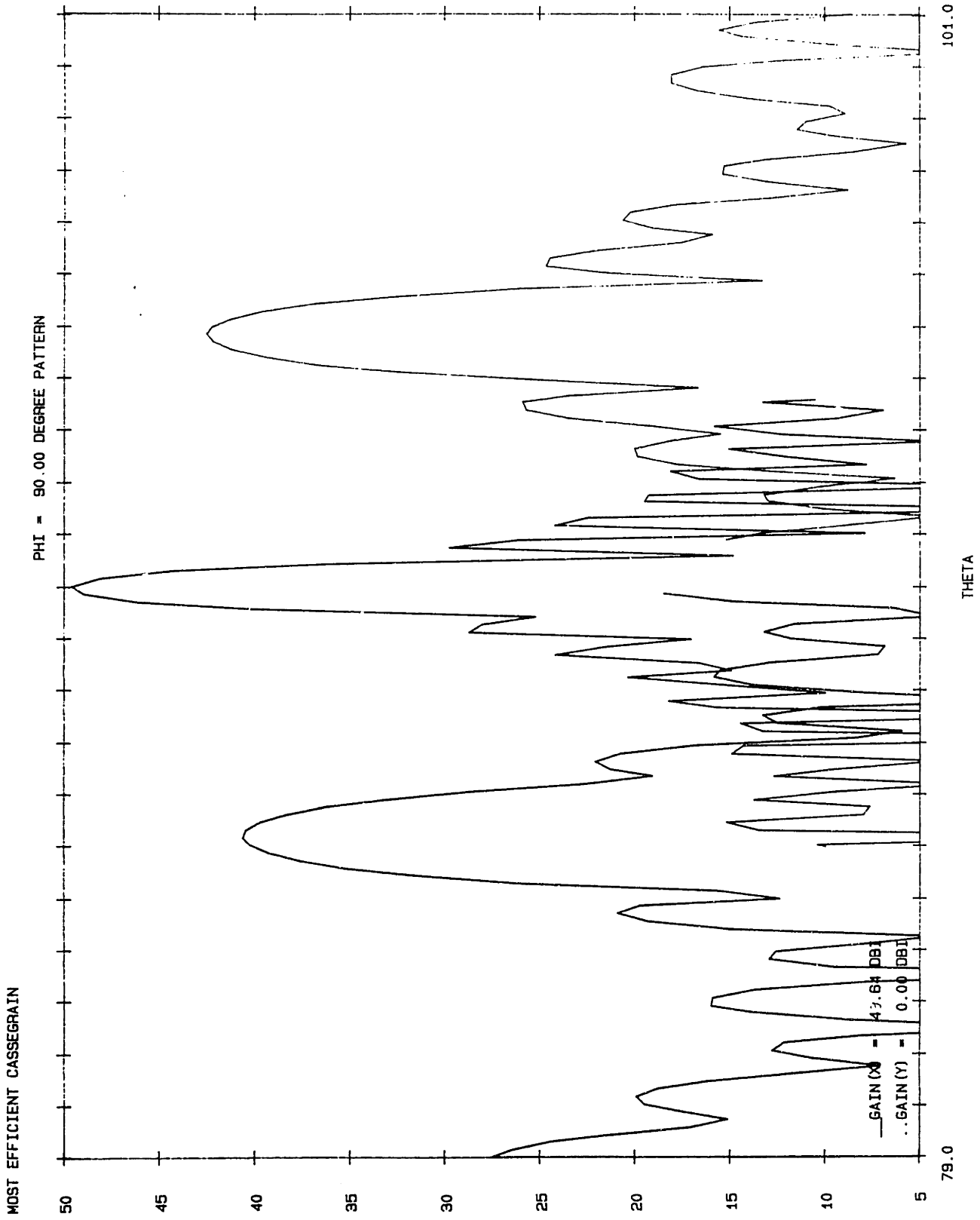


Figure 69. Elevation Scan Patterns for Type c Cassegrain: 7λ Feed

This is due to the 1-dB spillover past the main reflector. Being positioned farther back, the constant diameter main reflector subtends a smaller angle as seen from the subreflector.

For scanned beams, this repositioning of the main reflector has catastrophic effects. The spillovers past this surface are 6.09 and 7.34 dB for the $\pm 8^\circ$ beams, respectively. The beams appear well focused, with no visible coma aberrations. This is expected, since its focal length is so long. Also anticipated is the fact that although the feeds are in the same positions as for previous cases, the beams only scan $\pm 5^\circ$. This is because the equivalent paraboloid's beam deviation factor changes only about one-tenth [91] as quickly as the F/D ratio, so increasing the focal length causes focal region displacements to have less scanning effect.

A vain attempt was made to increase the lateral feed displacement in order to produce beams which scan the full $\pm 8^\circ$. It seems that the required displacement would cause all rays reflected off the first surface to miss the main reflector entirely. Thus, this is a situation illustrated in Figure 70 with a high magnification subreflector.

The design principle of maximizing focal length for single reflectors obviously does not apply in general for Cassegrains. Unlike single reflectors, dual reflectors are

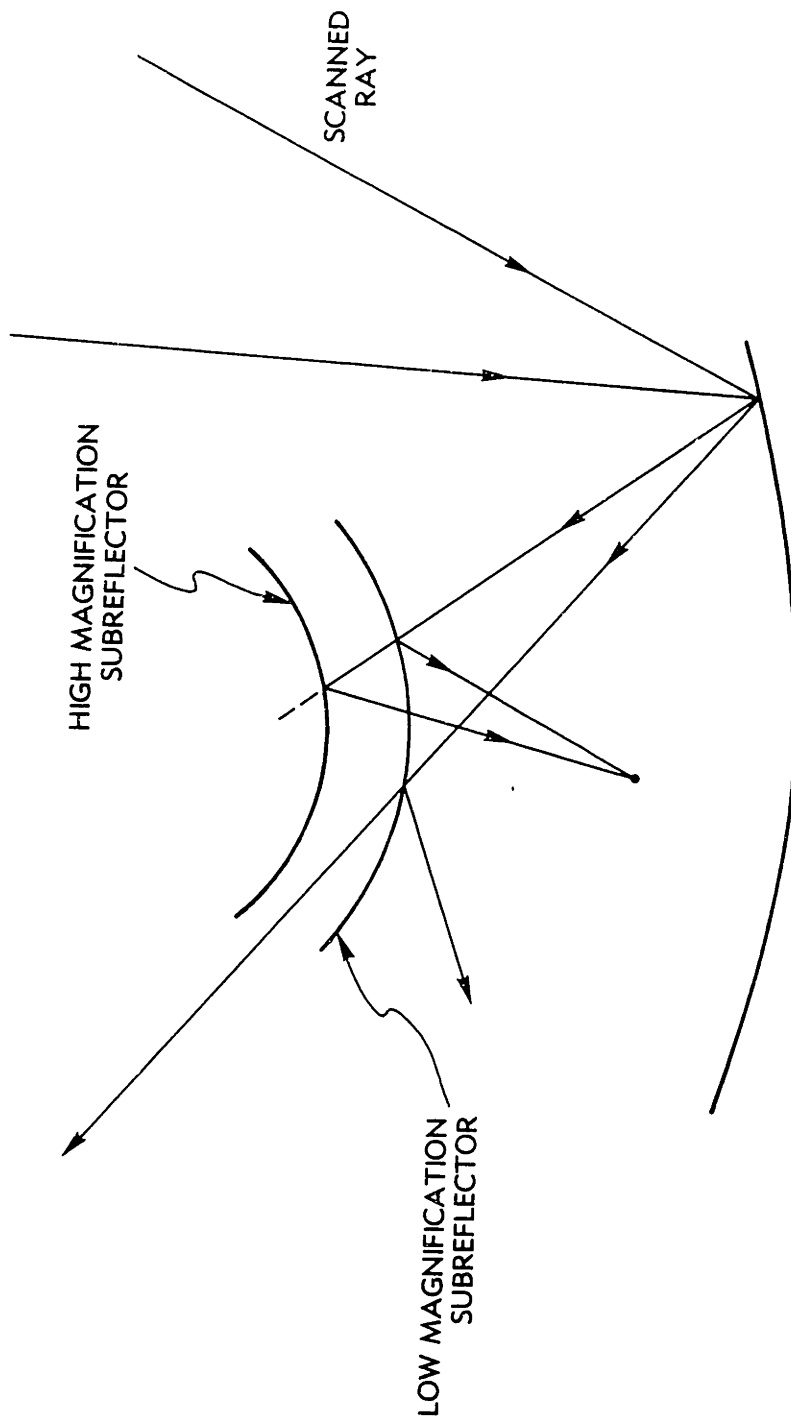


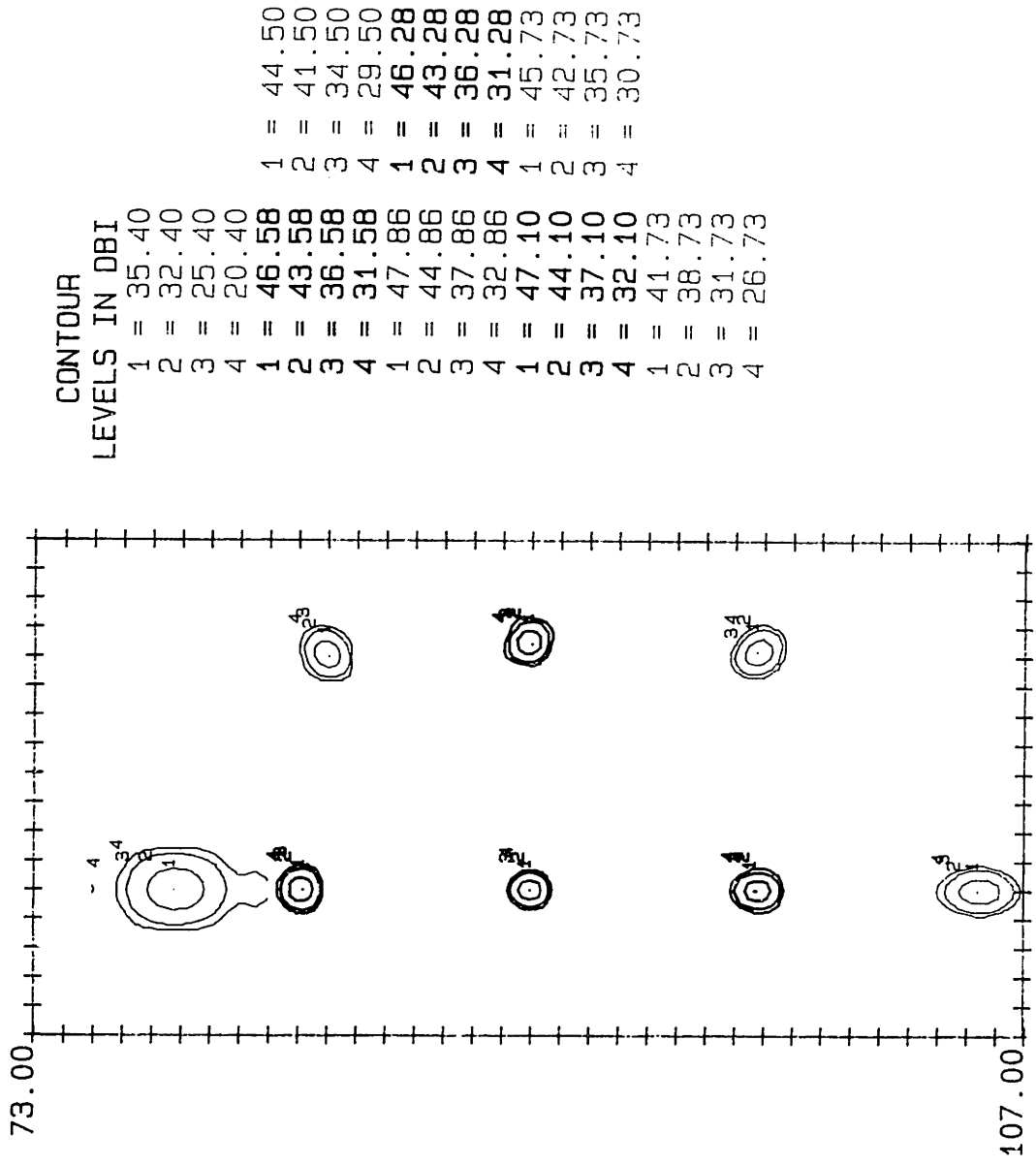
Figure 70. Differing Focusing Characteristics for High and Low Magnification (and curvature) Subreflectors

limited by spillover past one or both reflectors. Phase errors are secondary. Even with oversized reflectors, the Cassegrain still suffers from inefficient illumination and spillover. The primary advantage of the offset bifocal (and particularly the bifocal subreflector), then, is its ability to spread the feed energy more evenly over the output aperture without introducing costly phase errors. Comparing the subreflector profiles of the bifocal and Cassegrain once again (Figure 56), it is seen that the small additional curvature of the former provides this increased efficiency over the main reflector. Also, it is not too great a curvature to allow spillover.

Additional scanning analysis was performed to test the capabilities of the computer model beyond its intended scope. The elevation scanning was pushed to its extremes, displacing the feeds until the lower edge of the main reflector just barely intercepts rays from the feed to the upper edge of the subreflector; and, in the other direction, until the subreflector approaches a horizontal slit, subtending only 4° . Scanning in the azimuth plane, with feeds displaced perpendicularly to the offset plane, was also examined.

The results are shown in Figure 71. Notice that contour level number 1 is the peak gain level. All feeds were optimized for their particular scanning positions. Azimuth

OFFSET BIFOCAL WITH OPTIMIZED FEEDS,
INCLUDING EXTREME LIMITS AND AZIMUTH SCAN



CONTOUR

LEVELS IN DBI

- 1 = 35.40
- 2 = 32.40
- 3 = 25.40
- 4 = 20.40
- 1 = 46.58
- 2 = 43.58
- 3 = 36.58
- 4 = 31.58
- 1 = 47.86
- 2 = 44.86
- 3 = 37.86
- 4 = 32.86
- 1 = 47.10
- 2 = 44.10
- 3 = 37.10
- 4 = 32.10
- 1 = 41.73
- 2 = 38.73
- 3 = 31.73
- 4 = 26.73
- 1 = 44.50
- 2 = 41.50
- 3 = 34.50
- 4 = 29.50
- 1 = 46.28
- 2 = 43.28
- 3 = 36.28
- 4 = 31.28
- 1 = 45.73
- 2 = 42.73
- 3 = 35.73
- 4 = 30.73

95.00 PHI 78.00

MAX. GAIN = 47.86 DBI

Figure 71. Contour Plots for Entire Field of View

scanning in only one direction was computed since the reflectors are symmetrical about the offset plane.

The extreme scanned beams appear at -12° and $+16.5^\circ$. The upper beam has degraded very badly with 12 dB of gain loss, but the beam at $+16.5^\circ$ is only 6 dB down, with an almost acceptable contour shape.

For beams scanned -8° in the azimuth direction, the performance is surprisingly good: only 1.6-dB loss for the middle and lower beam, and 2 dB for the upper beam. Thus, the entire earth disk may be illuminated with a maximum of 3 dB variation over the field of view. Detailed contour plots of the three azimuth scan beams are provided in Figure 72. Sidelobe appears to be significantly below -15 dB down.

Again comparing the best fit offset Cassegrain (type a) to the bifocal, Figure 73 shows azimuth scanning for the former. The peak gains are lower in all but the upper elevation position. The contours also indicate less well-formed sidelobes, even for the middle beam.

Part of the explanation for the continued superior performance of the bifocal is the fact that the main reflector was specified as having a circular projected aperture large enough to capture all scanned rays from the subreflector. Thus, there are two large areas on the side edges of the main reflector which are not illuminated at all for beams scanned

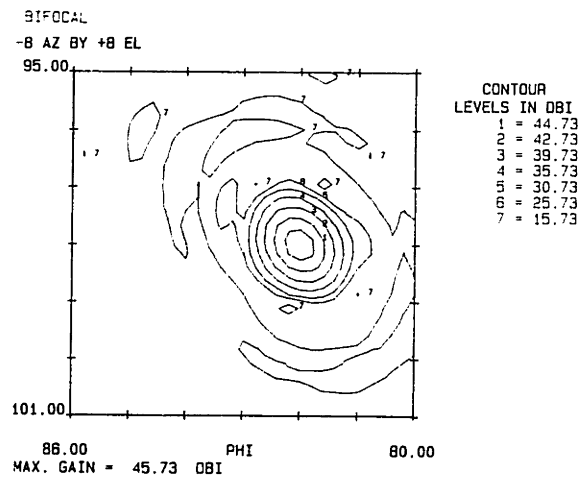
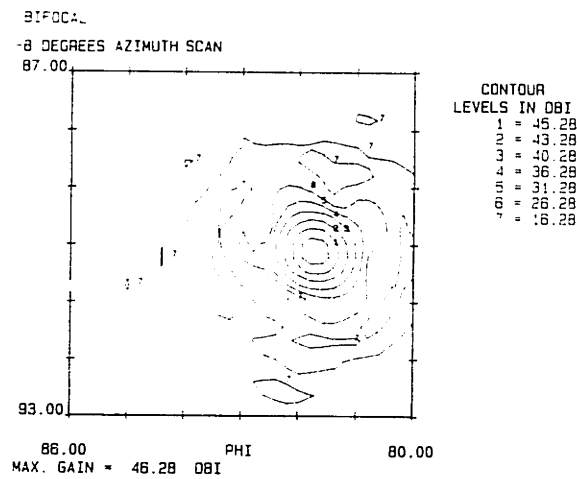
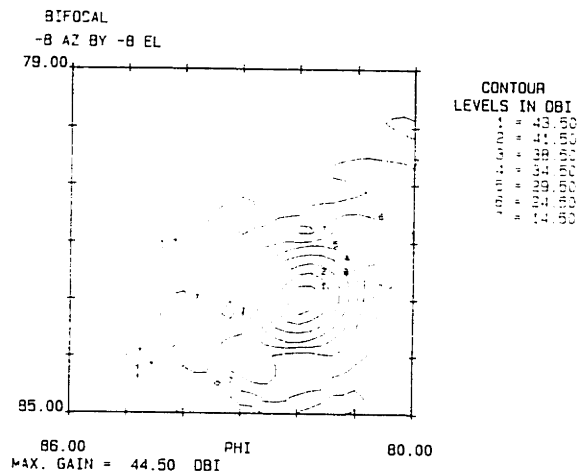


Figure 72. Beams Scanned in Both Azimuth and Elevation for Bifocal with Optimized Feeds

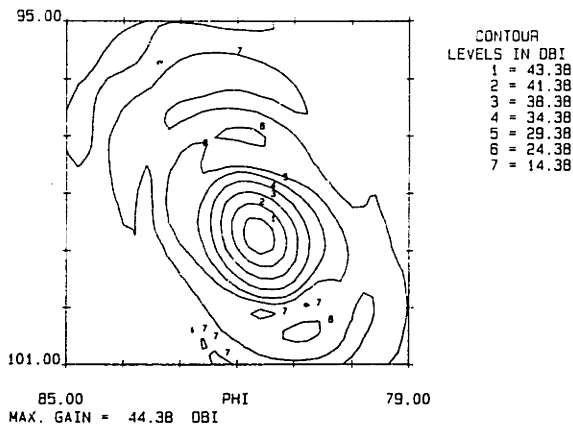
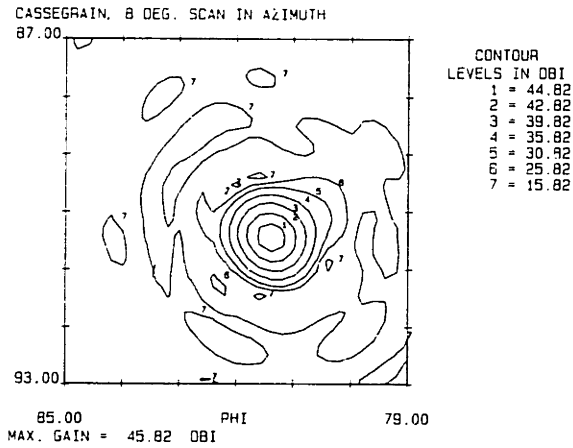
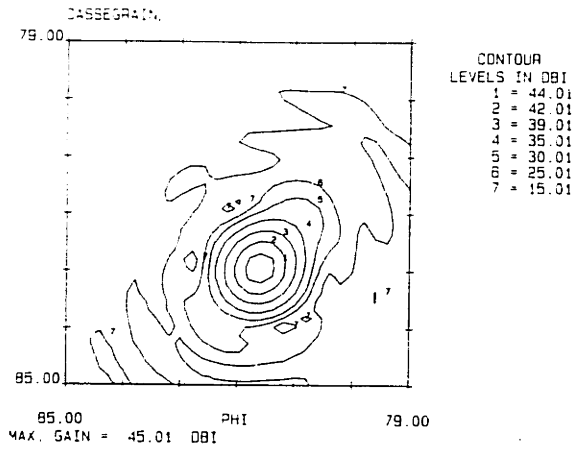


Figure 73. Type a Cassegrain Scanned in Both Azimuth and Elevation

in the elevation plane. However, they come into play whenever the beams are scanned in the azimuth plane. Another reason might be the smaller change in subreflector subtended angle for azimuth versus elevation displacement, as shown in Figure 74.

A high frequency test was tried for azimuth scanned beams. Figure 75 (with details in Figure 76) proves that the frequency independence of the offset bifocal is applicable only to the designed scan positions. Instead of rising 12 dB, the peak gains increased only 7.04, 7.50, and 10.01 dB. The contour pattern reveals the unsymmetrical and haphazard shape of these beams. Sidelobe levels are difficult to discern, but seem to fall about 15 dB down from the peak gain level.

As the final computer calculation, Figure 77 tests the limit of azimuth scanning at 0° elevation. This beam is scanned 13° with only 5.78 dB of scan gain loss. The first sidelobe level is above 15 dB below peak, but the higher gain contours are reasonably well-formed and circular.

The offset bifocal antenna can maintain well-focused beams over a 26° field of view in azimuth, and from -10° to +17°, with less than 6.5 dB of peak gain degradation and under -12 dB first sidelobe levels. It is superior for almost every scan position to any comparable Cassegrain or parabolic antenna held to the same volume constraints.

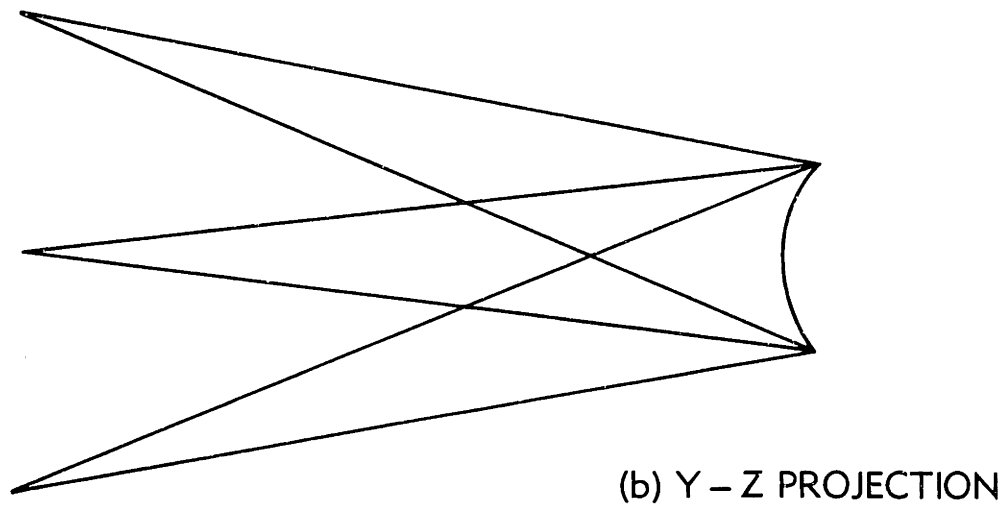
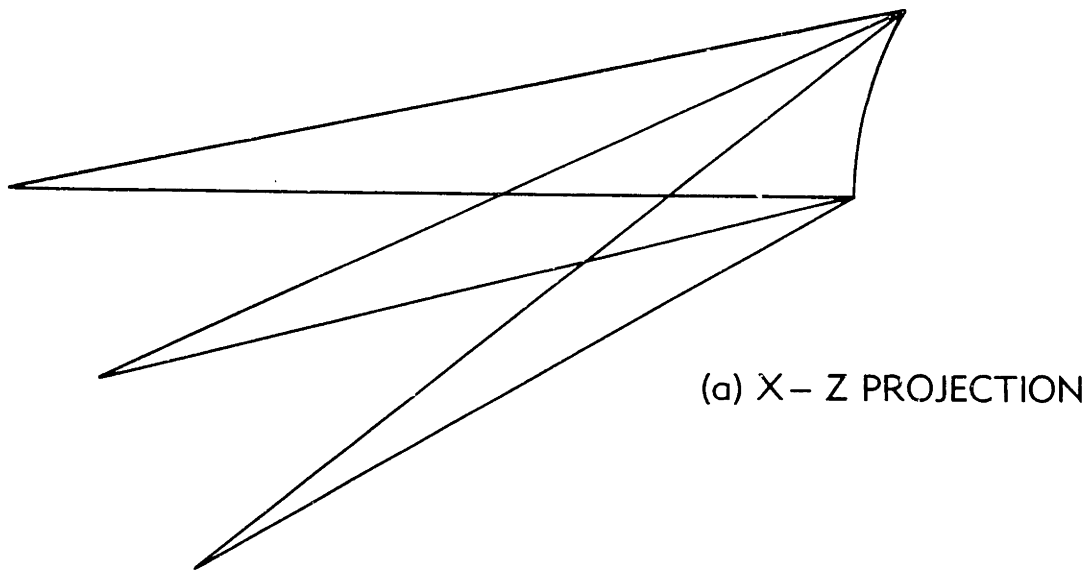
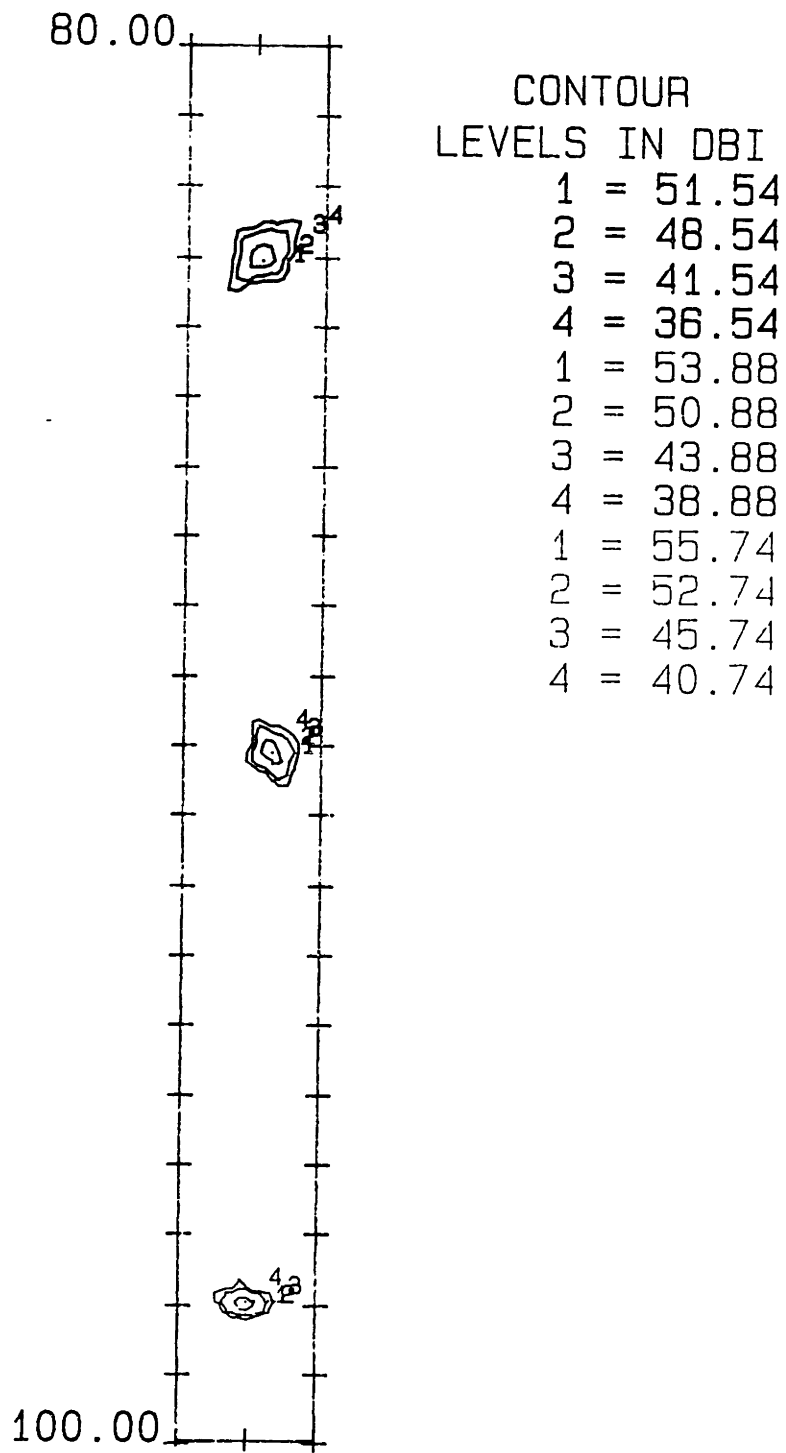


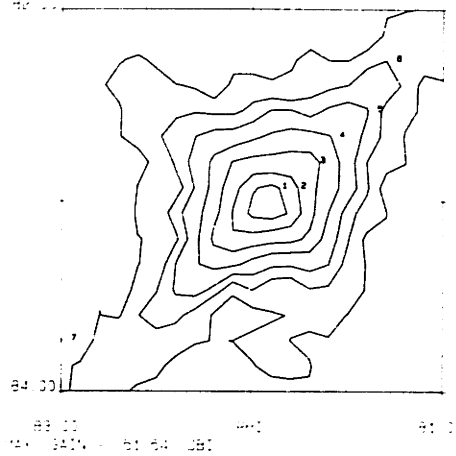
Figure 74. Feed Angle Variation for a) Elevation Scanning and b) Azimuth Scanning



83.00H1.00
 MAX. GAIN = 55.74 DBI

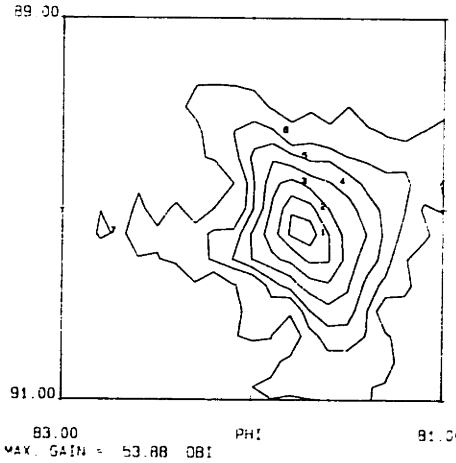
Figure 75. High Frequency Azimuth and Elevation Scanning: $\pm 32 \times \pm 32$ Beamwidths

-32 BEAMWIDTHS SCAN IN AZ. -28 IN EL



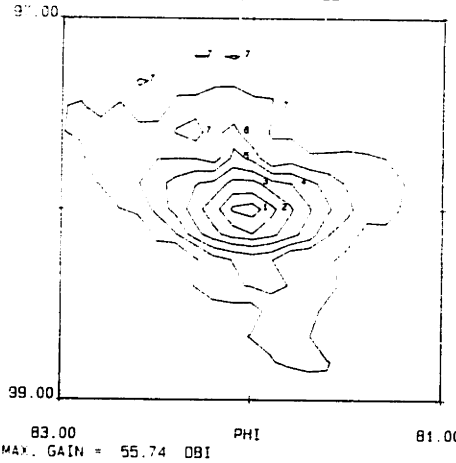
CONTOUR
LEVELS IN DBI
1 = 50.84
2 = 48.84
3 = 45.84
4 = 41.84
5 = 36.84
6 = 31.84
7 = 21.84

-32 BEAMWIDTHS SCAN IN AZIMUTH



CONTOUR
LEVELS IN DBI
1 = 52.88
2 = 50.88
3 = 47.88
4 = 43.88
5 = 38.88
6 = 33.88
7 = 23.88

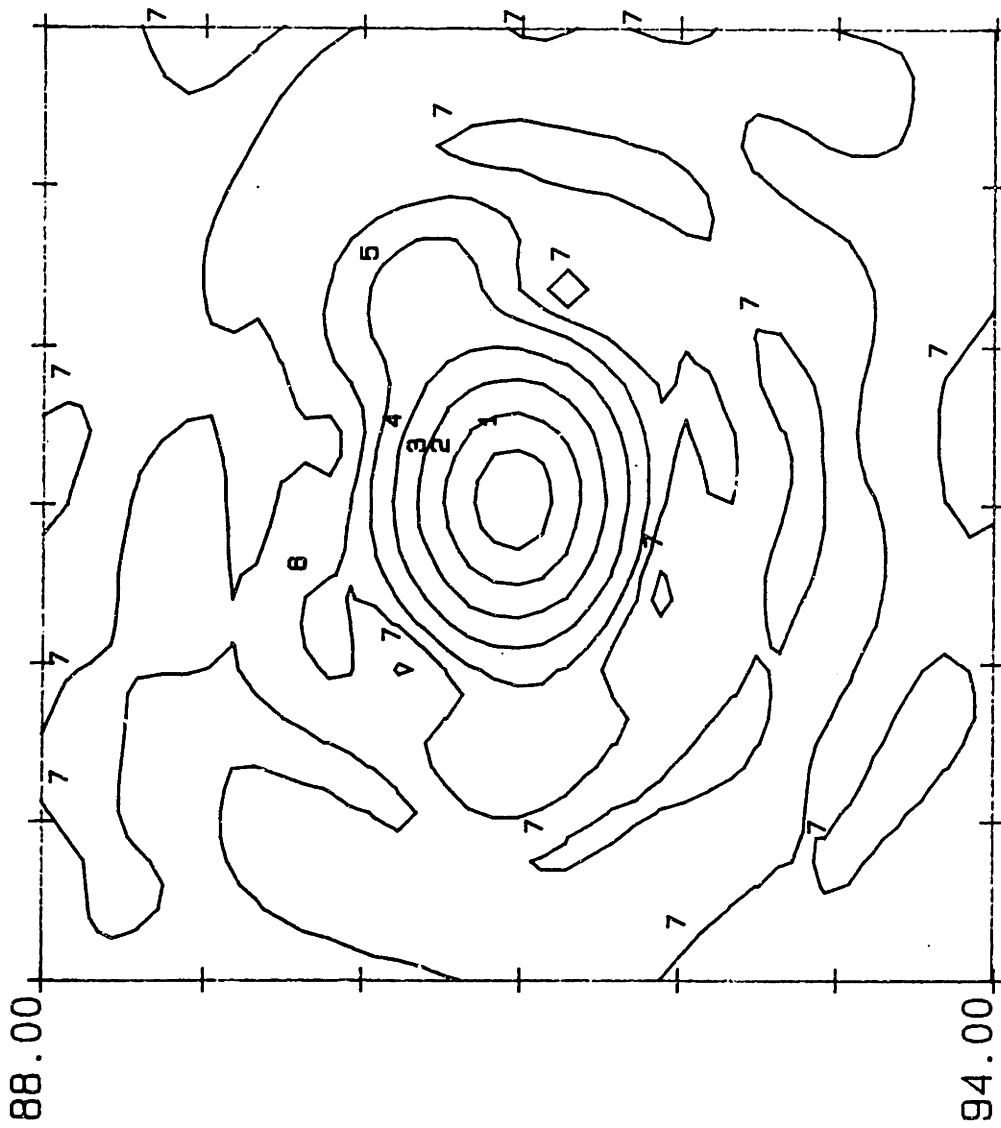
-32 BEAMWIDTHS SCAN IN AZ. +32 IN EL



CONTOUR
LEVELS IN DBI
1 = 54.74
2 = 52.74
3 = 49.74
4 = 45.74
5 = 40.74
6 = 35.74
7 = 25.74

Figure 76. Detail of High Frequency Azimuth and Elevation Scanning

EXTREME AZIMUTH SCAN: -13 DEGREES



CONTOUR
LEVELS IN DBI
1 = 42.08
2 = 40.08
3 = 37.08
4 = 33.08
5 = 28.08
6 = 23.08
7 = 13.08

80.00 PHI 74.00

MAX. GAIN = 43.08 DBI

Figure 77. Limits of Scanning with Offset Bifocal:
13 One Degree Beamwidths

APPENDIX IV. COMPUTER PROGRAM FEEDA
LISTING AND SAMPLE RUN

The FORTRAN program FEEDA determines the optimum orientation of a feed illuminating a circular reflector. Given the feed and reflector center location and the projected reflector radius, the program computes the unit vector along which the feed should be aligned.

```

C
C   *** FEED POINTING ANGLE PROGRAM
C   DIMENSION F (3),XENDS (2,2),FIRST (2),SECOND (2),CVEC (3)
C   *** DEFINE A FUNCTION Z, OF INDEPENDENT VARIABLE X, AND TYPE A.
      Z (X,A) = (.07066 -.02649*X + 1.2813*X**2 - 2.0985*X**3 + 1.2865*X**4) * (2-A)
      & + (-.25 + .7576*X**2) * (A-1)
      WRITE (6,1)
1   FORMAT (' ENTER TYPE OF SURFACE, X-CENTER AND REFLECTOR RADIUS')
      READ (5,*) AIN,XCENT,RAD
10  WRITE (6,2)
2   FORMAT (' ENTER THE COORDINATES OF THE FEED LOCATION')
      READ (5,*) F
      XENDS (1,1) = XCENT - RAD
      XENDS (2,1) = XCENT + RAD
C   *** XENDS ARE THE ENDPOINTS OF THE SURFACE. THE SECOND ARG IS
C   * 1 FOR X-VALUES, 2 FOR Z-VALUES.
C   * AIN IDENTIFIES THE SURFACE TYPE SPECIFIED ABOVE: 1 FOR SUBREF.,
C   * 2 FOR A PARABOLOID.
      DO 100 I=1,2
      XENDS (I,2) = Z (XENDS (I,1),AIN)
C   *** AFTER THE Z-VALUES AT THE ENDPOINTS ARE SOLVED, DETERMINE THE
C   * VECTORS FROM THE FEED TO EACH OF THESE POINTS.
C   * 'FIRST' IS THE DIFFERENCE IN X; 'SECOND', THE DIFFERENCE IN Z.
      FIRST (I) = XENDS (I,1) - F (1)
100 SECOND (I) = XENDS (I,2) - F (3)
C   *** FIND THE MAGNITUDES OF THE DISTANCES OF EACH VECTOR.
      AMAG = SQRT (FIRST (1) **2 + SECOND (1) **2)
      BMAG = SQRT (FIRST (2) **2 + SECOND (2) **2)
      PHI = ACOS (SECOND (1) / AMAG * (3. - 2. * AIN))
C   *** TAKE DOT PRODUCT WITH Z-AXIS ('-' FOR A = TYPE 2), AND CHOOSE
C   * NEGATIVE ANGLE IF THE VECTOR TO ENDPOINT 1 POINTS BACKWARD.
      IF (FIRST (1) .LT. 0.) PHI = -PHI
C   *** FIND THE INCLUDED ANGLE BETWEEN THE VECTORS.
      THETA = ACOS ((FIRST (1) * FIRST (2) + SECOND (1) * SECOND (2)) / AMAG / BMAG)
C   *** THE CENTRAL VECTOR IS THE SUM OF THE OFFSET FROM THE Z-AXIS AND
C   * HALF THE INCLUDED ANGLE.
      ANG = PHI + THETA / 2.
      PRINT *, PHI, THETA, ANG
      CVEC (1) = SIN (ANG)
C   *** SINCE THE Z COMPONENT OF THE CENTRAL VECTOR POINTS UP FOR THE
C   * SUBREFLECTOR, AND DOWN FOR THE PARABOLOID, USE THE SURFACE TYPE
C   * TO DETERMINE ITS PROPER SIGN.
      CVEC (3) = COS (ANG) * (3. - 2. * AIN)
C   *** THE Y COMPONENT WILL BE APPROXIMATELY THE Y OFFSET OF THE FEED
C   * DIVIDED BY THE MAGNITUDE OF THE AVERAGE X-Z VECTOR FROM THE FEED.
      CVEC (2) = -F (2) / (AMAG + BMAG) * 2
      THETA = THETA * 180. / 3.14159
      WRITE (6,150) CVEC, THETA
150 FORMAT (' CENTRAL VECTOR (',F6.4,',',F6.4,',',F6.4,') FULL ILLUMINA
      TION ANGLE ',F6.2/' ANOTHER POINT? (1 OR 0)')
      READ (5,*) L
      IF (L.EQ.1) GOTO 10
      RETURN
      END

```

V. MODEL FABRICATION

A. Support Structure

A scale model of the offset bifocal antenna system was constructed based upon the equations derived in the previous sections. Experiments with this model were performed to confirm the computed results. The frequency used, 36 GHz, was determined by the physical capacity constraints of the fabricating machinery and the desired beamwidth. This high frequency model is thus 9 or 6 times smaller than the full-scale standard 4- or 6-GHz satellite broadcast antennas.

The scale model consists of the main and subreflectors, the microwave horn feeds, and a support structure which rigidly and accurately positions the above components. This support framework, shown in Figure 78 with reflectors mounted, was designed for this offset bifocal system by a fellow COMSAT employee, Ken Pease. Measuring 7 ft x 7 ft x 3 ft, it is mounted to a Scientific Atlanta 3-axis mount. The feed horn is bolted on a fixture with 6 degrees of freedom. These include motion parallel and azimuthally perpendicular to the antenna axis--each along a pair of rails, driven by lead screws; vertical motion (perpendicular in elevation); refocusing motion parallel to the feed axis; elevation rotation; and azimuth rotation.

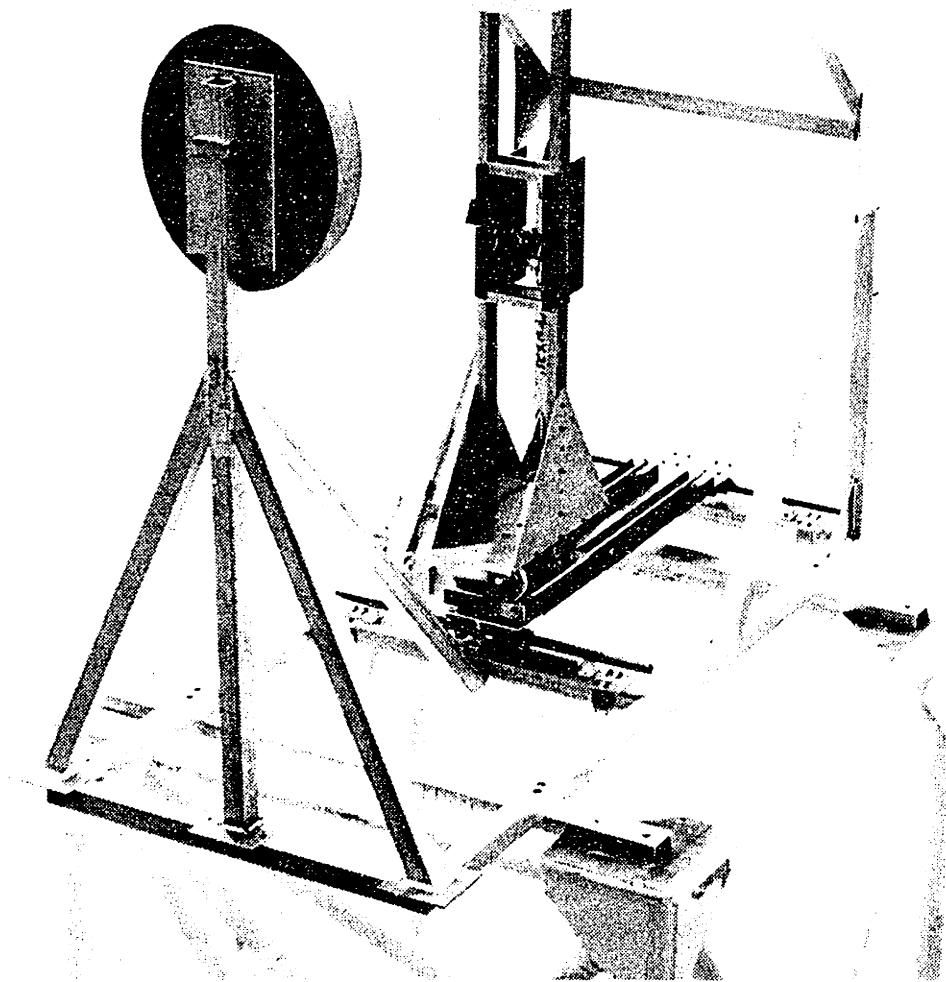


Figure 78. Support Framework for
Experimental Model

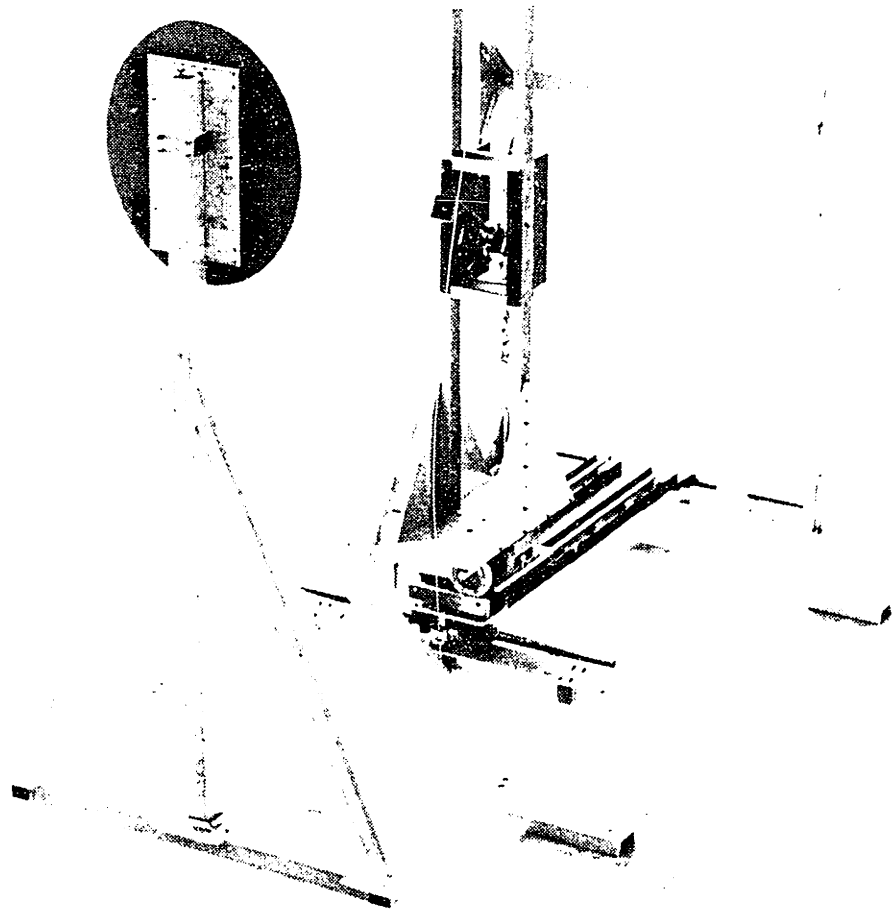


Figure 78. Support Framework for
Experimental Model

The vertical and antenna axial displacements allow the feed to be positioned at the designed locations, with elevation rotation providing the designed feed orientation. The refocusing adjustment accommodates different feed horn lengths (from 1 to 15 in.) without having to readjust the positions and orientations. The azimuthal motion and azimuth rotation allow transverse feed displacement and reorientation for azimuth scanning. The 36-in. vertical displacement and 24-in. azimuthal displacement provide approximately an 18° by 12° field of view.

The main reflector is mounted on a pivoting cross member, fixed in place with a lead screw. Two degrees of freedom are available: azimuthal displacement and elevation rotation. The rotation adjustment compensates for any elevation deviations of the 3-axis mount. Repositioning in azimuth is a more difficult adjustment, but is needed only for testing large amounts of azimuth scanning.

The subreflector is mounted on four lead screws which in turn mount to a vertical mast. The lead screws provide up to 8 in. of axial motion, and--since they can be turned separately--allow both azimuth and elevation adjustment of up to 20° . The entire subreflector assembly can be moved up or down along the mast, adding a fourth degree of freedom.

One further feature of the support structure is the option to reconfigure the system as a single reflector (prime focus) antenna. This is accomplished by removing the subreflector mast assembly, and moving the feed assembly forward into the paraboloid's focal region. This arrangement is useful for characterizing and aligning the main reflector.

B. Reflector Fabrication

The main reflector was specified to be an offset paraboloid section, so it could be cut from commercially available microwave reflectors. The subreflector, on the other hand, being a fourth-order surface, had to be fabricated using a Bostomatic numerically controlled milling machine. Full bit and table motion allowed milling within a 12-in. cube. This limitation provided the upper bound on physical size of the system. To minimize the test frequency, the largest surfaces possible were sought after.

To maximize the subreflector size, it is necessary to find the largest ellipse which will fit completely within a 12-in. cube. This ellipse corresponds to the projection of the subreflector surface onto the plane containing the upper and lower endpoints perpendicular to the plane of symmetry.

Thus, the ellipse is a slice through the convex solid subreflector which defines the surface boundaries. Since the projection of the subreflector onto the x-y plane is a circle, and the difference in z from one endpoint to the other is known, the relative lengths of the axes of the ellipse can be found. This value turns out to be 1.029. For practicality, the ellipse can be approximated as a circle.

Now consider the intersection of a plane with a cube such that the midpoints of six edges are included in the plane (Figure 79). These midpoints are connected consecutively, producing a regular hexagon with sides equal to $\sqrt{2}$ times the the cube edge. Thus a circle with radius:

$$\frac{\sqrt{3}}{2} (\sqrt{2}) (12) = 14.70 \text{ in.}$$

will fit within a one-ft cube. Going back to the ellipse, it is evident that with a major axis of 14.7 in., and thus a minor axis of 14.3 in., the biggest subreflector within the specified limits is obtained. Figure 80a, b, and c shows the three views of the subreflector in the double prime coordinate system. Figure 80a indicates the position of the ellipse on the tilted plane intersecting the cube.

Thus, by scaling, translating, rotating, and translating again, the equation of the subreflector model can be derived. The scale factor is 14.70 divided by the distance

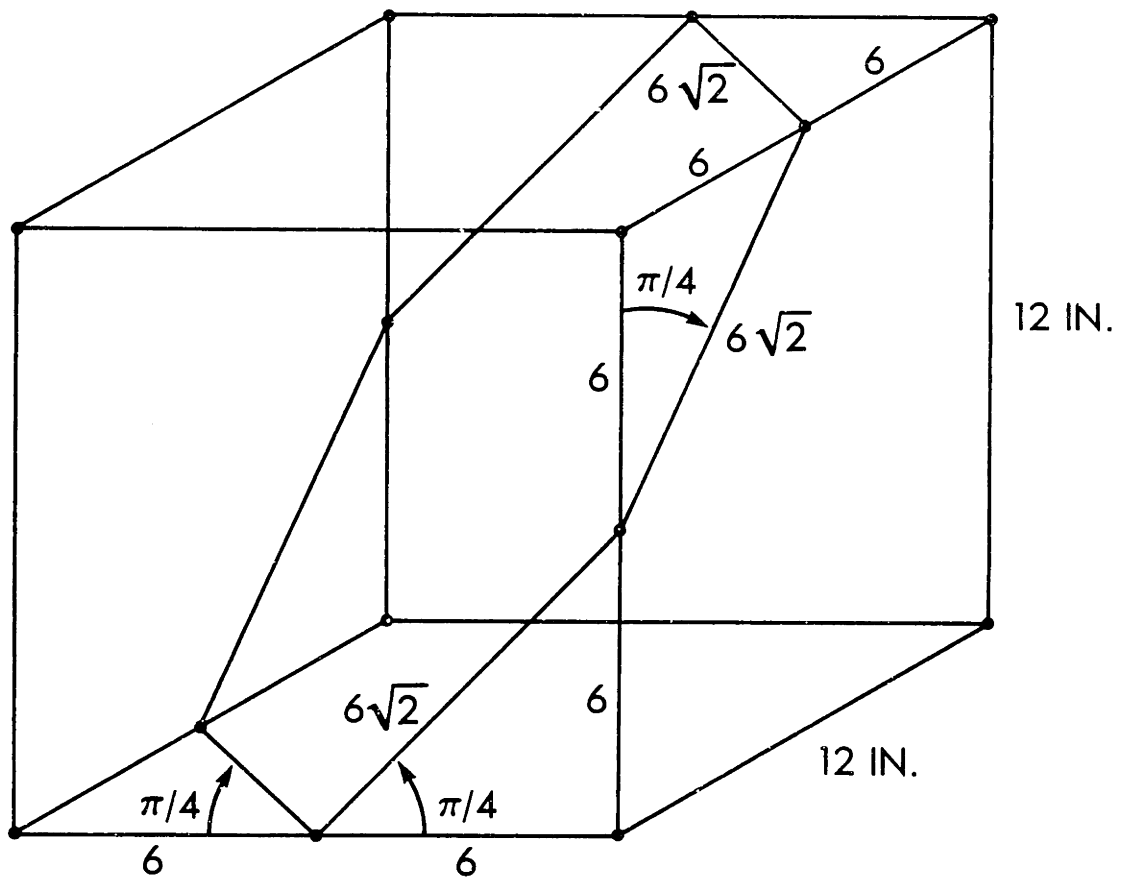


Figure 79. Intersection of the Limiting Cube and Subreflector Plane Yielding the Largest Inscribed Circle

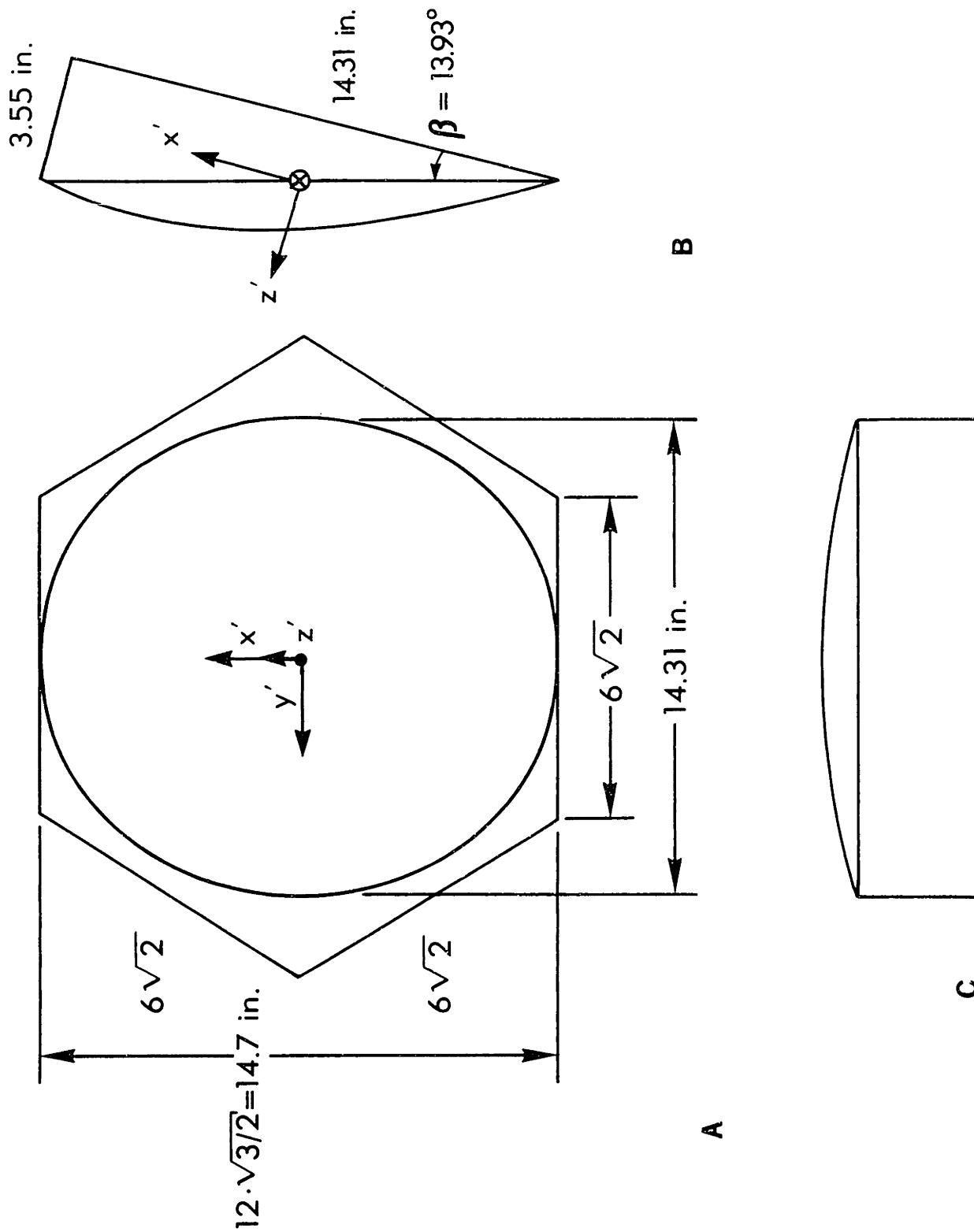


Figure 80. View of the Subreflector in the Double Prime Coordinate System:
a) Projection onto Hexagon, b) and c) Orthogonal Views

between the endpoints, or 145.4. The equation of the full scale surface becomes:

$$z = 10.104 - 0.02649 x + 0.00896 x^2 - 1.0262 \cdot 10^{-4} x^3 \\ + 4.399 \cdot 10^{-7} x^4 + 0.00489 y^2,$$

with limits

$$(x - 21.81)^2 + y^2 \leq (7.15)^2$$

The first translation places the midpoint of the segment connecting the endpoints at the origin. Thus, $(x', y', z') = (x - 21.81, y, z - 13.13)$. Then the surface is rotated by $180 + 41.7^\circ$ counterclockwise in the x-z plane, and then 45° in the x-y plane.

The first angle is derived by finding the desired angle of the endpoint segment (Figure 80b):

$$\theta = \sin^{-1} \frac{12}{14.7} \\ = 54.7^\circ,$$

and subtracting the angle the original endpoint segment makes with the x-axis:

$$\beta = \tan^{-1} \left(\frac{z_2 - z_1}{x_2 - x_1} \right) \\ \beta = \tan^{-1} \left(\frac{14.79 - 11.49}{28.97 - 14.66} \right) \\ = 13.0^\circ, \\ \alpha = \theta - \beta \\ = 41.7^\circ,$$

and then adding 180° to have the surface face up. The surface must face upward, since the mill operates by cutting from above. The rotation formulas are:

$$x'' = x' \cos \theta \cos \pi/4 - y' \sin \pi/4 - z' \sin \theta \cos \pi/4$$

$$y'' = x' \cos \theta \sin \pi/4 + y' \cos \pi/4 - z' \sin \theta \sin \pi/4$$

$$z'' = x' \sin \theta + z' \cos \theta$$

See Figure 81. The final translation moves the segment midpoint to the physical center of the cube; that is, at (6, 6, 6). Thus $(x''', y''', z''') = (x'' + 6, y'' + 6, z'' + 6)$. Figure 82 shows the final arrangement.

Notice that since the desired machined subreflector has a base which must be perpendicular to the original antenna axis (z-axis), the stock to be machined must be supported at 41.7° . A precision support structure inclined at this particular angle was built.

The subreflector surface is mathematically specified as a fourth order function. To machine the actual surface, the function is sampled at fine increments. These sample points can be connected by straight line segments to form an approximation to the surface. The sample points are quickly generated by computer and passed to fabrication machinery.

The numerically controlled milling machine cuts an object based on programmed instructions. These instructions consist of point specifications in three dimensions, and a

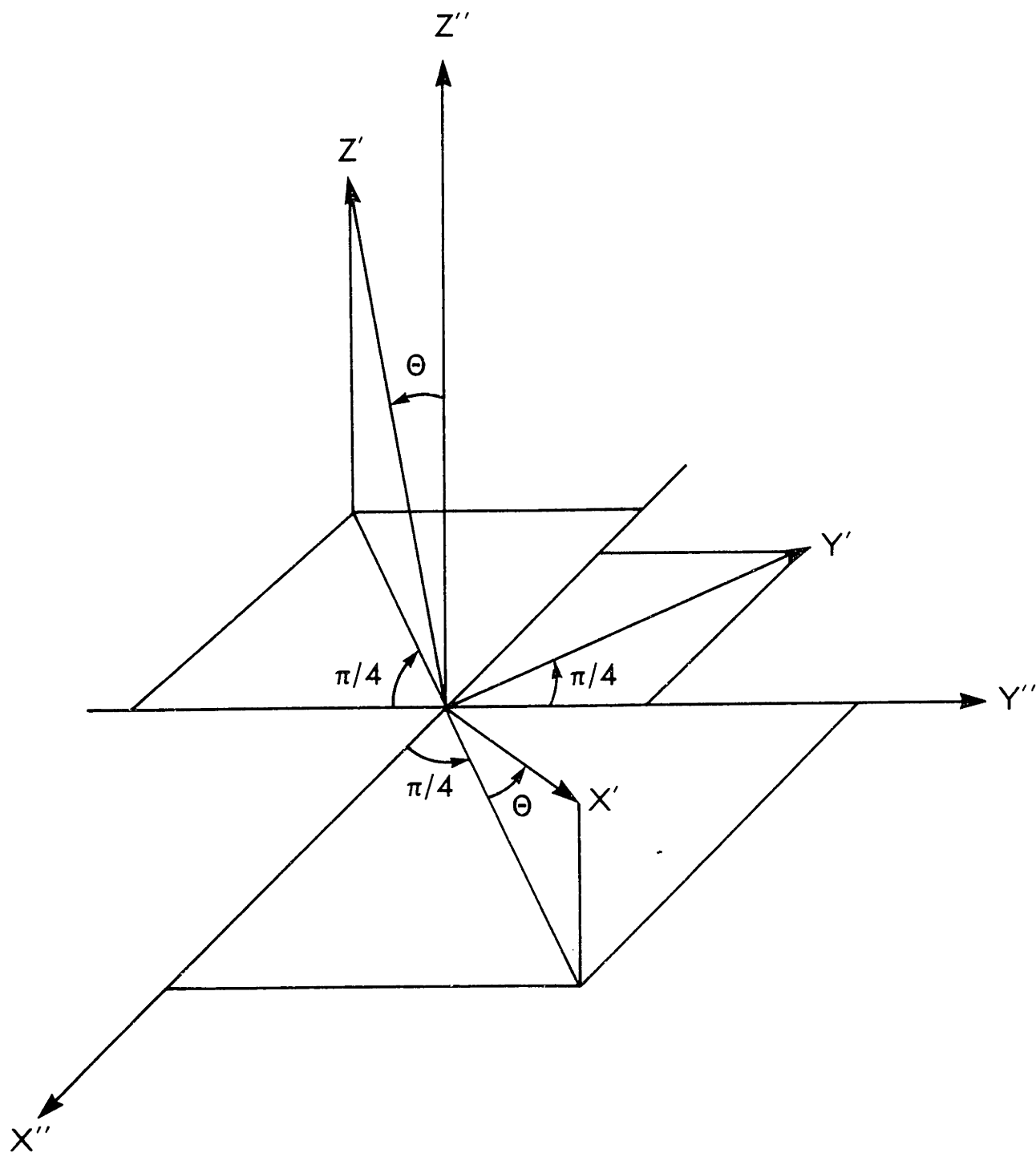
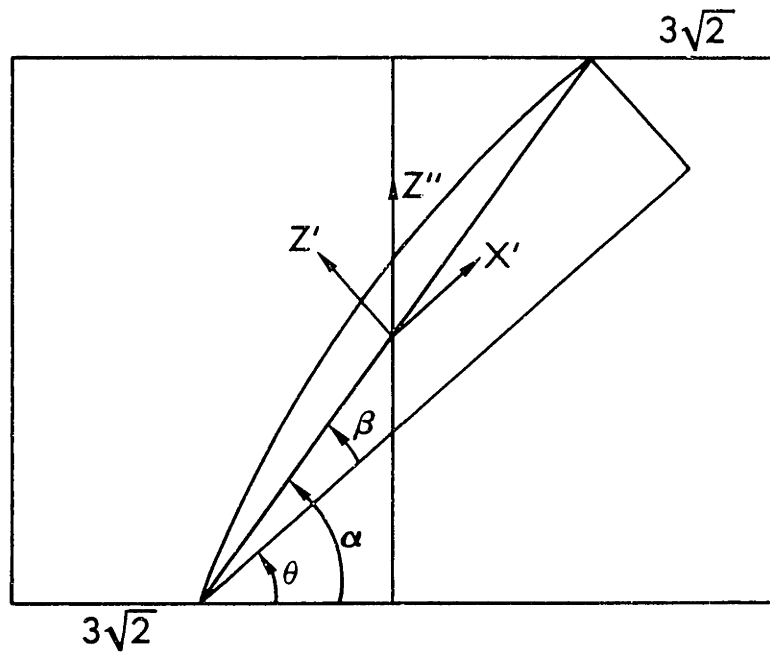


Figure 81. Geometry of Coordinate Rotation



$$\theta = \alpha - \beta$$

$$\text{TAN } \alpha = \frac{12}{12\sqrt{2} - 6\sqrt{2}}$$

$$= \sqrt{2}$$

$$\alpha = 54.74^\circ$$

$$\beta = 13.93^\circ$$

$$\theta = 40.81^\circ$$

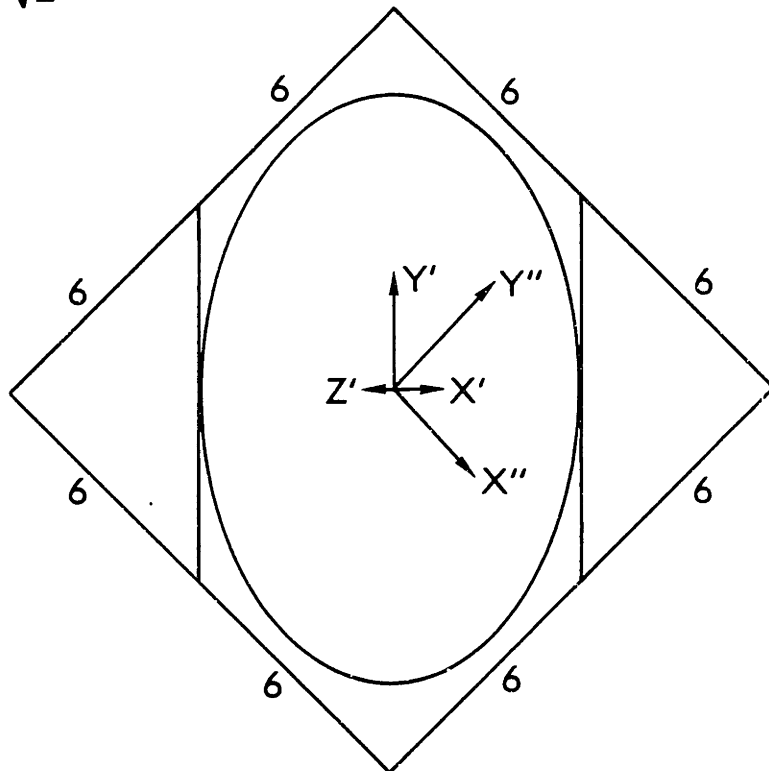


Figure 82. View of Subreflector Positioned Inside 12 in. Cube: Side Edge and Top Views

connection scheme. Programming is done in the high level language, "Compact II", and then externally compiled. The compiled version is then punched onto paper tape and fed to the mill's minicomputer.

The use of paper tape is one of many inefficiencies that were encountered in the subreflector fabrication. Apparently, because of the intensely metallic environment of a machine shop, magnetic tape was ruled out when the mill was designed.

The Compact II compiler is only available on a separate minicomputer processor/editor, which cannot be tied directly to the milling machine's minicomputer. Furthermore, this processor only accepts terminal or paper tape input. Thus the set of points passed from the generating computer must first be translated into Compact II source code, and then punched onto paper tape.

Appendix V provides listings of PL 1 programs, the first of which performs the required coordinate transformations, chooses the sample points, and specifies the point connection scheme, and another which provides output in the Compact II language. Also included is one sample Compact II program, produced by the PL 1 translator, and fed to the minicomputer compiler.

Unfortunately, the compiled code is peculiar to the milling machine. As a result, three computers and two sets of punched tape were needed to transfer the surface from its functional representation to a machine-readable form. The limitations of memory of the two minicomputers necessitated breaking the procedure into 13 separate runs, requiring 26 separate rolls of paper tape. The procedure would be immensely improved if the machine code were standardized and a direct link between computers existed.

The method of choosing and connecting the sampled points is a critical detail. Unless great care is taken, the approximation could deviate from the desired function by an intolerable amount. Of course, the number of points must be minimized to decrease the amount of data transfer and the cutting time.

The milling machine has the capability of cutting a straight path between any two points in three dimensions. In the original, untransformed coordinate system, the subreflector surface is sampled by holding the x component fixed and varying the y values. This is transformed to an arc in space which extends from one side of the surface to the other. This arc "cut" is divided into several roughly equal length straight-line segments--with endpoints at the sampled points

on the surface. The number of points per cut varies from one, at the upper and lower extremes, to 16 for the 94 cuts around the central section (see Figures 83 and 84). The two plots indicate a division of the mill paths into sections. This division, at 9 in. from the front edge, is necessary because of the presence of a protruding bar on the milling machine. The total number of cuts, or back and forth motions of the mill bit, is 350.

The spacing of points and cuts was determined based on maintaining an approximation tolerance which is more precise than the milling machine tolerance of 0.003 in. The bit used was a 0.75 in. ball end mill, which cuts a hemispherical hole. Consider the distance between the straight tangent segment touching two intersecting circles of radius R and the point of intersection (Figure 85). This distance, T , corresponds to the maximum deviation from a flat surface and that surface cut with the ball end mill.

If the circles are separated by a distance Δx ,

$$\begin{aligned}
 T &= R - R \sin \theta \\
 &= R \left(1 - \sqrt{1 - \left(\frac{\Delta x / 2}{R} \right)^2} \right) .
 \end{aligned}$$

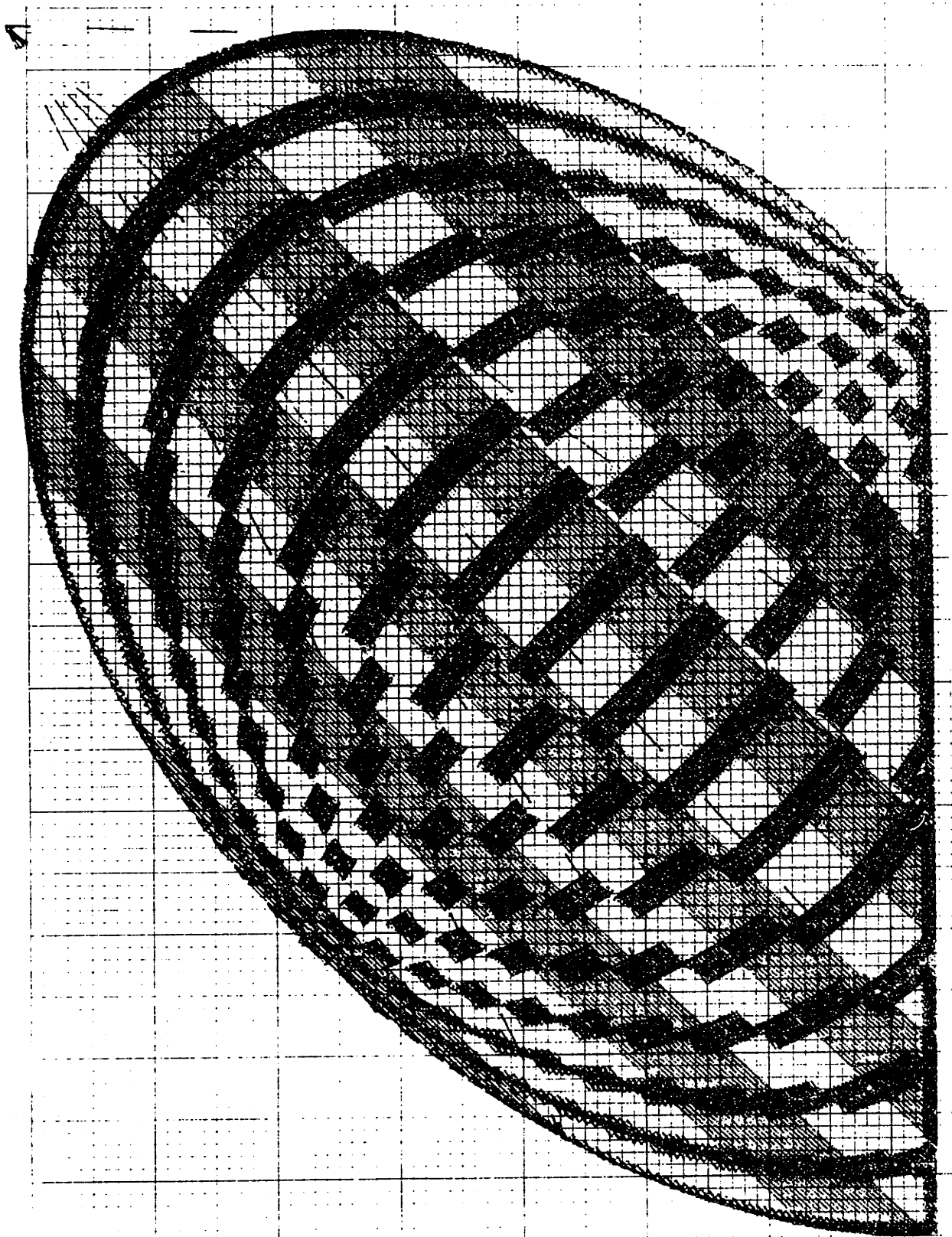


Figure 83. Left Half Mill Paths

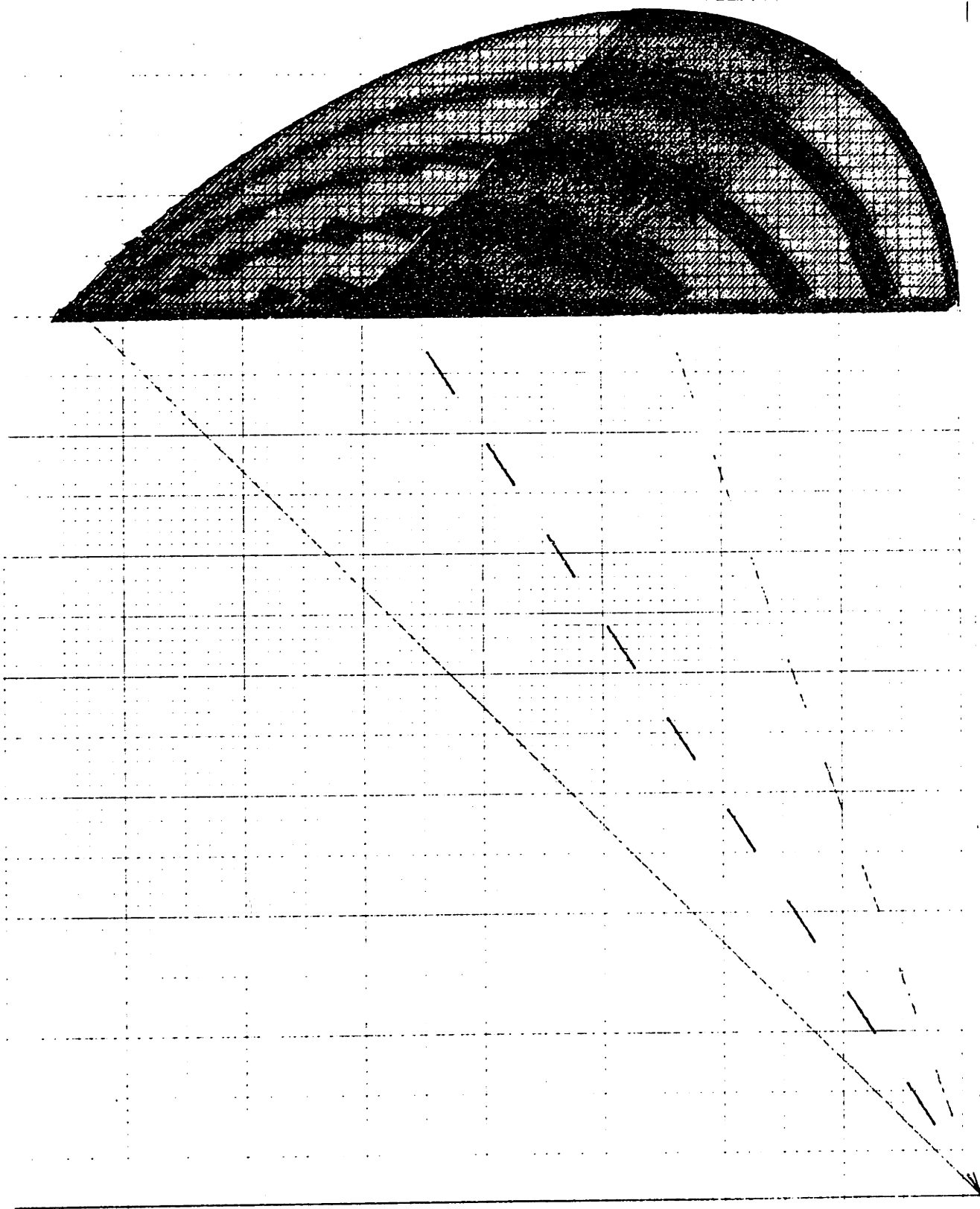


Figure 84. Right Half Mill Path

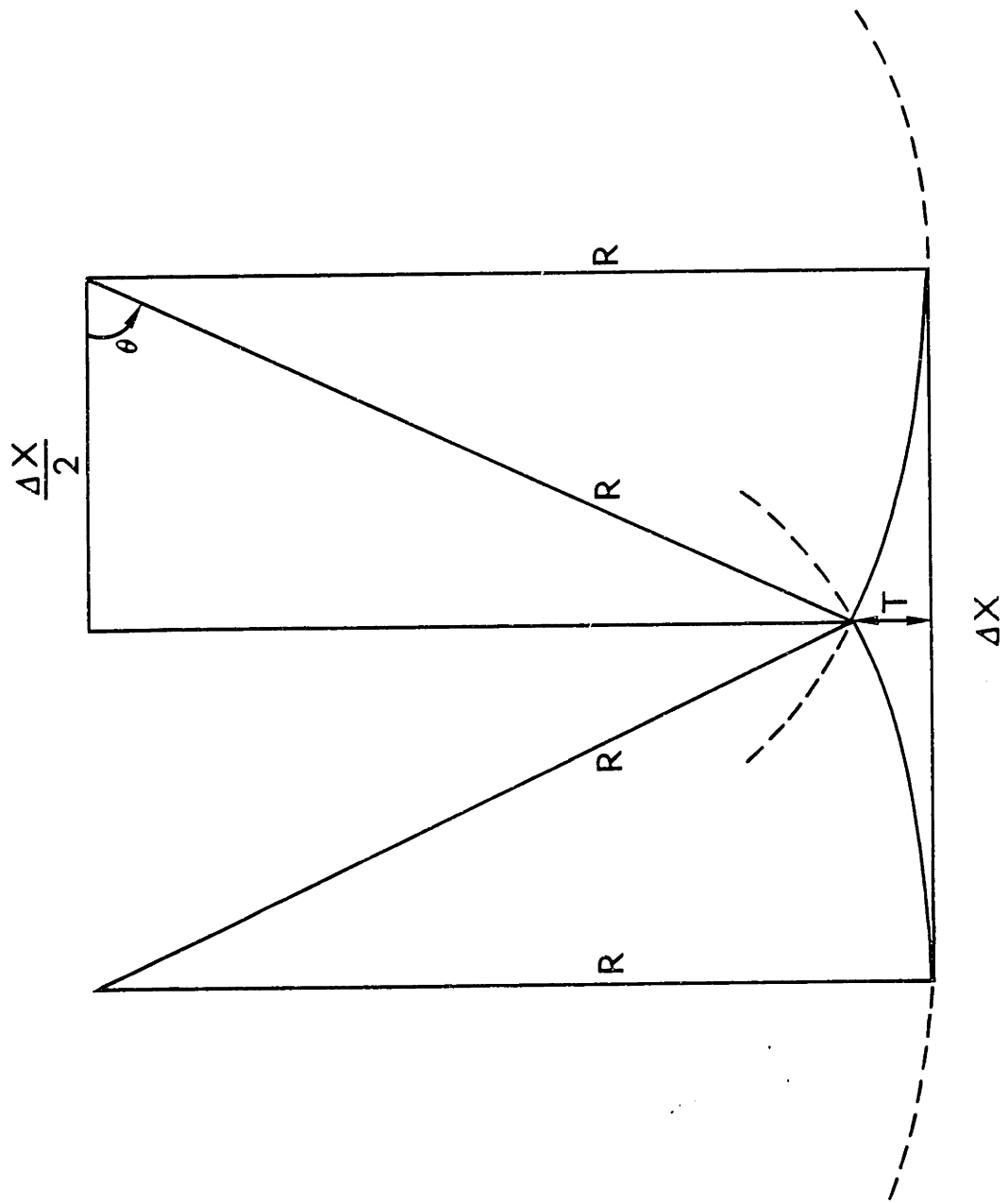


Figure 85. Error Between Cut Paths of a Ball End Mill

Expanding the square root and discarding higher order terms (since $R \gg \Delta x$):

$$T \approx R \left(1 - \left(1 - \frac{1}{2} \left(\frac{\Delta x}{2R} \right)^2 \right) \right)$$

$$\approx \frac{(\Delta x)^2}{8R}$$

$$\text{Or } \Delta x = \sqrt{8RT}$$

Thus, for a tolerance of 0.003 in., $\Delta x = 0.134$ in. In the actual machining, Δx --the distance between cuts--was reduced to 0.024 in. This was to take into account the tilting of the flat surface to 54.7° , and the fact that a series of sharp, periodic scallops may collectively cause constructive interference of reflected waves. The machine produces an rms surface tolerance of 0.003 in., but these errors are randomly distributed.

To determine the maximum number of points per cut, the cut was approximated as a circle, and an analysis similar to that above was used. Over its 14.3-in. maximum width, the subreflector bulges in the center by about 0.25 in. In Figure 86, these correspond to Δx and T_1 , respectively. If the arc (approximated as a circle) is divided into two segments of length Δx_2 , the error is T_2 . Now Δx_2 is greater than, but almost equal to, $\Delta x/2$. If the arc is divided into N segments, each cord Δx_N will be approximately $\Delta x_1/N$ in length. The error, T_N , will be an upper bound on the tolerance. The

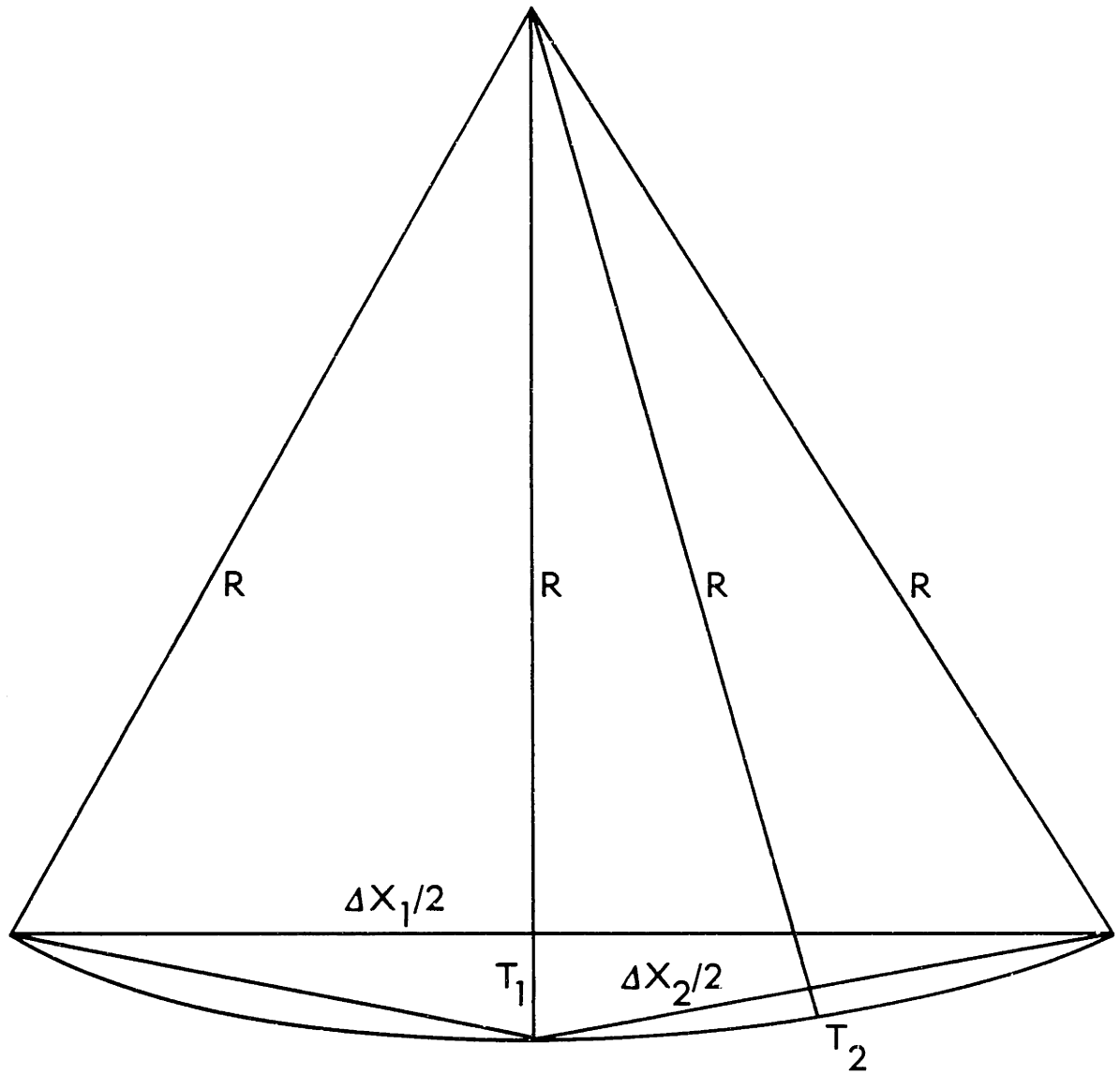


Figure 86. Error Between an Arc and a Straight Line

same formula as before applies, since this is simply the two-circle case shifted by half the separation distance.

$$\begin{aligned}\Delta x_N &\approx \frac{\Delta x_1}{N} \\ &= \sqrt{8RT_N} \quad , \\ \text{Or } N &= \frac{\Delta x_1}{\sqrt{8RT_N}} \quad .\end{aligned}$$

The value of R is determined by:

$$\begin{aligned}\Delta x_1 &= \sqrt{8RT_1} \quad , \\ \sqrt{8R} &= \frac{\Delta x_1}{\sqrt{T_1}} \quad .\end{aligned}$$

Substituting back,

$$N = \sqrt{\frac{T_1}{T_N}} \quad .$$

For $T_N = 0.003$, $N = 9.1$; or rounding up, $N = 10$. The actual number of points sampled per cut ($N + 1$) was 16. This accounts for any error resulting from approximating the arc with a circle, and minimizes the periodic effect.

High density styrofoam was the material used in fabricating the subreflector. Once machined, the surface was sealed to cover opened air cells, painted with a copper paint for conductivity, and painted with a layer of non-dispersive polyurethane paint for weather protection. Painted styrofoam was chosen over aluminum for several reasons, the primary

reason being the 10 to 1 speed advantage in machining styrofoam. Light weight, material availability, ease in precutting, and ease in sanding also favored the styrofoam.

The machine run time for the 13 runs was about 7 hours. A light sanding further improved the tolerance by removing the scallop peaks.

The main reflector, 39.1 in. in diameter, was cut out from a 6-ft surplus offset paraboloid with a 52-in. focal length and 11-in. offset height. The original dish consisted of flame-sprayed fiberglass. There was no observed distortion after cutting. This was checked using a template cut from an actual size computer plot.

The original paraboloid was specified as having a 0.015 in. rms surface tolerance. The actual figure is probably lower, since the section used comprises only one-quarter the area, and it is taken from the center of the reflector. This imperfection leads to a maximum drop in gain of 1.7 dB [92].

Several horn types were used as feeds. Preliminary alignment was performed using a 7λ pyramidal standard gain horn. More detailed measurements required conical horns with varying aperture diameters. All the conical horns have a 9° flare angle which was determined to be the optimum flare

from the range of aperture diameters [93]. These were electrofoamed on a slightly tapered aluminum mandril, with an oversized input guide. Two types of inserts, a standard circular waveguide fitting, and a Potter horn fitting, were designed and built to fit into the oversized horn openings.

The Potter horn design, with a step discontinuity before the output flare, was chosen because of its excellent linear polarizing feature. In the experimental testing, the transmitter is linearly polarized, so having a well matched feed approaches the most ideal case. Also, a linearly polarized feed allows more accurate cross-polarization measurements.

The relative positions of the components of the antenna system and their orientations are critical. Rough measurements were done by hand, but final alignment was performed electrically. This procedure is discussed in the next section.

APPENDIX V. PL 1 PROGRAMS TO GENERATE NUMERICALLY
CONTROLLED MILLING MACHINE INPUT TAPES,
AND SAMPLE RUN

```

10      0  PNT:PROC OPTIONS(MAIN);
/* CONSTANT DECLARATIONS
30      1  0  DCL X_STEPS          FLOAT(6) DEC INIT(32),
              Y_STEPS          FLOAT(6) DEC INIT(1),
              X_4              FLOAT(6) DEC INIT(1.2865),
              X_3              FLOAT(6) DEC INIT(-2.0985),
              X_2              FLOAT(6) DEC INIT(1.29129),
              X_1              FLOAT(6) DEC INIT(-2.649E-2),
              X_0              FLOAT(6) DEC INIT(7.066E-2),
              Y_2              FLOAT(6) DEC INIT(.7),
              R_XY             FLOAT(6) DEC INIT(.0492),
              D_X              FLOAT(6) DEC INIT(-.15),
              XX               FLOAT(6) DEC INIT(.5352),
              XY               FLOAT(6) DEC INIT(-.7071),
              XZ               FLOAT(6) DEC INIT(-.4621),
              YX               FLOAT(6) DEC INIT(.5352),
              YY               FLOAT(6) DEC INIT(.7071),
              YZ               FLOAT(6) DEC INIT(-.4621),
              ZX               FLOAT(6) DEC INIT(.6536),
              ZZ               FLOAT(6) DEC INIT(.7569),
              SCALE            FLOAT(6) DEC INIT(145.4),
/* VARIABLE DECLARATIONS
              LEVELS(*)        FIXED(15) BIN CTL,
              01 POINTS(*)     CTL,
              02 (X,Y,Z)       FIXED(15,11) BIN,
              (LX,LY,LZ)       FIXED(15,11) BIN,
              01 MID_POINT,
              02 (XM,YM,ZM)    FIXED(15,11) BIN,
              (D_Z,TEMP,R?,RR,
              X1,Y1,Z1,X2,
              Y2,Z2,TEMP2)     FLOAT(6) DEC,
              (I,J,K,L,M,N)    FIXED(31) BIN,
              (TABLE1,TABLE2)  FILE OUTPUT RECORD,
              SYSPRINT         FILE OUTPUT STREAM PRINT,
              (FLOOR, SORT, FIXED,
              CEIL, ABS)       RUTLTIN;

```

Portions of the text on the
following page(s) are not legible
in the original.

```

/* INITAIL SET UPS */
400 1 0 OPEN FILE(TARLE1);
410 1 0 OPEN FILE(TARLF2);
420 1 0 OPEN FILE(SYSPRINT) LINESIZE(132) PAGESIZE(55);
430 1 0 ON ENDPAGE(SYSPRINT) BEGIN;
440 2 0 PUT PAGE EDIT
(* # START START START END END END )(SKIP,A)
(* OF X Y Z X Y Z )(SKIP,A)
(*PNT )(SKIP,A);
450 2 0 PUT SKIP(2);
460 2 0 END;
500 1 0 X_4=X_4/(SCALE*SCALE*SCALE);
510 1 0 X_3=X_3/(SCALE*SCALE);
520 1 0 X_2=X_2/SCALE;
530 1 0 X_0=X_0*SCALE;
540 1 0 Y_2=Y_2/SCALE;
550 1 0 R_XY=R_XY*SCALE;
560 1 0 D_X=D_X*SCALE;
570 1 0 XX=-XX;
580 1 0 YX=-YX;
590 1 0 ZX=-ZX;
600 1 0 XZ=-XZ;
610 1 0 YZ=-YZ;
620 1 0 ZZ=-ZZ;
630 1 0 TEMP=R_XY-D_X;
640 1 0 D_Z=(((TEMP*X_4+X_3)*TEMP+X_2)*TEMP+X_1)*TEMP;
650 1 0 TEMP=-R_XY-D_X;
660 1 0 D_Z=-D_Z+(((TEMP*X_4+X_3)*TEMP+X_2)*TEMP+X_1)*TEMP)/2-X_0;
670 1 0 R2=R_XY*R_XY;
680 1 0 RR=R_XY+R_XY;
690 1 0 X_STEPS=RR/FLOOR(RR*X_STEPS);
/* MAKE SPACE FOR POINTS */
710 1 0 I=4*R2*Y_STEPS/X_STEPS;
720 1 0 ALLOCATE POINTS(I);
730 1 0 SIGNAL ENDPAGE(SYSPRINT);
740 1 0 I,M=0;
750 1 0 J=1;

```

```

770 1 0      DO X1=-R_XY TO R_XY BY X_STEPS:
          /* FIND RANGE OF Y AT GIVEN X VALUE */
790 1 1      TEMP2=SQRT(R2-X1*X1)*J;
          /* FIND NUMBER OF POINTS FOR Y NOT INCLUDING STARTING POINT */
910 1 1      K=J*CEIL(ARS(TEMP2+TEMP2)*Y_STEPS);
920 1 1      M=M+1;
930 1 1      LEVELS(M)=ARS(K)+1;
940 1 1      PUT SKIP EDIT(LEVELS(M))(F(3));
950 1 1      IF K=0 THEN DO L=0 TO K BY J;
          /* IF NOT THE FIRST OF LAST LEVEL */
970 1 2      Y1=-TEMP2+(TEMP2+TEMP2)*L/K;
980 1 2      I=I+1;
          /* FIND Z' */
990 1 2      TEMP=X1-D_X;
910 1 2      Z1=(((TEMP*X_4+X_3)*TEMP+X_2)*TEMP+X_1)*TEMP+X_0+
          Y1*Y1*Y_2+D_Z;
          /* FIND X", Y", & Z" */
940 1 2      X2=12-(X1*XX+Y1*XY+Z1*XZ+6);
950 1 2      Y2=12-(X1*YX+Y1*YY+Z1*YZ+6);
960 1 2      Z2= (X1*ZX+ Z1*ZZ+6);
          /* ROTATE AND CHANGE ORIGIN */
990 1 2      X(I)=FIXED(-Y2,15,11);
990 1 2      Y(I)=FIXED(X2-12,15,11);
1000 1 2      Z(I)=FIXED(Z2-12,15,11);
          /* IF FIRST OR LAST POINT THEN */
1020 1 2      IF L=0 | L=K THEN PUT EDIT(X(I),Y(I),Z(I))
          (3(X(2),F(7,3)));
1040 1 2      FND;
1050 1 1      ELSE DO;
          /* IF FIRST OR LAST LEVEL THEN */
1070 1 2      I=I+1;
          /* FIND Z' */
1090 1 2      TEMP=X1-D_X;
1100 1 2      Z1=(((TEMP*X_4+X_3)*TEMP+X_2)*TEMP+X_1)*TEMP+X_0+D_Z;
          /* FIND X", Y", & Z" */
1120 1 2      X2=12-(X1*XX+Z1*XZ+6);
1130 1 2      Y2=12-(X1*YX+Z1*YZ+6);
1140 1 2      Z2= (X1*ZX+Z1*ZZ+6);
          /* ROTATE AND CHANGE ORIGIN */
1160 1 2      X(I)=FIXED(-Y2,15,11);
1170 1 2      Y(I)=FIXED(X2-12,15,11);
1180 1 2      Z(I)=FIXED(Z2-12,15,11);
          /* PRINT START POINT WHICH = END POINT */
1200 1 2      PUT EDIT(X(I),Y(I),Z(I))(3(X(2),F(7,3)));
1210 1 2      FND;
          /* CHANGE DIRECTION TO CUT BACK NEXT TIME */
1230 1 1      J=-J;
1240 1 1      END;

```

Portions of the text on the
following page(s) are not legible
in the original.


```

/* STOP LISTING START END PAIRS */
1270 1 0 ON ENDPAGE(SYSPRINT) BEGIN;
1290 2 0 PUT PAGE EDIT('NUMBER LEVELS')(SKIP,A)
      ('OF POINTS')(SKIP,A);
1300 2 0 PUT SKIP(2);
1310 2 0 END;
1320 1 0 PUT PAGE EDIT('NUMBER OF POINTS = ',I)(A,F(9))
      ('NUMBER LEVELS')(SKIP(2),A)
      ('OF POINTS')(SKIP,A);
1350 1 0 J,K=1;
1360 1 0 DO WHILE(K<M);
1370 1 1 PUT SKIP EDIT(J,'')(X(3),F(2),A(4));
1380 1 1 L=11;
1390 1 1 DO WHILE(LEVELS(K)=J);
1400 1 2 IF L>127 THEN DO;
1410 1 3 PUT SKIP EDIT('')(A(13));
1420 1 3 L=14;
1430 1 3 END;
1440 1 2 PUT EDIT(K)(F(4));
1450 1 2 K=K+1;
1460 1 2 L=L+4;
1470 1 2 END;
1480 1 1 N=M;
1490 1 1 DO WHILE(LEVELS(M)=J);
1500 1 2 M=M-1;
1510 1 2 END;
1520 1 1 DO N=M+1 TO N;
1530 1 2 IF L>127 THEN DO;
1540 1 3 PUT SKIP EDIT('')(A(13));
1550 1 3 L=14;
1560 1 3 END;
1570 1 2 PUT EDIT(N)(F(4));
1580 1 2 L=L+4;
1590 1 2 END;
1600 1 1 J=J+1;
1610 1 1 END;

```

```

/* SPLIT INTO TWO CUTS AT THE LINE Y=-9 */
1640 1 0      LX=X(1);
1650 1 0      LY=Y(1);
1660 1 0      LZ=Z(1);
1670 1 0      DO J=1 TO I;
/* FOR EACH LINE BEING CUT BETWEEN TWO POINTS */
1690 1 1      IF LY>-9 THEN DO;
/* IF BOTH POINTS ARE ABOVE THE LINE THEN PUT THE NEXT POINT IN FIRST
      HALF */
1720 1 2      IF Y(J)>-9 THEN WRITE FILE(TABLE1) FROM(POINTS(J));
1730 1 2      ELSE DO;
/* IF GOING FROM ABOVE TO BELOW THEN PUT THE INTERSECT POINT BETWEEN
      BOTH LINES IN BOTH HALVES AND THE END POINT IN THE SECOND HALF */
1760 1 3      XM=(LX-X(J))/(LY-Y(J))*(-9-LY)+LX;
1770 1 3      YM=-9;
1780 1 2      ZM=(LZ-Z(J))/(LY-Y(J))*(-9-LY)+LZ;
1790 1 3      WRITE FILE(TABLE1) FROM(MID_POINT);
1800 1 3      XM=-8.875;
1810 1 3      YM=-12-((LX-X(J))/(LY-Y(J))*(-8.875-LY)+LX);
1820 1 3      ZM=(LZ-Z(J))/(LY-Y(J))*(-8.875-LY)+LZ;
1830 1 3      WRITE FILE(TABLE2) FROM(MID_POINT);
1840 1 3      XM=Y(J);
1850 1 3      YM=-12-X(J);
1860 1 3      ZM=Z(J);
1870 1 3      WRITE FILE(TABLE2) FROM(MID_POINT);
1890 1 2      END;
1900 1 2      FND;

1910 1 1      ELSE IF Y(J)<=-9 THEN DO;
/* IF BOTH POINTS ARE BELOW THE LINE THEN PUT THIS POINT IN THE SECOND
      HALF */
1940 1 2      XM=Y(J);
1950 1 2      YM=-12-X(J);
1960 1 2      ZM=Z(J);
1970 1 2      WRITE FILE(TABLE2) FROM(MID_POINT);
1980 1 2      FND;
1990 1 1      ELSE DO;
/* IF GOING FROM THE BELOW TO ABOVE THE LINE THEN PUT THE INTERSECT
      BETWEEN THE LINES IN BOTH HALVES AND PUT THE END POINT IN THE
      FIRST HALF */
2030 1 2      XM=(LX-X(J))/(LY-Y(J))*(-9-LY)+LX;
2040 1 2      YM=-9;
2050 1 2      ZM=(LZ-Z(J))/(LY-Y(J))*(-9-LY)+LZ;
2060 1 2      WRITE FILE(TABLE1) FROM(MID_POINT);
2070 1 2      WRITE FILE(TABLE1) FROM(POINTS(J));
2080 1 2      XM=-8.875;
2090 1 2      YM=-12-((LX-X(J))/(LY-Y(J))*(-8.875-LY)+LX);
2100 1 2      ZM=(LZ-Z(J))/(LY-Y(J))*(-8.875-LY)+LZ;
2110 1 2      WRITE FILE(TABLE2) FROM(MID_POINT);
2120 1 2      END;
/* THE LAST POINT IS NOW THIS POINT */
2140 1 1      LX=X(J);
2150 1 1      LY=Y(J);
2160 1 1      LZ=Z(J);
2170 1 1      END;
2180 1 0      FND;

```

```

000 0 0 OUT:PROC OPTIONS(MAIN);
010 1 0 /* VARIABLE AND FILE DECLARATIONS */
020 1 0 DCL TABLE FILE INPUT RECORD,
030 1 0 DISK FILE OUTPUT RECORD,
040 1 0 O1 POINTS(51),
050 1 0 O2 (X,Y,Z) FIXED(15,11) BIN,
060 1 0 (LX,LY) FIXED(15,11) BIN,
070 1 0 OUT_BUFF CHAR(80) BASED(OUT),
080 1 0 OUT POINTER,
090 1 0 SUBSTR BUILTIN,
100 1 0 EOF BIT(1) INIT('0'B),
110 1 0 (I,J,K,L,M) FIXED(15) BIN;
120 1 0 /* INITAIL SET UPS */
140 1 0 OPEN FILE(TABLE);
150 1 0 OPEN FILE(DISK);
160 1 0 ON ENDFILE(TABLE) EOF='1'R;
170 1 0 L,I=1;
180 1 0 READ FILE(TABLE) INTO(POINTS(I));
190 1 0 DO WHILE(-EOF);
200 1 0 /* PUT HEADING ON EACH JOB OF UP TO 500 POINTS */
210 1 1 LOCATE OUT_BUFF FILE(DISK);
220 1 1 OUT_BUFF='TMACHIN,POSTOMATICNC4*';
230 1 1 LOCATE OUT_BUFF FILE(DISK);
240 1 1 PUT STRING(OUT_BUFF) EDIT('IDENT,ROLL',L,'*')(A,P'Z9',A);
250 1 1 LOCATE OUT_BUFF FILE(DISK);
260 1 1 OUT_BUFF='SETUP,CMD01/1,M0015,7000RPM,LY,LX,LZ, ';
270 1 1 LOCATE OUT_BUFF FILE(DISK);
280 1 1 OUT_BUFF='LIMIT(X-12/0,Y-12/0,Z-12/0)*';
290 1 1 LOCATE OUT_BUFF FILE(DISK);
300 1 1 OUT_BUFF='BASE,XR,YR,ZR*';
310 1 1 LOCATE OUT_BUFF FILE(DISK);
320 1 1 OUT_BUFF='MTCHG,TOPL1,0GL,.750TD,2000RPM,50IPM,CON,DWELL6*';
330 1 1 IF L>1 THEN DO;
340 1 2 /* IF NOT FIRST ROLL MOVE TO WERE YOU LEFT OFF */
350 1 2 LOCATE OUT_BUFF FILE(DISK);
360 1 2 PUT STRING(OUT_BUFF) EDIT('DPT1.',LX,'XR,',LY,'YR,ZB*')
370 1 2 (A,2(P'S99.V999',A));
380 1 2 LOCATE OUT_BUFF FILE(DISK);
390 1 2 OUT_BUFF='MOVE,PTI*';
400 1 2 END;
410 1 1 L=L+1;
420 1 1 M=0;

```

```

460 1 1 DO WHILE(M<500 & ~EOF);
/* READ IN A LEVEL */
465 1 2 DO WHILE(~EOF & I<50);
470 1 3 I=I+1;
480 1 3 READ FILE(TABLE) INTO(POINTS(I));
490 1 3 END;
500 1 2 M=M+I;
/* DEFINE EACH POINT IN THE LEVEL */
510 1 2 DO J=1 TO I;
520 1 3 LOCATE OUT_BUFF FILE(DISK);
530 1 3 PUT STRING(OUT_BUFF) EDIT('DPT',J,',',X(J),'XB,',Y(J),
'YB.',Z(J),'ZB*')(A,P'Z9',A,3(P'S99.V999',A));
540 1 3 END;
/* PUT THE CUT STATEMENT IN TO CUT THE LEVEL */
550 1 2 LOCATE OUT_BUFF FILE(DISK);
560 1 2 SUBSTR(OUT_BUFF,1,7)='CUT,PT1';
570 1 2 J=9;
580 1 2 DO K=2 TO I;
590 1 3 IF J>74 THEN DO;
600 1 4 SUBSTR(OUT_BUFF,J,1)='*';
610 1 4 LOCATE OUT_BUFF FILE(DISK);
620 1 4 J=1;
630 1 4 END;
640 1 3 PUT STRING(SUBSTR(OUT_BUFF,J,5)) EDIT(';PT',K)(A,P'Z9');
650 1 3 J=J+5;
660 1 2 END;
/* END THE CUT */
670 1 2 SUBSTR(OUT_BUFF,J,1)='*';
680 1 2 IF M>=500 | EOF THEN DO;
/* IF THE END OF A TAPE MOVE TO THE TOP */
690 1 3 LOCATE OUT_BUFF FILE(DISK);
700 1 3 LX=X(I-1);
710 1 3 LY=Y(I-1);
720 1 3 PUT STRING(OUT_BUFF) EDIT('DPT1,',LX,'XB,',LY,'YB,ZB*')
(A,?(P'S99.V999',A));
730 1 3 LOCATE OUT_BUFF FILE(DISK);
740 1 3 OUT_BUFF='MOVE,PT1';
750 1 3 POINTS(1)=POINTS(I);
760 1 3 I=1;
770 1 3 END;
780 1 2 ELSE I=0;
790 1 2 END;
/* MARK THE END OF A POLL */
800 1 1 LOCATE OUT_BUFF FILE(DISK);
810 1 1 OUT_BUFF='END/';
820 1 1 END;
830 1 0 CLOSE FILE(TABLE);
840 1 0 CLOSE FILE(DISK);
850 1 0 END;

```

TMACHIN,BOSTOMATICCNC4*
 IDENT,ROLL 1*
 SETUP,CMOD 1/1,MOD15,7000RPM,LY,LX,LZ,
 LIMIT(X-12/0,Y-12/0,Z-12/0)*
 BASE,XB,YB,ZB*
 MTCBG,TOOL 1,0GL,-.750TD,2000RPM,50IPM,CON,DWELL6*
 DPT 1,-02.869XB,-09.000YB,-00.080ZB*
 DPT 2,-02.473XB,-08.580YB,-00.102ZB*
 DPT 3,-02.893XB,-09.000YB,-00.101ZB*
 DPT 4,-02.922XB,-09.000YB,-00.125ZB*
 DPT 5,-02.291XB,-08.372YB,-00.128ZB*
 DPT 6,-02.155XB,-08.209YB,-00.155ZB*
 DPT 7,-02.702XB,-08.751YB,-00.150ZB*
 DPT 8,-02.950XB,-09.000YB,-00.150ZB*
 DPT 9,-02.979XB,-09.000YB,-00.175ZB*
 DPT10,-02.675XB,-08.696YB,-00.175ZB*
 DPT11,-02.043XB,-08.071YB,-00.181ZB*
 DPT12,-01.946XB,-07.948YB,-00.207ZB*
 DPT13,-02.652XB,-08.645YB,-00.200ZB*
 DPT14,-03.007XB,-09.000YB,-00.200ZB*
 DPT15,-03.036XB,-09.000YB,-00.224ZB*
 DPT16,-03.018XB,-08.981YB,-00.224ZB*
 DPT17,-02.440XB,-08.407YB,-00.226ZB*
 DPT18,-01.860XB,-07.835YB,-00.233ZB*
 DPT19,-01.783XB,-07.731YB,-00.259ZB*
 DPT20,-02.409XB,-08.347YB,-00.251ZB*
 DPT21,-03.032XB,-08.967YB,-00.248ZB*
 DPT22,-03.064XB,-09.000YB,-00.248ZB*
 DPT23,-03.092XB,-09.000YB,-00.273ZB*
 DPT24,-03.046XB,-08.953YB,-00.273ZB*
 DPT25,-02.381XB,-08.291YB,-00.276ZB*
 DPT26,-01.711XB,-07.633YB,-00.286ZB*
 DPT27,-01.646XB,-07.541YB,-00.312ZB*
 DPT28,-02.355XB,-08.237YB,-00.301ZB*
 DPT29,-03.061XB,-08.938YB,-00.297ZB*
 DPT30,-03.122XB,-09.000YB,-00.297ZB*
 DPT31,-03.149XB,-09.000YB,-00.323ZB*
 DPT32,-02.778XB,-08.628YB,-00.323ZB*
 DPT33,-02.183XB,-08.040YB,-00.328ZB*
 DPT34,-01.585XB,-07.454YB,-00.338ZB*
 DPT35,-01.527XB,-07.370YB,-00.364ZB*
 DPT36,-02.155XB,-07.983YB,-00.353ZB*
 DPT37,-02.778XB,-08.600YB,-00.348ZB*
 DPT38,-03.178XB,-09.000YB,-00.348ZB*
 DPT39,-03.206XB,-09.000YB,-00.372ZB*
 DPT40,-02.779XB,-08.572YB,-00.372ZB*
 DPT41,-02.128XB,-07.929YB,-00.378ZB*
 DPT42,-01.474XB,-07.290YB,-00.391ZB*
 DPT43,-01.423XB,-07.212YB,-00.416ZB*
 DPT44,-02.104XB,-07.977YB,-00.403ZB*
 DPT45,-02.780XB,-08.545YB,-00.397ZB*
 DPT46,-03.234XB,-09.000YB,-00.397ZB*
 DPT47,-03.263XB,-09.000YB,-00.421ZB*
 DPT48,-02.782XB,-08.519YB,-00.421ZB*
 DPT49,-02.081XB,-07.826YB,-00.429ZB*

Portions of the text on the
following page(s) are not legible
in the original.

DPT50,-01.375XB,-07.137YB,-00.443ZB*
CUT,PT1;PT 2;PT 3;PT 4;PT 5;PT 6;PT 7;PT 8;PT 9;PT10;PT11;PT12;PT13;PT14;PT15*
;PT16;PT17;PT18;PT19;PT20;PT21;PT22;PT23;PT24;PT25;PT26;PT27;PT28;PT29;PT30*
;PT31;PT32;PT33;PT34;PT35;PT36;PT37;PT38;PT39;PT40;PT41;PT42;PT43;PT44;PT45*
;PT46;PT47;PT48;PT49;PT50*

·
·
·

DPT1,-03.005XB,-06.896YB,ZB*
MOVE,PT1*
END/

VI. TEST MEASUREMENTS

A. Experimental Setup

All measurements of the offset bifocal scale model were performed at the outdoor antenna range at COMSAT Laboratories. The model was fixed to a Scientific Atlanta three-axis mount at a corner of the roof of the main building. The transmitter, mounted on an 8-meter tower 800 meters from the building, consists of a signal generator, precision attenuator, and a 0.5-meter circular prime focus paraboloidal reflector mounted on a polarization rotating plate.

This range was chosen over the more environmentally controlled anechoic chamber, because the minimum range length, as determined by the $2D^2/\lambda$ far-field condition, is approximately 250 meters. Thus, many sources of error were present in the experiment. Wind--even as slow as 5 mph--had a noticeable effect. Movements on the roof or at the transmitting tower also caused vibrations which produced non-negligible phase differences at 36 GHz. Reflections off the corner of the building, off the field and road between transmitter and receiver, and off trees near the transmitter have unknown effects. Rain caused so much signal attenuation that measurements could not be made in inclement weather.

The test mount is precision remotely controlled. Only one of the three axes can be varied at a time. The lower azimuth table was altered only once, at the beginning of the experiment, so that when the upper azimuth and elevation positioners are set to zero, the antenna points directly at the transmitter. The upper azimuth and elevation controls also control the horizontal chart paper motion. Vertical pen motion is determined by the output from a dual channel receiver.

The receiver is configured with one input as a reference, receiving a signal from a fixed 0.5-meter paraboloid, the other input being the antenna model under test. The reference channel provides a steady signal for phase locking. This prevents the receiver from losing lock when the test antenna is oriented with a null pointing to the transmitter.

The receiver was tuned to the tenth harmonic of the fundamental 3.6 GHz. Thus the available dynamic range was fairly low. Amplifiers were not available at 36 GHz, so the useful power range was limited to a minimum gain of about 15 dB. With peak gains of the order of 45 dB, this precluded resolution below 30 dB down. Only the first two or three sidelobes could be accurately measured.

For each beam measured, it is necessary to find the orientation of the beam peak. This is accomplished by iteratively maximizing the azimuth and elevation adjustments in turn until the same peak value is reached for each. At this point, the two patterns are the principal plane cuts of the beam.

Gain measurements were made using calibrated standard gain horn reference. The receiver linearity was checked by adjusting the precision attenuator at the transmitter. Thus, measured values of gain could be determined from the relative position of the test antenna to the known value of the standard gain horn.

B. Experimental Results

Despite many difficulties in performing measurements of the scale model, reasonably good agreement was found between computed and experimental results. The experimental procedure was very cautious and methodical, similar to reported techniques used with scanning and offset reflectors [94]-[96]. Because the frequency used was 36 GHz, tolerance of the order 0.01 in. became important. Alignment of the main reflector, subreflector, and feed was accomplished first by mechanical measurement, and then by electrical tuning.

First, the main reflector was positioned and tested independently. With the model configured as a prime focus antenna, azimuth and elevation patterns were generated. Since the focal length of the parent paraboloid was known, a template could be used for rough mechanical measurements. Following these, the feed was adjusted in and out at various heights to completely characterize the focal region. This served two purposes: it verified the performance of the main reflector by providing gain and sidelobe information, and also precisely determined the main reflector's focal point. Although knowledge of this focal point is more useful when measuring true Cassegrains, it nonetheless fixes an absolute reference point for the system. This point, because it is determined electrically, is more accurate a reference than any mechanically determined points. Figure 87 depicts the prime focus setup.

Once the main reflector was aligned, the feed fixture was repositioned behind it--in the focal region of the bifocal--and the subreflector was installed. Again, a template, based on actual size computer plotted curves, was used for rough alignment. This template also confirmed the shape of the milled subreflector. The feed was aligned using rules and bubble level indicators. Originally, it was positioned at the on-axis "focus" to check the resulting beam direction.

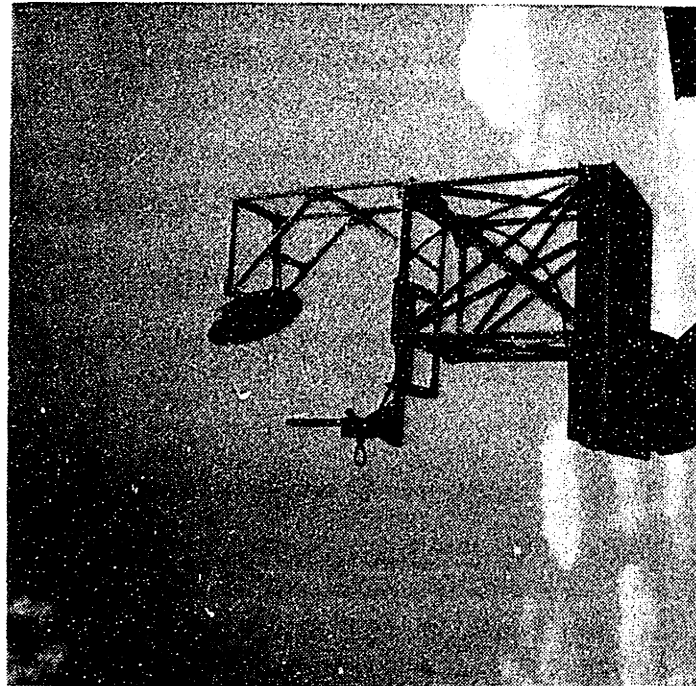
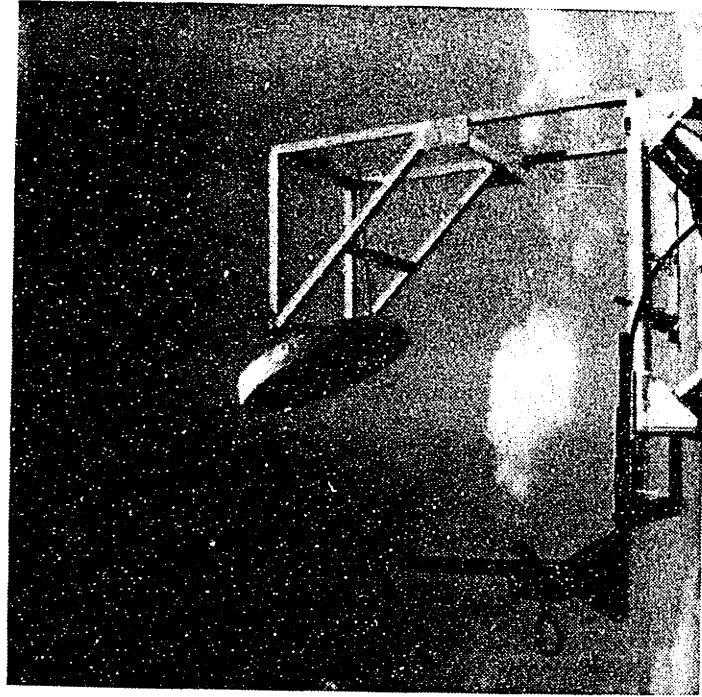


Figure 87. Prime Focus Configuration Test

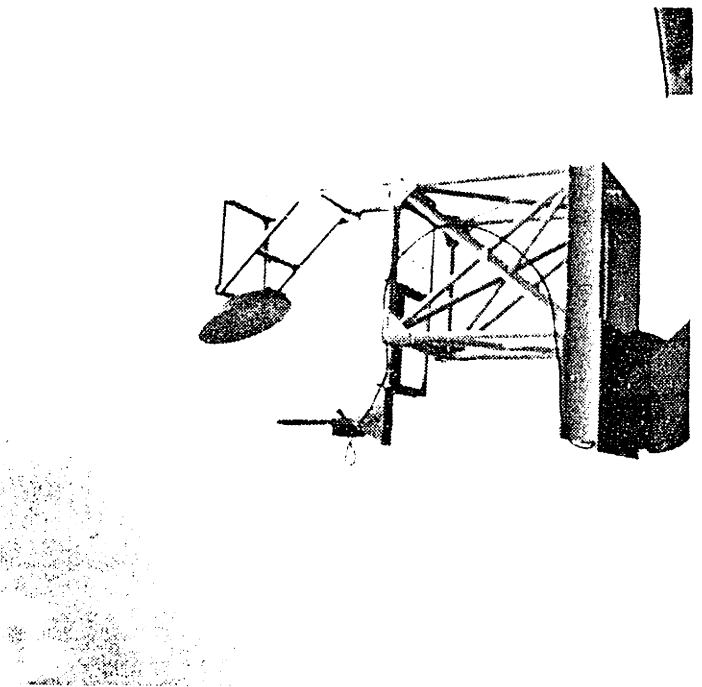
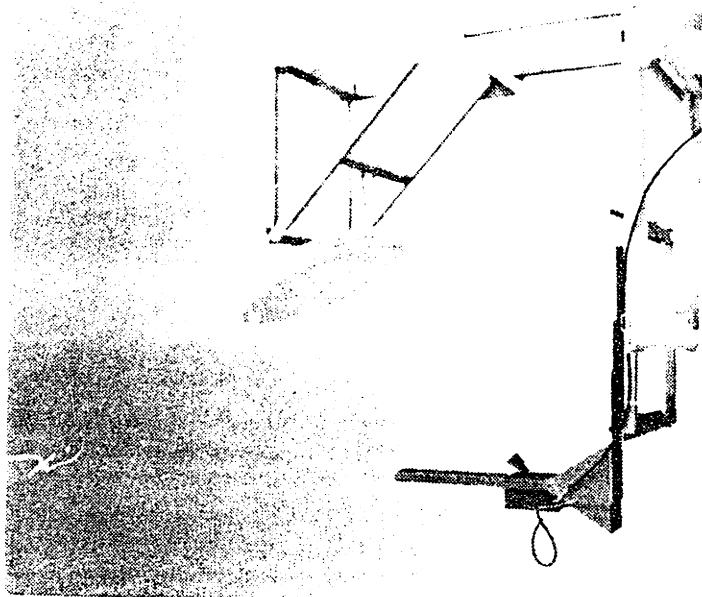


Figure 87. Prime Focus Configuration Test

The subreflector was then adjusted in small increments in both elevation rotation and axial position until maximum gain and proper beam direction was found. Then the feed was moved to the scan positions to verify the subreflector position. Again this reflector was adjusted for maximum performance. Figures 88 through 90 show the final configurations.

Although this was a very tedious process, convergence to the optimum arrangement was rather fast. The measured patterns at this point agree very closely with those generated by computer. Figure 91 represents the computed elevation cut patterns for a 7λ pyramidal horn feeding the bifocal for -8° , 0° , and $+8^\circ$. Figure 92 is an expanded and reversed version of the central beam, which is plotted on scales which are in the same proportion as those of the chart recorder paper.

Measured results are shown in Figures 93 through 125. The measured patterns all have both azimuth and elevation cuts through the peak gain point on the same set of axes. It is important to notice that for the high resolution chart paper used, the horizontal (angle) scale only extends to $\pm 5^\circ$ before repeating. A beam at 7.5° appears at -2.5° . Thus, all beams scanned more than 5° are 10° from the indicated position. These measurements are intended to indicate beam shape rather than position.

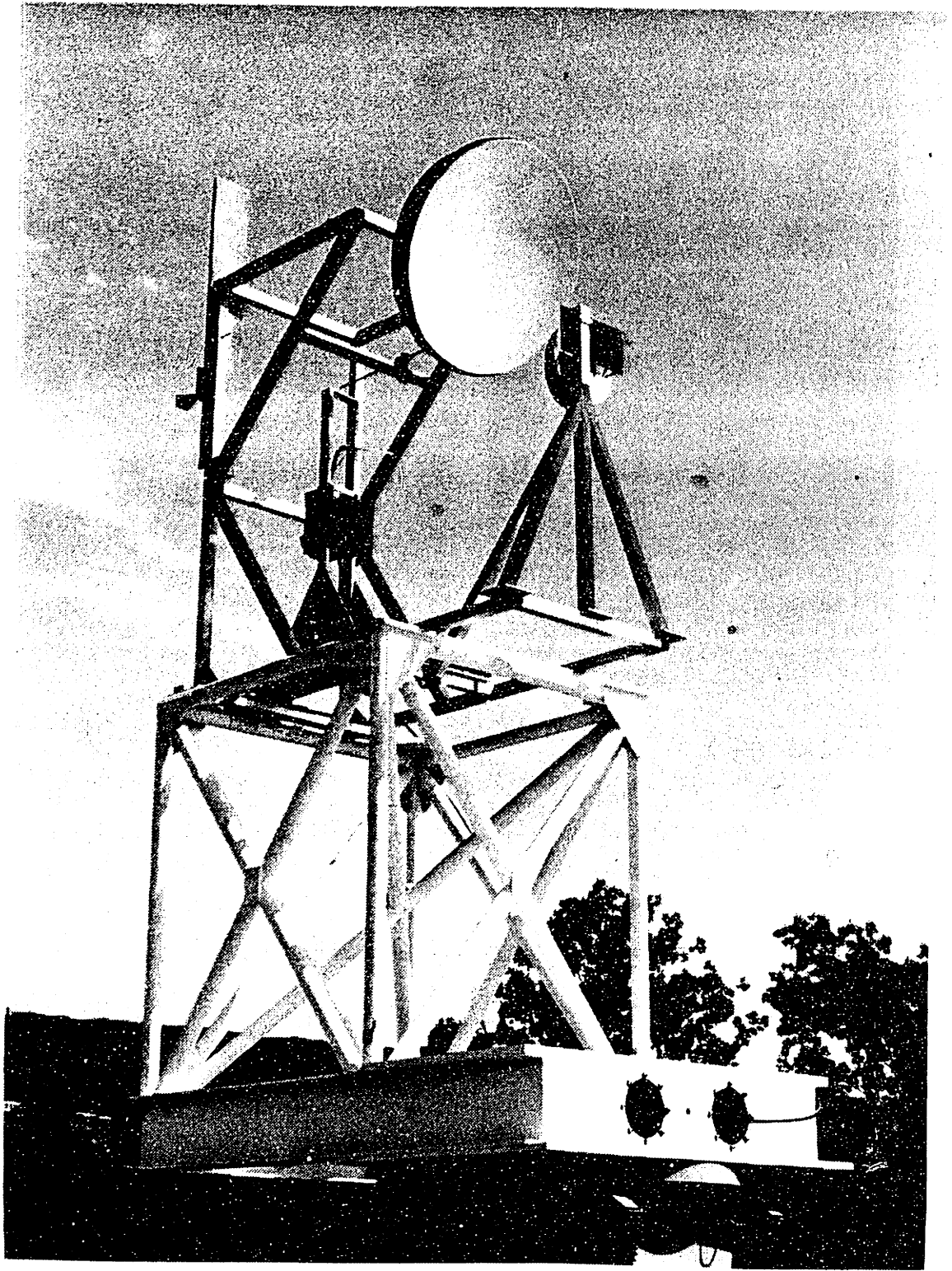


Figure 88. The Offset Bifocal Antenna--View 1

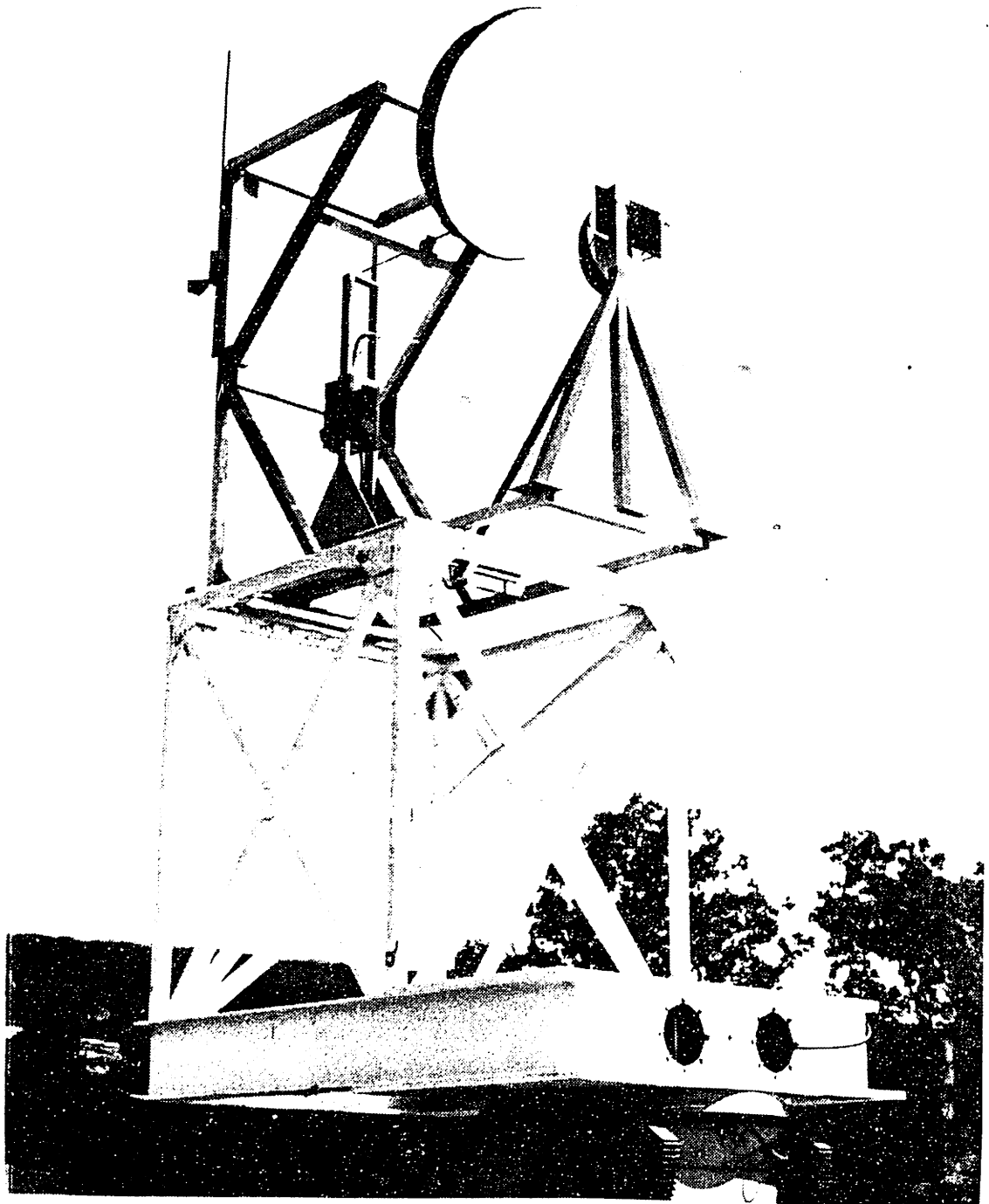


Figure 88. The Offset Bifocal Antenna--View 1

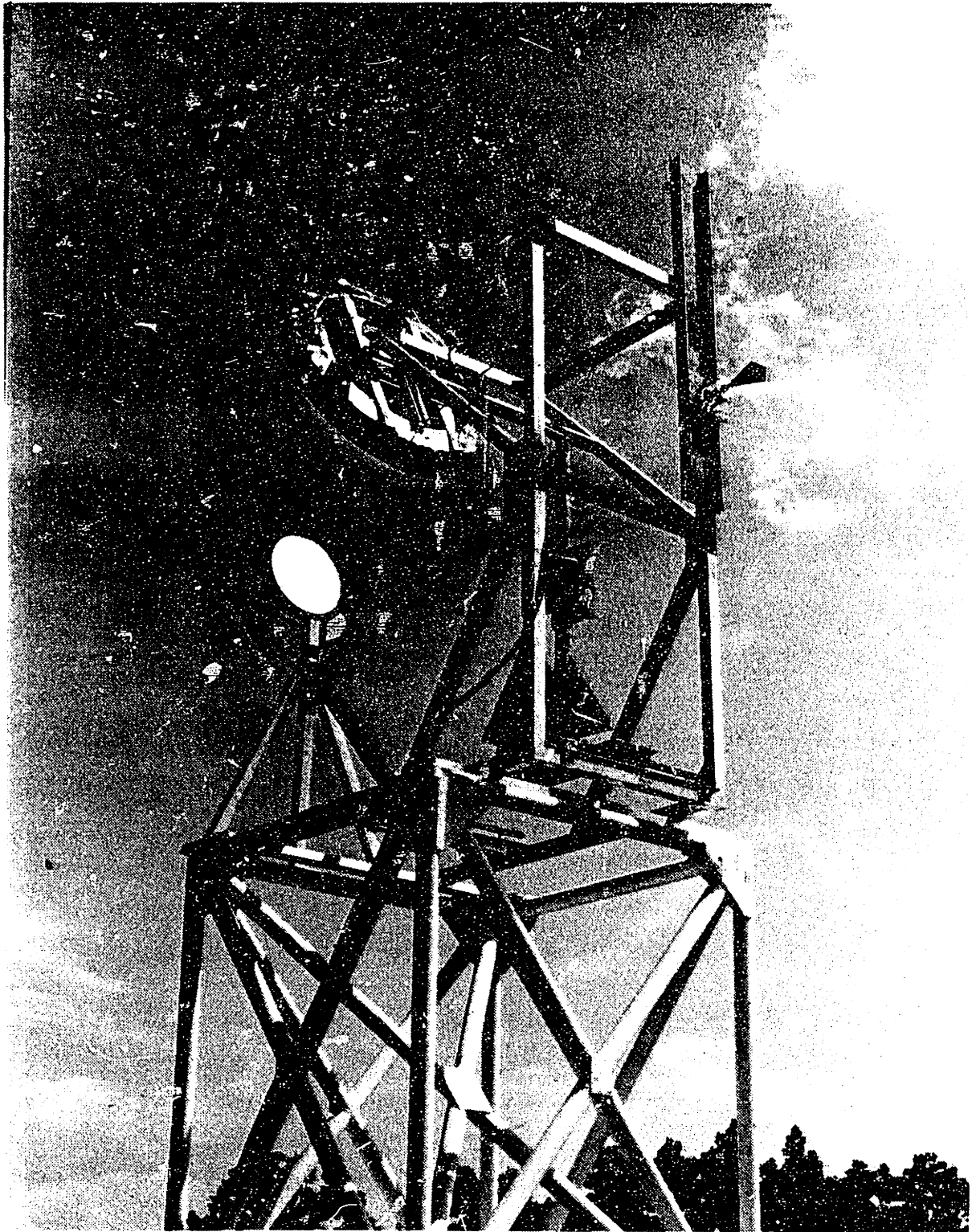


Figure 89. The Offset Bifocal Antenna--View 2

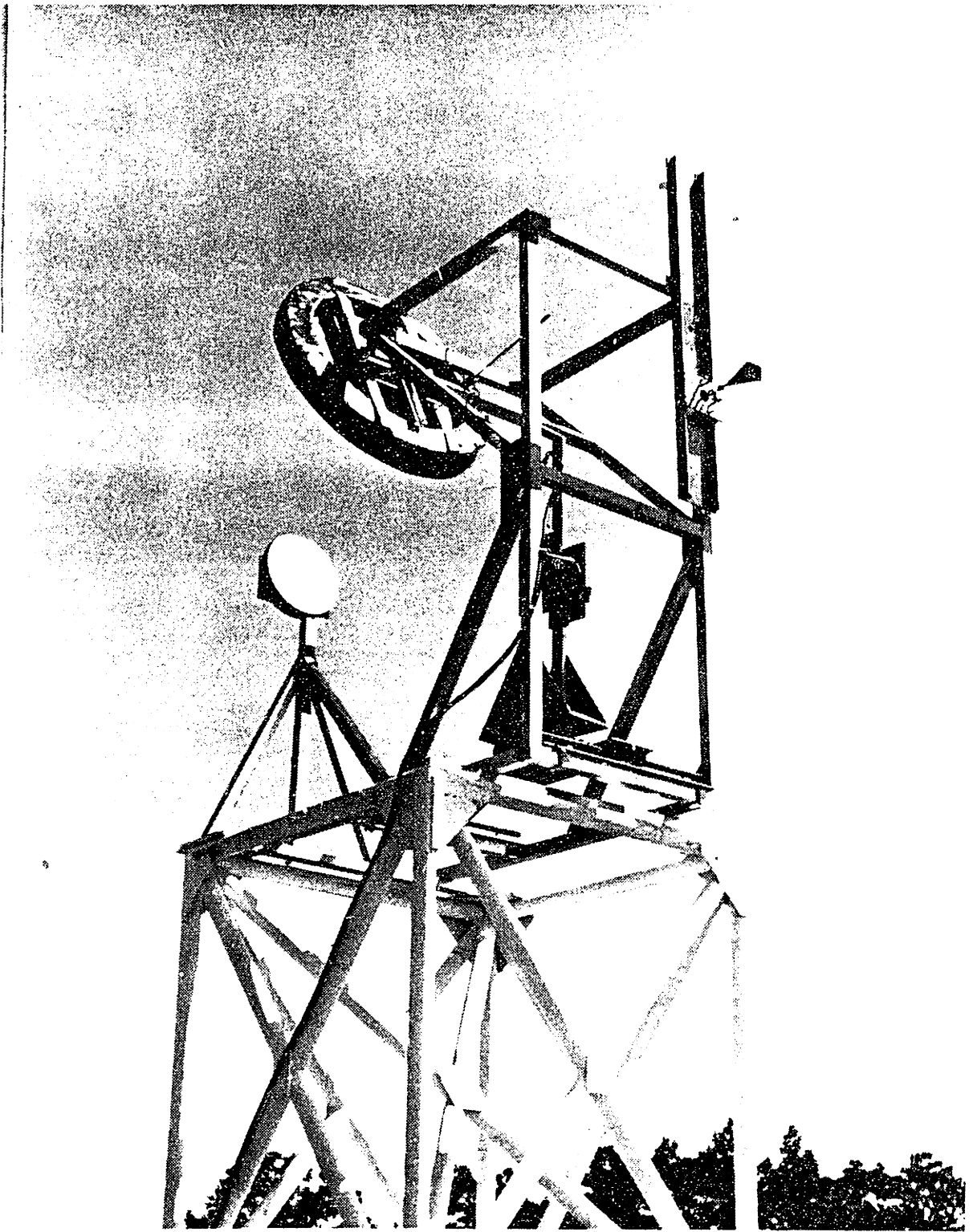


Figure 89. The Offset Bifocal Antenna--View 2

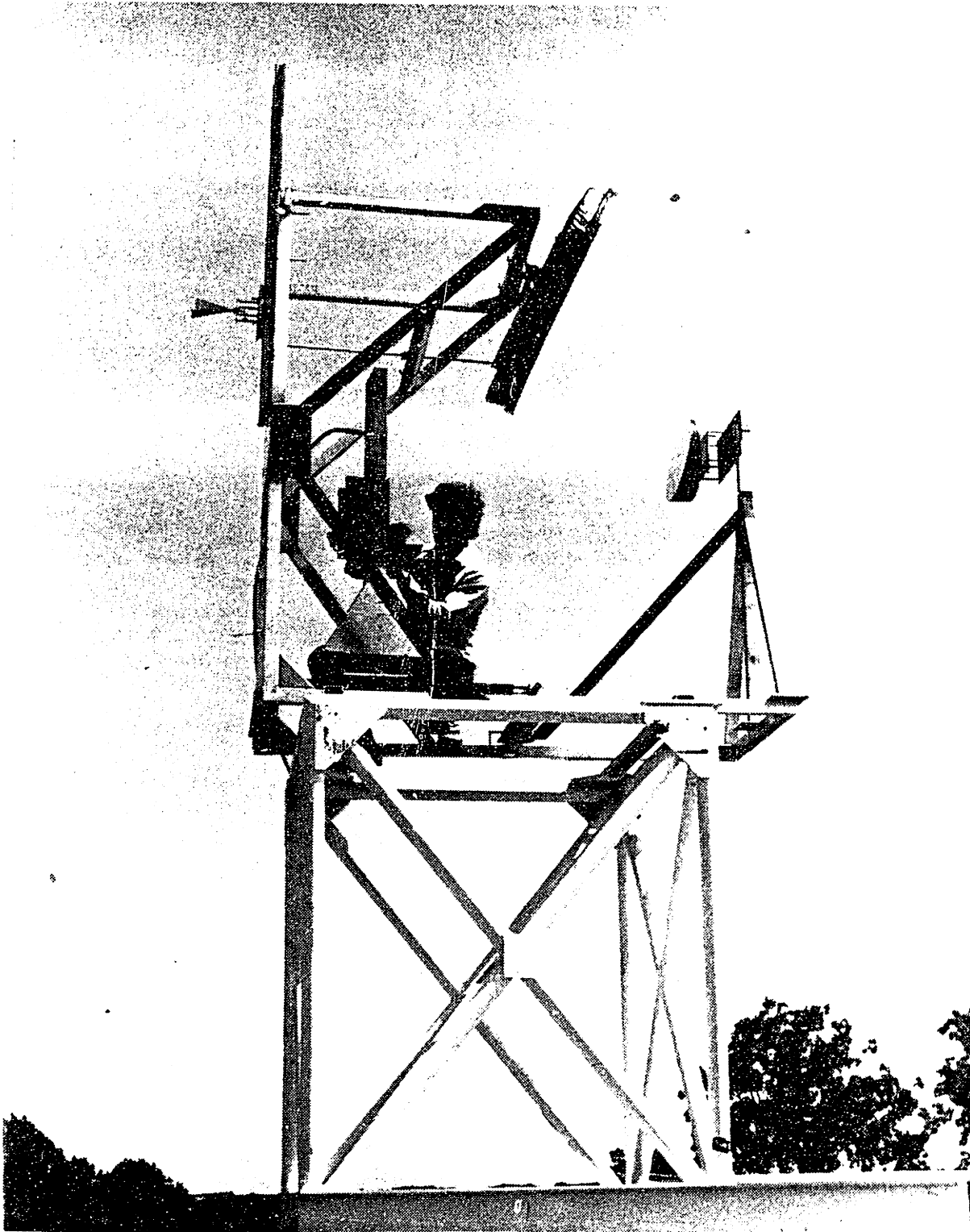


Figure 90. Author Making Adjustments on Test Antenna



Figure 90. Author Making Adjustments on Test Antenna

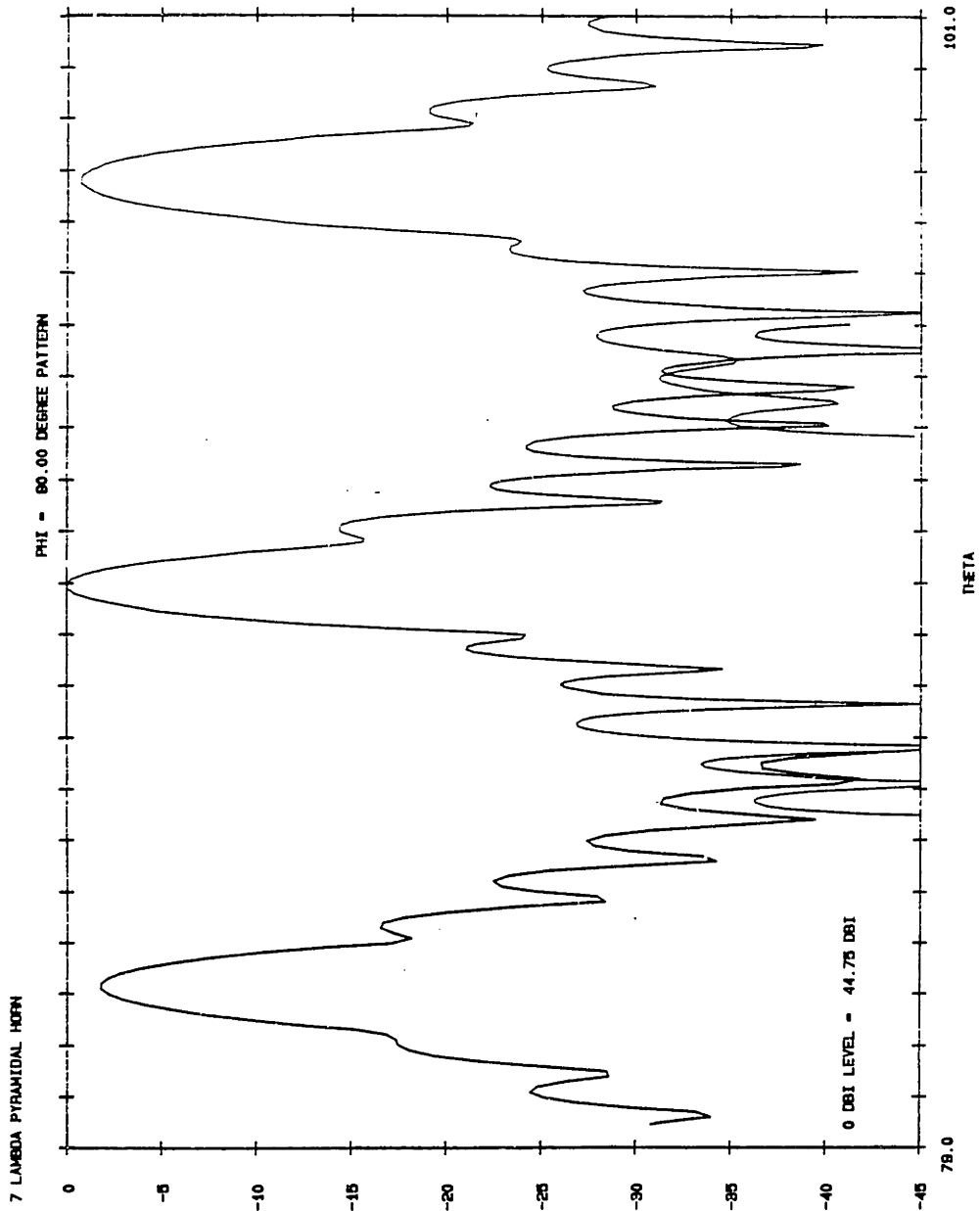


Figure 91. Computed Elevation Scan Patterns
for 7λ Pyramidal Horn Feed

COMPUTED ON AXIS ELEVATION CUT

PHI = 90.00 DEGREE PATTERN

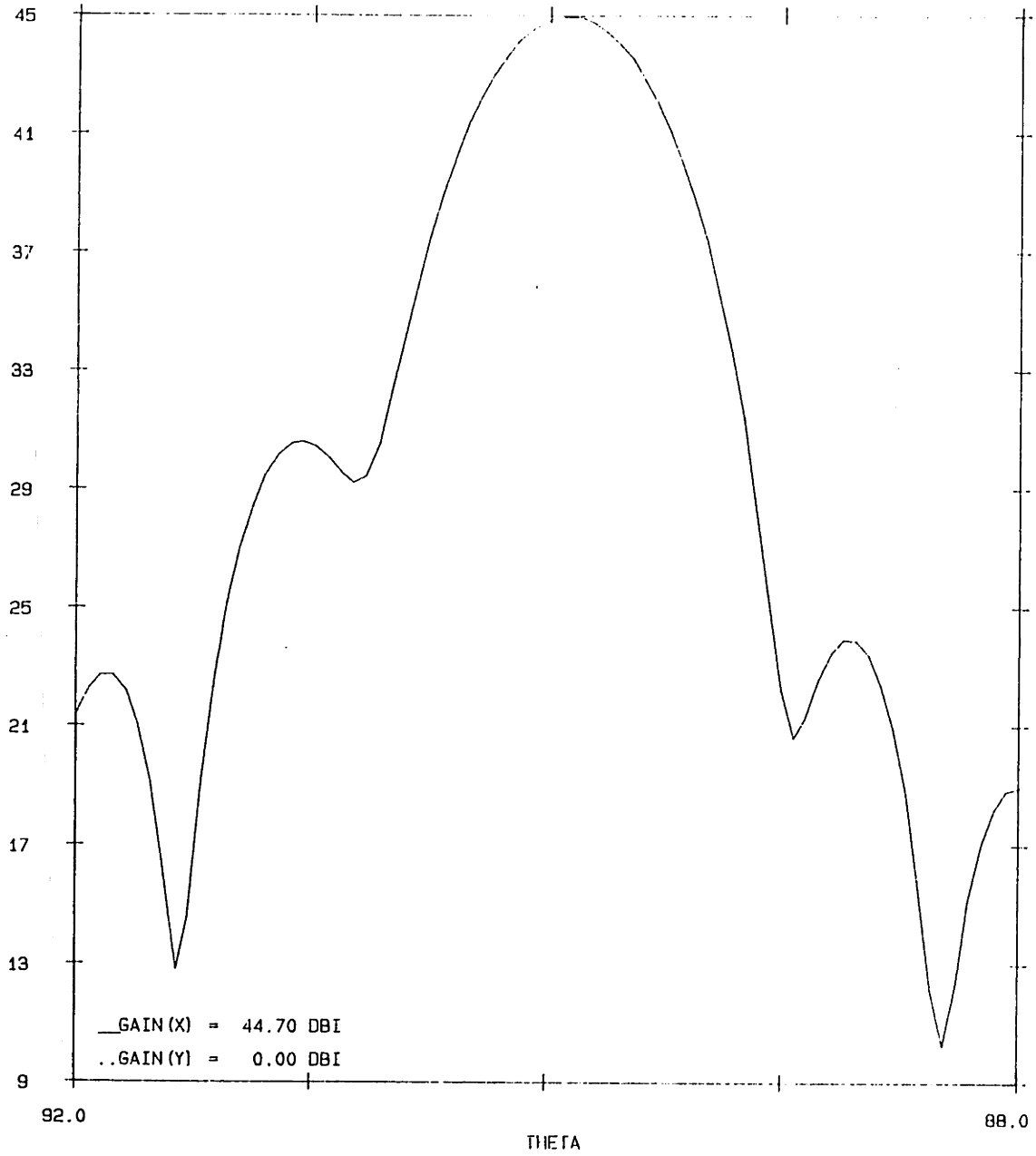


Figure 92. Detail of Unscanned Beam Using 7λ Pyramidal Horn

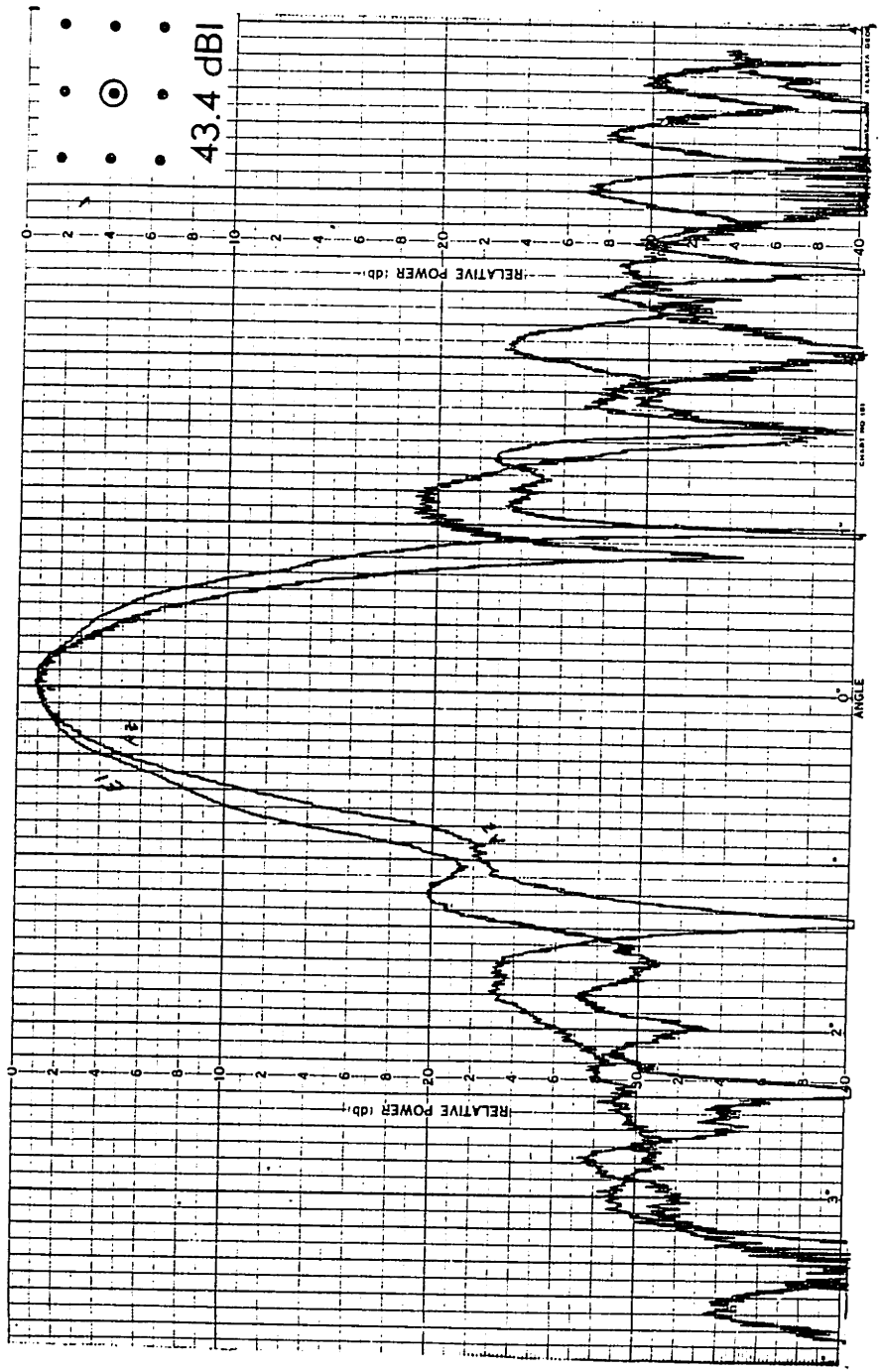


Figure 93. Measured Unscanned Beam, 7λ Pyramidal Horn

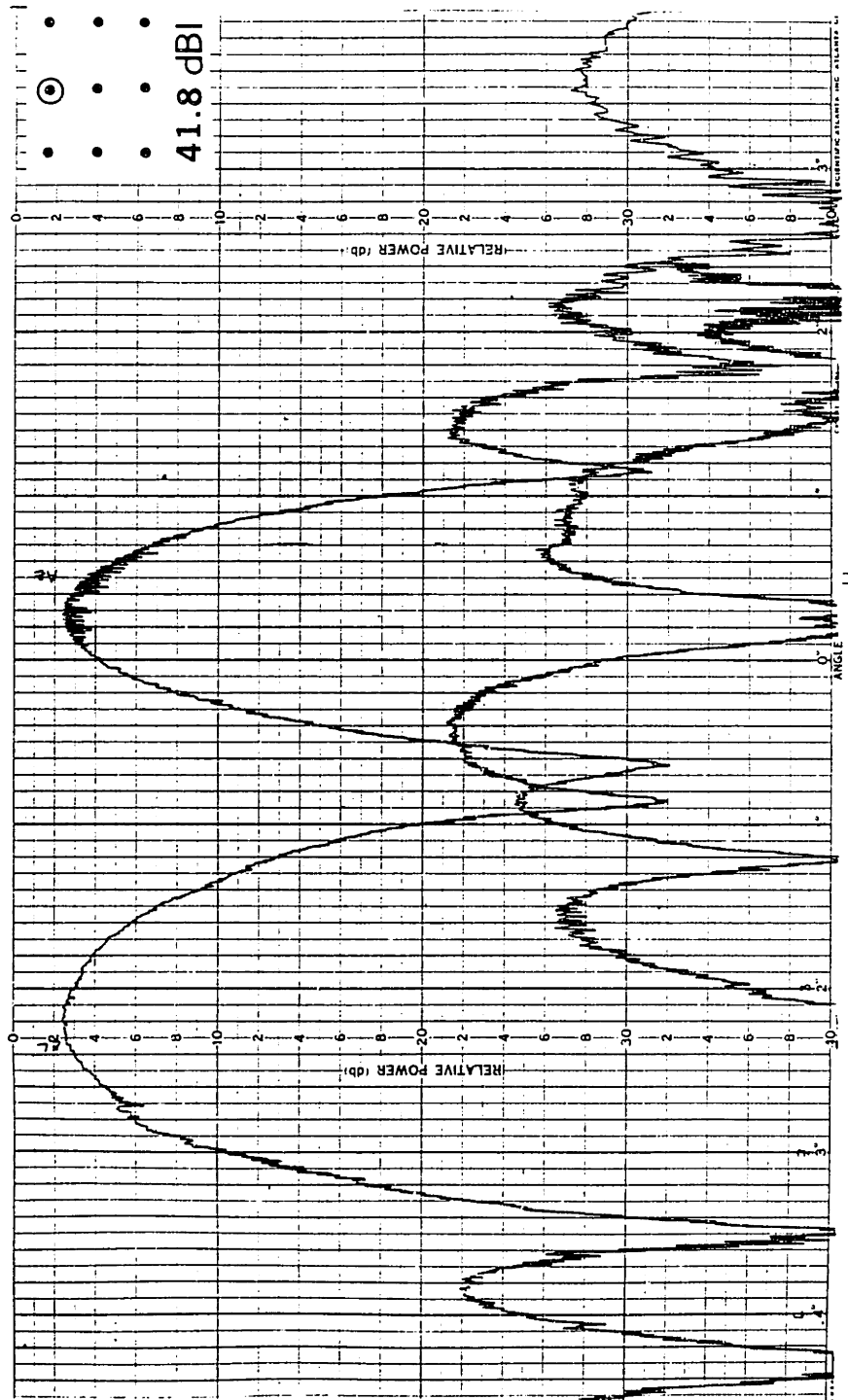


Figure 95. 7λ Pyramidal Horn (0.3° , 7.8°)

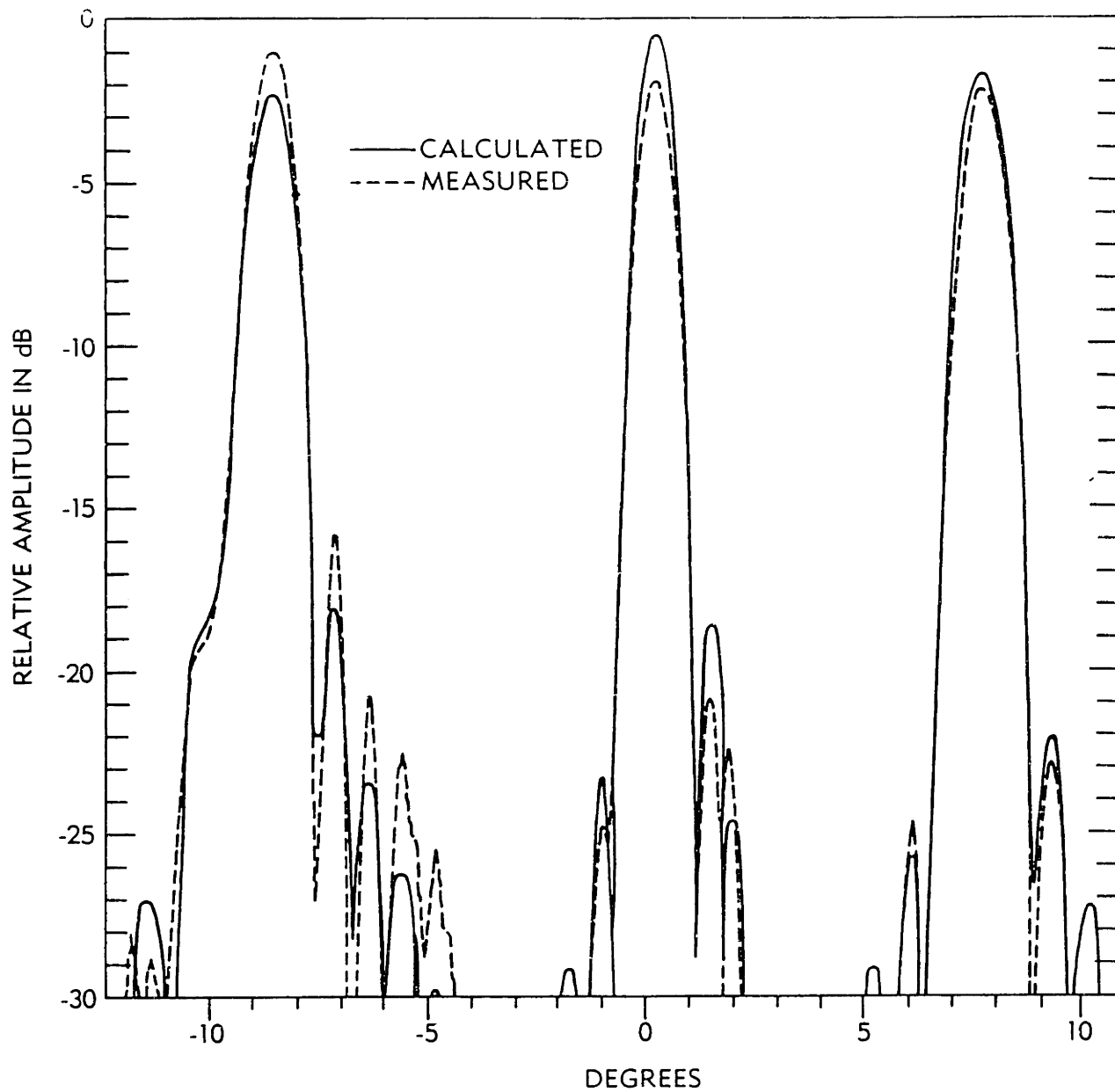


Figure 96. Computed versus Measured Performance with 7λ Pyramidal Horn: -8° , 0° , and $+8^\circ$

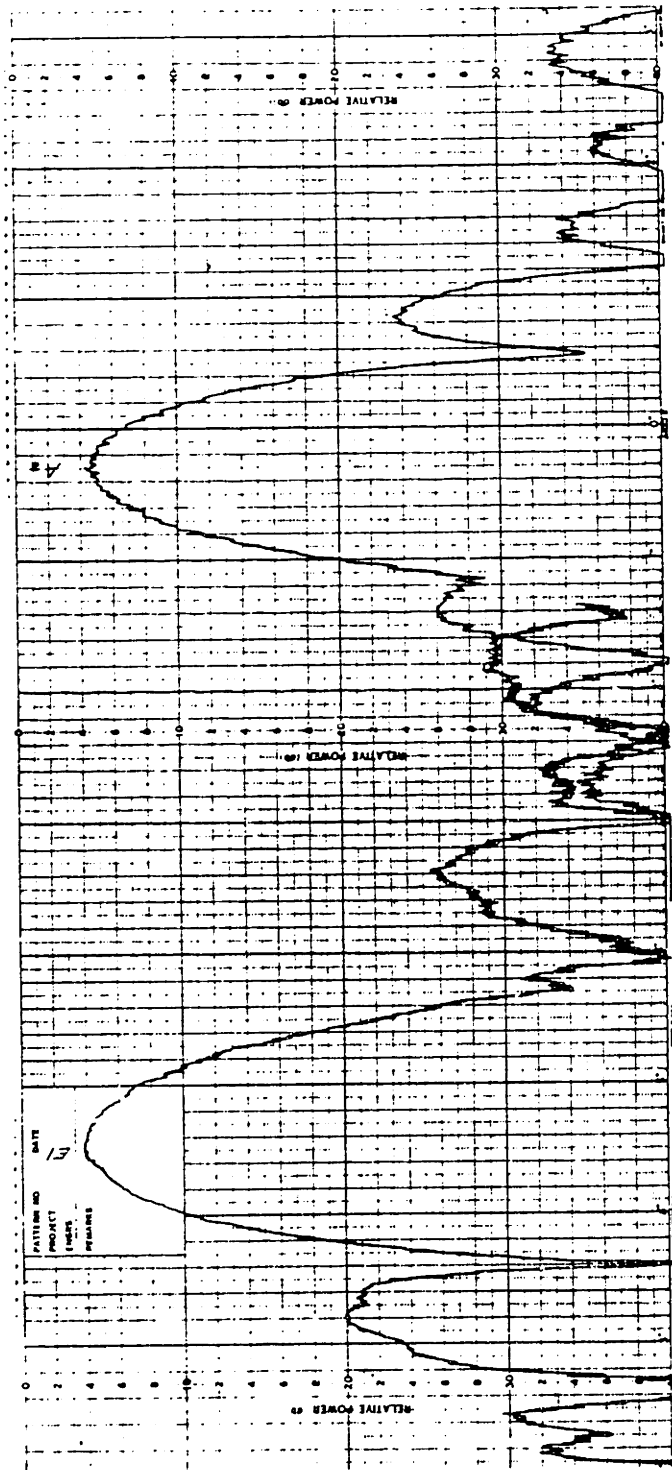


Figure 97. 7λ Pyramidal Horn (-0.3° , -5.5°)

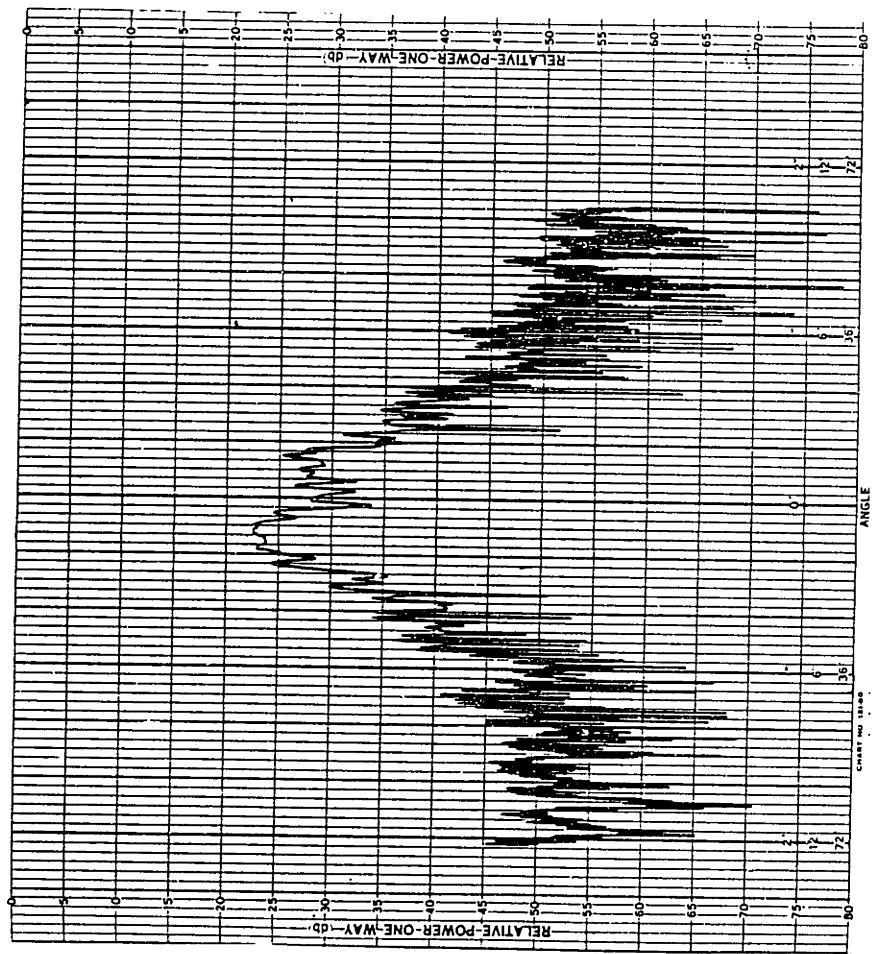


Figure 98. Subreflector Spillover Pattern Before Recoating

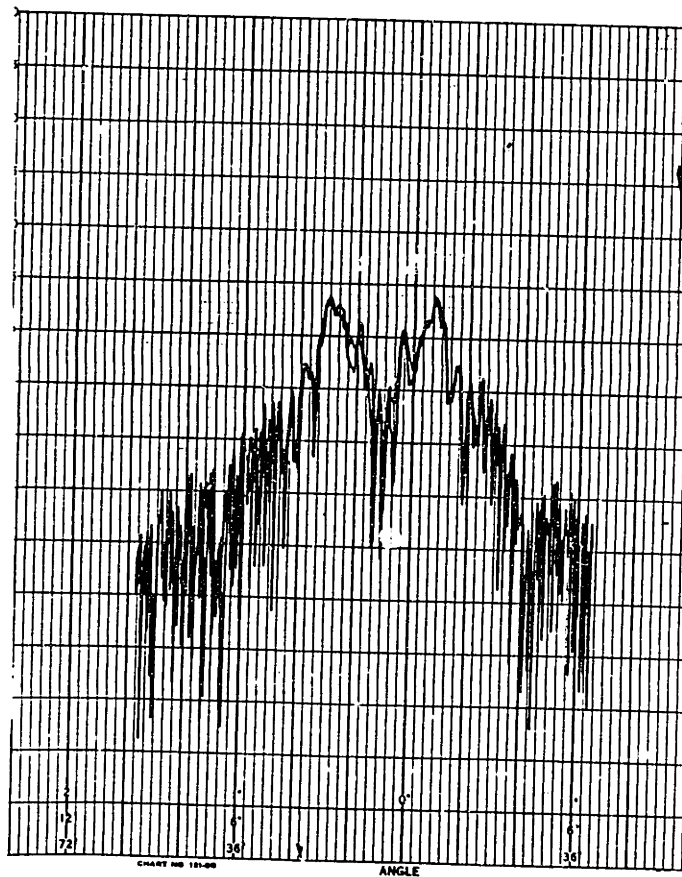


Figure 99. Subreflector Spillover (with Mylar covering)

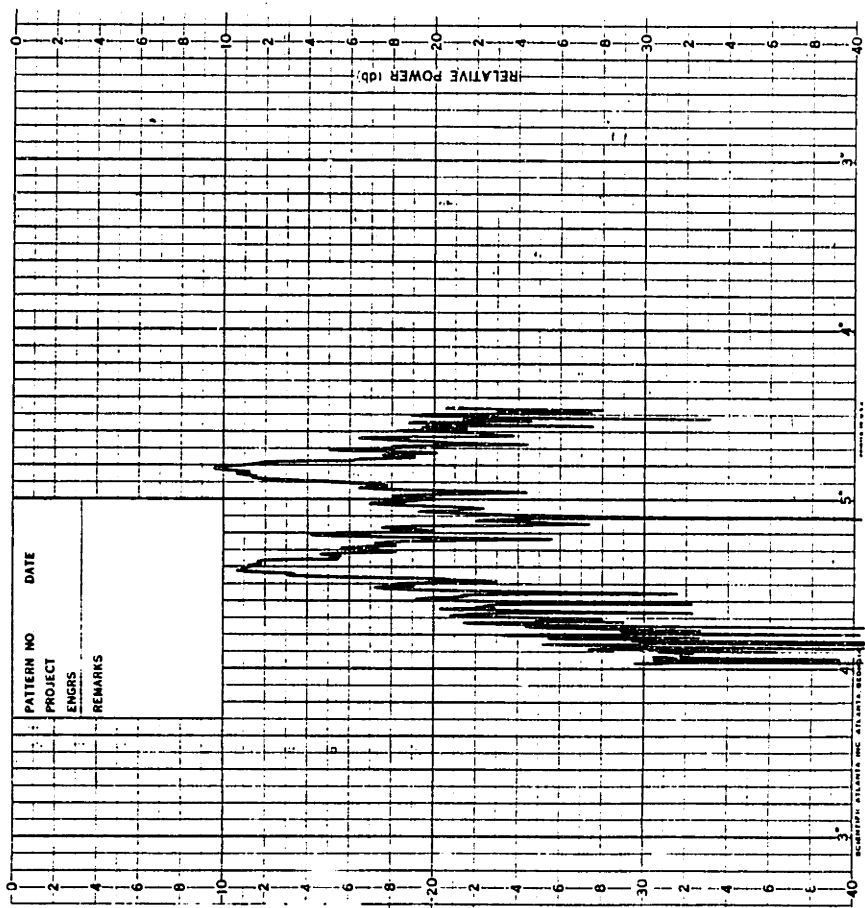


Figure I00. Subreflector Spillover After Recoating

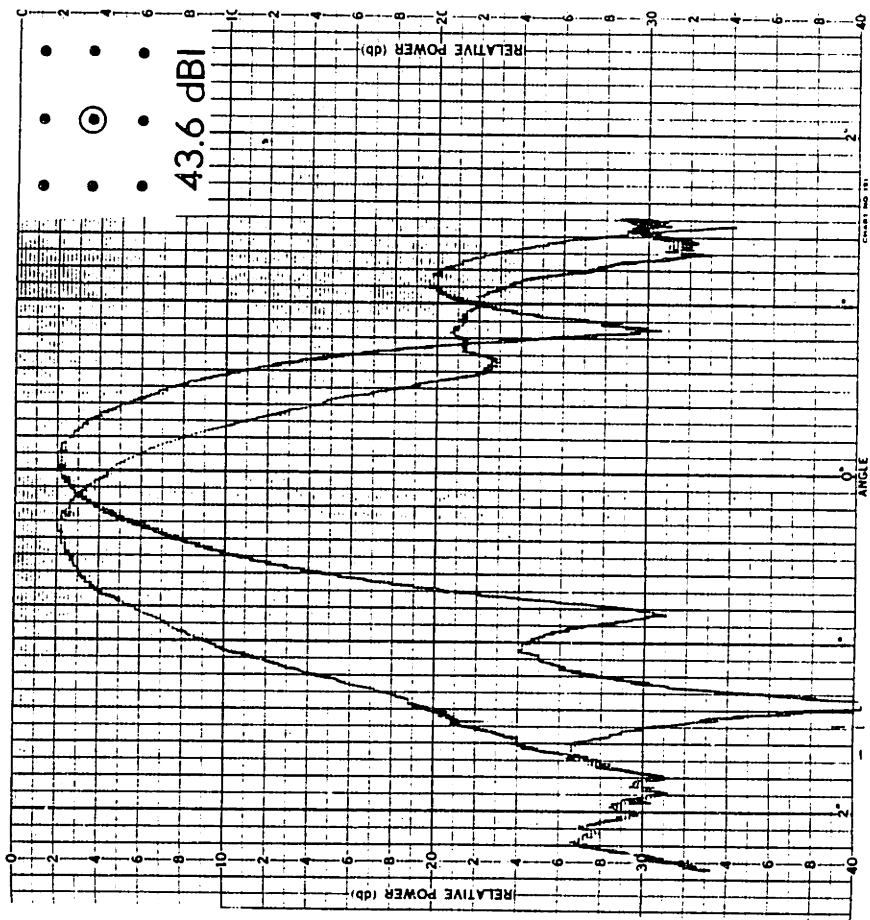


Figure 101. 7λ Pyramidal Horn--Unscanned Beam
After Subreflector Recoating (0°, 0.3°)

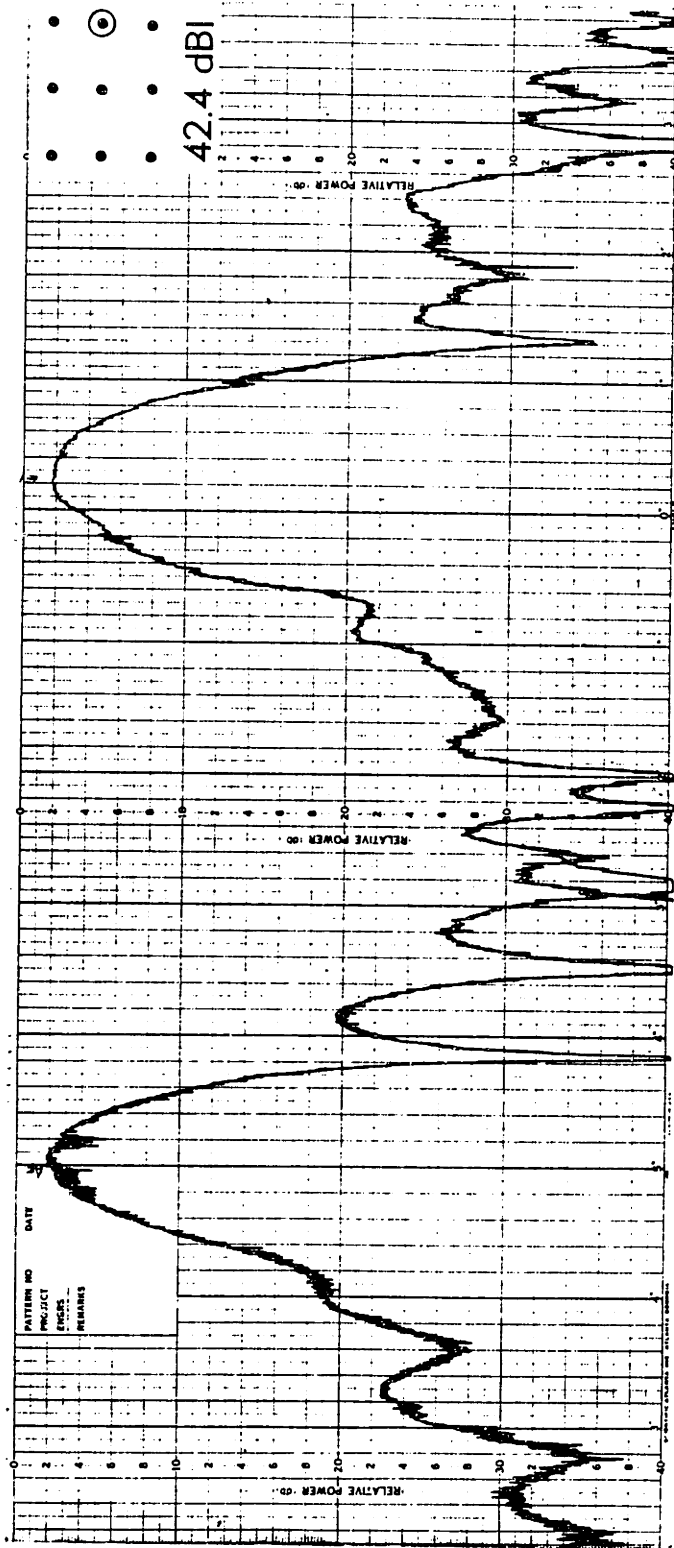


Figure 102. 7λ Pyramidal Horn (-5° , 0.2°)

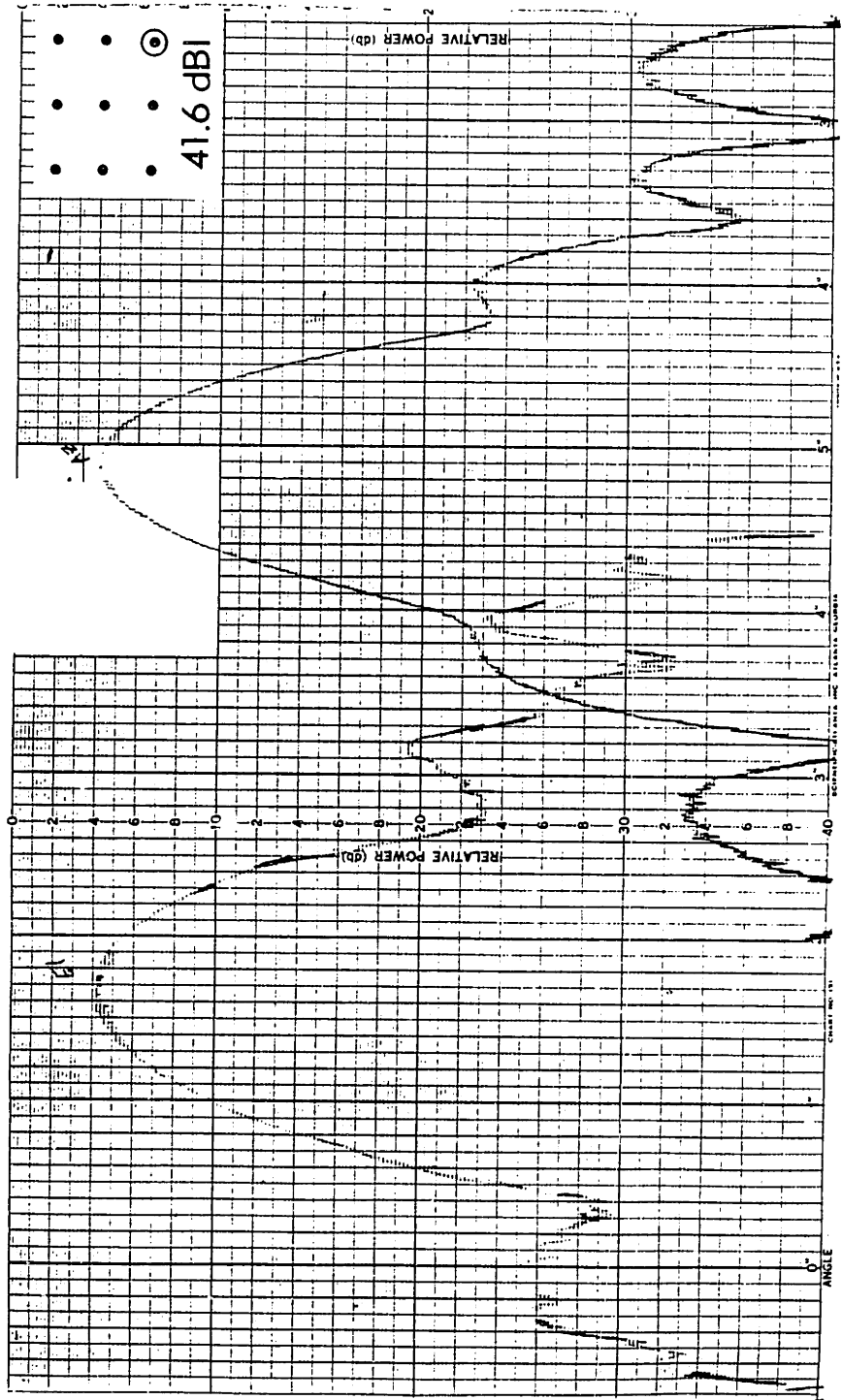


Figure 104. 7λ Pyramidal Horn (-5.1° , -8.5°)

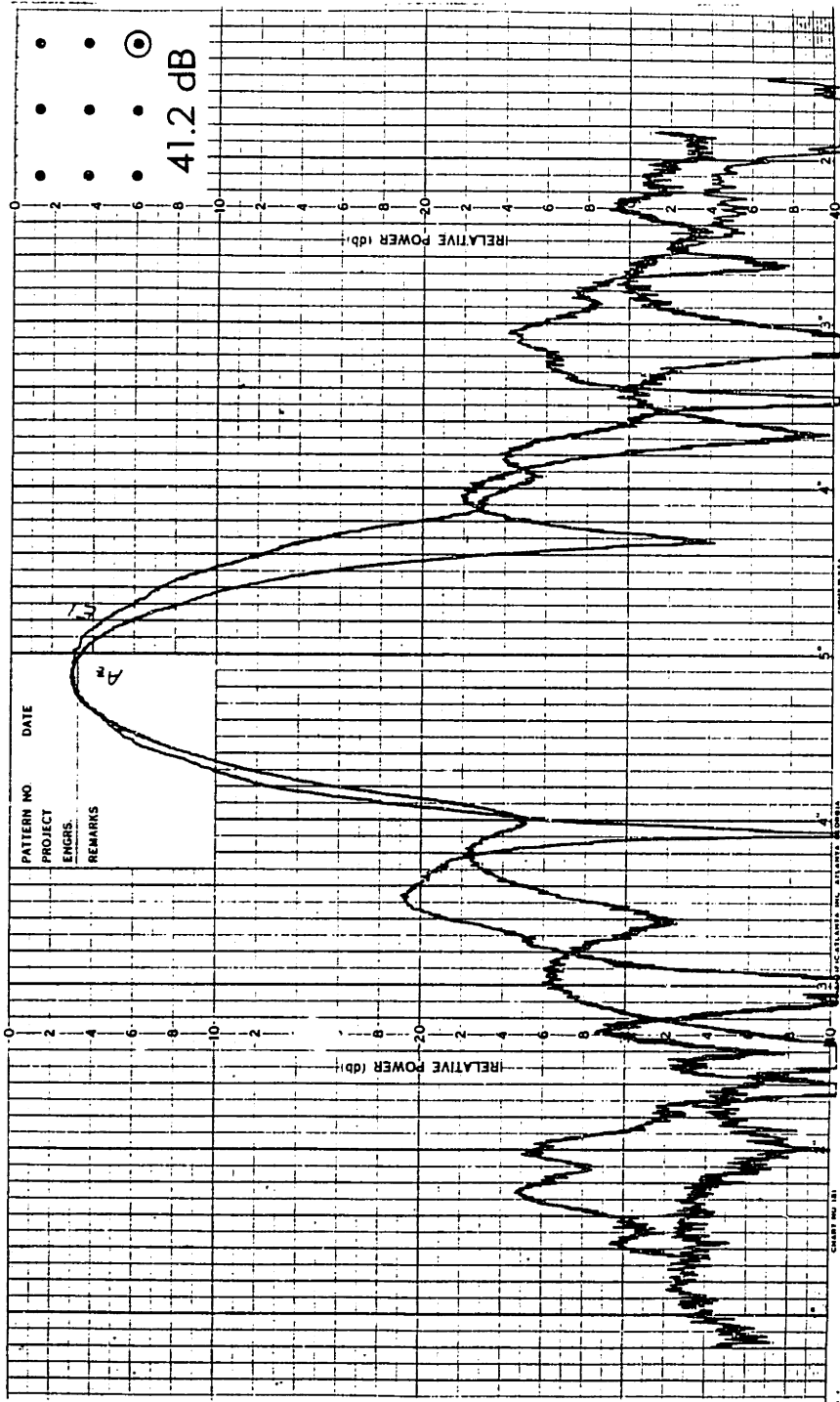


Figure 105. 7λ Pyramidal Horn (-5.2° , -5.2°)

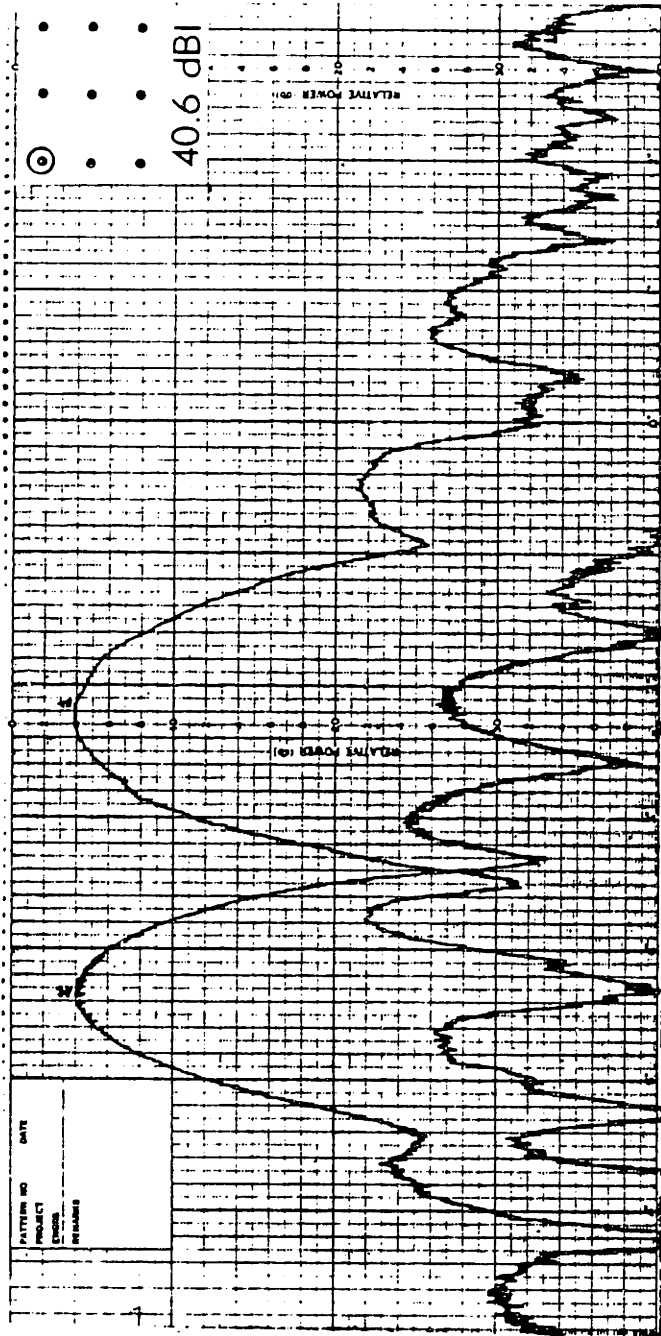


Figure 107. 7λ Pyramidal Horn (5.6° , 7.8°)

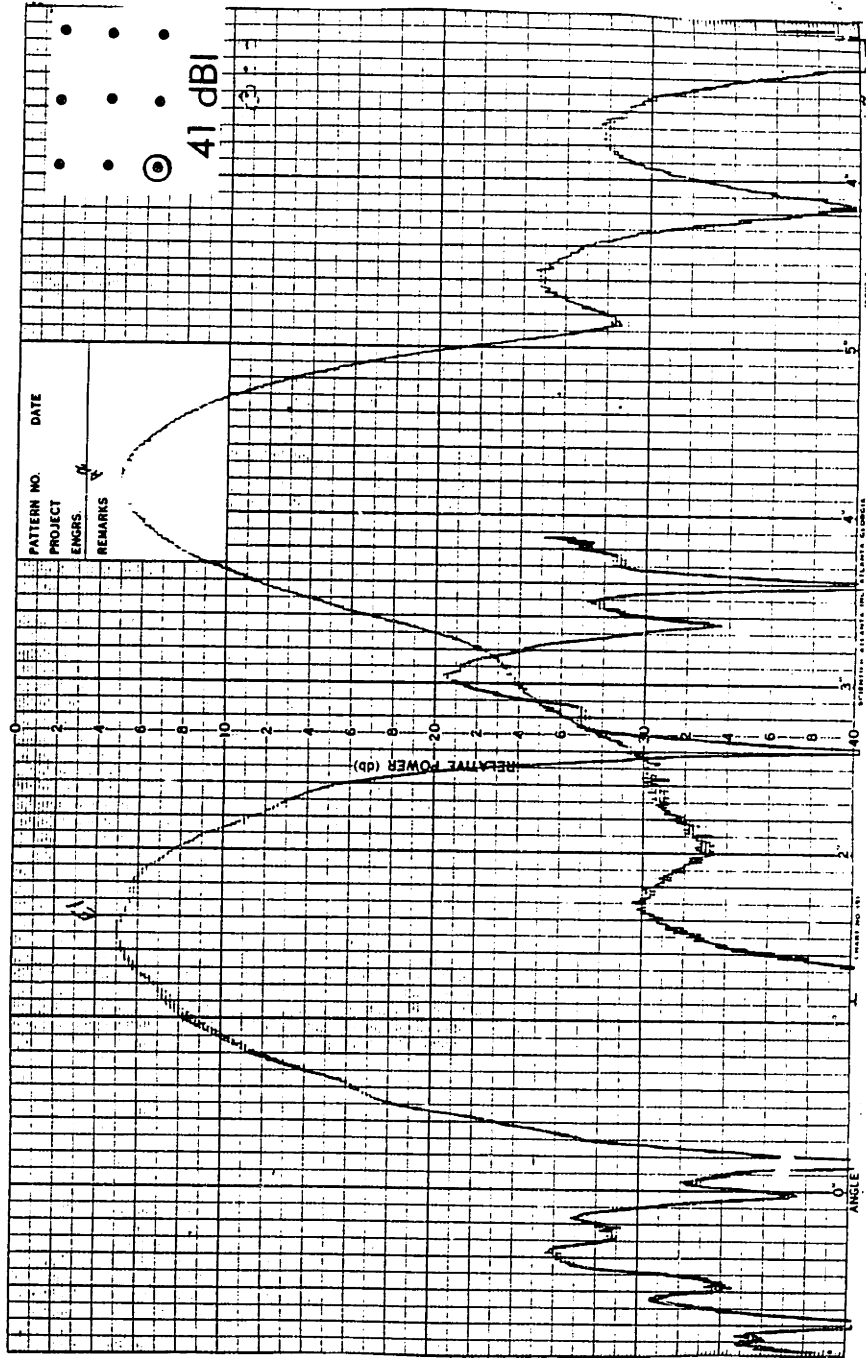


Figure 108. 7λ Pyramidal Horn (4.2° , -8.5°)

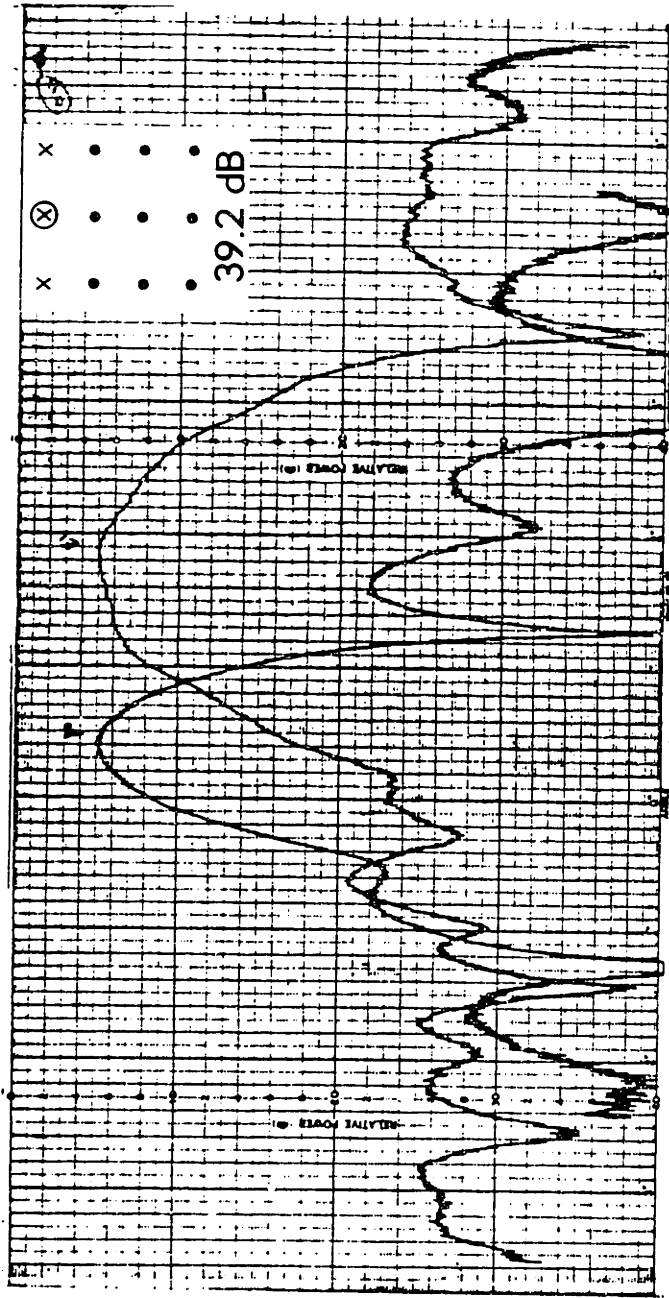


Figure 110. 7λ Pyramidal Horn, Extended Scan (-0.4° , 11.8°)

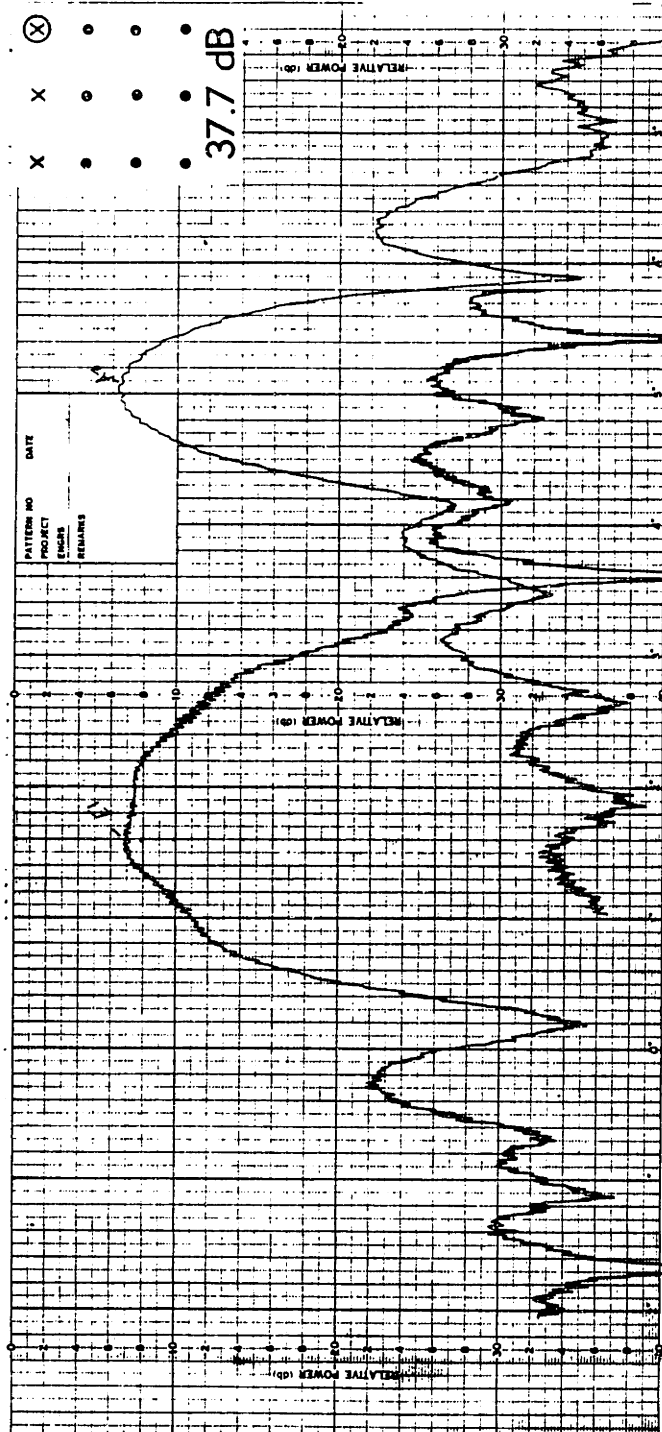


Figure 111. 7λ Pyramidal Horn, Extended Scan (-4.9° , 11.6°)

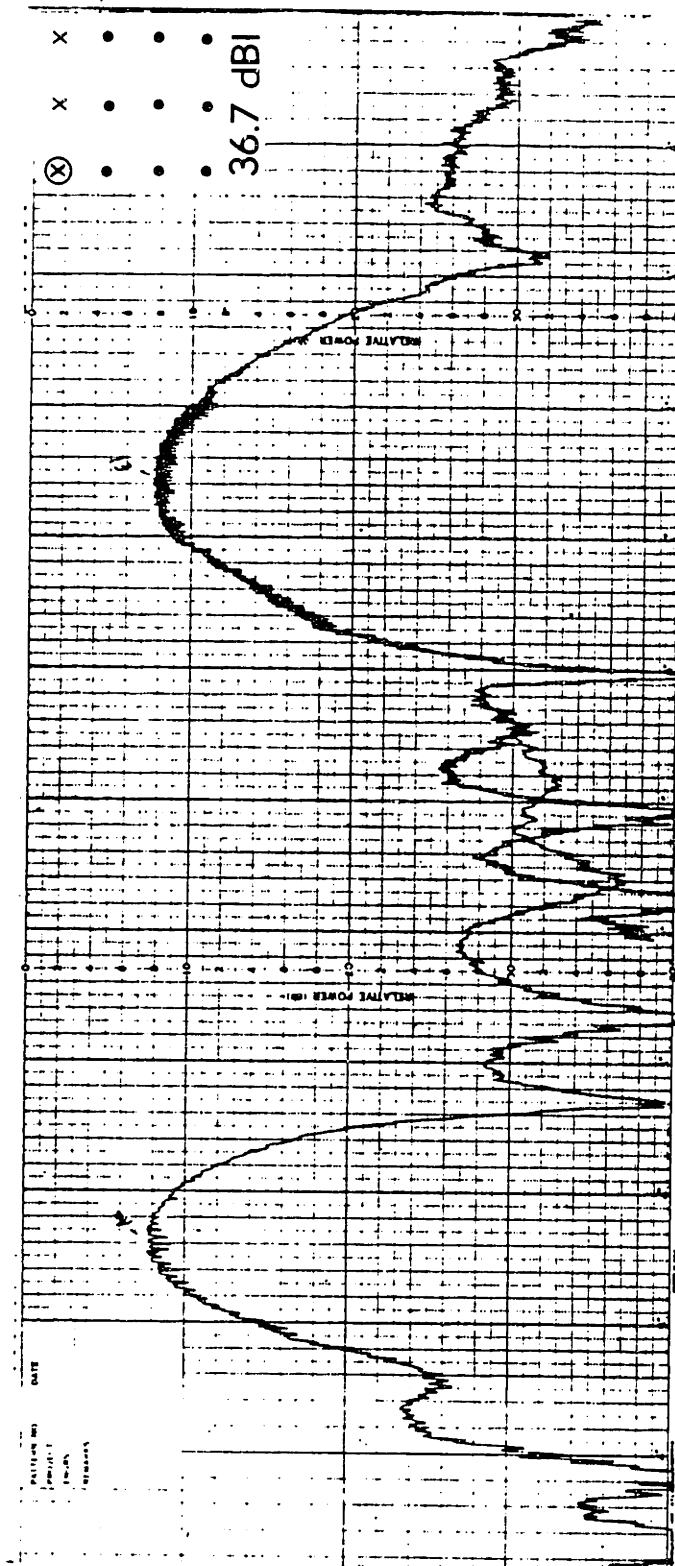


Figure 112. 7λ Pyramidal Horn, Extended Scan (5.6° , 11.5°)

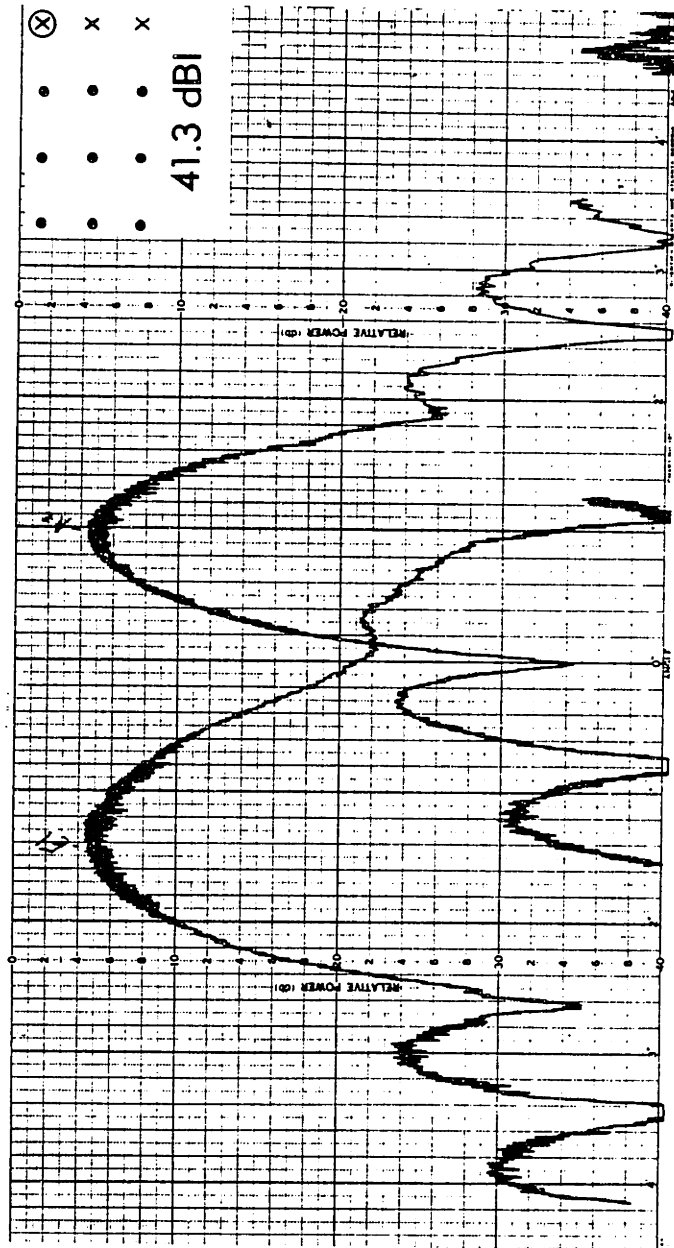


Figure 114. 7λ Pyramidal Horn, Wide Azimuth Scan (-9.0° , 8.6°)

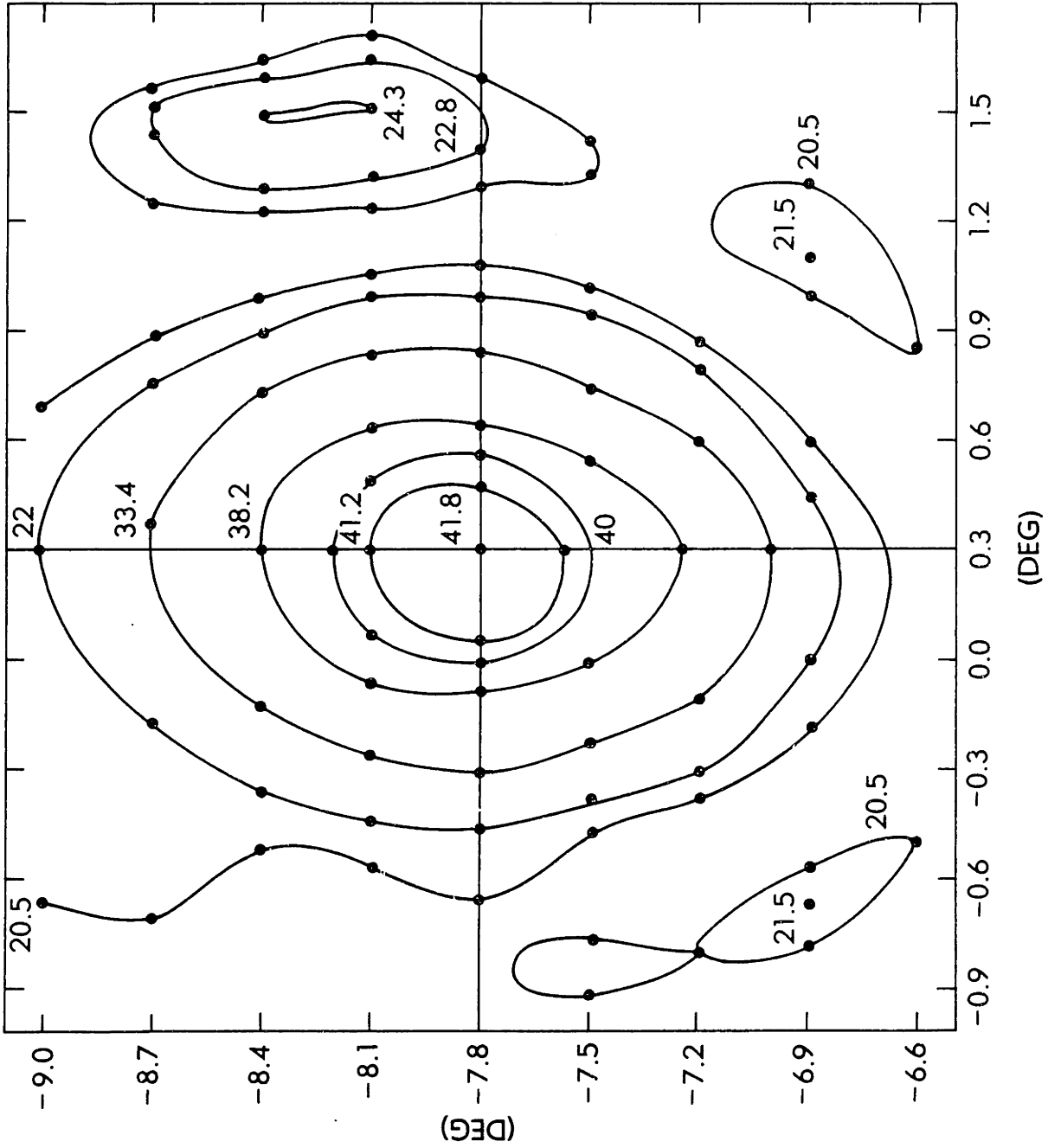


Figure 116. Typical Measured Contour Pattern (0.3° , 7.8°)

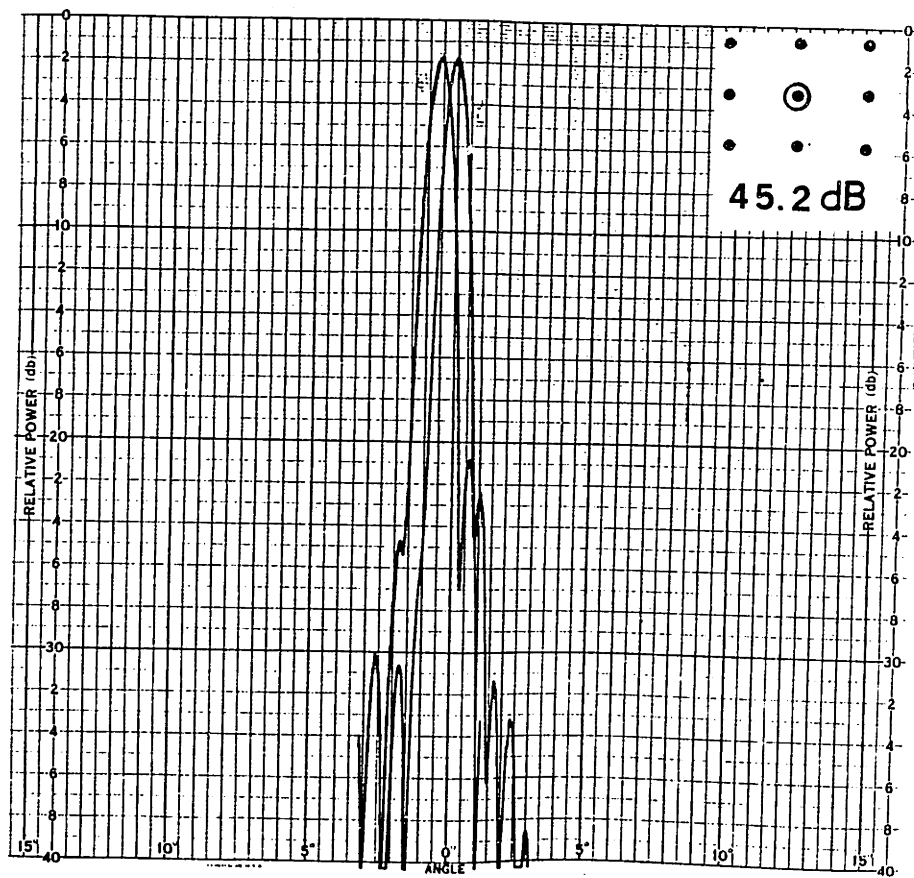


Figure 117. Optimized Horn Feed (0° , -0.5°)

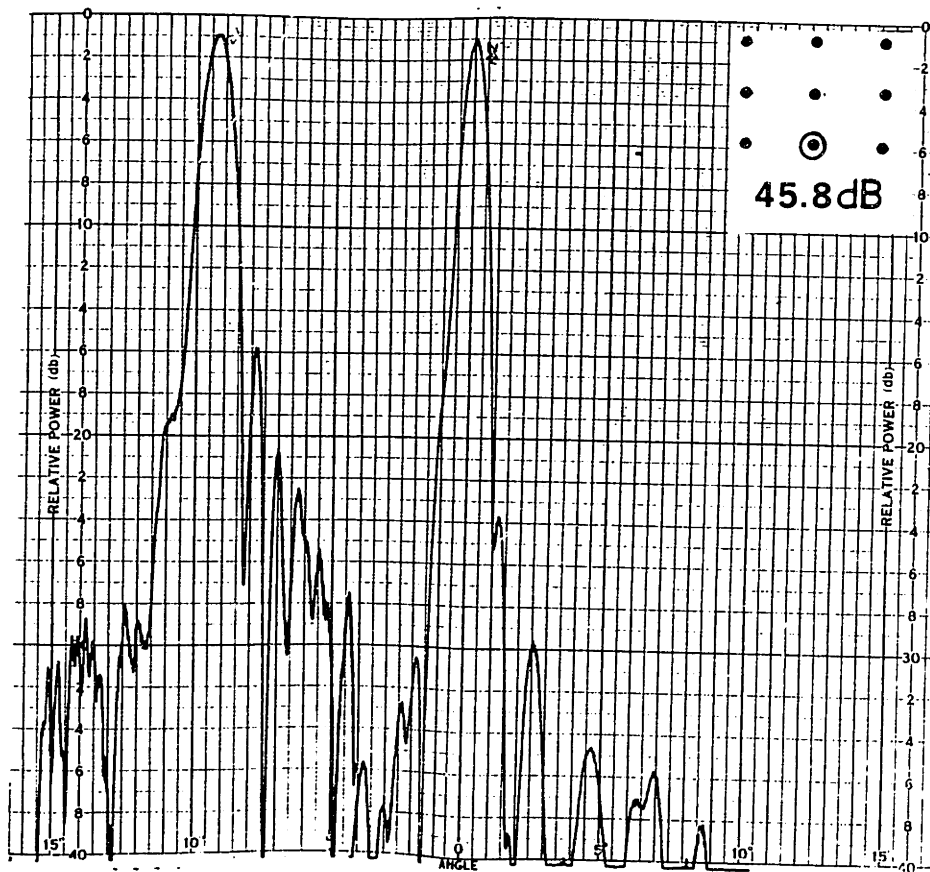


Figure 118. Optimized Horn Feed (0° , -9.2°)

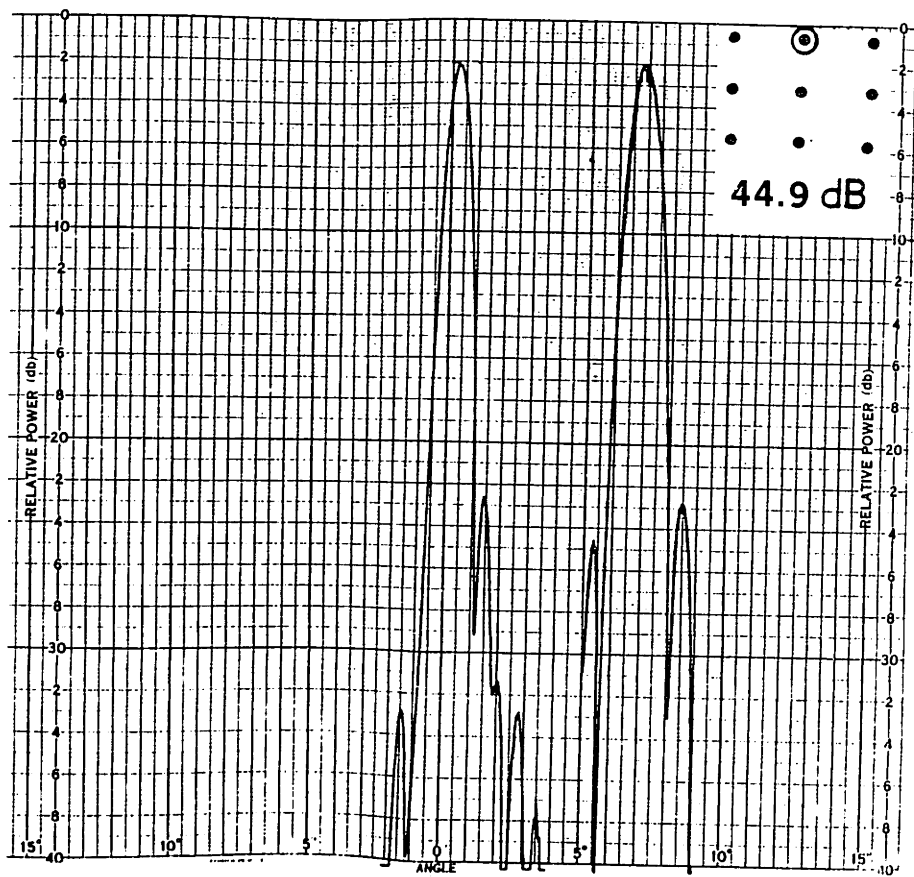


Figure 119. Optimized Horn Feed (0°, 7°)

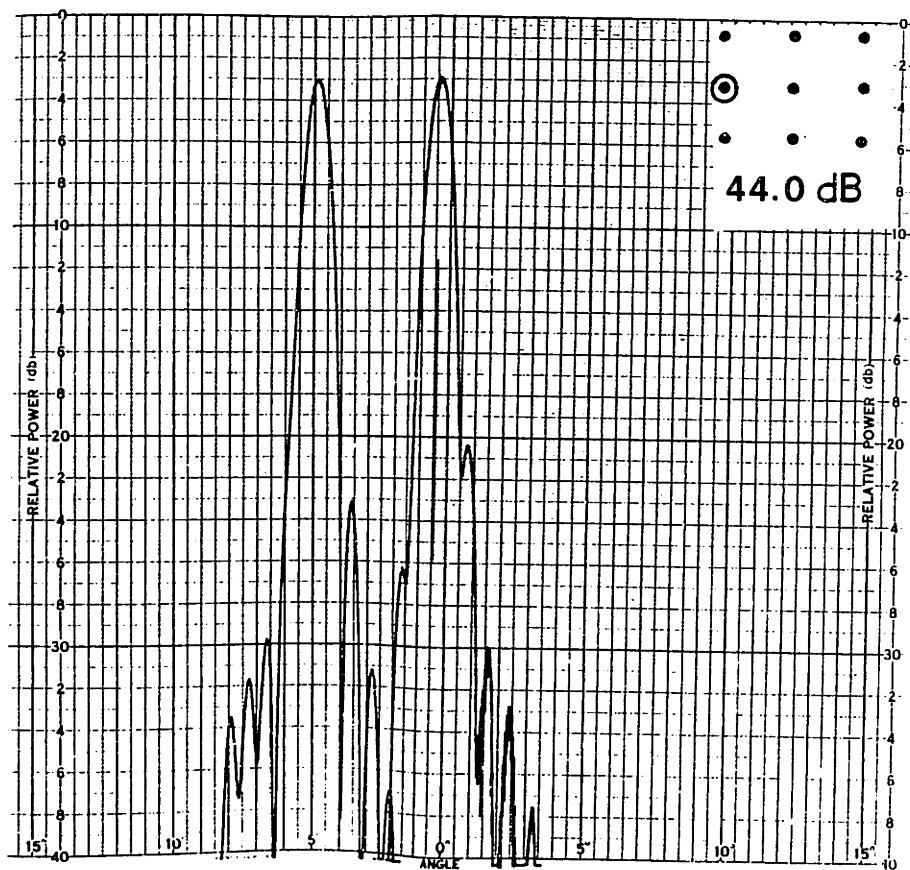


Figure 120. Optimized Horn Feed (-5.0°, -0.5°)

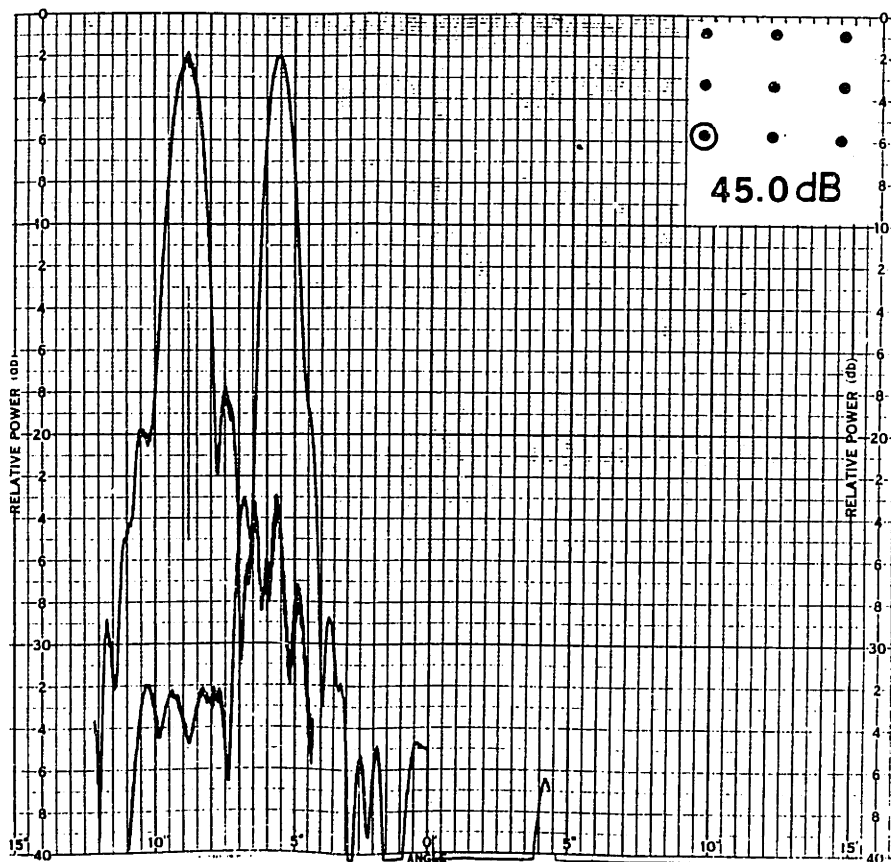


Figure 121. Optimized Horn Feed (-5.5° , 8.8°)

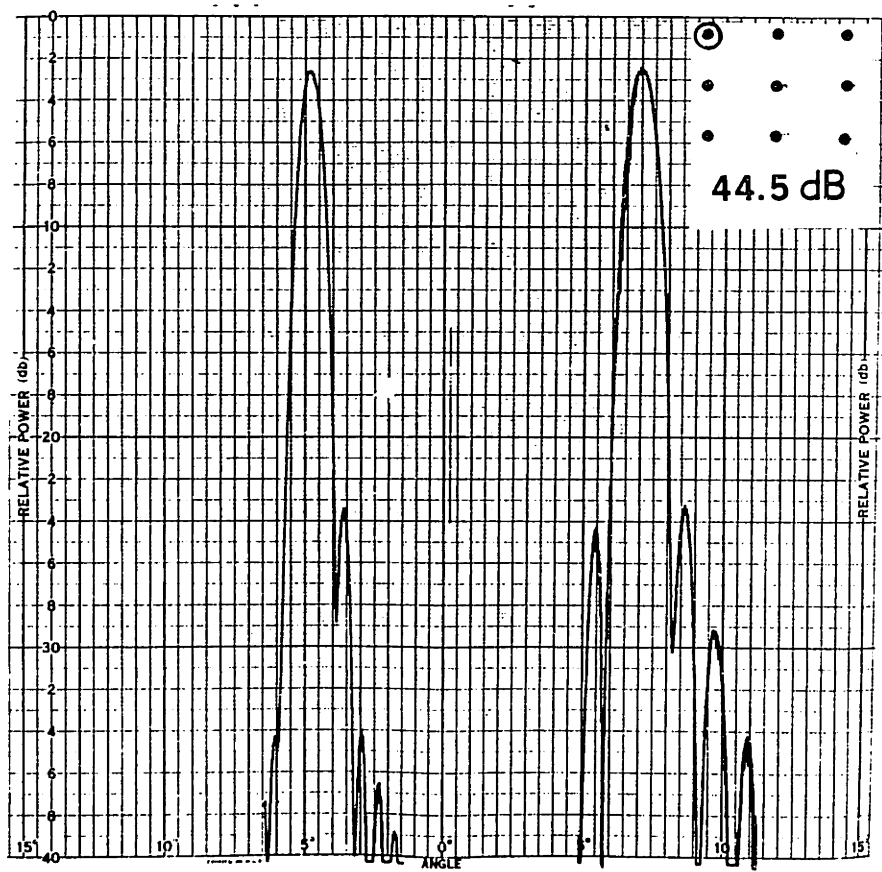


Figure 122. Optimized Horn Feed (-5.0° , 7.0°)

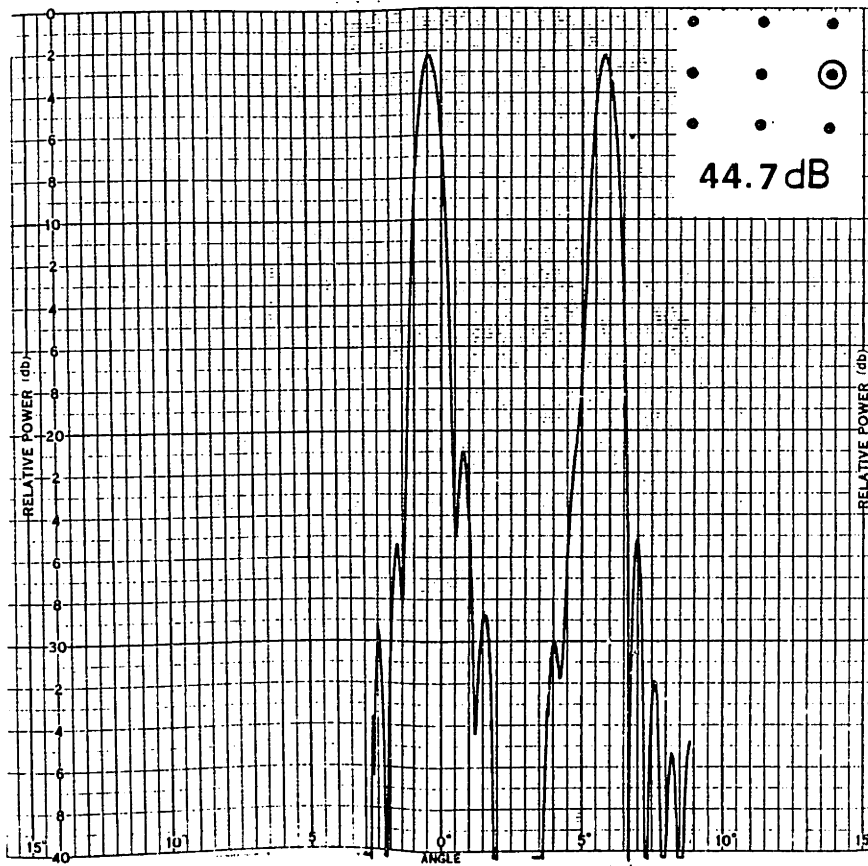


Figure 123. Optimized Horn Feed (5.0° , -0.5°)

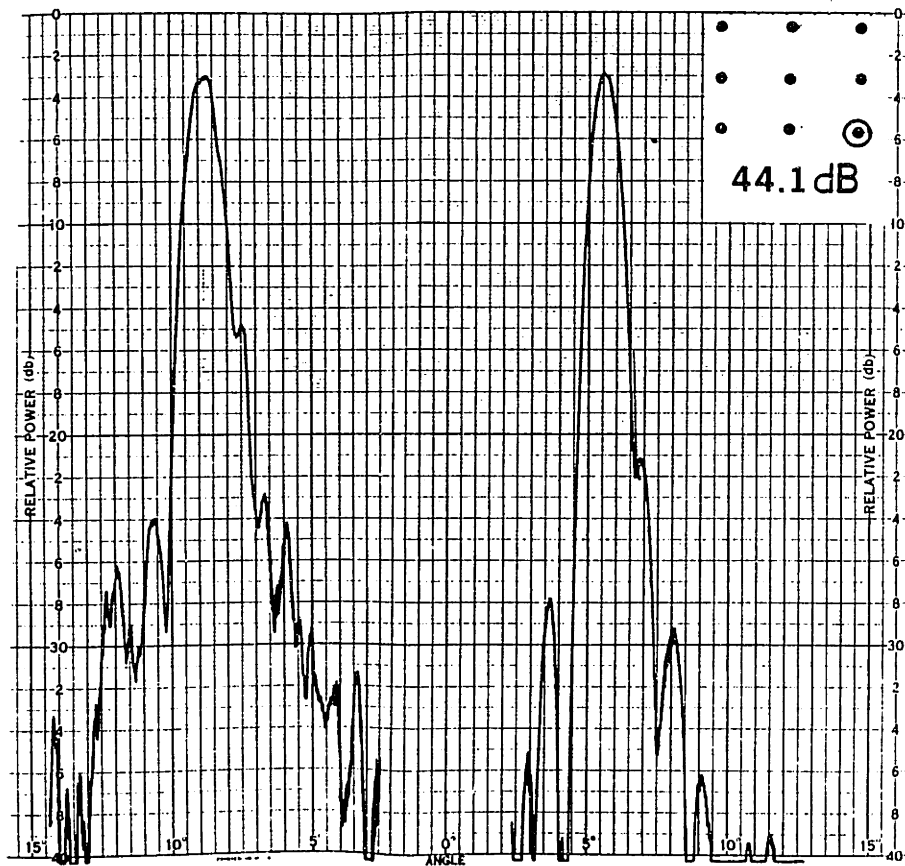


Figure 124. Optimized Horn Feed (5.5°, -8.8°)

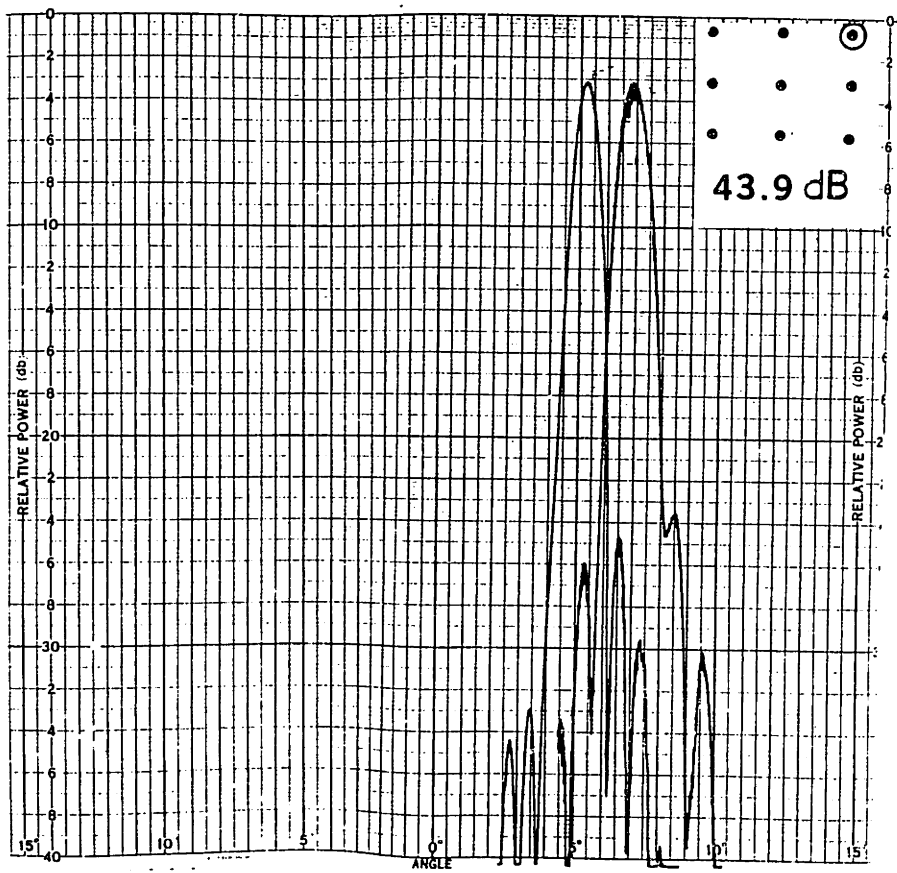


Figure 125. Optimized Horn Feed (5.0°, 7.0°)

In Figure 93 it is noticed that the azimuth pattern is fairly symmetrical, with a narrower beamwidth than for the elevation cut. There is excellent agreement with the computed pattern of Figure 92. This is as expected from the elongated contour patterns presented earlier. The azimuth cut sidelobes differ by 3 dB, with much more null filling on the negative side. This was a characteristic of all patterns, but could not be improved by subreflector realignment. Its most probable cause is the slight azimuthal error of the main reflector. These asymmetries, however, are rather minor and presumably correctable, and do not interfere with demonstration of acceptability of this design.

The elevation pattern, however, is remarkably similar to the computed pattern. The general shape is the same and the first sidelobe levels are 19 and 22 dB down compared to 15 and 21 dB predicted by computer. These encouraging results were present for all focal positions tested.

Figures 94 and 95 compare with the two computed scan positions. The gains, as expected, have only dropped 1.3 and 1.9 dB for excellent agreement. The $+8^\circ$ case shows even elevation sidelobes, 19 dB below peak compared to only 15 in the computer plot. The -8° case has exactly the predicted 15 dB down first sidelobe. Figure 96 juxtaposes the computed and measured patterns, showing excellent agreement. Figure 97

shows the intermediate scan position of -5.5° , indicating a steady progression across the field of view.

It should be pointed out that the experiments were performed using two different subreflectors. For the 0° , $+8^\circ$, and -5.5° elevation patterns, the original styrofoam with conductive paint reflector was used. However, the peak gain values, though quite good relative to one another, are all about 1.4 dB lower than predicted. Gain measurements were made to analyze peak values. The on-axis measured peak value was 43.4 dB, as compared to the predicted 44.75 dB.

The gain discrepancy was not attributable to imprecise alignment. In fact, peak gain was found to be very insensitive to movements of the feed and subreflectors. Only a few tenths of a decibel would result from motion as great as a centimeter. Although a possible source of error could come from the 0.05λ surface tolerance of the main reflector, it was concluded that the subreflector was the major source of gain loss.

It was discovered that the conductive paint coating used did not provide total reflectivity. This was tested by observing the subreflector spillover pattern, Figure 98. The axis of symmetry of this pattern corresponds to the maximum blockage point of the subreflector. If it were a perfect conductor, the power at this point and for 5° to either side

should be in the noise regions: 40 dB down. The reflector was covered with aluminized Mylar to guarantee reflectivity. The difference is evident in Figure 99. Although the conductive paint provided direct current conductivity, its RF reflectivity was very poor.

The subreflector was removed, sanded, and recoated with another type of conductive paint. This improved reflectivity, as shown in Figure 100, but the tight tolerances could not be kept in the sanding procedure. Replacing the subreflector and repeating the on-axis pattern measurement yielded Figure 101 which compares to the previous Figure 93.

The peak gain increased only 0.2 dB, owing to the additional phase errors present with this second subreflector. The azimuthal sidelobes are less symmetrical, though more well defined; but still 18 dB below peak gain. The elevation pattern suffers the most, with smeared nulls and a shoulder on the left side. The significant information: gain, beamwidth, first sidelobe level, and beam shape is all readily ascertainable. It was not felt that remachining the surface would have been necessary. The -8° beams were all measured using this second subreflector.

Figures 102 through 109 show the results for azimuthal as well as elevational scanning. There is fairly good correspondence between beams scanned positively and negatively in the azimuth. The negative scans are about 0.5 dB higher in general than their positive counterparts. The relative peak gains for the -0.5° azimuth scan beams vary only 0.3 and 0.8 dB from the maximum--less scan loss than for pure elevation scanning. The lowest peak gain for the entire $8^\circ \times 5^\circ$ field of view is 40.6 dB, only 1.8 dB below the maximum value at (0, 0).

A few limiting cases were measured to test the bifocal's extended scan range. The greatest feed displacement, which corresponded to $+11.8^\circ$ in elevation, produced fairly distorted elevation patterns: Figures 110, 111, and 112. Blockage by the subreflector is a serious problem in this case. The azimuth cuts are surprisingly well formed. The peak gains have fallen to 39.2, 37.7, and 36.7 dB, with large losses for azimuth scanning resulting from main reflector spillover.

Extending the azimuth scanning to its limit--which involved repositioning the main reflector--was much more encouraging. The resulting beam was scanned approximately 9° in azimuth. Figures 113, 114, and 115 are the patterns for 0.7° , $+8.6^\circ$, and -4.6° in elevation. The azimuth plane sidelobes

are even more well formed than in previous patterns, although the first sidelobe levels are only 17 dB below peak. The elevation plane patterns are less well formed, with shoulders on both sides of the main beam. The elevation sidelobes are much worse for beams scanned in elevation as well as azimuth. This observation again agrees with computed results. The peak gain values, however, were surprisingly high. There is only a 0.5-dB difference for the pure azimuth scan from 0° to -8.6° . The combined azimuth and elevation scanning resulted in gain values 1.7 dB below the pure azimuth beam. Thus, it appears that a scan loss of only 2.3 dB can be maintained with the offset bifocal over the entire $\pm 8^\circ \times \pm 9^\circ$ field of view. With the 7λ pyramidal horn feed used, adjacent 4-dB contours overlap.

Figure 116 shows a typical measured contour pattern at one of the designed scan positions.

A set of measurements was performed using the spillover optimized conical feeds. The numerical analysis used circular waveguides as feeds, so the measured performance should be lower than the prediction. Figures 117 through 125 show the measured azimuth and elevation plane cuts for the scanned nine-beam location. In general, there is an improvement of about 2 dB in gain over the measured pyramidal horn data. The peak gain levels are still 2.3 dB below the predicted levels.

The first sidelobe levels are slightly better than for the pyramidal horn case: averaging about 18 dB below the peak gain level.

The improvements using large conical feed horns are significant. However, these horn apertures are of the order of 1.5 times as large as the interfeed spacing for adjacent 3-dB beam spots. Thus, it is seen that for shaped contour beams, the advantage of improving efficiency using a high gain horn is outweighed by the disadvantage of wide beam separation.

VII. SUMMARY AND CONCLUSIONS

The offset bifocal system was designed for the specific purpose of wide angle scanning with optimum ray collimation. It has been demonstrated--both analytically and experimentally--that this dual reflector can scan the entire $\pm 9^\circ$ of the earth disk with peak gain variation of only 2 dB and first sidelobe level greater than 16 dB below maximum. There is no aperture blockage for all scan positions. Scanning is accomplished by feed displacement with reflectors fixed. Also, the 3-dB contour circles of two adjacent beams can be placed tangent to each other, providing flexible shaped beam contours for any region in the field of view. The system is relatively frequency independent, owing to the geometric optics method of design.

There are several improvements over previous antenna designs. Only the Schwarzschild and symmetric bifocal specifically address the problem of scanning while maintaining perfect focusing. Both of these suffer from significant sub-reflector blockage. A specific offset design, instead of selected offset sections of the symmetric antenna, offers greater performance.

The offset bifocal is superior to the previous symmetric design in several aspects. The two focal points which are rotated into a focal "ring" in the latter are perfect foci

for the offset case. Of course, there is no blockage, so gain, sidelobe performance, and noise temperature characteristics are improved. Also, the feed array is located much more conveniently behind the main reflector, out of the path of the reflected rays.

It has been shown that with the proper choice of initial parameters, the main reflector can be successfully approximated as a paraboloid. Thus the subreflector becomes a wide-angle scanning corrector, providing the paraboloid with a far greater field of view. The freedom to alter the surfaces in the transverse plane is particular to the offset design. The rotational symmetry of the symmetric bifocal prevents the main reflector from ever being closely approximated as a paraboloid.

An unexpected, but perhaps extremely useful, outcome of this research is application of the offset bifocal design method to the design of scanning Cassegrain antennas. Practical methods for designing Cassegrains with wide-angle scan properties are very limited.

The lengthy comparisons in the previous pages of various Cassegrains to the bifocal seem to indicate that the best scanning Cassegrain for the particular volume was the one which most closely matched the bifocal. Although the bifocal

is better, the Cassegrain is certainly simpler to analyze and fabricate. Once the bifocal is designed, the initial parameters, including the off-axis "focal" points, are readily available, and the optimum paraboloid-hyperboloid pair can be derived.

This systematic procedure is straightforward and efficient, and provides a bonus in that the resulting amount of scanning versus feed position is already known.

The large size of the focal locus for the offset bifocal has certain disadvantages. Covering the earth with spot beams would require an array practically the size of the main reflector. The question is raised whether it may not be preferable to use just a phase array of feeds, fed by a Butler network. Fourier transform theory indicates that for N component feeds in the array, N spatially orthogonal beams can be produced. Therefore, an ideal phased array can have as many degrees of freedom as a reflector system.

Unfortunately, there do exist major difficulties with the phased array principle. The Butler network is a complex structure with $\log_2 N$ levels of power splitters and phase shifters. For high power levels, these components are physically large, lossy, and lack the precision necessary for accurate beam steering. Furthermore, the elements of the array

are very frequency dependent. Also, in general all the elements in the array must be excited to some extent to produce even a single beam. With the reflector antenna, only the elements which correspond to desired beams need be excited. Since the required coverage area at the edges of the earth is relatively small, only a small fraction of the feed locus will have sources. This represents a great weight advantage over the phased array design. For further tradeoff discussion, see Shelton [97].

The comparatively large feed/subreflector distance in the offset bifocal is a disadvantage which cannot be eliminated. This large separation necessitates the use of high gain feeds. The feed horns thus are very large and heavy. Fortunately, the focal region is large enough to accommodate wide feed horns.

Even with high gain feeds, the problem of subreflector spillover is a major source of gain degradation. A careful tradeoff study between efficient illumination and spillover must be done.

Despite the large feed subreflector distance, the offset bifocal can be contained in a fairly small package. The main reflector, positioned close to the subreflector, requires a smaller uninterrupted aperture region in the given volume

than a similar prime focus paraboloid. Stowing and deployment of the antenna appears to be fairly simple, with the reflectors folding in towards the feed array.

Comparing the ideal uniformly illuminated aperture gain with the actual resulting gain in the offset bifocal indicates the relatively low efficiency of the design. It was pointed out, however, that scanning systems require different sections of a stationary reflector to be illuminated for different beam directions. In the design presented, the subreflector is efficiently illuminated for all beams as a tradeoff for illuminating only one quarter of the main reflector with each beam. This choice was made to minimize the subreflector size and hence, the problem of blockage.

One final difficulty with the antenna is its mathematical complexity. Both analysis and fabrication of the surfaces are sophisticated operations. The synthesis procedure is straightforward for point generation, but it is not easy to join the points and form surfaces. The physical realizability of the surfaces depends strongly on the initial parameter selection. A great deal of trial and error study is necessary for the optimum design.

Analysis of a dual reflector with transcendental surfaces is very tedious. Perhaps the best method involves using a finite element approach. Each surface is broken up into triangular elements whose vertices are exactly specified, and whose interiors are third-order polynomials determined by the locations and normals of the vertices. Then analysis proceeds as with a standard reflector, tracing rays to a particular element and treating it as the localized surface. Since the bifocal is specified by points and normals, it is well suited for this type of analysis.

The inherent lack of symmetry makes the fabrication process challenging. However, using a numerically controlled milling machine, very accurate results are possible. There is a size limitation depending upon the capacity of the mill, but very large surfaces can be made up from smaller panels. With the design tested, the curvature is so slight--a variation from planar of only $1/70$ of the length--that segmentation is extremely feasible.

The theory of the offset bifocal is by no means complete. The Gregorian configuration has not been explored here. Although the focal length and subreflector size are larger than for the convex design, there may be certain advantages in illumination efficiency, blockage reduction, or overall system compaction. The Gregorian configuration is

synthesized in the same manner as presented above, with only a change in the initial parameters.

Another design variation not considered is a bifocal offset in the plane perpendicular to the line connecting the focal points. This design is an exact symmetric bifocal with an alternate way of extension to three dimensions. Scanning takes place in the symmetry plane rather than the offset plane. It is more suited to offset applications than the rotationally symmetric bifocal.

Certainly a more systematic way of choosing initial parameters would be of use. Minimizing the trial and error in finding the curves with the least amount of blockage and smallest volume to aperture area ratio would make the designing procedure simpler. Perhaps the most useful improvement would be to find an algorithm which would guarantee the realizability of a 3-dimensional surface connecting the points.

An extension of the bifocal idea to many reflector systems is worth considering. There exists a limited amount of literature on three or more reflector systems [98]-[102]. Allowing the possibility of a third reflector could theoretically lead to a trifocal system. The more complicated arrangement might prove more efficient than the dual-reflector.

APPENDIX VIII. DESCRIPTION AND PROGRAM LISTING
OF THE BIFOCAL GENERATING PROGRAM

The formulas derived in the previous sections are implemented using the FORTRAN program GENBIF. This program successively generates main and subreflector points, fits curves to the x-z and x-y projections, and then determines the surfaces which best fit the curves. GENBIF also conditions the surface data for various computer testing routines, displays both reflector surfaces using 3-dimensional graphics, and formats output data used in fabrication of the test model.

Before any extensions to surfaces can be done, several checks on this profile are used. First, the physical realizability of the profile is examined. The sequences of five sub- and main-reflector points are found, the two Lagrange interpolated polynomials are determined--each of fourth order, and then the program cycles back to test a point on the subreflector curve. With a specified increment Δx , the corresponding $\Delta z = f_4(\Delta x)$ (where f_4 is the polynomial curve representing the subreflector profile) and the normal $(-f_4'(\Delta x), 1)$ is found. Then, using the point $(\Delta x, \Delta z)$ and its normal as the input starting parameters \bar{S} and n_{S1} , a new set of point sequences is found. Comparing the resulting best fit polynomial with the previously derived curve indicates how well the curve fits both the points and their normals.

The second check on the profiles requires graphical trial and error examination. The proper sections of the sub- and main reflectors are selected by tracing rays through the system.

Once the 2-dimensional profiles are established, the actual surfaces are generated. Specifying the transverse polynomial can be done by the user or by the default case. This case uses the hyperbola which would result from a Cassegrain with the corresponding focus and main reflector vertex. User specified increments in the transverse (y) direction are used to evaluate successive starting points on the transverse polynomial. New curves are generated and checked for surface realizability.

The points which satisfy the bifocal conditions can be joined in many ways. Since each starting subreflector point generates a particular sequence of points, it is natural to join these with a best fitting space curve before trying to fit a surface to all the points. The curve is most easily specified by using the two independent projections onto the x-z and x-y planes. Thus, the generated points are projected onto these planes, and the best fitting fourth order polynomial for each plane is found. This is done for all curves of both reflectors. Once these sets of curves are found, an

improved representation of the surfaces can be made by specifying sample points (x,y,z) for regular spacings of x and y .

A major portion of GENBIF involves choosing the proper sample points of the surfaces. The various curves for each surface must be close enough to provide values at each of the desired sampling intervals. Since the curve projections on the x - y plane are not parallel, more curves must be available than sample intervals.

The subroutine POINTS performs the surface sampling. First, the grid of (x,y) sample points is chosen. It is based on the projected reflector circle (or ellipse) center and perimeter, the number of sample points, and the type of grid: Cartesian or triangular. The triangular grid is useful primarily for the finite element analysis technique. The z values at the sample points are found by calling subroutine FUNC. FUNC evaluates y and z separately for each x using the x - y and x - z projected polynomials. The z value for the exact x sample value and closest y sample value is thus determined. If the separation between space curves is small, the difference between the actual value of $z(x,y)$ and the closest sampled value of z will be negligible. If the separation is too small, the sample point will have more than one z value assigned to it. Averaging the multiple values leads to the best sample value.

Once the surfaces exist in the form of sample points, it can be plotted in 3-dimensional perspective using GRAF3, or approximated with a fourth-order function of x and y using FITFOR. The most accurate method of electrically analyzing a transcendental surface is to use finite elements.

The idea behind the finite element method is to break the surface up into many triangular regions, and then perform the required analyses locally. Given the vertices and surface normal at each vertex, the relatively small triangular region can be accurately described by a third-order function of x and y. Thus, wild surface fluctuations can be studied in smooth pieces. This method is particularly useful when a large number of sample points are known, but the functional form of the surface is not.

When a triangular sample grid is used in POINTS and the space curve normals are sampled along with point locations, the surface is well suited for finite element analysis. The sample points are numbered using subroutine GRIDP, and the individual elements defined by the grid points are identified using ELEM. Two files, one containing the point locations and normals and the other containing the element definitions, are filled.

The two files are used as input for the GAP finite element option. Rays are traced from the feed to a particular element. The element is identified and the local surface functional form is determined. The reflected ray is found and analysis proceeds as usual.

There are a few disadvantages with using the finite element method which must be mentioned. It should be apparent that the procedure is very difficult to program. Since the sequencing of points and elements is crucial, a single error could have disastrous results. Furthermore, the computation time grows faster than the number of elements, since each element must be checked to see if an incident ray intersects it. Rays with steep incident angles are not as accurately reflected as those approaching normal incidence.

Finally, since the projected region is divided into triangles, it is difficult to provide a close fitting perimeter. Nonetheless, the finite element method is an excellent way to represent a complex surface.

```

C *****
C *****
C **
C **          AUTOMATIC 3-D BIFOCAL GENERATION PROGRAM          **
C **
C *****          WRITTEN BY CAREY RAPPAPORT          *****
C *****          1981          *****
C

```

```

C -----
C      THIS PROGRAM WILL GENERATE, AND TEST THE PHYSICAL REAL-
C      IZABILITY OF A BIFOCAL REFECTOR ANTENNA SYSTEM.  GIVEN SUITABLE
C      PARAMETERS (WHICH ARE REQUESTED WITH PROMPS) A PAIR OF SURFACES
C      WILL BE DERIVED, POINT BY POINT, CURVES IN TWO DIMENSIONS WILL
C      BE FIT TO CUTS PARALLEL TO THE AXIS, FINITE ELEMENT FILES WILL
C      BE SET UP, FOURTH ORDER POLYNOMIAL APPROXIMATIONS WILL BE DETER-
C      MINED, AND A THREE-DIMENSIONAL PLOT WILL BE MADE.

```

```

C      THIS MAIN PROGRAM CALLS THE FOLLOWING SUBROUTINES:
C      * BIFOFF *      WHICH GENERATES THE POINTS OF THE BIFOCAL SYSTEM
C      * INTERP *     USED IN FINDING THE BEST FIT Y-Z POLYNOMIALS.
C      * TYPOUT *    USED FOR DISPLAYING OUTPUT IN A READABLE FORM.
C      * ELEM *      WHICH SETS UP THE FINITE ELEMENT SPECIFICATIONS.
C      * GRIDP *    WHICH PREPARES POINT VALUES FOR FINITE ELEMENT.
C      * FITFOR *   GENERATES FOURTH ORDER REPRESENTATION OF SURFACE
C -----

```

```

C
C      DIMENSION FI1(3),FI2(3),S1(3),SN1(3),SX1(3),SNX1(3),
C      & ZSAMPL(7),YSAMPL(7),PY(7),ZY1(4,20,20,2),POFSET(7),
C      & E(7),XS4(5),XM4(5),P(7),P2D(10,7)

```

```

C      COMMON OP,ZSURF(4,20,20,2),ZXSURF(4,20,20,2),ZDRAW(30,30,2),
C      & CENTX,CENTY,KUTSYM,JBDY(20),PPROJ(7,20,2),QPROJ(7,20,2),
C      & XPSS(4,20,2),CEMTX,CEMTY,Y1(4,20,20,2),
C      & XPLT(30,2),YPLT(30,2)

```

```

C      LOGICAL OUTPUT/.FALSE./,OP

```

```

C      *** INITIALIZE ARRAY VARIABLES TO ZERO ***

```

```

C      5 AUTO=0.
C      DO 140 MNIT=1,2
C      DO 120 IINT=1,30
C      DO 120 JJNT=1,30
120 ZDRAW(IINT,JJNT,MNIT)=0.
C      DO 140 INIT=1,20
C      DO 130 LNIT=1,7
C      PPROJ(LNIT,INIT,MNIT)=0.
130 QPROJ(LNIT,INIT,MNIT)=0.

```

```

DO 140 JNIT=1,20
DO 140 KNIT=1,4
ZSURF(KNIT,INIT,JNIT,MNIT)=0.
ZXSURF(KNIT,INIT,JNIT,MNIT)=0.
ZY1(KNIT,INTI,JNIT,MNIT)=0.
XPSS(KNIT,INIT,MNIT)=0.
140 Y1(KNIT,INIT,JNIT,MNIT)=0.
OP=.TRUE.
NTIT=1
KUTSYM=1
NORD=6
ZTRANS=0.
CNTX2=0.
CNX2=0

```

C
C *** WRITE OUT PROMPTS AND READ INPUT VALUES ***
C

```

WRITE(6,1100)
1100 FORMAT('1DO YOU WISH TO CHANGE ANY INPUT VALUES? (0 TO CHANGE ALL
& , 1 FOR FOCAL POINTS, 2 FOR L, 3 FOR ANGLES, 4 FOR C1,C2)')
READ(5,*)NVAL
IF(NVAL.LT.0.OR.NVAL.GT.4)GOTO 12
IF(NVAL.NE.0)GOTO 7
WRITE(6,1200)
1200 FORMAT('1INPUT INITIAL FOCAL POINTS, L, ALPHA1, ALPHA2, BETA1,
& BETA2, C1, C2')
READ(5,*)FI1,FI2,XL,ALPH1,ALPH2,BET1,BET2,C1,C2
GOTO 12
7 GOTO (8,9,10,11),NVAL
8 READ(5,*)FI1,FI2
GOTO 12
9 READ(5,*)XL
GOTO 12
10 READ(5,*)ALPH1,ALPH2,BET1,BET2
GOTO 12
11 READ(5,*)C1,C2
12 WRITE(6,1300)
1300 FORMAT('1INPUT STARTING COORDINATES (X,Y,Z), STARTING NORMAL (X,Y,
& Z), AND NUMBER OF INTERATIONS')
READ(5,*)S1,SN1,NITER
DELX=0.
DELY=0.
IF(NITER.EQ.1)GOTO 13

```

C
C *** CURVE VERIFICATION SECTION ***
C THIS PART OF THE PROGRAM IS USED TO INSURE THAT THE POINTS
C AND THEIR CORRESPONDING NORMALS ARE ON THE SAME CURVE. THIS IS
C AN ESSENTIAL CHECK WHEN SYNTHESIZING OFFSET SYSTEMS. FIRST,

C THE CURVE WHICH BEST FITS THE DERIVED POINTS IS FOUND. THEN,
C AN INCREMENT IS ADDED TO THE X OR Y COORDINATE OF THE SUBREFLEC-
C TOR STARTING POINT. A NEW Z VALUE IS FOUND BY SUBSTITUTING
C THE INCREMENTED X OR Y VALUE INTO THE FUNCTION REPRESENTING THE
C BEST FITTING CURVE. THUS, A NEW STARTING POINT IS SPECIFIED,
C AND ANOTHER CURVE IS GENERATED. IF THIS NEW CURVE IS THE SAME
C AS THE FIRST ONE, THE DERIVED STARTING POINT WAS, IN FACT, ON
C THE ORIGINAL CURVE, AND THIS BEST FIT CURVFE IS A GOOD SOLTION.
C

C
C WRITE(6,1400)
1400 FORMAT(' ENTER THE X-INCREMENT, AND THE Y-INCREMENT')
READ(5,*)DELX,DELY
13 WRITE(6,1500)
1500 FORMAT(' ENTER 1 FOR AUTOMATIC SURFACE GENERATION')
READ(5,*)AUTO
IF(AUTO.NE.1.)GOTO 950
WRITE(6,1600)
1600 FORMAT(' INPUT INCREMENT, NUMBER OF ITERATIONS, SUB CENTER (X,Y),
&AND MAIN CENTER (X,Y)')
READ(5,*)DIFFY,KUTIME,CENTX,CENTY,CEMTX,CEMTY
WRITE(6,1700)
1700 FORMAT(' INPUT 1 FOR SUBREFLECTOR POINTS, 0 FOR MAIN REFLECTOR, OR
& 2 FOR BOTH')
READ(5,*)SUBMN
WRITE(6,1800)
1800 FORMAT(' INPUT 0 TO SUPRESS OUTPUT')
READ(5,*)SUP
IF(SUP.EQ.0.)OP=OUTPUT
WRITE(6,1900)
1900 FORMAT(' ENTER 0 FOR HYPERBOLIC CUTS')

C
C *** IF A SURFACE IS TO BE CREATED AUTOMATICALLY, THE STARTING
C POINTS IN THE TRANSVERSE PLANE MUST BE SPECIFIED. THIS IS
C ACCOMPLISHED EITHER BY SUPPLYING A SIXTH ORDER 'CUT POLYNOMIAL'
C OR BY USING AN EQUIVALENT 2-DIMENTIONAL CASSEGRAIN, FOR WHICH
C THE CUT POLYNOMIAL IS A HYPERBOLA. IN THIS CASE, THE NEW
C STARTING Z-VALUE IS DERIVED EACH CYCLE (ACCEPT FOR THE FIRST).
C

C
C READ(5,*)IHYPCT
C IF(IHYPCT.EQ.0)GOTO 950
C WRITE(6,2000)
2000 FORMAT(' ENTER 7 COEFFICIENTS OF THE CUT POLYNOMIAL')
C READ(5,*)POFSET
C **** CHECK TO SEE IF THE CUT POLYNOMIAL IS AN EVEN FUNCTION***
C IF(POFSET(2).GT..00001.OR.POFSET(4).GT..00001.OR.POFSET(6).
& GT..00001)KUTSYM=0
C GOTO 950

```

900 NTIT=NTIT+1
C     **** COUNT THE NUMBER OF CURVES GENERATED, AND STOP WHEN THE
C     * LIMIT IS REACHED.
      IF(NTIT.GT.KUTIME)GOTO 910
      WRITE(6,2100)NTIT
2100 FORMAT('1'//' AUTO GENERATOR NUMBER ',I3/' _____',
&         ' _____ '/')
C
C     *** THE FIRST CURVE GENERATED IS IN THE X-Z PLANE. SUCCEEDING
C     CURVES ALL START FROM A POINT ON THE CUT POLYNOMIAL, WHICH
C     LIES IN THE Y-Z PLANE.
C
910 S1(2)=DIFFY+S1(2)
C     *** INCREMENT THE Y VALUE OF THE STARTING POINT, UNTIL THE LIMIT
C     * IS REACHED. THE X VALUE AND THE X-NORMAL ARE/WERE FOUND AFTER
C     * THE FIRST CALL TO BIFOFF.
      S1(1)=CENTX2
      SN1(1)=CNX2
      TOP=DIFFY*(KUTIME-1)
      IF(S1(2).GT.TOP)GOTO 250
      IF(IHYPCT.EQ.0)GOTO 920
C
C     *** IF A USER SUPPLIED CUT POLYNOMIAL IS USED, FIND THE VALUE OF
C     * OF Z CORRESPONDING TO THE NEW Y VALUE BY CALLING THE FUNCTION
C     * EVALUATING SUBROUTINE.
C     * SINCE THE CUT POLYNOMIAL SHAPE DOES NOT DEPEND ON THE
C     * CONSTANT TERM, IT IS SET TO THE Z VALUE OF THE FIRST CURVE
C     * WHERE X IS HALF OF CENTX. (ZTRANS IS ASSIGNED AFTER THE FIRST
C     * CALL TO BIFOFF.)
C
      POFSET(1)=ZTRANS
      PRINT *,POFSET
      CALL FUNC(S1(2),S1(3),SN1(2),NORD,POFSET)
      GOTO 950
C     ****FOR HYPERBOLOID WITH FP=.368 C+A=.32 H=.117****
C     * SUCCESSIVE VALUES OF THE STARTING POINTS ARE CALCULATED FOR
C     * THE HYPERBOLOID CASE.
920 A=.17
      C=.25
      B=SQRT(C**2-A**2)
C     *** FOR A HYPERBOLOID WITH PARAMETERS A, B, C, THE HYPERBOLA
C     * THAT RESULTS FROM THE INTERSECTION OF A PLANE X=CENTX/2 TRANS-
C     * LATED SO THAT IT INTERSECTS THE FIRST BIFOCAL CURVE IS:
      XDIP=(CENTX/2./B)**2
      SS13=SQRT((S1(2)/B)**2+1+XDIP)
      S1(3)=A*(SS13-SQRT(1+XDIP))+ZTRANS
      SN1(2)=A/B/B*S1(2)/SS13
C     *** HAVING DETERMINED THE NEW VALUES OF Y, Z, AND THE Y-NORMAL

```

```

C      * OF THE SUBREFLECTOR STARING POINT, REINITIALIZE THE X VALUE
C      * AND X-NORMAL.
C
950 CONTINUE
C      *** NORMALIZE THE NORMAL VECTOR (DIVIDE EACH COMPONENT BY THE
C      * MAGNITUDE).
      FNORM=0.
      DO 15 I=1,3
15  FNORM=SN1(I)**2+FNORM
      DO 16 I=1,3
16  SN1(I)=SN1(I)/SQRT(FNORM)
C
C      *** FIND THE POINTS OF THE BIFOCAL SYSTEM WITH THE ABOVE DEFINED
C      * STARTING PARAMETERS.
C
      CALL BIFOFF(S1,SN1,FI1,FI2,ALPH1,ALPH2,BET1,BET2,XL,C1,C2,P,AUTO,
&  NTIT)
C      *** FIND THE Z VALUE OF THE FIRST BIFOCAL CURVE AT X=CENTX/2
C      PRINT *, P
      CNTX2=CENTX/2.
      IF(NTIT.NE.1)GOTO 22
      CALL FUNC(CNTX2,ZTRANS,CNX2,NORD,P)
C      PRINT *,CNTX2,ZTRANS,CNX2
C      *** STORE THE FIRST CUT POLYNOMIAL (IN X,Z) FOR BOTH REFLECTORS
C      * FOR USE IN FOURTH-ORDER SURFACE FITTING (SUBROUTINE FITFOR).
      DO 21 LDEX=1,5
      XS4(LDEX)=PPROJ(LDEX,1,1)
21  XM4(LDEX)=PPROJ(LDEX,1,2)
22  IF(NITER.LE.1)GOTO 110
C
C      FIND NEXT Z AND SURFACE NORMAL, GIVEN A NEW
C      X OR Y, USING THE POLYNOMIAL RETURNED FROM THE CALL TO BIFOFF.
C
      DO 24 ISX=1,3
      SX1(ISX)=S1(ISX)
24  SNX1(ISX)=SN1(ISX)
      X=S1(1)
      Y=S1(2)
      DO 100 I=2,NITER
      IF(OUTPUT)WRITE(6,*)SX1,SNX1
      Y=Y+DELY
      X=X+DELX
      CALL BIFOFF(SX1,SNX1,FI1,FI2,ALPH1,ALPH2,BET1,BET2,XL,C1,C2,E,
&  AUTO,NTIT)
      ZX=0.
      ZY=0.
      IF(OUTPUT)PRINT *,P
C      *** DETERMINE WHETHER THE X OR Y VALUE WAS INCREMENTED, AND CALL

```

```

C      * THE RESPECTIVE FUNCTION EVALUATOR.
      IF(DELY.NE.0.)GOTO 25
      CALL FUNC(X,Z,ZX,NORD,P)
      GOTO 30
25 CALL FUNC(Y,Z,ZY,NORD,P)
30 CONTINUE
C      *** NORMALIZE THE NEW STARTING SURFACE NORMAL.
      DIV=SQRT(1+ZX*ZX+ZY*ZY)
      SNX1(1)=ZX/DIV
      SNX1(2)=ZY/DIV
      SNX1(3)=-1./DIV
      SX1(1)=X
      SX1(2)=Y
      SX1(3)=Z
100 P2D(I,1)=1.
110 CONTINUE
C
C      *** CYCLE BACK TO GENERATE ANOTHER CURVE.
      IF(AUTO.EQ.1)GOTO 900
      GOTO 500
C      *** IF THE LAST CURVE HAS BEEN GENERATED PERFORM SURFACE
C      * MANIPULATIONS.
250 IF(AUTO.NE.1)GOTO 500
      NGRID=15
C      *** PLOTTING SECTION
450 NGRAF=NGRID*2
      WRITE(6,2500)
2500 FORMAT('1DO YOU WANT A PLOT? (1 FOR YES)')
      READ(5,*)NPLT
      IF(NPLT.EQ.1)CALL GRAF3(ZDRAW,NGRAF)
C
C      *** ASK TO IF OUTPUT OF Z AND Y VALUES IN ORIGINAL FORM IS
C      * REQUIRED. THIS IS PRIMARILY FOR DEBUGGING TO CHECK IF THE
C      * CORRECT Y VALUES ARE USED.
      WRITE(6,2600)
2600 FORMAT('1ENTER 1 FOR SAMPLE OUTPUT')
      READ(5,*)SAMOUT
      IF(SAMOUT.NE.1.)GOTO 260
      WRITE(6,2700)((Y1(L,I,J,1),J=1,15),I=1,15),L=1,4)
      WRITE(6,2700)((ZSURF(L,I,J,1),J=1,15),I=1,15),L=1,4)
2700 FORMAT(15(1X,F7.3))
C
C      *** FIND SURFACE PARTIAL IN THE Y DIRECTION FOR EACH SURFACE
C
260 ISIZE=(NGRID+1)/4
C      *** SUBMN IS 0 FOR SUB., 1 FOR MAIN REFL., AND 2 FOR BOTH.
C      * IF IT IS 2 START THE ISMN LOOP.
      ISMN=SUBMN+1

```

```
DO 490 IS=1,2
IF(SUBMN.NE.2.)GOTO 265
ISMN=IS
```

```
C
C   *** FOR EACH INTESECTION OF THE SURFACE WITH PLANES X=CONSTANT,
C   * SAMPLE THE Z VALUES FOR SEVERAL Y VALUES. THEN FIND THE BEST
C   * FIT CURVE TO THE SET OF Y-Z POINTS USING THE INTERPOLATION
C   * SUBROUTINE.
C   * INCX IS THE VALUE OF X, CONSTANT FOR THE Y-Z PLANE CUTTING THE
C   * SURFACE.
C   * IHALF IDENTIFIES THE RIGHT OR LEFT HALF SPACE, X>0, OR X<0
C   * ITIME IDENTIFIES THE RIGHT OR LEFT HALF SPACE, Y>0, OR Y<0
C   * ISPACE COUNTS THE NUMBER OF SAMPLES IN EACH Y HALF SPACE.
C   * KQUAD IDENTIFIES THE QUADRANT NUMBER.
C   * LINDEX COUNTS THE NUMBER OF NON-ZERO SAMPLES FOR EACH X-PLANE
```

```
C
C 265 CONTINUE
```

```
PRINT *,ISMN,SUBMN
DO 300 INCX=1,NGRID
```

```
C   *** INCX IS THE SPACING OF X VALUES ALONG A PARTICULAR CUT.
C   * IHALF IDENTIFIES THE POSITIVE (1) AND NEGATIVE (2)
C   * X HALF PLANES.
```

```
DO 300 IHALF=1,2
```

```
C   *** FIND THE SAMPLES IN Y AND THE CORRESPONDING Z(Y), BUT ONLY
C   * FOR THE ODD NUMBERED CUTS. USE THE PREVIOUSLY CALCULATED
C   * Z(Y) FOR EVEN NUMBERED CUTS.
```

```
IF(MOD(INCX,2).EQ.0)GOTO 287
```

```
LINDEX=1
```

```
C   *** INITIALIZE THE SAMPLE ARRAYS.
```

```
DO 270 INDEW=1,7
```

```
YSAMPL(INDEW)=0.
```

```
270 ZSAMPL(INDEW)=0.
```

```
C
C DO 280 ITIME=1,2
```

```
DO 280 ISPACE=1,3
```

```
KQUAD=ITIME+2*IHAF-2
```

```
YSAMPL(1)=0.
```

```
ZSAMPL(1)=ZSURF(KQUAD,INCX,1,ISMN)
```

```
C   *** INCY IS THE SPACING OF Y-SAMPLES WITHIN EACH PLANE.
```

```
INCY=ISIZE*ISPACE+1
```

```
C   *** THE FOUR ARGUMENTS OF Y1, ZSURF, AND ZY1, ARE THE QUADRANT
```

```
C   * NUMBER, THE X-COORDINATE, THE Y-COORDINATE, AND SUB OR MAIN #.
```

```
IF(Y1(KQUAD,INCX,INCY,ISMN).EQ.0.)GOTO 280
```

```
IF(OUTPUT)PRINT *,Y1(KQUAD,INCX,INCY,ISMN)
```

```
IF(ZSURF(KQUAD,INCX,INCY,ISMN).EQ.0.)GOTO 280
```

```
C   *** LINDEX IS INCREMENTED EVERY TIME BOTH THE Y AND Z VALUES ARE
```

```
C   * NON-ZERO.
```

```
LINDEX=LINDEX+1
```



```

      YSAMPL(LINDEX)=Y1(KQUAD, INCX, INCY, ISMN)
      ZSAMPL(LINDEX)=ZSURF(KQUAD, INCX, INCY, ISMN)
280 CONTINUE
C
C      *** IF THE LAST TWO Z SAMPLES ARE TOO CLOSE, THE INTERPOLATING
C      * FUNCTION WILL BLOW UP.  IF SO, FLUSH THE LAST VALUE.
      IF(ABS(ZSAMPL(6)-ZSAMPL(7)).LT..00005.AND.ZSAMPL(7).NE.0.)
&      LINDEX=LINDEX-1
      IF(SAMOUT.NE.1)GOTO 285
      OP=.TRUE.
      WRITE(6,2800)YSAMPL,ZSAMPL
2800 FORMAT(//' YSAMPLE',7(1X,F8.4)/' ZSAMPLE',7(1X,F8.4))
      285 CALL INTERP(LINDEX,YSAMPL,ZSAMPL,PY,OP)
      287 CONTINUE
      PRINT *,PY
C
C      *** CALCULATE DZ(X,Y)/DY GIVEN Z=F(Y).
C      * IHALF CONTINUES TO IDENTIFIES THE X HALF SPACE IN THIS OUTER
C      * LOOP.
C      * ITIME ONCE AGAIN IDENTIFIES THE Y HALF SPACE.
C      * KO IS THE COUNTER FOR THE POINTS IN THE Y DIRECTION, FOR EACH
C      * HALF PLANE, ALONG EACH X PLANE.
C
      DO 300 ITIME=1,2
      KQUAD=ITIME+2*IHALF-2
      DO 300 KO=1,NGRID
C
C      *** ZY1 WILL HOLD THE VALUES OF THE PARTIAL IN THE Y DIRECTION.
C      * THIS VALUE IS OBTAINED BY SUMMING THE DERIVATIVES OF EACH
C      * TERM OF THE FUNCTION DETERMINED FROM INTERPOLATING THE SAMPLES
C
      ZY1(KQUAD, INCX, KO, ISMN)=PY(2)
      DO 290 I=3,7
      ZY1(KQUAD, INCX, KO, ISMN)=ZY1(KQUAD, INCX, KO, ISMN)+
&      (I-1)*PY(I)*Y1(KQUAD, INCX, KO, ISMN)**(I-2)
290 CONTINUE
C      *** IF THE OBTAINED VALUES ARE VERY SMALL, SET THEM TO ZERO.
      IF(ABS(ZY1(KQUAD, INCX, KO, ISMN)).LT..000001)ZY1(KQUAD, INCX, KO, ISMN)
&=0.
      300 CONTINUE
C
C      ****OUTPUT ACCUMULATED RESULTS ****
      CALL TYP0UT(ZSURF,NGRID, ISMN)
      CALL TYP0UT(ZXSURF,NGRID, ISMN)
      CALL TYP0UT(ZY1,NGRID, ISMN)
C
      485 IF(SUBMN.NE.2.)GOTO 495
      490 CONTINUE

```

```

C
C *****SET UP FILES FOR GAP IF DESIRED *****
  495 WRITE(6,3000)
 3000 FORMAT(' INPUT 1 TO SET UP FINITE ELEMENT FILE FOR GAP')
      READ(5,*)FELEM
      IF(FELEM.NE.1)GOTO 498
      CALL ELEM(NGRID,JBDY)
      CALL GRIDP(NGRID,JBDY,XPSS,Y1,ZSURF,ZXSURF,ZY1,2)
  498 WRITE(6,3400)
 3400 FORMAT(' DO YOU WANT TO APPROXIMATE THE SURFACES WITH A FOURTH-OR
&ER POLYNOMIAL?')
      READ(5,*)APROX
      IF(APROX.NE.1.)GOTO 500
      CALL FITFOR(30,XPLT,YPLT,ZDRAW,XS4,XM4)
C
C *****CYCLE BACK TO REPEAT ENTIRE PROCESS *****
  500 WRITE(6,3500)
 3500 FORMAT('LAGAIN?, (1 FOR YES)')
      READ(5,*)NANS
      IF(NANS.EQ.1)GOTO 5
      STOP
      END
C
C
C *****ITERATIVE OFFSET BIFOCAL CURVE GENERATION SUBROUTINE *****
C-----
C          GIVEN A STARTING SUBREFLECTOR POINT AND ITS NORMAL, AND THE
C          CHARACTERISTIC PARAMETERS OF THE ANTENNA SYSTEM, A SET OF POINTS
C          IS GENERATED FOR BOTH A SUBREFLECTOR AND A MAIN REFLECTOR.
C          THE POINTS LIES ON A PARTICULAR CURVE IN SPACE. THE MAIN
C          PROGRAM CALLS THIS SUBROUTINE SEVERAL TIMES VARYING THE STARTING
C          POINTS AND THEN FITS A SURFACE TO THE CURVES.
C          BIFOFF CALLS SEVERAL OTHER SUBROUTINES.
C          * NORMAL * -- WHICH FINDS THE NORMAL TO A POINT, GIVEN AN
C          INCIDENT AND REFLECTED VECTOR.
C          * SNELL * -- WHICH FINDS THE REFLECTED VECTOR AT A POINT, GIVEN
C          THE INCIDENT VECTOR AND THE NORMAL AT THAT POINT.
C          * INTERP * -- WHICH FITS A 2-DIMENSIONAL CURVE TO A PROJECTION
C          OF THE GENERATED POINTS.
C          * POINTS * -- WHICH TRANSFORMS THE PROJECTED CURVES INTO A SPACE
C          CURVE AND PREPARES THE RESULTS FOR STORAGE
C-----
C
C
C          SUBROUTINE BIFOFF(S1,SN1,FI1,FI2,ALPH1,ALPH2,BET1,BET2,XL,C1,C2,
&          PPASS,AUTO,ITIME)
C
C          DIMENSION FI1(3),FI2(3),SN1(3),S1(3),S(10,3),XM(10,3),SN(10,3),

```

```

&   XMN(10,3),DUMMY(7),RT(10,3),R1(10,3),R2(10,3),R3(10,3),
&   R1P(10,3),R2P(10,3),R3P(10,3),SNP(10,3),XORY(10),ZORY(10),
&   Z(4,20,20),ZX(4,20,20),XPASS(4,20),Y(4,20,20),
&   PARRAY(7),RARRAY(7),PPASS(7),PP(7,2),QP(7,2),
&   XPLOT(30),YPLOT(30),ZPLOT(30,30)
C
COMMON OP,ZSURF(4,20,20,2),ZXSURF(4,20,20,2),ZDRAW(30,30,2),
&   CENTX,CENTY,KUTSYM,JBDY(20),PPROJ(7,20,2),QPROJ(7,20,2),
&   XPSS(4,20,2),CEMTX,CEMTY,YONE(4,20,20,2),
&   XPLT(30,2),YPLT(30,2)
C
LOGICAL OUTP/.FALSE./,OP
C   *** OP IS AN OUTPUT DISABLE.  IF IT IS PASSED AS "FALSE",
C   * CERTAIN WRITES ARE IGNORED.
IF(OP)WRITE(6,15)FI1,FI2,S1,SN1
15 FORMAT('1INITIAL FOCAL POINTS',2(2X,3(2X,F7.5))/' 1ST SUBREFLECTOR
&   POINT',2X,3(2X,F7.5))/' 1ST SUBREFLECTOR NORMAL',4X,3(F8.5,2X))
IF(OP)WRITE(6,20)ALPH1,ALPH2,BET1,BET2,XL,C1,C2
20 FORMAT(1X,'ALPHA1 ALPHA2 BETA1 BETA2 L C1 C2'/1X,
&   4(F6.2,2X),F6.3,1X,F6.3,1X,F6.3)
IF(OP)WRITE(6,35)
35 FORMAT('1',//,' SUBREFECTOR POINTS SUBREFECTOR NORMAL',5X,
&   'MAIN REFECTOR POINTS MAIN REFLECTOR NORMAL'/1X)
ALPH1=ALPH1*3.14159/180.
ALPHA2=ALPH2*3.14156/180.
BETA1=BET1*3.14159/180.
BETA2=BET2*3.14159/180.
DO 40 I=1,7
40 PARRAY(I)=0.
C   *** ONLY 5 POINTS ARE NECESSARY FOR DEFINING A CURVE OF UP TO 4TH
C   * ORDER.  CYCLE THROUGH THE TRANSMIT/RECEIVE ANALYSIS 5 TIMES.
DO 1000 K=1,5
C
C   ***TRANSMIT CASE***
C
DEN=0.
C   *** LOAD INPUT VALUES AND UNITIZE THE FIRST TRANSMIT VECTOR.
DO 50 I=1,3
S(1,I)=S1(I)
SN(1,I)=SN1(I)
RT(K,I)=S(K,I)-FI1(I)
50 DEN=DEN+RT(K,I)**2
DENOM=SQRT(DEN)
DO 60 I=1,3
60 R1(K,I)=RT(K,I)/DENOM
C   *** THE NORMAL AND INCIDENT VECTOR ARE USED TO FIND THE FIRST
C   * REFLECTED VECTOR.
CALL SNELL(R1,SN,R2,K)

```

```

C     *** LOAD THE 2ND REFLECTED VECTOR (WHICH IS NORMAL TO THE
C     * APERTURE PLANE).
      DENR3=1.-(SIN(ALPHA1)*SIN(BETA1))**2
      R3(K,1)=SIN(ALPHA1)*COS(BETA1)/DENR3
      R3(K,2)=COS(ALPHA1)*SIN(BETA1)/DENR3
      R3(K,3)=COS(ALPHA1)*COS(BETA1)/DENR3
C     *** FIND THE NORMAL AT THE MAIN REFLECTOR POINT.
      CALL NORMAL(R3,R2,XMN,K)
C     *** FIND THE LENGTH OF THE FIRST REFLECTED VECTOR
      P=1.-(R2(K,1)*R3(K,1)+R2(K,2)*R3(K,2)+R2(K,3)*R3(K,3))
      Q=(C1-S(K,1))*R3(K,1)+(C2-S(K,2))*R3(K,2)-S(K,3)*R3(K,3)
      DISTR2=(XL-DENOM-Q)/P
C     WRITE(6,*)P,Q,DENOM,DISTR2
      DO 70 I=1,3
C     *** FIND THE KTH POINT OF THE MAIN REFLECTOR BY ADDING THE
C     * FIRST REFLECTED VECTOR TO THE SUBREFLECTOR POINT.
70    XM(K,I)=R2(K,I)*DISTR2+S(K,I)
C
C     ***RECEIVE CASE***
C
      DENR3P=1.-(SIN(ALPHA2)*SIN(BETA2))**2
      R3P(K,1)=SIN(ALPHA2)*COS(BETA2)/DENR3P
      R3P(K,2)=COS(ALPHA2)*SIN(BETA2)/DENR3P
      R3P(K,3)=COS(ALPHA2)*COS(BETA2)/DENR3P
C     *** AFTER LOADING THE SECOND REFLECTED VECTOR, AND HAVING JUST
C     * FOUND THE MAIN REFLECTOR NORMAL, FIND THE FIRST REFLECTED
C     * VECTOR.
      CALL SNELL(R3P,XMN,R2P,K)
C     *** COMPUTE THE LENGTH OF THE FIRST REFLECTED VECTOR.
      DISR3P=(C1-XM(K,1))*R3P(K,1)+(C2-XM(K,2))*R3P(K,2)
&      -XM(K,3)*R3P(K,3)
      A=XL-DISR3P
      AA=FI2(1)-XM(K,1)
      BB=FI2(2)-XM(K,2)
      CC=FI2(3)-XM(K,3)
      B=AA*AA+BB*BB+CC*CC
      C=AA*R2P(K,1)+BB*R2P(K,2)+CC*R2P(K,3)
      DISR2P=.5*(A*A-B)/(A+C)
C     WRITE(6,*)DISR3P,A,B,C,DISR2P
      DO 130 I=1,3
C     *** FIND THE NEXT SUBREFLECTOR POINT BY ADDING THE 1ST REFLECT
C     * TO THE MAIN REFLECTOR POINT.
130   S(K+1,I)=XM(K,I)-DISR2P*R2P(K,I)
C
      DENP=0.
      DO 110 I=1,3
C     *** FIND THE FIRST VECTOR, KNOWING THE SUBREFLECTOR POINT AND
C     * THE RECEIVE FOCUS.

```

```

      RT(K,I)=S(K+1,I)-FI2(I)
110 DENP=DENP+RT(K,I)**2
      DENOMP=SQRT(DENP)
C      *** NORMALIZE AND FIND THE SUBREFLECTOR NORMAL
      DO 120 I=1,3
120 R1P(K,I)=RT(K,I)/DENOMP
      CALL NORMAL(R2P,R1P,SNP,K)
      DO 150 I=1,3
150 SN(K+1,I)=SNP(K,I)
C
      IF(OP)WRITE(6,23)(S(K,I),I=1,3),(SN(K,I),I=1,3),(XM(K,I),I=1,3),
&      (XMN(K,I),I=1,3)
23  FORMAT(1X,4(F6.3,1X,F6.3,1X,F6.3,4X))
1000 CONTINUE
      IF(.NOT.OUTP)GOTO 200
      WRITE(6,25)((R1(K,I),I=1,3),(R1P(K,I),I=1,3),K=1,5)
      WRITE(6,25)((R2(K,I),I=1,3),(R2P(K,I),I=1,3),K=1,5)
      WRITE(6,25)((R3(K,I),I=1,3),(R3P(K,I),I=1,3),K=1,5)
25  FORMAT(1X,2(5X,3(F6.3,2X)))
C
C      ****PROJECTION AND POINT GENERATION*****
C
C      *** THIS SUBSECTION OF BIFOFF SETS UP AND ACCUMULATES POINTS ON
C      * BOTH SURFACES BY CALLING 'POINTS'.
C
200 CONTINUE
      PROJY=0.
      ISYM=0
      NUMPTS=5
C      *** ALL 5 OF THE GENERATED SUB- OR MAIN REFLECTOR POINTS ARE
C      * USE FOR THE OFFSET CASE.
C      * IF THE SYSTEM IS SYMMETRICAL, HOWEVER, 7 OF THE POINTS
C      * CAN BE USED. THIS IS SO, SINCE 3 OF THE PAIRS ARE SIMPLY
C      * MIRROR IMAGES OF THOSE GENERATED (ONE IS ON THE AXIS).
      IF(FI1(1).NE.-FI2(1).OR.FI1(2).NE.FI2(2).OR.FI1(3).NE.FI2(3))
&      GOTO 210
C      *** SET A FLAG IF IT IS A SYMMETRIC SYSTEM.
      ISYM=2
      NUMPTS=4
C      *** IF A SURFACE IS BEING GENERATED, SET THE AUTOMATIC PRO-
C      * JECTION VALUE 'PROJ' TO 1, THEN 3 (X-Z, AND X-Y PROJECTIONS).
210 IF(AUTO.NE.1.)GOTO 220
      DO 250 IAUTO=1,3,2
      PROJ=IAUTO
      GOTO 230
C      *** WRITE OUT A PROMPT IF NOT AUTOMATIC.
220 WRITE(6,225)
225 FORMAT('LAGRANGE INTERPOLATION CURVFITTING'/' WHICH PROJECTION

```

```

&      (ENTER 1 FOR X-Z; 2 FOR Y-Z; 3 FOR X-Y)')
      READ(5,*)PROJ
230 IF(PROJ.NE.3.)GOTO 235
C     *** IF A X-Y PROJECTION IS DESIRED, RESET PROJ TO 1 (FOR X
C     * VALUES), AND SET PROJY TO 1 (FOR Y VALUES).
      PROJ=1.
      PROJY=1.
235 CONTINUE
      DO 240 IPONT=1,NUMPTS
C     *** IF PROJ IS 1, LOAD XORY (X OR Y) WITH THE X-COORDINATES,
C     * IF IT IS 2, LOAD THE Y-COORDINATES.
      XORY(IPONT)=S(IPONT,1)*(2.-PROJ)+S(IPONT,2)*(PROJ-1.)
C     *** IF PROJY IS 1, LOAD ZORY WITH THE Y-COORDINATES, ZERO FOR
C     * Z-COORDINATES.
      ZORY(IPONT)=S(IPONT,3)*(1.-PROJY)+S(IPONT,2)*PROJY
      IF(ISYM.NE.2)GOTO 240
C     *** REFLECT THE POINTS ABOUT THE Z-AXIS IF THE SYSTEM IS
C     * SYMMETRIC.
      XORY(IPONT+3)=-XORY(IPONT)
      ZORY(IPONT+3)=ZORY(IPONT)
240 CONTINUE
C     WRITE(6,*)XORY,ZORY
      NCAL=5+ISYM
C     *** THE TOTAL NUMBER OF POINTS IS 5 FOR OFFSET, 7 FOR SYMMETRIC
C     * CALCULATE THE BEST 4TH OR 6TH ORDER POLYNOMIAL FITTING THE
C     * SUBREFLECTOR POINTS GENERATED ABOVE. STORE THE RESULT IN
C     * PARRAY.
      CALL INTERP(NCAL,XORY,ZORY,PARRAY,OP)
C     *** STORE THE FIRST SUB POLYNOMIAL IN PPASS, TO BE PASSED TO
C     * THE MAIN PROGRAM FOR THE CURVE VERIFICATION AND INITIAL POINT
C     * DERIVATION.
      IF(IAUTO.EQ.3)GOTO 244
      DO 243 LCONT=1,7
243 PPASS(LCONT)=PARRAY(LCONT)
C     *** REPEAT THE ABOVE PROCEDURE FOR MAIN REFLECTOR POINTS, WITH
C     * PARRAY HOLDING THE 4TH OR 6TH ORDER POLYNOMIAL.
C     * RECALL THAT XM HOLDS THE MAIN REFLECTOR POINTS.
244 DO 245 IPONT=1,NUMPTS
      XORY(IPONT)=XM(IPONT,1)*(2.-PROJ)+XM(IPONT,2)*(PROJ-1.)
      ZORY(IPONT)=XM(IPONT,3)*(1.-PROJY)+XM(IPONT,2)*PROJY
      IF(ISYM.NE.2)GOTO 245
C     *** WHILE THE FIRST SUBREFLECTOR POINT LIES ON THE Z-AXIS, NONE
C     * OF THE MAIN REFLECTOR POINTS ARE, AND SO THEY CAN ALL BE
C     * REFLECTED ABOUT IT.
      XORY(IPONT+4)=-XORY(IPONT)
      ZORY(IPONT+4)=ZORY(IPONT)
245 CONTINUE
C     WRITE(6,*)XORY,ZORY

```

```

NCAL=5+ISYM
C   *** 7 POINTS IS THE MAXIMUM NUMBER THAT CAN BE SENT TO INT
CALL INTERP(NCAL,XORY,ZORY,RARRAY,OP)
DO 242 ISMN=1,2
DO 242 IND=1,7
IF(IAUTO.EQ.3)GOTO 1241
C   *** ISMN IS 2 IF A SUBREFLECTOR SURFACE IS TO BE CONSTRUCTED
C   * 1 FOR A MAIN REFLECTOR SURFACE. PPROJ STORES X-Z.
C   * GO TO 1241 AND USE QPROJ FOR X-Y POLYNOMIALS.
1240 PPROJ(IND,ITIME,ISMN)=PARRAY(IND)*(ISMN-1)+RARRAY(IND)*(2-ISMN)
PP(IND,ISMN)=PPROJ(IND,ITIME,ISMN)
GOTO 242
C   *** STORE THE X-Y PROJECTION. 1241 IS REACHED WHEN IAUTO=3
C   * THE LAST ARG. IN PPROJ AND QPROJ DETERMINES WHICH SURFACE
1241 QPROJ(IND,ITIME,ISMN)=PARRAY(IND)*(ISMN-1)+RARRAY(IND)*(2-ISMN)
QP(IND,ISMN)=QPROJ(IND,ITIME,ISMN)
C   PRINT *,ISMN,PP,QP
242 CONTINUE
250 CONTINUE
IF(AUTO.NE.1.)GOTO 290
C   *** IF A SURFACE IS BEING GENERATED, CONVERT THE PROJECTED
C   * CURVES TO SPACE CURVES, AND RETAIN ONLY THE PORTIONS WITHIN
C   * A CIRCULAR BOUNDARY CENTERED AT (CENTX,CENTY).
C   * Z WILL CONTAIN SURFACE INFORMATION SUITABLE FOR FINITE
C   * ELEMENT ANALYSIS.
C   * ZX WILL CONTAIN THE SURFACE PARTIALS IN THE X DIRECTION
C   * THE SAME POINTS WHERE Z IS SPECIFIED.
C   * ZPLOT WILL CONTAIN SURFACE INFORMATION USED FOR PLOTTING
C   * NUMERICALLY CONTROLLED MILLING MACHINE DATA.
DO 280 ISMN=1,2
IF(ISMN.EQ.1) GOTO 253
C
CALL POINTS(PP,QP,XPASS,Y,Z,XPLOT,YPLOT,ZPLOT,ZX,KUTSYM,
& CENTX,CENTY,ISMN,JBDY)
GOTO 254
C
253 CALL POINTS(PP,QP,XPASS,Y,Z,XPLOT,YPLOT,ZPLOT,ZX,KUTSYM,
& CEMTX,CEMTY,ISMN,JBDY)
254 DO 255 MX=1,15
C   *** THE FOLLOWING WRITES ARE FOR DEBUGGING PURPOSES. THEY
C   * THE VALUES RECENTLY OBTAINED FROM POINTS.
IF(.NOT.OUTP)GOTO 255
WRITE(6,1260)MX,(ZPLOT(MX,MY),MY=8,18)
WRITE(6,1260)MX,(Z(1,MX,MY),MY=1,10)
WRITE(6,1260)MX,(ZX(1,MX,MY),MY=1,10)
1260 FORMAT(' Z, ZPLOT',1X,I2,1X,10(F6.4,1X))
255 CONTINUE
256 CONTINUE

```

```

C      WRITE(6,2000) ISMN
2000  FORMAT(' SURFACE TYPE ',I2)
      DO 2560 IPLT=1,30
      XPLT(IPLT, ISMN)=XPLOT(IPLT)
2560  YPLT(IPLT, ISMN)=YPLOT(IPLT)
C      PRINT *, ISMN
C      *** ASSEMBLE A SURFACE BY ADDING THE Z VALUES OBTAINED IN POINTS
C      * TO THE SURFACE ARRAY ON A POINT-BY-POINT BASIS. DO THE SAME
C      * WITH THE SURFACE NORMALS IN THE X-DIRECTION.
      DO 270 IQ=1,30
      DO 270 JQ=1,30
      DO 260 KQ=1,4

C      *** THE SAME LOOPS ARE BEING USED FOR SETTING UP BOTH TRIANGLE
C      * OUTPUT AND CARTESIAN (FOR PLOTTING) OUTPUT. SKIP THE TRIANGLE
C      * SECTION WHEN THE LOOP INDEX GETS TOO HIGH.

      IF(IQ.GT.20.OR.JQ.GT.20)GOTO 260
C      *** ACCUMULATE THE X AND Y VALUES.
      XPSS(KQ, IQ, ISMN)=XPASS(KQ, IQ)
      YONE(KQ, IQ, JQ, ISMN)=Y(KQ, IQ, JQ)
      IF(ABS(ZSURF(KQ, IQ, JQ, ISMN)).LT..00001.OR.
&      ABS(Z(KQ, IQ, JQ)).LT..00001)GOTO 257
C      *** IF A Z VALUE FOR THE SURFACE ALREADY EXISTS, IT IS BECAUSE
C      * THE CURVES ARE VERY CLOSE TOGETHER. TAKE THE AVERAGE OF THE
C      * NEW AND OLD VALUES.
      ZSURF(KQ, IQ, JQ, ISMN)=(ZSURF(KQ, IQ, JQ, ISMN)+Z(KQ, IQ, JQ))/2.
      ZXSURF(KQ, IQ, JQ, ISMN)=(ZXSURF(KQ, IQ, JQ, ISMN)+ZX(KQ, IQ, JQ))/2.
      GOTO 260
257  ZSURF(KQ, IQ, JQ, ISMN)=ZSURF(KQ, IQ, JQ, ISMN)+Z(KQ, IQ, JQ)
      ZXSURF(KQ, IQ, JQ, ISMN)=ZXSURF(KQ, IQ, JQ, ISMN)+ZX(KQ, IQ, JQ)
260  CONTINUE
C      *** REPEAT THE ABOVE PROCEDURE FOR SURFACE POINTS STORED IN
C      * ZPLOT
      IF(ZDRAW(IQ, JQ, ISMN).EQ.0..OR.ZPLOT(IQ, JQ).EQ.0.)GOTO 265
      ZDRAW(IQ, JQ, ISMN)=(ZDRAW(IQ, JQ, ISMN)+ZPLOT(IQ, JQ))/2.
      GOTO 270
265  ZDRAW(IQ, JQ, ISMN)=ZDRAW(IQ, JQ, ISMN)+ZPLOT(IQ, JQ)
270  CONTINUE
280  CONTINUE
C      *** THE NEXT SET OF WRITES CHECK THE ACCUMULATE VALUES AS THE
C      * ARE ACCUMULATED. THEY ARE USED TO CHECK IF THE SPACING OF
C      * CURVES IS TOO WIDE.
      IF(.NOT.OUTP)GOTO 350
      WRITE(6,1270)((ZDRAW(IF, JF, ISMN), JF=8, 17), IF=1, 30), ISMN=1, 2)
      WRITE(6,1270)((ZSURF(1, IF, JF, ISMN), JF=1, 10), IF=1, 15), ISMN=1, 2)
      WRITE(6,1270)((ZXSURF(1, IF, JF, ISMN), JF=1, 10), IF=1, 15), ISMN=1, 2)
1270  FORMAT('1', 15(10(2X, F6.3)/))

```



```

      GOTO 350
C     *** ARRIVE AT 290 IF ONLY ONE CURVE IS GENERATED (NO SURFACE).
290  WRITE(6,1280)
1280  FORMAT('ANOTHER PROJECTION? (ENTER 1 FOR YES)')
      READ(5,*)ANSP
      IF(ANSP.EQ.1.)GOTO 200
350  RETURN
      END

C     *** FIND THE REFLECTED VECTOR GIVEN THE INCIDENT VECTOR AND THE
C     * NORMAL SPECIFIED AT THE KTH POINT.
C
      SUBROUTINE SNELL(INC,NORM,REF,K)
      REAL INC(10,3),NORM(10,3),REF(10,3),MULT
      MULT=0.0
      DO 100 I=1,3
100  MULT=MULT+NORM(K,I)*INC(K,I)
      DO 200 I=1,3
200  REF(K,I)=INC(K,I)-2.*MULT*NORM(K,I)
      RETURN
      END

C     *** FIND THE SURFACE NORMAL GIVEN THE REFLECTED AND INCIDENT
C     * VECTORS. THE ARGUMENT 'K' IDENTIFIES WHICH OF THE POINTS
C     * GENERATED ABOVE IS BEING EXAMINED.
C
      SUBROUTINE NORMAL(REF,INC,NORM,K)
      REAL REF(10,3),INC(10,3),NORM(10,3),DEN,DENOM
      DEN=0.
      DO 100 I=1,3
100  DEN=DEN+(REF(K,I)-INC(K,I))**2
      DENOM=SQRT(DEN)
      DO 200 I=1,3
200  NORM(K,I)=(REF(K,I)-INC(K,I))/DENOM
      RETURN
      END

C     **** LAGRANGE INTERPOLATING SUBROUTINE ****
C     * GIVEN N POINTS WITH COORDINATES (X,Y), AN N-1 ORDER POLYNOMIAL
C     * IS FOUND AND STORED IN THE ARRAY 'P'. THE ARGUMENT 'OUT', IS
C     * THE OUTPUT DISABLE.
C
      SUBROUTINE INTERP(N,X,Y,P,OUT)
      DIMENSION X(7),Y(7),AP(8),PX(8),A(8,8),P(7)
      LOGICAL OUT
      IF(N.LE.7)GOTO 6
C     *** THE MAXIMUM ORDER OF THE BEST FIT POLYNOMIAL IS 6.
      WRITE(6,5)N

```

```

5  FORMAT('!TOO MANY POINTS SPECIFIED  N = ',I3)
   GOTO 2000
C   *** INITIALIZE WORK ARRAYS AND CONSTANTS.
6  DO 10 INDEX=1,7
   PX(INDEX)=0.
10  P(INDEX)=0.
   LESS=0
   IFLG=0
   JFLAG=0
   NX=N-1
C   *** IF TWO X VALUES ARE THE SAME, THE FORMULA FOR THE POLYNOMIAL
C   * WILL FAIL.  CHECK FOR DUPLICATIONS, AND ELIMINATE THEM.
   DO 20 I=1,NX
   IZ=I+1
   DO 15 J=IZ,N
   IF(ABS(X(J)-X(I)).LT..0000001)GOTO 17
15  CONTINUE
   GOTO 20
17  IF(OUT)WRITE(6,1999)X(I),I
   IFLG=I
   JFLAG=J
C   *** COUNT THE NUMBER OF DUPLICATE X VALUES WITH 'LESS'.
   LESS=LESS+1
20  CONTINUE
   N=N-LESS
C
C   *** ACCORDING TO THE FORMULA FOR LAGRANGE INTERPOLATION,
C   * SOLVE FOR THE NTH-ORDER CONTINUED PRODUCT, AND MULTIPLY IT OUT
C   * TO FIND THE COEFFICIENTS OF THE POWER SERIES.
C
   DO 1000 J=1,N
   AP(J)=1.
   DO 30 I=1,N
   IF(I.EQ.J)GOTO 30
   IF(I.EQ.IFLG.AND.J.EQ.JFLAG)GOTO 30
   AP(J)=AP(J)*(X(J)-X(I))
30  CONTINUE
   A(1,J)=Y(J)/AP(J)
   DO 50 IX=1,N
   INDEX=IX+1
50  A(INDEX,J)=0.
   DO 100 I1=1,N
   IF(I1.EQ.J)GOTO 100
   IF(I1.EQ.IFLG.AND.J.EQ.JFLAG)GOTO 100
   A(2,J)=A(2,J)+X(I1)
   I2S=I1+1
   IF(I2S.GT.N)GOTO 800
   DO 200 I2=I2S,N

```

```

IF(I2.EQ.J)GOTO 200
IF(I2.EQ.IFLG.AND.J.EQ.JFLG)GOTO 200
A(3,J)=A(3,J)+X(I1)*X(I2)
I3S=I2+1
IF(I3S.GT.N)GOTO 100
DO 300 I3=I3S,N
IF(I3.EQ.J)GOTO 300
IF(I3.EQ.IFLG.AND.J.EQ.JFLG)GOTO 300
A(4,J)=A(4,J)+X(I1)*X(I2)*X(I3)
I4S=I3+1
IF(I4S.GT.N) GOTO 200
DO 400 I4=I4S,N
IF(I4.EQ.J)GOTO 400
IF(I4.EQ.IFLG.AND.J.EQ.JFLG)GOTO 400
A(5,J)=A(5,J)+X(I1)*X(I2)*X(I3)*X(I4)
I5S=I4+1
IF(I5S.GT.N)GOTO 300
DO 500 I5=I5S,N
IF(I5.EQ.J)GOTO 500
IF(I5.EQ.IFLG.AND.J.EQ.JFLG)GOTO 500
A(6,J)=A(6,J)+X(I1)*X(I2)*X(I3)*X(I4)*X(I5)
I6S=I5+1
IF(I6S.GT.N)GOTO 400
DO 600 I6=I6S,N
IF(I6.EQ.J)GOTO 600
IF(I6.EQ.IFLG.AND.J.EQ.JFLG)GOTO 600
A(7,J)=A(7,J)+X(I1)*X(I2)*X(I3)*X(I4)*X(I5)*X(I6)
I7S=I6+1
IF(I7S.GT.N)GOTO 500
DO 700 I7=I7S,N
IF(I7.EQ.J)GOTO 700
IF(I7.EQ.IFLG.AND.J.EQ.JFLG)GOTO 700
A(8,J)=A(8,J)+X(I1)*X(I2)*X(I3)*X(I4)*X(I5)*X(I6)*X(I7)
700 CONTINUE
600 CONTINUE
500 CONTINUE
400 CONTINUE
300 CONTINUE
200 CONTINUE
100 CONTINUE
800 PX(1)=PX(1)+A(1,J)
NMI=N-1
DO 900 IX=1,NMI
INDEX=IX+1
900 PX(INDEX)=PX(INDEX)+A(INDEX,J)*A(1,J)
1000 CONTINUE
DO 1050 IJK=1,N
P(IJK)=PX(N+1-IJK)

```

```

      IF(MOD((IJK+N),2).EQ.1)P(IJK)=-P(IJK)
1050 CONTINUE
      IF(OUT)WRITE(6,1001)NM1,(P(INDEX),INDEX=1,N)
1001 FORMAT('1COEFFICIENTS FOR THE POLYNOMIAL OF ORDER ',I2,' ARE '/
& 7(2X,F10.5))
      GOTO 2000
1999 FORMAT('1THE POINT ',F8.4,' APPEARS TWICE IN THE INPUT LIST. I
& ',I1,' POINT IGNORED')
2000 RETURN
      END

```

C
C
C

****POINT GENERATOR PROGRAM****

C
C
C
C

```

      SUBROUTINE POINTS(P,Q,XPASS,Y,Z,XPLOT,YPLOT,ZPLOT,ZX,KUTSYM,
& CENTX,CENTY,ISMN,JBDY)
      DIMENSION XPASS(4,20),Y(4,20,20),Z(4,20,20),ZPLOT(30,30),
& XPLOT(30),YPLOT(30),JBDY(20),ZX(4,20,20),YF(30,30),X(20),
& P(7,2),Q(7,2),P1(7)
      LOGICAL OUTP/.FALSE./

```

C
C
C
C
C

```

      PRINT *,P,Q
      DO 6 KLEAR=1,7
      P1(KLEAR)=P(KLEAR,ISMN)
      IF(ABS(P1(KLEAR)).LT..00000001)P1(KLEAR)=0.
      IF(ABS(Q(KLEAR,ISMN)).LT..00000001)Q(KLEAR,ISMN)=0.
6 CONTINUE

```

C
C
C
C

*** ISMN IS 2 WHEN GENERATING A SUBREFLECTOR, 1 FOR MAIN.

*** FOR THE DESIGN OF 8/81, THE RADII WERE CHOSEN TO BE
* .0492 FOR THE SUB. AND .1347 FOR THE MAIN REFLECTOR.

```

A=.0492*(ISMN-1)+.1347*(2-ISMN)
B=A

```

C
C
C
C

```

      PRINT *,A,B,CENTX,CENTY,ISMN
      *** M AND N ARE THE NUMBER OF POINTS IN THE PROJECTION GRID
      * IN THE POSITIVE X AND Y DIRECTIONS, WITH THE ORIGIN AT
      * (CENTX,CENTY)

```

```

M=15
N=15
XN=N-1

```

C
C

*** THE FIRST Z AND ZX POINTS ARE FOUND FOR A TRIANGLE PROJECT
* GRID PLANE, AS REQUIRED BY THE FINITE ELEMENT ROUTINE IN G.A

```

      DO 100 I=1,N
      DO 12 JJJ=1,M
      DO 11 KKK=1,4
11 Z(KKK,I,JJJ)=0.
12 ZPLOT(I,JJJ)=0.
      YPLOT(I)=0.
      XI=I

```

C

*** THE X VALUES ARE SEPARATED BY A DISTANCE OF THE RADIUS


```

C      *** IF THE Y(X) FUNCTION IS SYMMETRIC ABOUT THE X-AXIS, CHECK
C      * THE MIRROR IMAGE OF THE Y VALUE.
IF(KUTSYM.NE.0.AND.ABS(Y(KOUNT,I,J)+YCL).LE.2./1.732*A/XN)GOTO 5
Z(KOUNT,I,J)=0.
ZX(KOUNT,I,J)=0.
55 IF(Z(KOUNT,I,J).NE.0..AND.OUTP)PRINT *,KOUNT,I,J,XPASS(KOUNT,I),
&    Y(KOUNT,I,J),Z(KOUNT,I,J)
60 CONTINUE

C
C      *** ESTABLISH THE NORMALIZED DISTANCE FROM THE CENTER OF THE
C      * SURFACE (TO COMPARE WITH THE MAXIMUM RADIUS.)
PER=((YF(I,J)-CENTY)/B)**2+((X(I)-CENTX)/A)**2
GOTO 50
80 JBDY(I)=J
100 CONTINUE

C
C*****PLOTTING POINT GENERATOR*****
C      *** IN THIS SECTION, THE GRID POINTS ARE ON A CARTESIAN PROJECT
C      * (RECTANGULAR) GRID. REPEAT THE ABOVE PROCEDURE ON THIS
C      * ALTERNATE GRID.
NT2=30
MT2=30
XNT2=NT2-1
XMT2=MT2-1
DO 500 I=1,NT2
C      *** THE SPACING OF POINTS IN X IS THE DIAMETER DIVIDED BY THE
C      * NUMBER OF POINTS. THE ORIGIN OF THIS SYSTEM IS A CORNER
C      * DETERMINED BY THE MOVING OUT ONE RADIUS IN THE X AND Y
C      * DIRECTIONS FROM THE CENTER (CENTX,CENTY).
XPLOT(I)=(FLOAT(I)-1.)*2.*A/XNT2-A+CENTX
C      *** FIND THE Y VALUE AT THE GIVEN X VALUE USING THE PROJECTED
C      * Y(X) POLYNOMIAL.
YPL=Q(1,ISMN)
DO 350 IDEG=1,NORD
ADDXP=XPLOT(I)**IDEG*Q(IDEG+1,ISMN)
YPL=YPL+ADDXP
350 CONTINUE
C      *** FIND THE Z VALUE AT THE GIVEN X VALUE.
CALL FUNC(XPLOT(I),ZPLO,DUM,NORD,P1)
DO 500 J=1,MT2
C      *** SET THE Y VALUES, WITH CORRECT SPACING.
YPLOT(J)=(FLOAT(J)-1.)*2.*A/XMT2-A+CENTY
ZPLOT(I,J)=ZPLO
C      *** FLUSH THE POINT IF THE PROJECTED DISTANCE (IN X-Y) IS
C      * GREATER THAN THE SPECIFIED RADIUS.
IF(((XPLOT(I)-CENTX)**2/A/A+(YPLOT(J)-CENTY)**2/B/B.GT.1.)
&    ZPLOT(I,J)=0.
C      *** FLUSH THE POINTS UNLESS THE Y VALUES ARE WITH ONE SPARTIC

```

```

C      * OF THE Y(X), FOR THE GIVEN X.
IF(ABS(YPLOT(J)-YPL).LE.2.*A/XMT2)GOTO 400
C      *** CHECK FOR MIRROR IMAGES IF THE SYSTEM IS SYMMETRIC ABOUT
C      * THE X-AXIS.
IF(KUTSYM.NE.0.AND.ABS(YPLOT(J)+YPL).LE.2.*A/XMT2)GOTO 400
ZPLOT(I,J)=0.
400 CONTINUE
IF(ZPLOT(I,J).NE.0..AND.OUTP)PRINT *,I,J,XPLOT(I),YPLOT(J),
&    ZPLOT(I,J)
500 CONTINUE
RETURN
END

C
C      *** THIS SUBROUTINE FINDS THE VALUE OF Z(X,Y) AND DZ(X,Y)/DX
C      * GIVEN POLYNOMIAL OF ORDER NORD.
C
SUBROUTINE FUNC(X,Z,ZX,NORD,P)
DIMENSION P(7)
C      *** LOAD THE CONSTANT TERM
Z=P(1)
ZX=P(2)
MX=NORD+1
DO 50 N=1,MX
IF(N.EQ.1)GOTO 50
C      *** ACCUMULATE INCREASING POWERS OF X, BEING CAREFUL NOT TO
C      * RAISE A NUMBER (POSSIBLY ZERO) TO A ZERO POWER.
Z=Z+P(N)*X**(N-1)
IF(N.EQ.2)GO TO 50
C      *** THE PARTIAL IN THE X DIRECTION IS FOUND BY ADDING EACH
C      * TERM'S PARTIAL.
ZX=ZX+P(N)*X**(N-2)*FLOAT(N-1)
50 CONTINUE
RETURN
END

C
C      *** THIS SUBROUTINE PLOTS THE SUBREFLECTOR IN THREE DIMENSIONS
C      * USING A PLOTTING PACKAGE AVAILIBLE AT COMSAT LABS.
C
SUBROUTINE GRAF3(ZPL2,N)
DIMENSION ZPLOT(30,30),ZPL2(30,30,2)
DO 600 ISMN=1,2
WRITE(6,1000) ISMN
1000 FORMAT(' SURFACE NUMBER',I2)
SUBMN:=ISMN-1
ZMIN=.07*SUBMN-.175*(1.-SUBMN)
ZMAX=-10.
C      *** THE MAXIMUM VALUE OF THE FUNCTION IS FOUND.
DO 100 I=1,N

```

```

DO 100 J=1,N
ZPLOT(I,J)=ZPL2(I,J,ISMN)
IF(ZPLOT(I,J).GT.ZMAX)ZMAX=ZPLOT(I,J)
100 CONTINUE
C   *** TO EMPHASIZE THE CURVATURE, ONLY THE REGION BETWEEN THE
C   * MINIMUM AND MAXIMUM SURFACE VALUE ARE DISPLAYED.
ZMAX=ZMAX-ZMIN
DO 200 I=1,N
DO 200 J=1,N
ZPLOT(I,J)=ZPLOT(I,J)-ZMIN
IF(SUBMN.EQ.0)GOTO 200
C   *** FOR SUBREFLECTORS, THE SURFACE IS INVERTED, SINCE IN THE
C   * 3-D PLOT THE POSTIVE Z-AXIS POINTS UP, AND SO ONLY THE
C   * CONCAVE 'BACK' OF THE SUBREFLECTOR WOULD BE VISIBLE.
IF(ZPLOT(I,J).GT.0.)ZPLOT(I,J)=ZMAX-ZPLOT(I,J)
IF(ZPLOT(I,J).LT.0.)ZPLOT(I,J)=0.
200 CONTINUE
300 WRITE(6,350)
350 FORMAT('1INPUT THETA AND PHI')
READ(5,*)THET,PHI
C   *** THE FOLLOWING SUBROUTINES ARE INCLUDED IN THE PLOTTING
C   * PACKAGE.
CALL PLOTS (IDUM, JDUM, KDUM)
CALL PLOT3D(ZPLOT,ZMAX,0.,30,30,1,1,N,1,1,N,-3,THET,PHI)
CALL PLOFF
CALL ANMODE
CALL TINPUT(IXYZ)
WRITE(6,500)
500 FORMAT(' DO YOU WANT ANOTHER PLOT OF THE SAME SURFACE? (YES=1)')
READ (5,*)IANS
IF(IANS.EQ.1)GOTO 300
600 CONTINUE
RETURN
END

C   *** THIS SUBROUTINE WRITES OUT VALUES FOR ALL QUADRANTS IN
C   * QUASY PROPER ORIENTATION.

SUBROUTINE TYP0UT(ARR,NGRID,ISMN)
DIMENSION ARR(4,20,20,2)
DO 100 KW=1,4
C   *** FOR THE FIRST OR THIRD QUADRANT, WRITE OUT A SPACER HEADING.
IF(KW.EQ.1.OR.KW.EQ.3)WRITE(6,10)KW
10 FORMAT(' REFLECTOR OUTPUT STARTING WITH QUADRANT ',I1)
DO 100 JWR=1,NGRID
J=NGRID+1-JWR
IF(KW.EQ.2.OR.KW.EQ.4)GO TO 90
C   *** THE X VALUES ARE CYCLED FIRST, WITH THE Y VALUES INVERTED

```



```

C      * FOR THE FIRST OR THIRD QUADRANTS.
      WRITE(6,200)(ARR(KW,I,J,ISMN),I=1,15)
      GOTO 100
    90 WRITE(6,200)(ARR(KW,I,JWR,ISMN),I=1,15)
    100 CONTINUE
    200 FORMAT(15(1X,F7.5))
      RETURN
      END

```

```

C      ***** ELEMENT SPECIFICATION SUBROUTINE USED FOR FINITE ELEMENT
C      ANALYSIS USING GAP*****

```

```

C      *      IN ORDER TO SPECIFY THE REFLECTOR SURFACES, WHICH ARE NOT
C      *      SIMPLE, SECOND-ORDER FUNCTIONS, THE METHOD OF FINITE ELEMENTS
C      *      IS USED.  THE SURFACE IS BROKEN UP INTO DISCRETE, TRIANGULAR
C      *      ELEMENTS, AND EACH SURFACE ELEMENT IS TREATED AS A LOCAL
C      *      THIRD-ORDER FUNCTION.  TWO SUBROUTINES ARE USED IN THE FINITE
C      *      ELEMENT ANALYSIS:  GRIDP, WHICH IDENTIFIES THE COORDINATES OF
C      *      OF THE VERTICIES OF THE TRIANGULAR ELEMENTS, AND THE X, AND Y
C      *      PARTIALS; AND ELEM, WHICH DETERMINES WHICH VERTICES ARE
C      *      CONNECTED TO FORM THE PARTICULAR ELEMENTS.
C      *      EQUILATERAL TRIANGLES ARE PROJECTED ONTO THE SURFACE FROM
C      *      THE X-Y PLANE.  ASSUMING THE TRIANGLES HAVE BASES PARALLEL TO
C      *      THE X-AXIS, EITHER POINTING UP OR DOWN, WITH A FOURTH POINT
C      *      PLACED IN THE CENTER OF EACH, EACH COLUMN OF CONSTANT X HAS
C      *      A COLUMN OF TRIANGLES ALTERNATELY POINTING UP AND DOWN.
C      *      THERE ARE JBDY(X) Y-VALUES IN EACH COLUMN BEFORE THE CIRCULAR
C      *      BOUNDARY IS REACHED.
C      *      TO DETERMINE THE MEMBERS OF EACH ELEMENT, THE POINTS IN
C      *      EACH QUADRANT ARE ORDERED STARTING AT THE ORIGIN, INCREASING
C      *      WITH Y UNTIL THE BOUNDARY IS REACHED, AND THEN CONTINUING WITH
C      *      THE NEXT COLUMN OF Y'S, AND SO FORTH.

```

```

C      SUBROUTINE ELEM(N,JBDY)
      DIMENSION JBDY(20),LISTEL(400,4)
      IN=-1
      ITOT=0
      LAST=0
      DO 100 I=1,N
C      *** THE NUMBER OF Y-VALUES IN EACH COLUMN ARE PRINTED.
      PRINT *,JBDY(I)
      J=0
C      *** EACH ELEMENT EXTENDS OVER 3 COLUMNS, THE NUMBER OF Y-VALUES
C      *      IN THE CURRENT AND TWO SUCCESSIVE COLUMNS ARE RETRIEVED.
      IB=JBDY(I)
      IBP1=JBDY(I+1)
      IBP2=JBDY(I+2)
C      *** SET THE SECOND (AND FIRST) COLUMN NUMBER OR POINTS TO 0 IF

```

```

C      * THE LEFT VERTEX IS ONE COLUMN (OR ON) THE EDGE OF THE BOUNDARY
      IF(I-N+1)30,25,20
20  IBP1=0
25  IBP2=0
30  CONTINUE
C      *** THERE ARE TWO TYPES OF POSSIBLE TRIANGLES: TYPE 1 ARE
C      * POINTING UP (POSITIVE Y), AND TYPE 2 POINTING DOWN.
C      * MD IDENTIFIES WHETHER THIS IS AN ODD OR EVEN COLUMN.
      MD=MOD(I+1,2)
40  IN=IN+2
C      *** THE ELEMENT COUNTER, 'IN' IS DOUBLY INCREMENTED, SINCE BOTH
C      * UP-POINTING TRIANGLES (TYPE 1), AND DOWN POINTING TRIANGLES
C      * (TYPE 2) ARE PROCESSED ON EACH LOOP CYCLE.
C      *** J COUNTS THE NUMBER OF Y-VALUES ENCOUNTERED IN THE CURRENT
C      * COLUMN.
      J=J+1
C      *** JFIR IS THE Y-VALUE OF THE FIRST VERTEX OF TYPE 1 TRIANGLES.
C      * THESE VALUES ARE SPACED EVERY THIRD J, STARTING ON THE X-AXIS
C      * FOR EVEN COLUMNS (LIKE THE Y-AXIS, FOR EXAMPLE) WHERE J=1,
C      * AND SKIPPING THE FIRST Y-VALUE (J=2) FOR ODD COLUMNS.
      JFIR=3*(J-MD)-2+MD
C      *** IF J=1 AND MD=1 (THE FIRST POINT IN AN ODD COLUMN), A TYPE 2
C      * TRIANGLE APPEARS FIRST, SO THE ELEMENT COUNTER IS DECREMENTED
C      * AND THE PROGRAM PROCEEDS TO PROCESSING TYPE 2.
      IF(MD.NE.1.OR.J.NE.1)GOTO 45
      IN=IN-1
      GOTO 55
C      *** IF THE STARTING PT. OF ELEMENT TYPE 1 IS TOO CLOSE TO THE
C      * BOUNDARY, FLUSH THE ELEMENT.
C      * THIS OCCURS WHEN EITHER JFIR < IB, OR IB-JFIR < IB-IBP1+1+MD,
C      * OR IB < IBP2.
45  IF(JFIR.LE.IB.AND.JFIR.LE.IBP1-1-MD.AND.JFIR.LE.IBP2)GOTO 50
C      *** IF A TYPE 1 IS TOO CLOSE, THERE IS NO POSSIBILITY OF A
C      * TYPE 2 EXISTING. REPLACE THE ELEMENT COUNTER, AND PROCEED TO
C      * THE NEXT COLUMN.
      IN=IN-2
      GOTO 100
C
C      *****FIRST TYPE TRIANGLE *****
C      * 'LAST' IS THE SUM OF THE PAST NUMBERS OF Y-VALUES IN THE
C      * PREVIOUS COLUMNS. ONCE THE ELEMENT'S FIRST VERTEX IS FOUND,
C      * IT IS USED AS A REFERENCE FOR THE OTHER VERTICIES. THE FOURTH
C      * IS IN THE NEXT COLUMN, WHICH IS EITHER IB MORE THAN THE FIRST
C      * VERTEX, OR IB+1 MORE, IF IT IS IN AN ODD COLUMN. THE THIRD
C      * IS AT THE NEXT HIGHER Y-VALUE, AND THE SECOND IS TWO BOUND
C      * VALUES MORE THAN THE FIRST. THE NUMBERING IS CRITICAL, IN
C      * ORDER TO MEET THE RIGHT-HANDED ELEMENT DEFINITION EXPECTED IN
C      * GAP.

```

```

C
50 LISTEL(IN,1)=JFIR+LAST
   LISTEL(IN,4)=LISTEL(IN,1)+IB+MD
   LISTEL(IN,3)=LISTEL(IN,4)+1
   LISTEL(IN,2)=LISTEL(IN,4)+IBP1-MD
   ITOT=ITOT+1
C   *** ITOT ACCUMULATES THE TOTAL NUMBER OF ELEMENTS FOUND IN THE
C   * FIRST QUADRANT.
C   *** THE TYPE 2 TRIANGLES HAVE THEIR FIRST VERTEX 3 Y-VALUES
C   * ABOVE THE FIRST VERTEX OF THE TYPE 1 TRIANGLE. IF THIS Y-
C   * VALUE IS ABOVE THE BOUND OF THE COLUMN, OR IF THE VERTEX TWO
C   * COLUMNS OVER IS GREATER THAN THE BOUND THERE, THEN THE
C   * TRIANGLE WON'T FIT. DECREMENT THE ELEMENT COUNTER AND MOVE ON
C   * TO THE NEXT COLUMN.
55 IF(JFIR+3.LE.IB.AND.JFIR+3.LE.IBP2)GOTO 60
   IN=IN-1
   GOTO 100
C   **** SECOND TYPE TRIANGLE ****
60 LISTEL(IN+1,1)=JFIR+LAST+3
   LISTEL(IN+1,2)=LISTEL(IN+1,1)+IB-2+MD
C   *** SINCE THIS TRIANGLE IS POINTING DOWN, THE FOURTH VERTEX IS
C   * 1 MORE THAN THE SECOND VERTEX, AND THE THIRD IS LEVEL WITH THE
C   * FIRST.
   LISTEL(IN+1,4)=LISTEL(IN+1,2)+1
   LISTEL(IN+1,3)=LISTEL(IN+1,1)+IB+IBP1
   ITOT=ITOT+1
   GOTO 40
C   *** CONTINUE PROCESSING TRIANGLES UNTIL THE BOUND IS APPROACHED
C   * AND THEN ACCUMULATE ANOTHER BOUND VALUE AND PROCEED TO THE
C   * NEXT COLUMN.
100 LAST=LAST+IB
C
C   ****4TH QUADRANT ELEMENTS
C
   DO 250 I4=1,ITOT
C   *** THERE WERE ITOT ELEMENTS IN THE FIRST QUADRANT. FOR THE 4TH
C   * QUADRANT, ADD THE TOTAL OF THE PAST ACCUMULATION OF BOUND
C   * VALUES TO EACH VERTEX. TO PRESERVE ORIENTATION, THE 2ND AND
C   * 3RD VERTICIES ARE SWITCHED.
   DO 200 L=1,4,3
200 LISTEL(I4+ITOT,L)=LISTEL(I4,L)+LAST
   LISTEL(I4+ITOT,2)=LISTEL(I4,3)+LAST
250 LISTEL(I4+ITOT,3)=LISTEL(I4,2)+LAST
C
C   *****2ND AND 3RD QUADRANT ELEMENTS
C
   I2ITOT=2*ITOT
   LASTTW=2*LAST

```

```

C      *** FOLLOWING THE ABOVE REASONING, FIND THE TOTAL NUMBER OF
C      * TRIANGLES AND THE SUM OF THE BOUND VALUES AND ADD IT TO THE
C      * APPROPRIATE INDICES. AGAIN, SWITCH THE 2ND AND 3RD VERTICIES.
DO 350 I23=1,I2ITOT
DO 300 L=1,4,3
300 LISTEL(I23+I2ITOT,L)=LISTEL(I23,L)+LASTTW
LISTEL(I23+I2ITOT,2)=LISTEL(I23,3)+LASTTW
350 LISTEL(I23+I2ITOT,3)=LISTEL(I23,2)+LASTTW
C
C      *****ELEMENTS ALONG Y-AXIS
C
C      *** THE TRIANGLES LIE FLAT AGAINST THE X-AXIS, BUT NOT AGAINST
C      * THE Y-AXIS. TRIANGLES ARE DERIVED FOR THESE CASES.
IB1=JBDY(1)
IB2=JBDY(2)
I4ITOT=4*ITOT
C      *** IAXTOT COUNTS THE NUMBER OF ELEMENTS ALONG THE POS. Y-AXIS.
IAXTOT=0
C      *** SET A COUNTER TO IDENTIFY THE UPPER AND LOWER HALF PLANE.
DO 500 I=1,2
IX=I-1
C      *** IYAX COUNTS THE TRIANGLES ALONG THE YAXIS.
IYAX=-1+IAXTOT
J=0
400 IYAX=IYAX+2
IM=IYAX+I4ITOT
J=J+1
C      *** CHECK IF THE TYPE 1 TRIANGLE IS TOO CLOSE TO THE BOUNDARY.
IF(3*J-1.LE.IB2)GOTO 420
IM=IM-1
GOTO 450
420 LISTEL(IM,1)=3*J-2+LAST*IX
LISTEL(IM,4)=LISTEL(IM,1)+1
C      *** IX=1 FOR THE LOWER HALF PLANE, WHERE THE 2ND AND 3RD MUST
C      * BE REVERSED.
LISTEL(IM,2+IX)=LISTEL(IM,4)+IB1
LISTEL(IM,3-IX)=LISTEL(IM,2+IX)+LASTTW
IAXTOT=IAXTOT+1
C      *** INCREMENT THE Y-AXIS ELEMENT COUNTER.
C      *** CHECK IF A TYPE 2 TRIANGLE WILL FIT WITHIN THE BOUNDARY.
450 IF(3*J+1.LE.IB1)GOTO 470
IN=IN-1
GOTO 500
470 LISTEL(IM+1,1)=3*J+1+LAST*IX
LISTEL(IM+1,4)=LISTEL(IM+1,1)-1
LISTEL(IM+1,3-IX)=LISTEL(IM+1,1)-2+IB1
LISTEL(IM+1,2+IX)=LISTEL(IM+1,3-IX)+LASTTW
IAXTOT=IAXTOT+1

```

```

GO TO 400
500 CONTINUE
C   *** IML IS THE TOTAL NUMBER OF ELEMENTS WITHIN THE BOUNDARY.
    IML=IM
    WRITE(6,600)
600  FORMAT(' CHECK ELEMENT CONNECTIVITY?')
    READ(5,*)INS
    DO 800 I=1,IML
    WRITE(9)(LISTEL(I,J),J=1,4)
    IF (INS.EQ.1) WRITE(6,1000)I,(LISTEL(I,J),J=1,4)
800  CONTINUE
1000 FORMAT(I8,2X,4I5)
    RETURN
    END

C
C   *** THIS SUBROUTINE SETS UP A GRID POINT FILE FOR USE IN THE
C   * FINITE ELEMENT ANALYSIS.  FILE 10 IS THE OUTPUT DEVICE.
C
SUBROUTINE GRIDP(NGRID,JBDY,X,Y,ZSURF,ZX,ZY,ISMN)
DIMENSION JBDY(20),X(4,20,2),Y(4,20,20,2),ZSURF(4,20,20,2),
&          ZX(4,20,20,2),ZY(4,20,20,2)
REAL*8 XD(4,20),YD(4,20,20),ZSURFD(4,20,20),ZXD(4,20,20),
&          ZYD(4,20,20)
KOU=0
WRITE(6,75)
75  FORMAT(' CHECK GRID POINT LOCATIONS? (1 FOR YES)')
    READ(5,*)GP
C   *** CYCLE THROUGH EACH QUADRANT.
    DO 100 K=1,4
    DO 100 I=1,NGRID
C   *** FOR EACH ROW OF X VALUES, THEIR ARE JBDY(X) Y VALUES.
    IB=JBDY(I)
    DO 100 J=1,IB
C   *** COUNT THE TOTAL NUMBER OF RECORDS WRITTEN INTO THE FILE.
    KOU=KOU+1
    IF(GP.NE.1..OR.K.NE.1)GOTO 50
    WRITE(6,10)X(1,I,ISMN),Y(1,I,J,ISMN),ZSURF(1,I,J,ISMN),
&          ZX(1,I,J,ISMN),ZY(1,I,J,ISMN)
10  FORMAT(5(2X,F7.4))
C   *** GAP EXPECTS DOUBLE PRECISION NUMBERS, SO TRANSFER THE VALUES
C   * TO THE APPROPRIATE ARRAYS.
50  XD(K,I)=X(K,I,ISMN)
    YD(K,I,J)=Y(K,I,J,ISMN)
    ZSURFD(K,I,J)=ZSURF(K,I,J,ISMN)
    ZXD(K,I,J)=ZX(K,I,J,ISMN)
    ZYD(K,I,J)=ZY(K,I,J,ISMN)
100 WRITE(10)XD(K,I),YD(K,I,J),ZSURFD(K,I,J),ZXD(K,I,J),ZYD(K,I,J)
    RETURN

```

END

```
C
C *** FOURTH ORDER SURFACE APPROXIMATION SUBROUTINE
C
C *** THIS SUBROUTINE FINDS THE VALUES OF Y**2*X AND Y**2*X**2 FOR
C * EACH SURFACE. GIVEN THE FOURTH ORDER CURVES IN JUST X AND JUST
C * Y, THIS ALLOWS REPRESENTATION OF THE SUFACES AS AFOURTH ORDER
C * POLYNOMIAL IN BOTH X AND Y.
C * THE TWO INDEPENDENT FUNTIONS ARE FIRST SUBTRACTED FROM ALL THE
C * POINTS ON EACH SURFACE, AND THEN THE LEAST SQUARES POLYNOMIAL
C * FITTING ROUTINE IS CALLED.
C
SUBROUTINE FITFOR(NVT,X,Y,Z,XS4,XM4)
REAL X(30,2),Y(30,2),Z(30,30,2),XS4(5),XM4(5),WK(3)
REAL*8 XFORTH(5,2),YFORTH(5),A(900,2),B(900,1),T(2,1),SUBTX,SUBTY,
&ACOMP1,ACOMP2
WRITE(6,1)((Z(IZ,JZ,LZ),JZ=1,NVT),IZ=1,NVT),LZ=1,2)
1 FORMAT(15(1X,F7.5))
IHALF=15
DO 10 ICH=1,5
C *** COPY THE FOURTH ORDER POLYNOMIALS DERIVED IN BIFOFF FOR EACH
C * REFLECTOR INTO IT DOUBLE PRECISION COUNTERPART.
XFORTH(ICH,1)=XS4(ICH)
10 XFORTH(ICH,2)=XM4(ICH)
DO 200 ISMN=1,2
JP=0
WRITE(6,1000)
1000 FORMAT(' INPUT THE FOURTH ORDER POLYNOMIAL APPROXIMATION IN THE TR
&ANSVERSE (Y) DIRECTION FOR SUB/MAIN REFLECTOR. ')
READ(5,*)YFORTH
PRINT *,XFORTH,YFORTH
DO 150 K=1,NVT
C *** K IS THE Y-COUNTER *
C *** ACCUMULATE THE VALUE OF THE FOURTH ORDER FUNCTION IN Y AT
C * THE GIVEN Y VALUE.
SUBTY=YFORTH(1)
DO 50 KF=2,5
50 SUBTY=YFORTH(KF)*Y(K,ISMN)**(KF-1)+SUBTY
DO 150 J=1,NVT
C *** J IS THE X-COUNTER *
C *** DETERMINE THE DISTANCE TO THE TEST POINT FROM THE ORIGIN,
C * AND FLUSH IT IF IT EXCEEDS A SPECIFIED RADIUS.
IF((J-IHALF)**2+(K-IHALF)**2.GE.(13.5)**2)GOTO 150
JP=JP+1
WHY=Y(K,ISMN)**2
C *** SET UP THE MATRIX OF ESTIMATORS.
A(JP,1)=X(J,ISMN)*WHY
A(JP,2)=X(J,ISMN)**2*WHY
```

```

C      *** CHECK TO MAKE SURE THAT NO ESTIMATORS ARE TOO CLOSE TO 0.
IF(JP.LT.2)GOTO 75
JPINDX=JP-1
DO 70 ICHK=1,JPINDX
ACOMP1=DABS(A(ICHK,1)-A(JP,1))
ACOMP2=DABS(A(ICHK,2)-A(JP,2))
IF(ACOMP1.GT..000000001.AND.ACOMP2.GT..000000001)GOTO 70
JP=JP-1
GOTO 150
70 CONTINUE
C      *** ACCUMULATE AND SUBTRACT OFF THE FOURTH ORDER POLYNOMIAL OF
C      * X.
75 SUBTX=XFORTH(1,ISMN)
DO 80 JF=2,5
80 SUBTX=XFORTH(JF,ISMN)*X(J,ISMN)**(JF-1)+SUBTX
IF(Z(J,K,ISMN).NE.0.)GOTO 90
C      *** FLUSH THE POINT IF ITS Z VALUE IS ZERO (IMPLYING OUTSIDE THE
C      * CIRCLE).
WRITE(6,1080)J,K,ISMN
1080 FORMAT(' ZPLOT VALUE EQUAL TO ZERO, (J,K)='2I4,' ISMN=',I4)
GOTO 200
90 B(JP,1)=Z(J,K,ISMN)-SUBTX-SUBTY
WRITE(6,110)K,J,JP,(A(JP,L),L=1,2),Z(J,K,ISMN),B(JP,1)
110 FORMAT(1X,3(I3,1X),2X,4(1X,F8.6))
150 CONTINUE
IA=900
IB=900
IT=2
NS=1
NF=2
NV=JP
C PRINT *, ISMN,Z
C      *** CALL THE IMSL LEAST-SQUARES POLYNOMIAL ROUTINE.
CALL OFIMA3(A,IA,B,IB,NV,NS,NF,T,IT,WK,IER)
WRITE (6,300)T(1,1),T(2,1)
300 FORMAT(1X,'THE X*Y**2, AND (X*Y)**2 TERMS ARE ',2(F10.7,5X))
PRINT *,T
200 CONTINUE
WRITE(6,1)(B(JP,1),JP=1,225)
RETURN
C      ***** WE MADE IT !!!*****
END

```

APPENDIX IX. PARAMETER STUDY

There are a great many input parameters in the offset bifocal design. This appendix will attempt to indicate the effects of varying any specific one.

First, consider the symmetric bifocal and the parameters it has in common with the offset design. Figures 126-133 show the effects of increasing the scan angle. For all cases, the focal points are at $(0,0,0.1)$ and $(0,0,-0.1)$, the subreflector vertex $(0,0,0.3)$ and its normal $(0,0,-1)$, and the path length, L , is 1. Superimposed on the bifocal profiles are the best fitting Cassegrainian parabola-hyperbola combination. Note how as scan angle increases, the subreflector curvature decreases until, at 6.6° , it starts becoming a Gregorian configuration. Of course, tracing some rays demonstrates that the subreflector becomes bigger than the main reflector in this case. This is not necessarily bad as long as an offset configuration is used.

Next, Figure 134 shows the effect of changing just the subreflector vertex. These are for $\pm 8^\circ$ scanning, L equaling 1 and focal points at $(0,0,0.2)$ and $(0,0,-0.2)$. The progression from $(0,0,0.5)$ to $(0,0,0.18)$ --where the algorithm breaks down--shows an increasing subreflector curvature and a flattening of the main reflector. The breakdown which occurs when the subreflector is moved too close comes about since the main

SIGNAL MODE

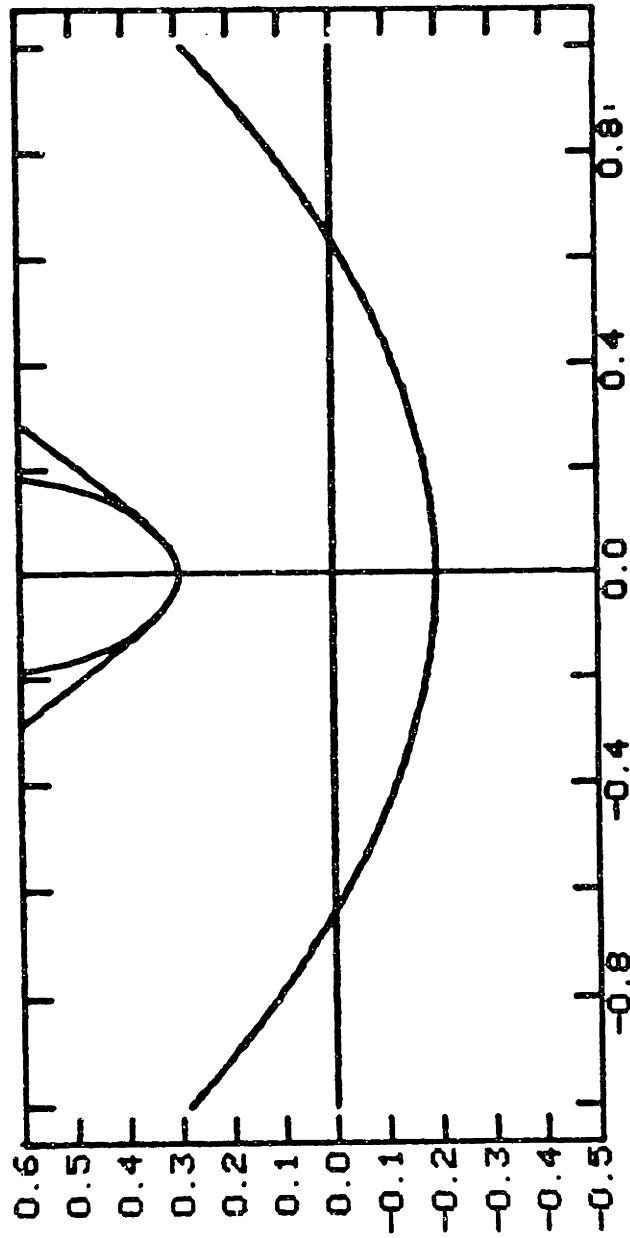


Figure 126. Scan Angle Study 1°

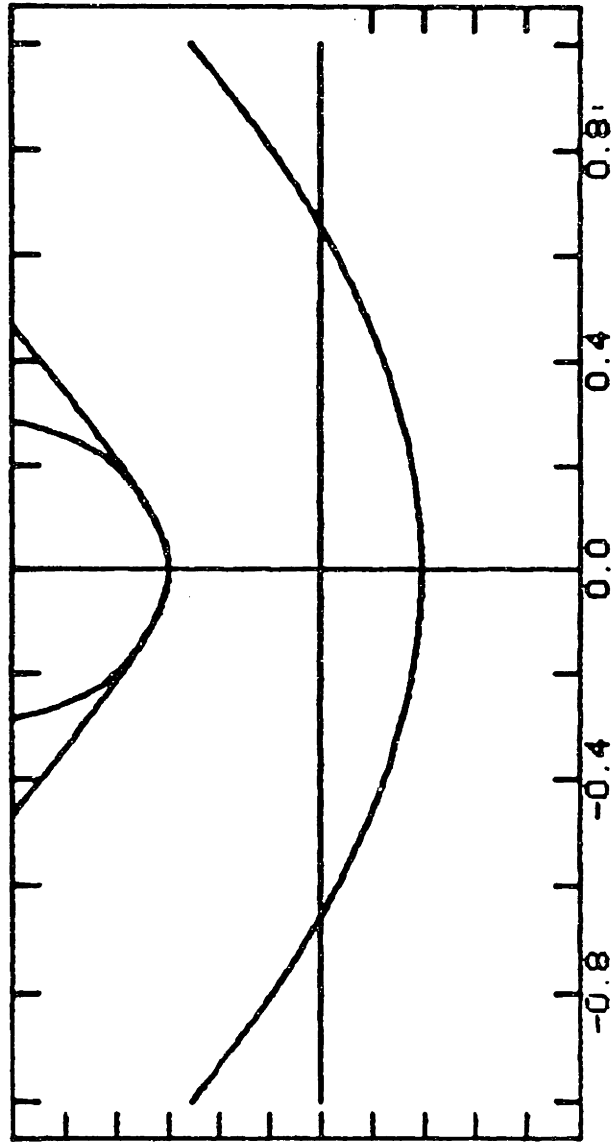


Figure 127. Scan Angle Study 2°

ANNUAL NODE

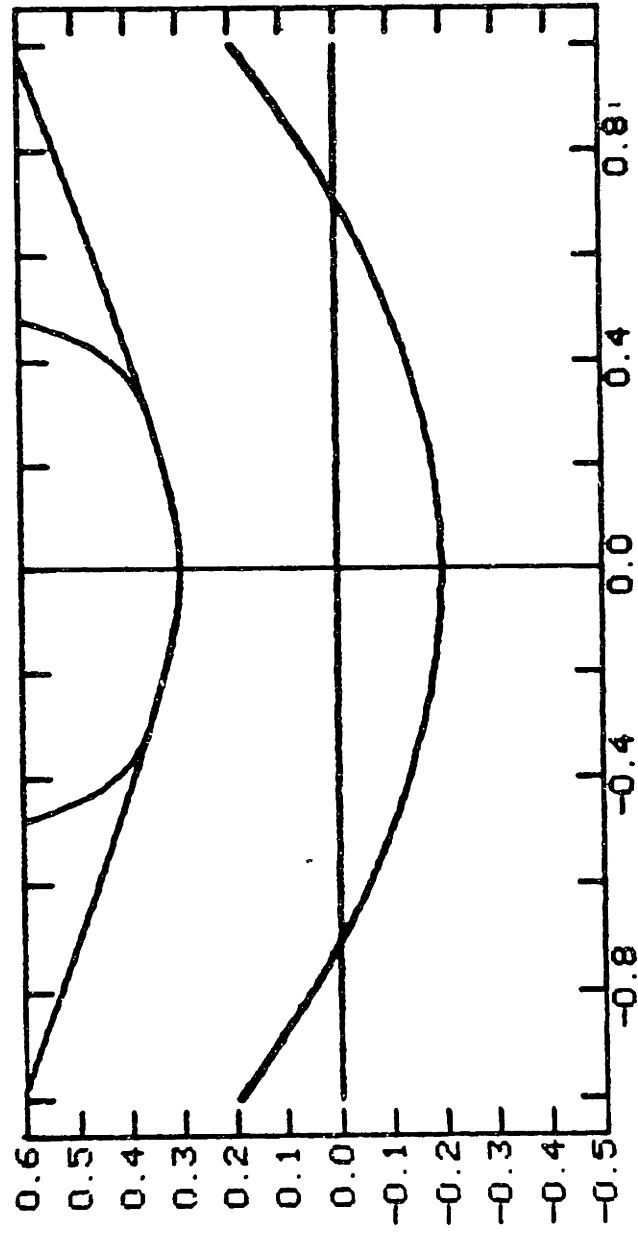


Figure 128. Scan Angle Study 4°

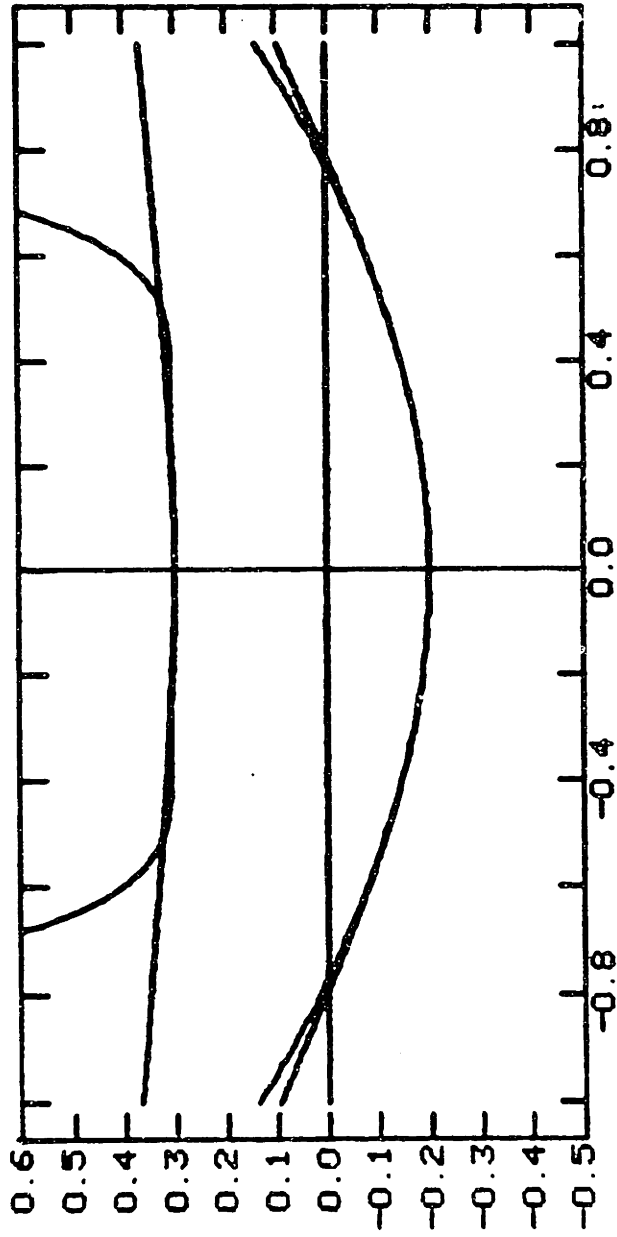


Figure 129. Scan Angle Study 6°

MANUAL MODE

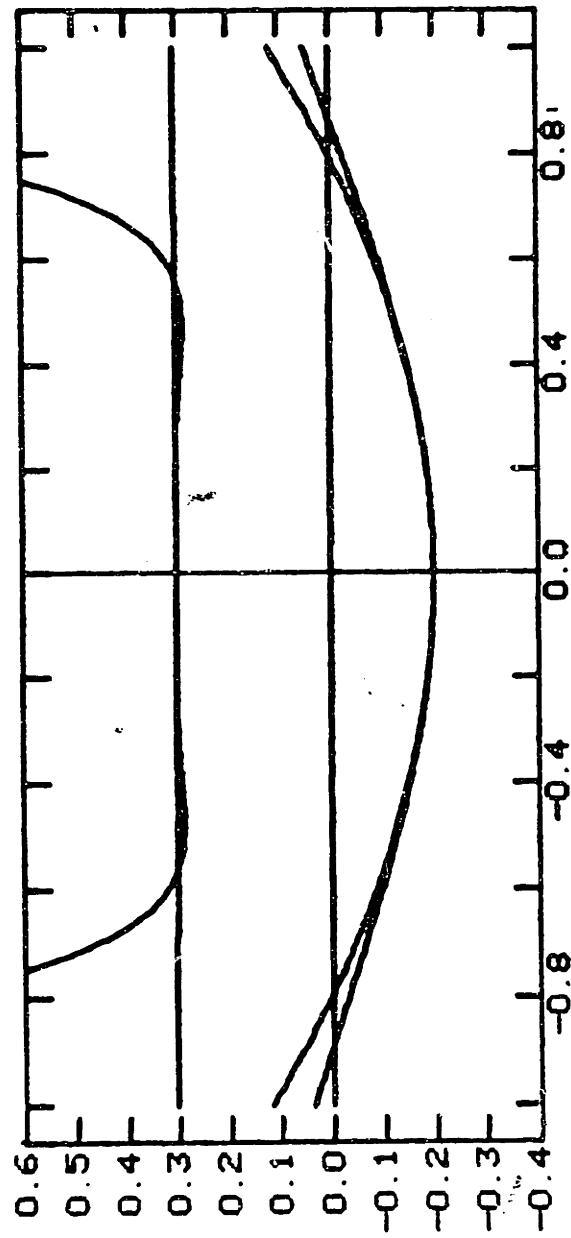


Figure 130. Scan Angle Study 6.6°

BIENNIAL MODE
i -

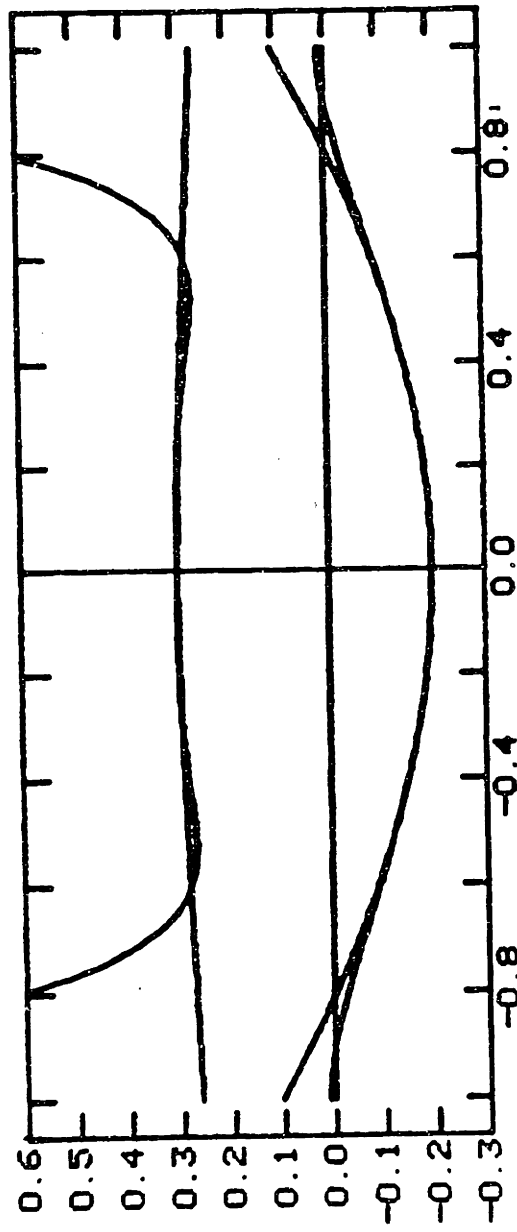


Figure 131. Scan Angle Study 7°

SCINUAL NODE

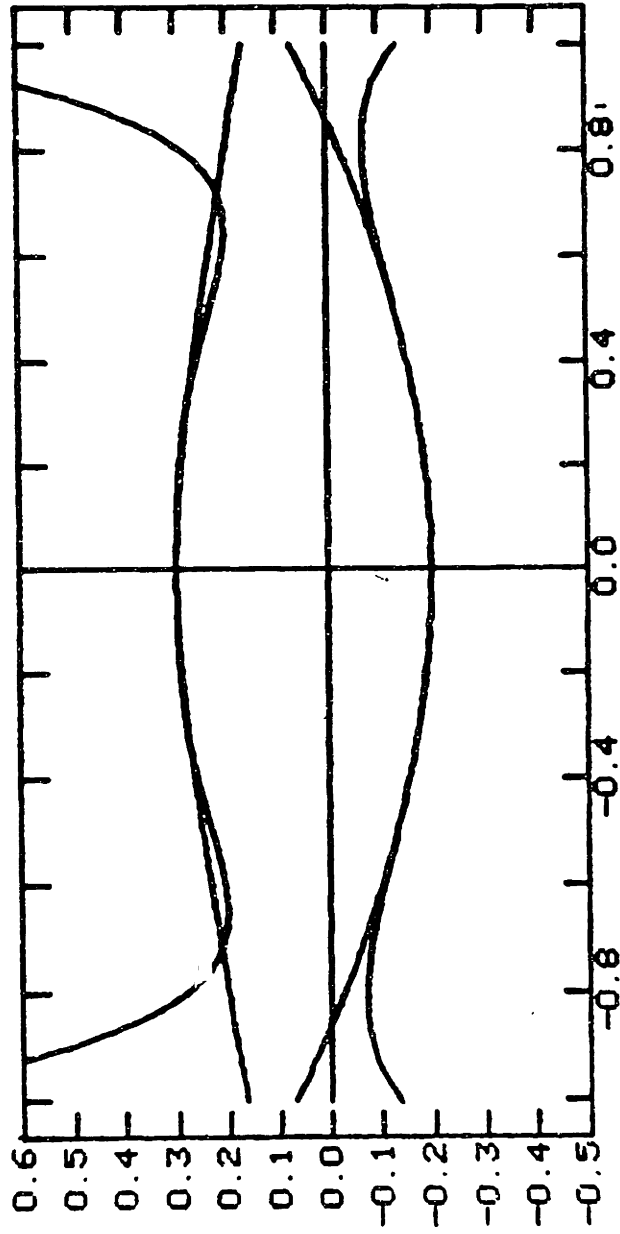


Figure 132. Scan Angle Study 8°

ANNUAL MODE
i-

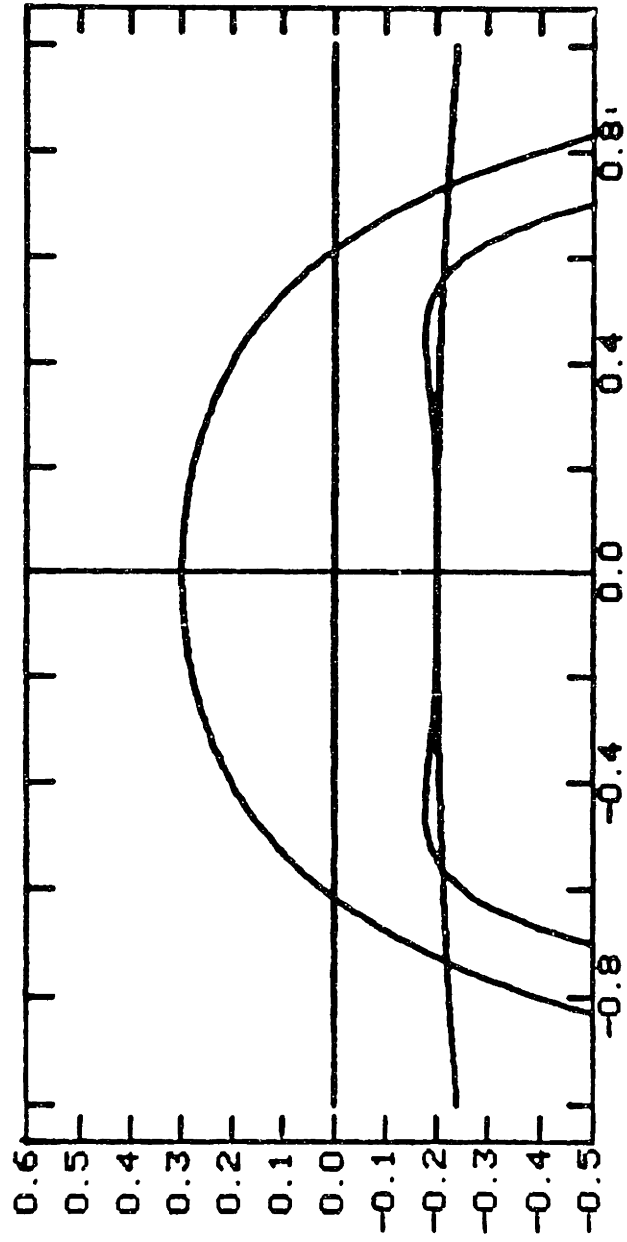


Figure 133. Scan Angle Study 12°

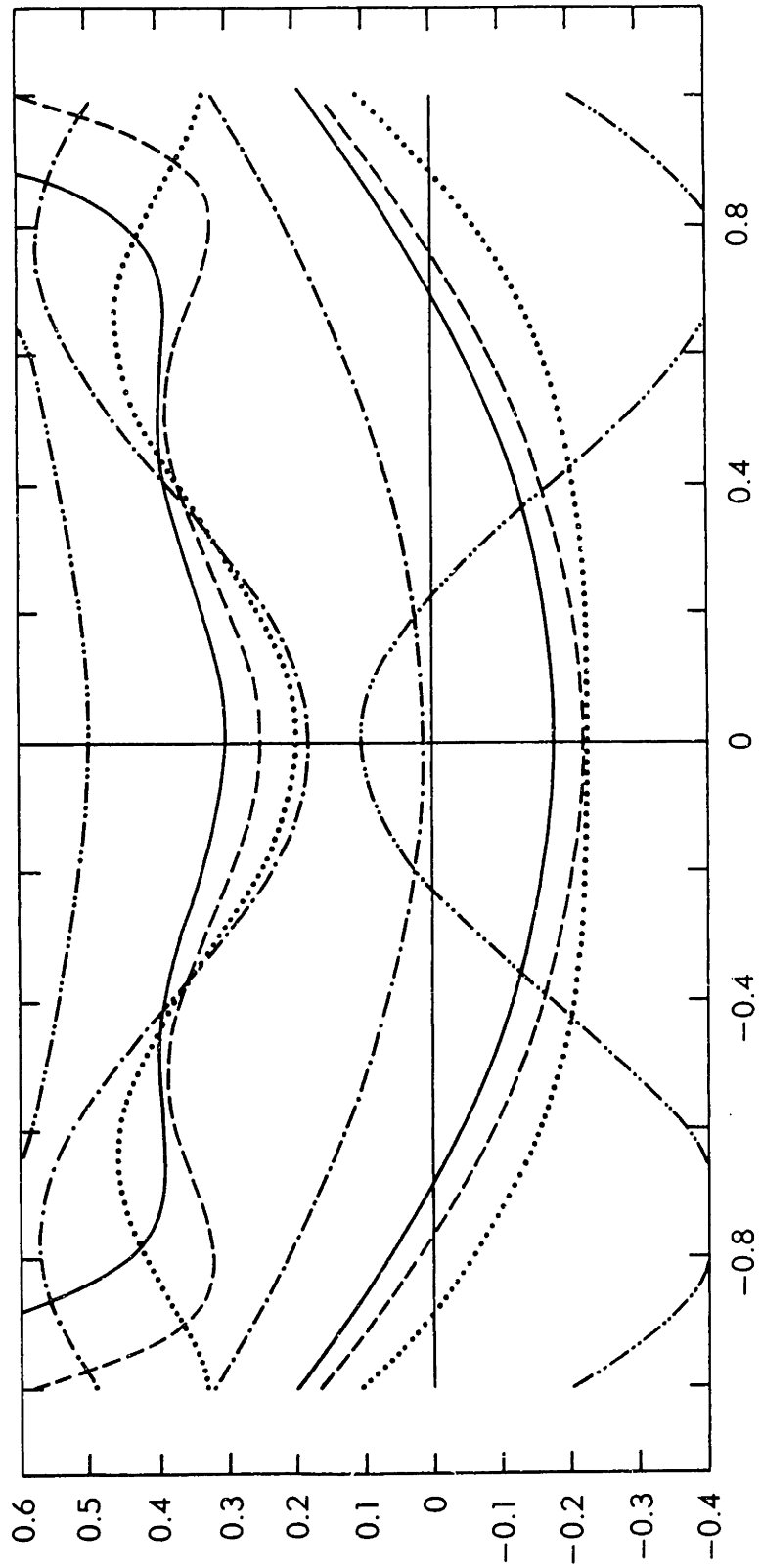


Figure 134. Subreflector Vertex Study

reflector points generated are spread apart too greatly to be reasonably fit by a representative curve.

Figure 135 illustrates the effects of changing the path lengths to the aperture planes. Also shown are the closest Cassegrain profiles for each case.

Figure 136 shows a progression of symmetric bifocal profiles with varying both foci and subreflector vertex. This is actually just a translation of the aperture center, since the distance from focus to subreflector remains constant.

Now consider the variation of those parameters specific to the offset configuration: C_1 , and \hat{n}_{S1} . The angle made by the segment connecting the foci and the axis is also an important offset parameter. However, there is enough indication of the effects of introducing this asymmetry if comparisons are made to the symmetric cases.

Figures 137 through 142 show the results of varying the aperture center C_1 . All the other parameters are the same as for the final design (see Figure 35). Clearly, the only realizable curve which fits the points is for $C_1 = 0.352$.

Figures 143 through 145 are similar to the previous ones. As the first subreflector normal becomes less steep, the profile becomes more realizable and then less so. Obviously, the optimum value depends on C_1 as well. Together C_1 and \hat{n}_{S1} are adjusted to produce the most reasonable profiles.

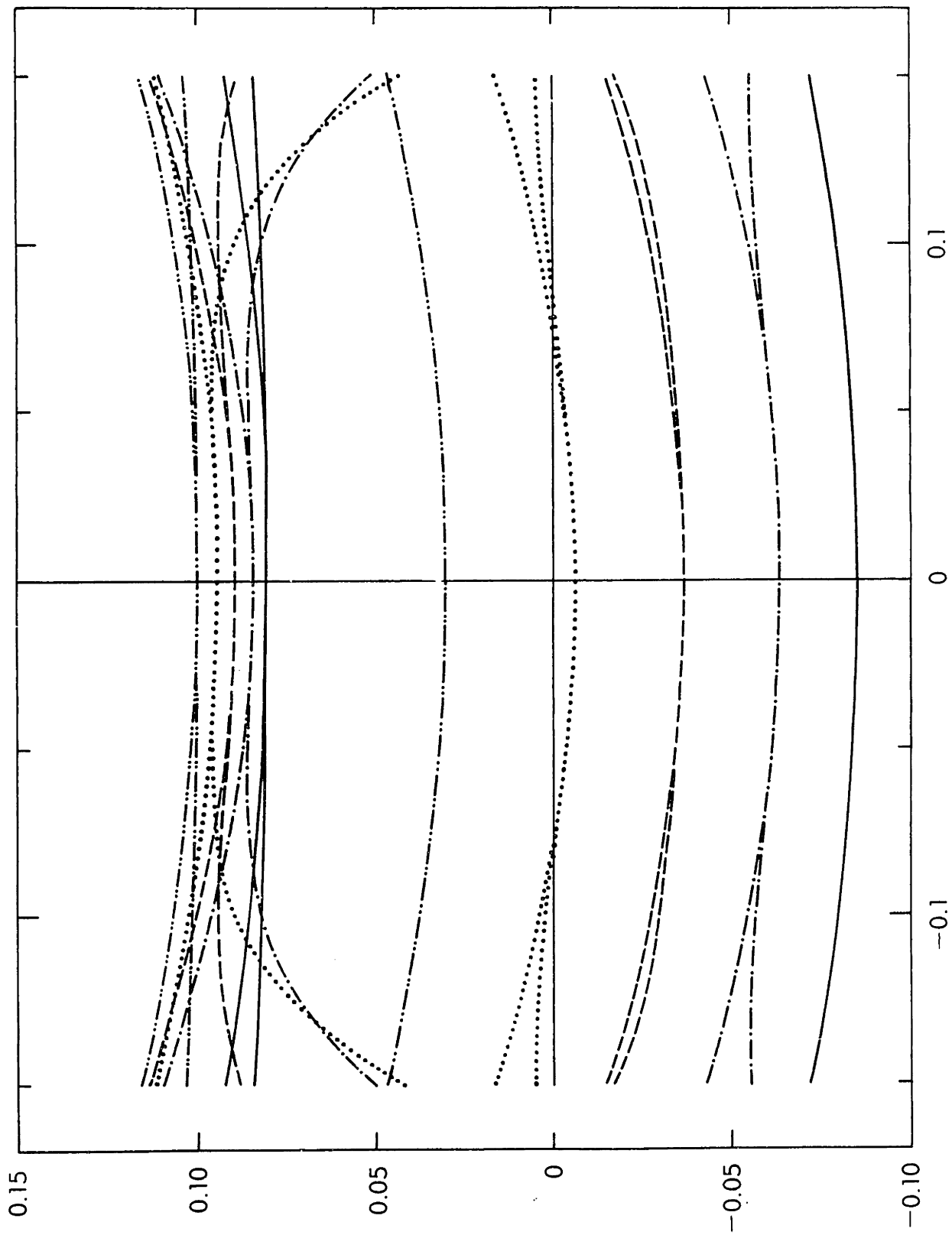


Figure 135. Path Length Study

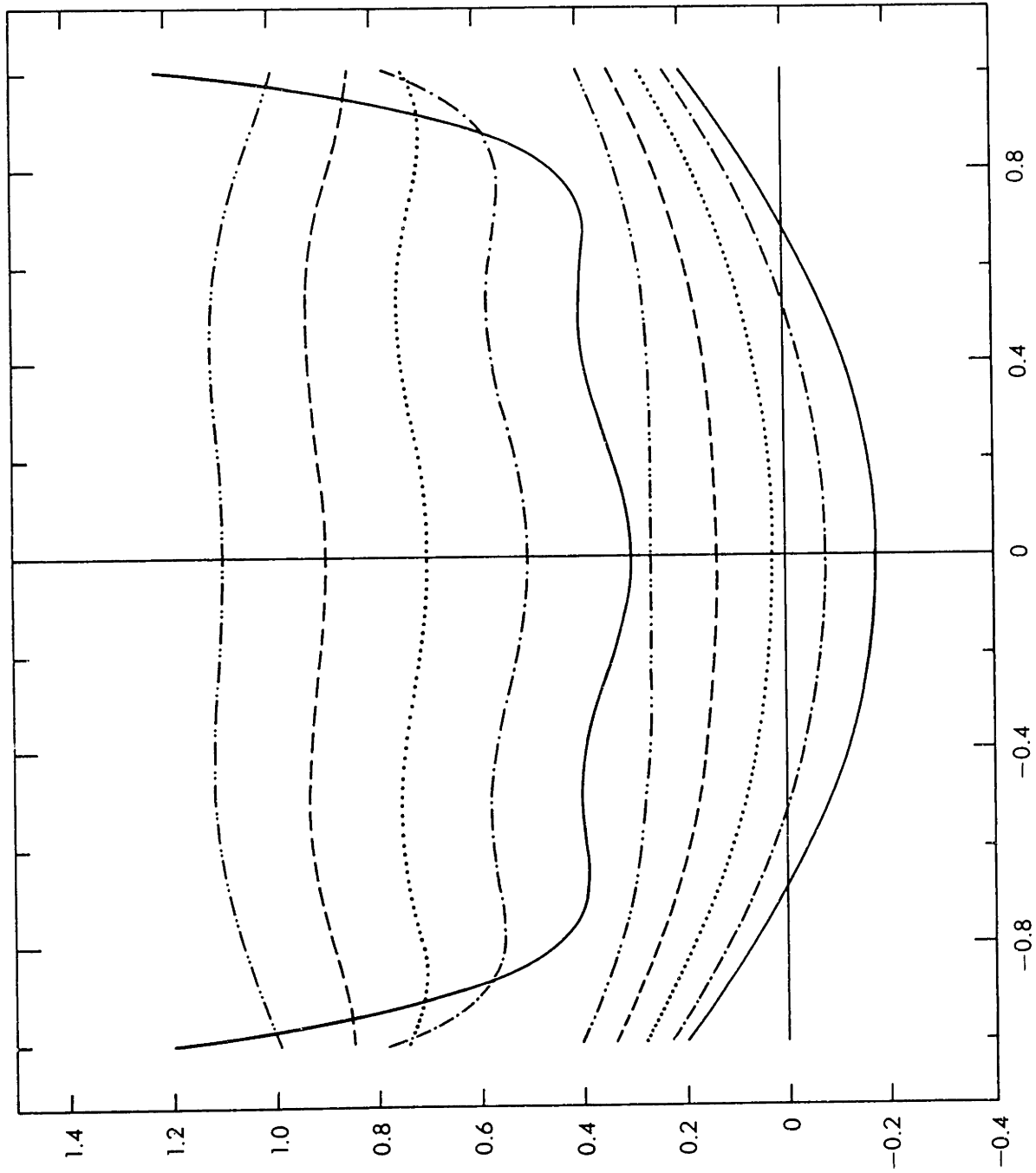


Figure 136. Aperture Center Location Study

```

A (A 10 COMPONENT ARRAY)
.1066 -.8055 2.452 -3.517 1.72 0 0 0 0 0
B (A 10 COMPONENT ARRAY)
-2.313 24.54 -96.85 162.58 -97.9 0 0 0 0 0
YMIN = -.3 XMIN = -.1 XMAX = .5 YBEST = 0
INPUT NEW VALUES IF DESIRED
PAUSE
:

```

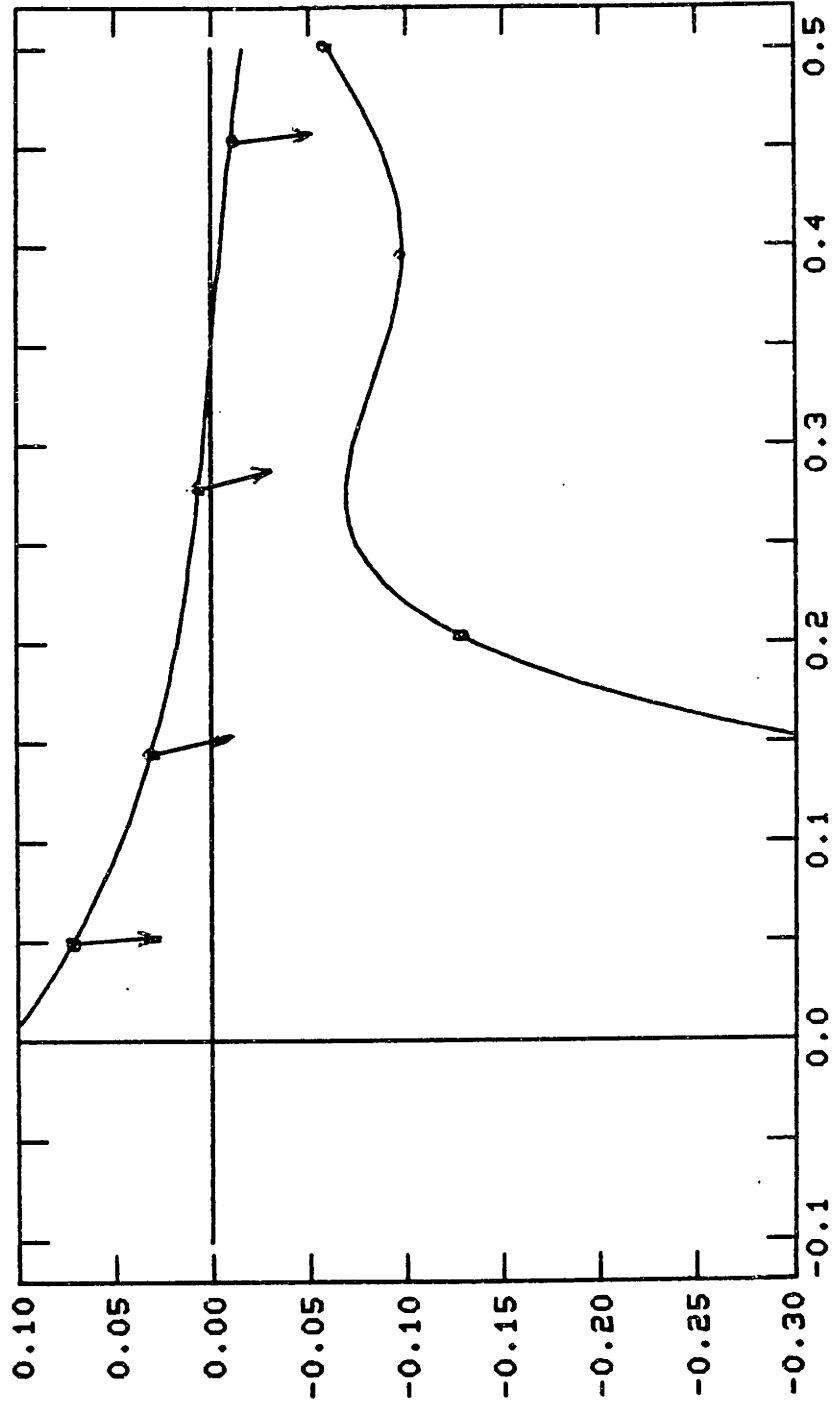


Figure 137. Aperture Position Study $C_1 = 0$

A (A 10 COMPONENT ARRAY)
 .6966 -1.6343 2.246 -3.375 1.867 0 0 0 0 0
 B (A 10 COMPONENT ARRAY)
 -.866 1.69 -7.07 13.55 -8.5 0 0 0 0 0

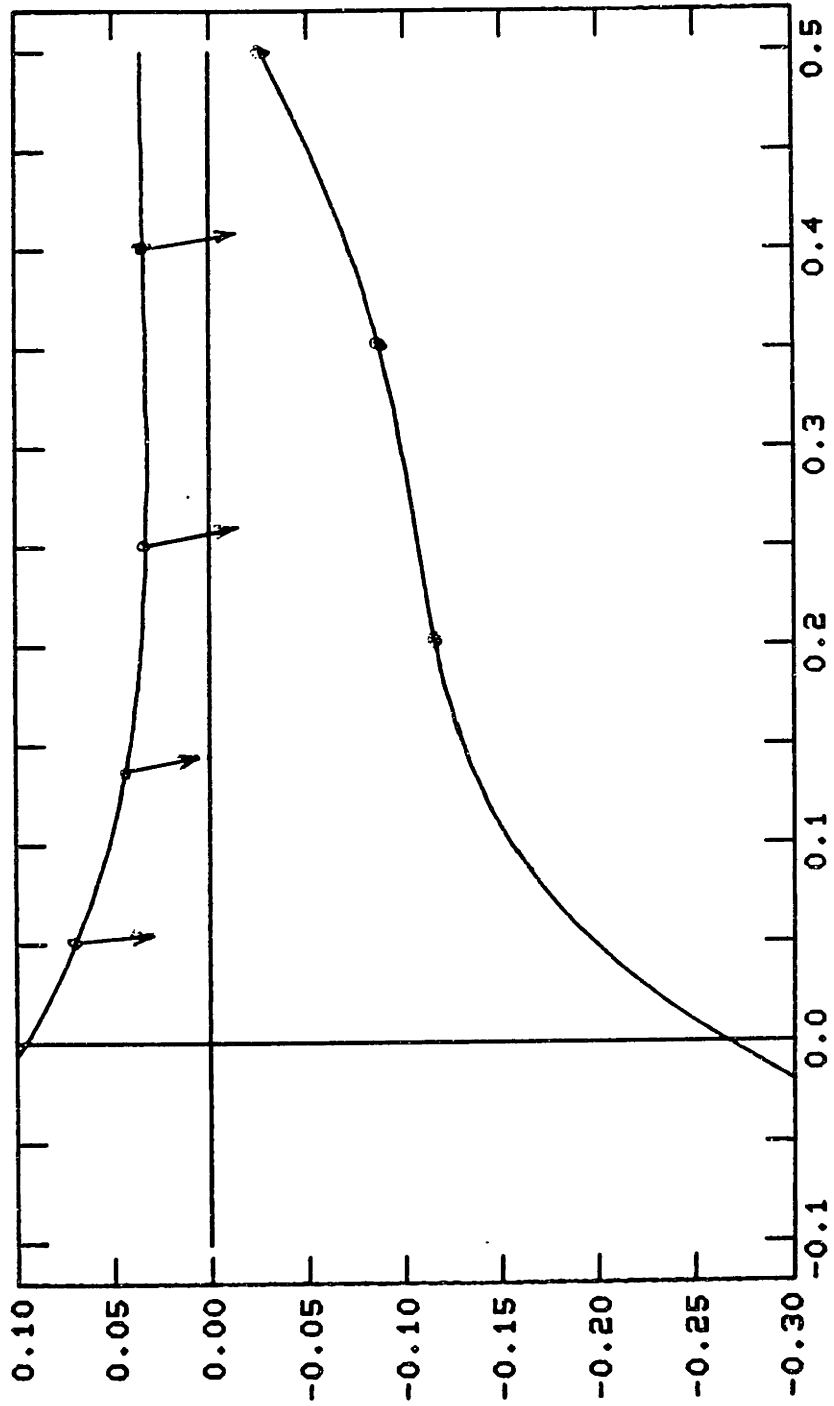


Figure 138. Aperture Position Study $C_1 = 0.1$

A (A 10 COMPONENT ARRAY)
 .0848 -1.424 1.89 -2.86 1.64 0 0 0 0 0
 B (A 10 COMPONENT ARRAY)
 -.131 .1143 -.408 2.16 -1.45 0 0 0 0 0

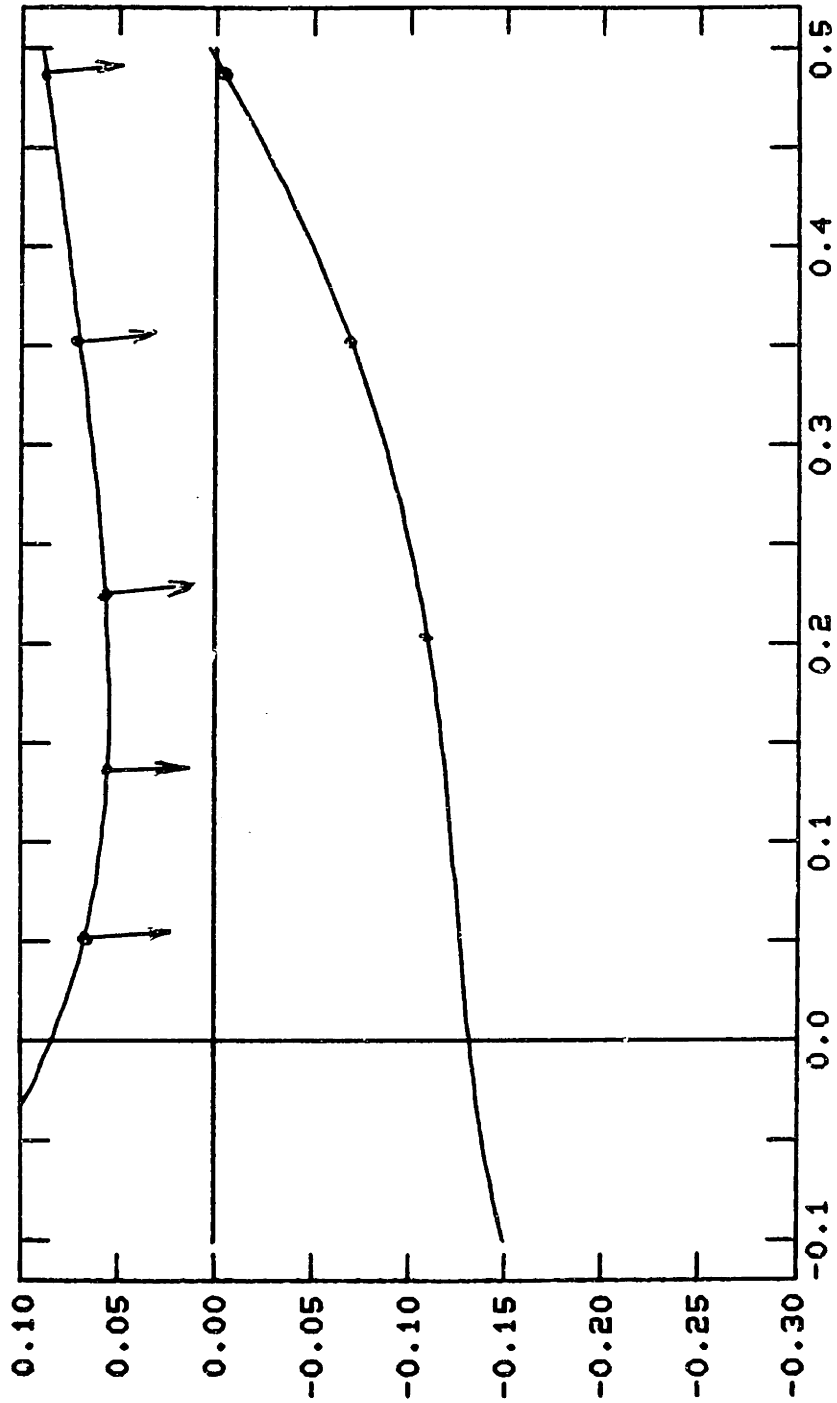


Figure 139. Aperture Position Study $C_1 = 0.2$

A (A 10 COMPONENT ARRAY)
 .0751 -0.1728 1.48 -2.871 1.31 0 0 0 0 0 0
 B (A 10 COMPONENT ARRAY)
 -.1863 .0861 .373 .722 -.538 0 0 0 0 0 0

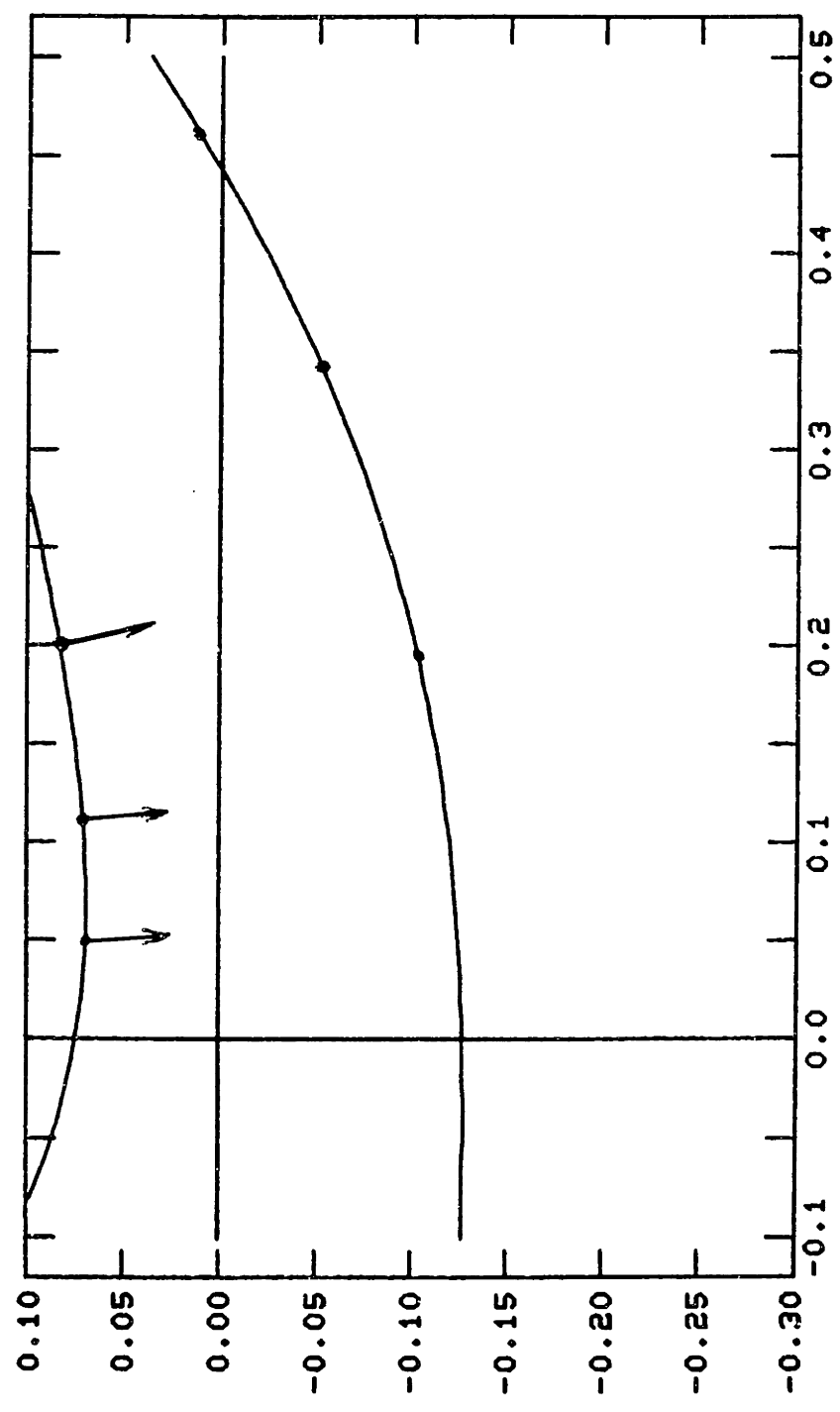


Figure 140. Aperture Position Study $C_1 = 0.3$

A (A 10 COMPONENT ARRAY)
 .9457 .4116 1.808 -0.83 8.36 0 0 0 0 0 0
 B (A 10 COMPONENT ARRAY)
 -.148 .1753 .803 -.0836 -.089 0 0 0 0 0 0

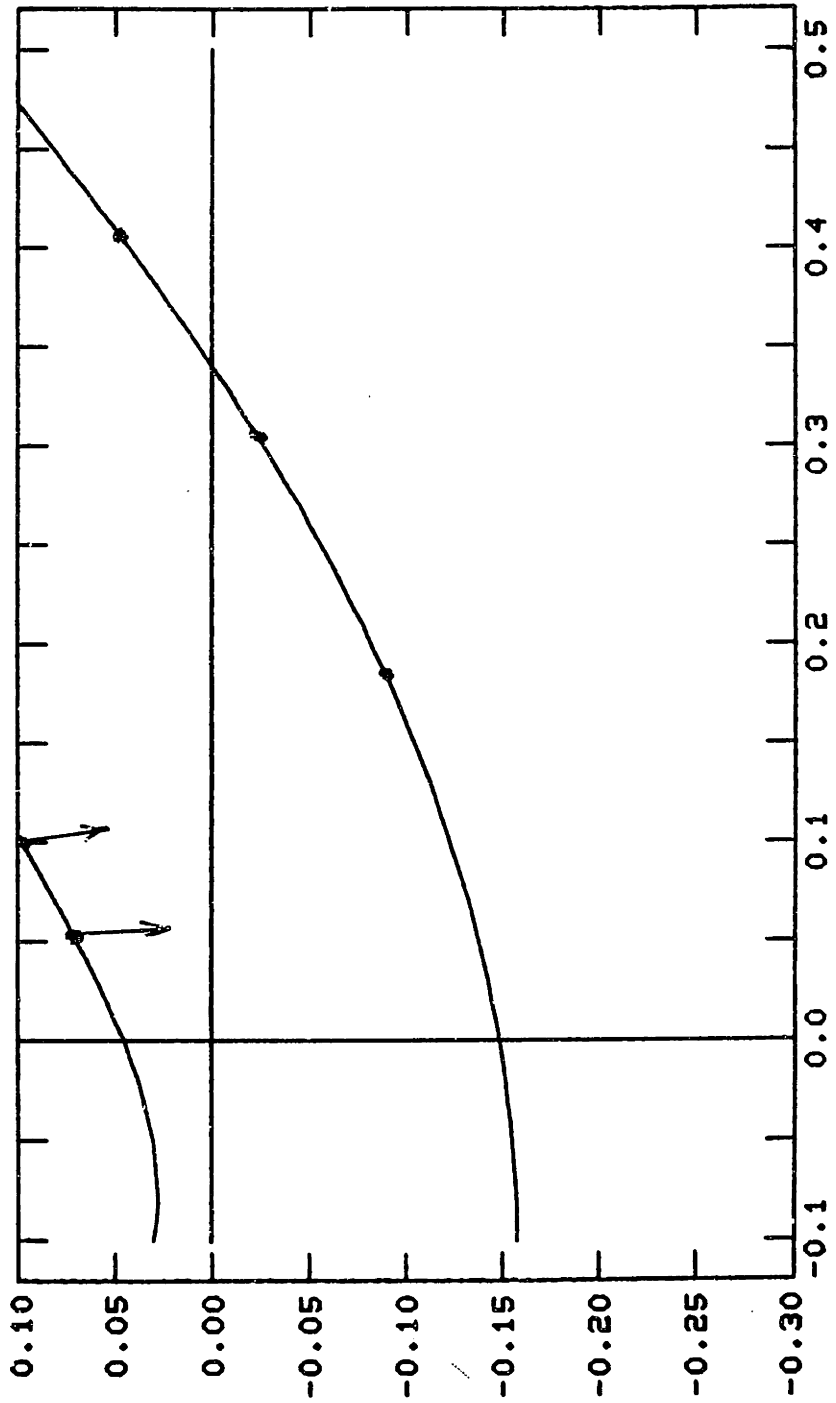


Figure 141. Aperture Position Study $C_1 = 0.4$

A (A 10 COMPONENT ARRAY)
 .03697 .5356 6.27 -31.5 48.77 0 0 0 0
 B (A 10 COMPONENT ARRAY)
 -.1575 .2086 1.346 -.97 .373 0 0 0 0 0

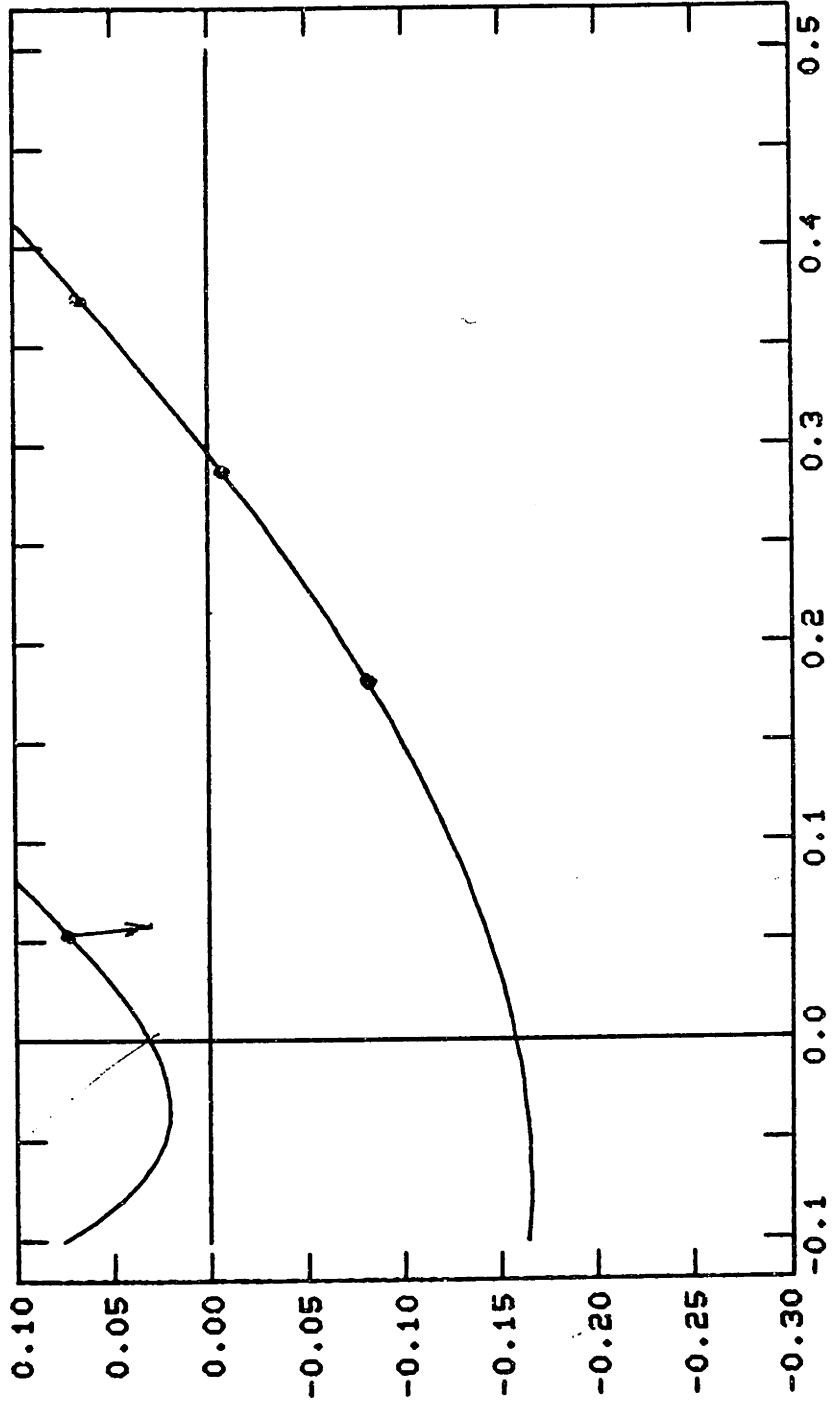


Figure 142. Aperture Position Study $C_1 = 0.5$

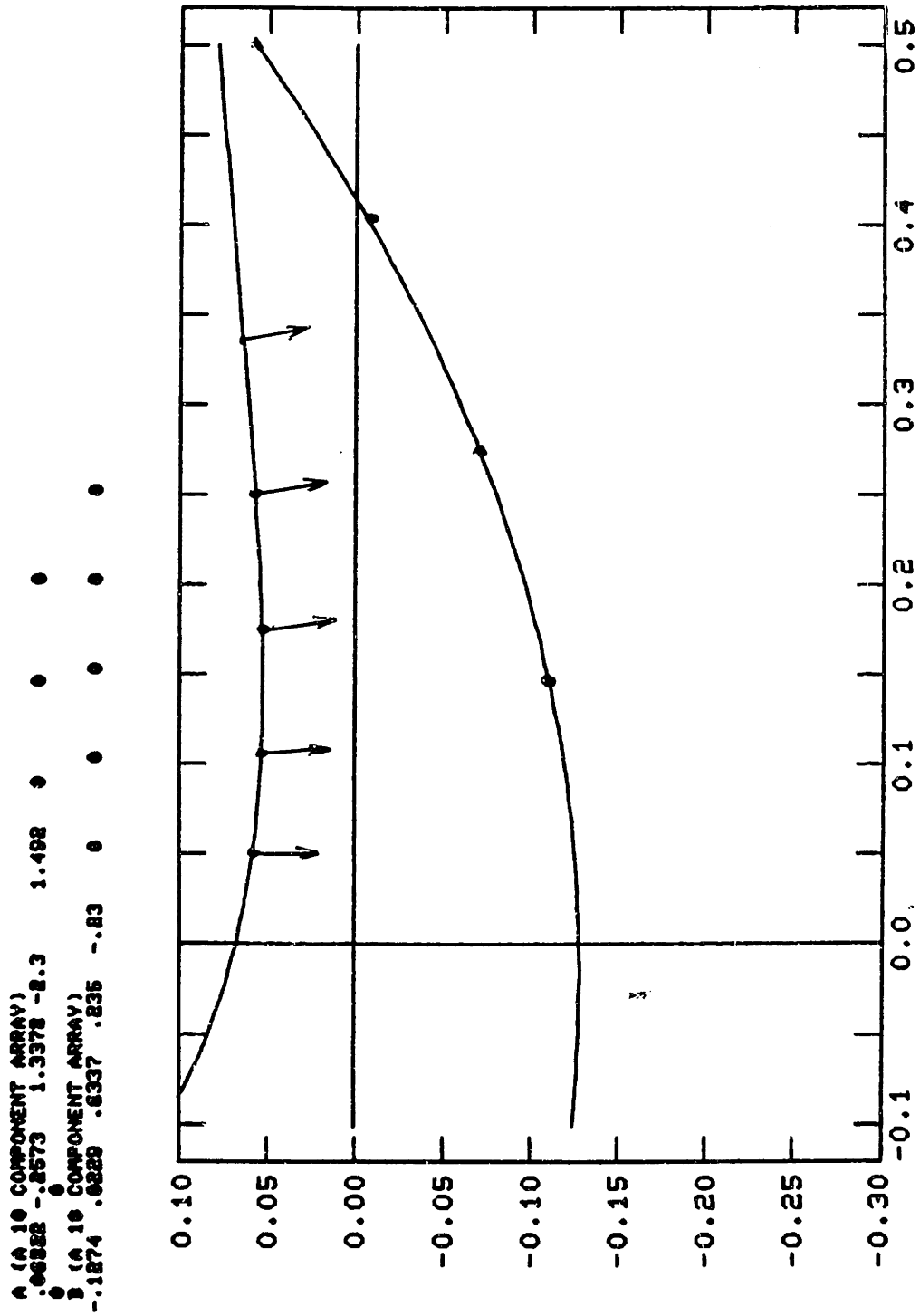


Figure 143. First Subreflector Normal Study $\hat{n}_s = (0,0,-1)$

A (A 10 COMPONENT ARRAY)
 .06785 - .0155 1.281 -2.132 1.31 0 0 0
 B (A 10 COMPONENT ARRAY)
 -.1488 .2452 -.1792 1.51 -.956 0 0 0
 YMIN 0

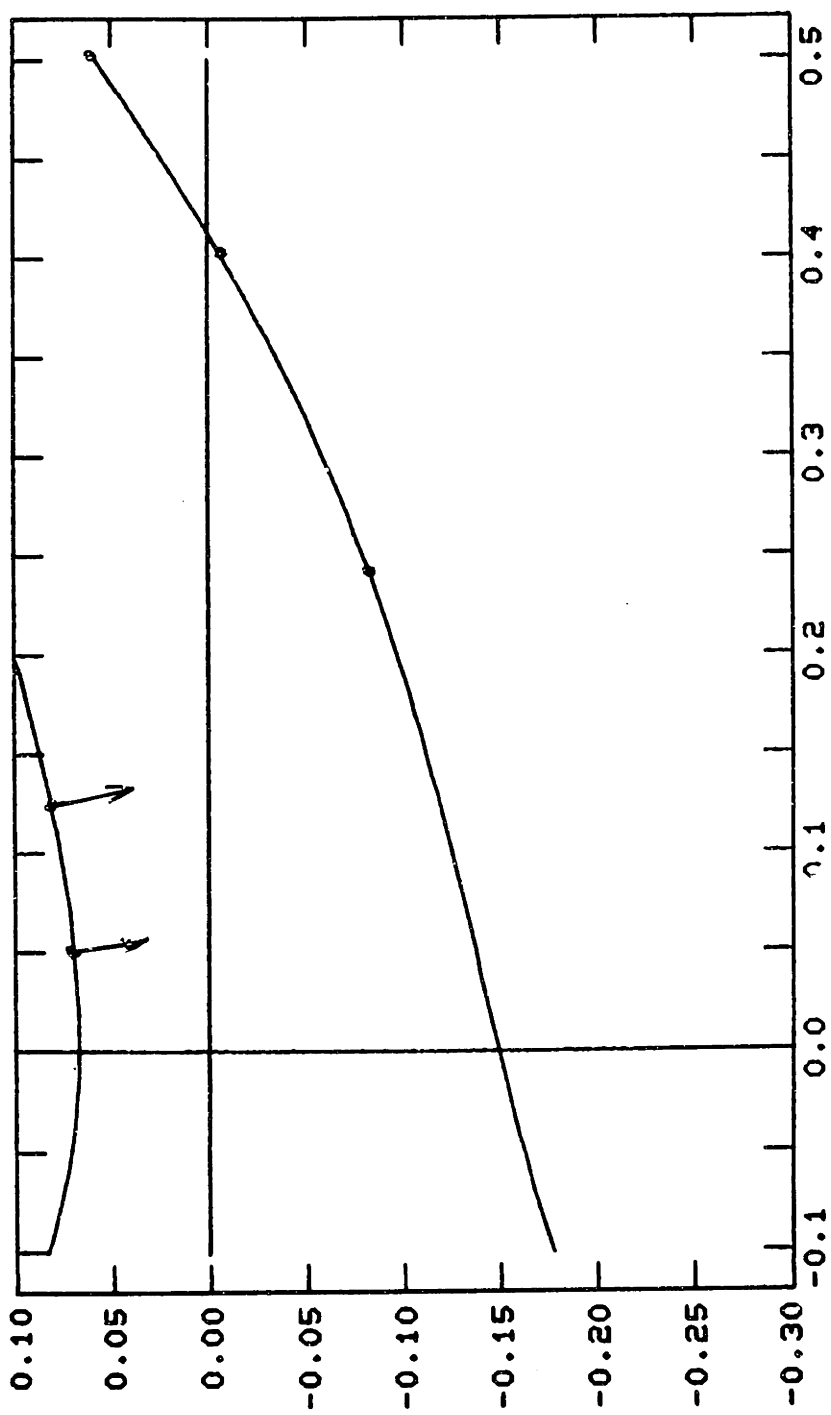


Figure 144. First Subreflector Normal Study $\hat{n}_{S1} = (0.1, 0, -1)$

A (A 10 COMPONENT ARRAY)
 .0661 .08674 1.115 -1.77 .987 0 0 0 0
 B (A 10 COMPONENT ARRAY)
 -.2534 1.1677 -3.0360 5.343 -2.849 0 0 0 0

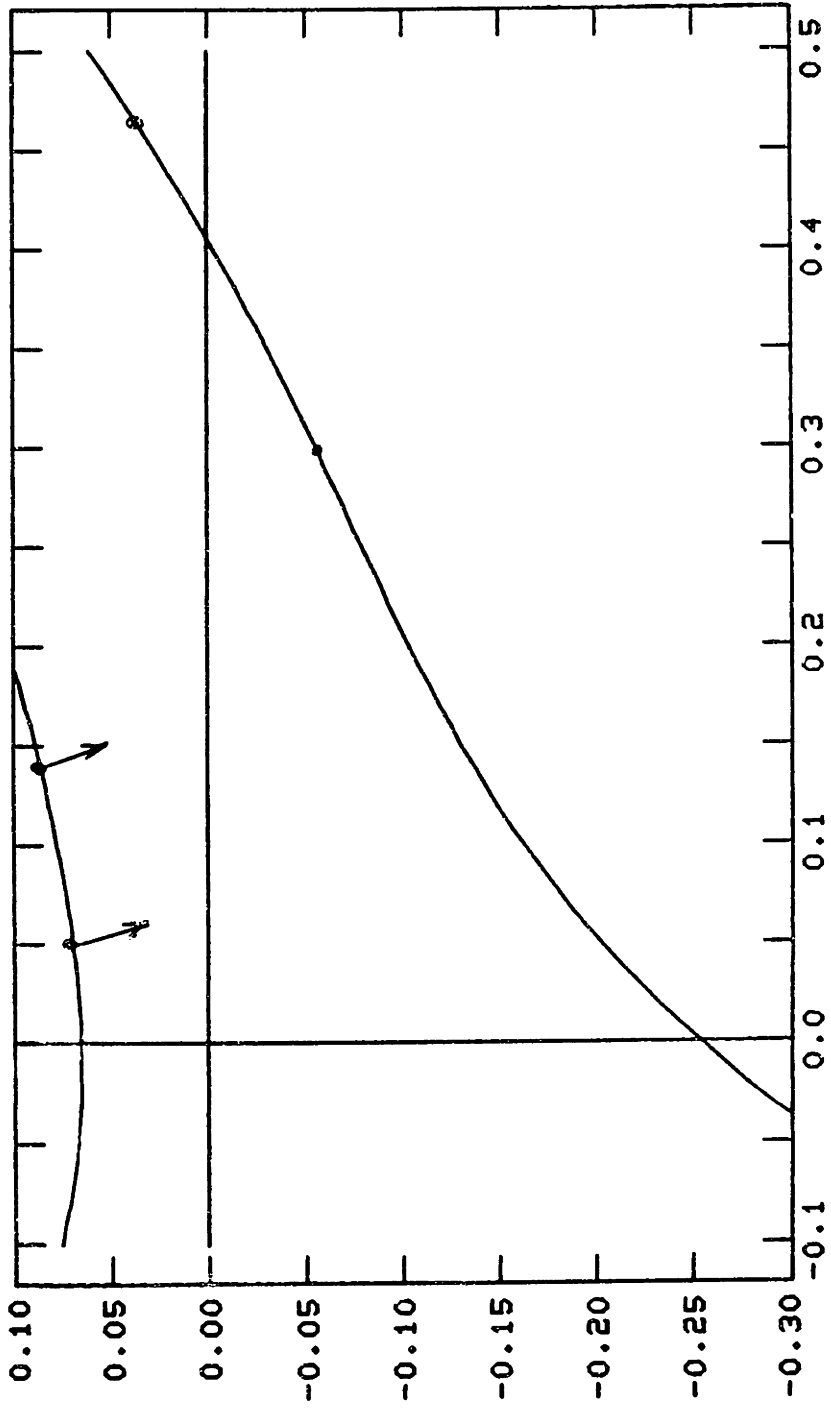


Figure 145. First Subreflector Normal Study $\hat{n}_{S1} = (0.2, 0, -1)$

REFERENCES

1. Silver, S., Ed., Microwave Antenna Theory and Design, Dover Publications, Inc., New York, 1965.
2. Rusch, W. V. T., and Potter, P.D., Analysis of Reflector Antennas, Academic Press, New York, 1970.
3. Collin, R. E., and Zucker, F. J., Antenna Theory, McGraw-Hill, New York, 1969.
4. Kraus, J. D., Antennas, McGraw-Hill, New York, 1950.
5. Elliot, R. S., Antenna Theory and Design, Prentice Hall Inc., Englewood Cliffs, New Jersey, 1981.
6. Cheng, D. K., "Effect of Arbitrary Phase Error on the Gain and Beamwidth Characteristics of Radiation Pattern," IRE Transactions on Antennas and Propagation, Vol. AP-3, July 1965, pp. 145-147.
7. Vu, T. B., "The Effect of Phase Errors on the Forward Gain," IEEE Transactions on Antennas and Propagation, Vol. AP-13, November 1965, pp. 981-982.
8. Kelleher, K. S., "Antenna Wavefront Problems," Naval Research Lab., Washington, D.C., September 1949.
9. Born, M., Wolf, E., Principles of Optics, Pergamon Press, New York, 1970.
10. Clarricoats, P. J. B., "Some Recent Developments in Microwave Reflector Antennas," Proceedings of the IEE, Vol. 126, No. 1, January 1979, pp. 9-25.

11. Cogdell, J. R., and Davis, J. H., "Astigmatism in Reflector Antennas," IEEE Transactions on Antennas and Propagation, Vol. AP-21, July 1973, pp. 565-567.
12. Ruze, J., "Lateral Feed Displacement in a Paraboloid," IEEE Transactions on Antennas and Propagation, Vol. AP-13, September 1965, pp. 660-665.
13. Imbriale, W. A., Ingerson, P. G., and Wong, W. C., "Large Lateral Feed Displacements in a Parabolic Reflector," IEEE Transactions on Antennas and Propagation, Vol. AP-22, November 1974, pp. 742-743.
14. Rusch, W. V. T., and Ludwig, A. C., "Determination of the Maximum Scan-Gain Contours of a Beam-scanning Paraboloid and Their Relation to the Petzval Surface," IEEE Transactions on Antennas and Propagation, Vol. AP-21, March 1973, pp. 141-147.
15. Rudge, A. W., "Multiple-Beam Antennas: Offset Reflectors with Offset Feeds," IEEE Transactions on Antennas and Propagation, Vol. AP-23, May 1975, pp. 234-239.
16. Balling, P., Jorgensen, R., and Pontoppidan, K., "Study of Techniques for Design of High Gain Antennas with Contoured Beams," Final Report ESTEC Contract No. 3371/77/NL/AK, December 1978.

17. Isber, A. M., "Obtaining Beam Pointing Accuracy with Cassegrain Antennas," Microwaves, August 1967, pp. 40-44.
18. Hannan, P. W., "Microwave Antenna Derived from the Cassegrain Telescope," IRE Transactions on Antennas and Propagation, Vol. AP-9, March 1961, pp. 140-153.
19. White, W. D. and DeSize, L. K., "Focal Length of a Cassegrain Reflector," IRE Transactions on Antennas and Propagation, Vol. AP-9, January 1961, p. 412.
20. Wong, W. C., "On the Equivalent Parabola Technique to Predict the Performance Characteristics of a Cassegrainian System with an Offset Feed," IEEE Transactions on Antennas and Propagation, Vol. AP-21, May 1973, pp. 335-339.
21. Rusch, W. V. T., "Scattering from a Hyperboloidal Reflector in a Cassegrainian Feed System," IEEE Transactions on Antennas and Propagation, Vol. AP-11, July 1963, pp. 414-421.
22. Potter, P. D., "Application of Spherical Wave Theory to Cassegrainian-Fed Paraboloids," IEEE Transactions on Antennas and Propagation, Vol. AP-15, November 1967, pp. 727-736.

23. Potter, P. D., "Aperture Illumination and Gain of a Cassegrain System," IEEE Transactions on Antennas and Propagation, Vol. AP-71, May 1963, pp. 373-375.
24. DeSize, L. K., Owen, D. J., and Skahill, G. K., "Investigation of Multibeam Antennas and Wide-Angle Optics," Airborne Instruments Laboratory, Report No. 7358-1, January 1960.
25. Sorensen, O. and Rusch, W. V. T., "Application of the Geometric Theory of Diffraction to Cassegrain Subreflectors with Laterally Defocused Feeds," IEEE Transactions on Antennas and Propagation, Vol. AP-73, September 1975, pp. 698-701.
26. Mentzer, C. A., and Peters, L., "A GTD Analysis of the Far-Out Sidelobes of Cassegrain Antennas," IEEE Transactions on Antennas and Propagation, Vol. AP-23, September 1975, pp. 702-709.
27. Kinber, B. Ye, "On Two Reflector Antennas," Radio Engineering and Electronic Physics, Vol. 6, June 1962, pp. 914-921.
28. Galindo, V., "Design of Dual Reflector Antennas with Arbitrary Phase and Amplitude Distributions," IEEE Transactions on Antennas and Propagation, Vol. AP-12, July 1964, pp. 403-408.

29. Brickell, F. and Westcott, B. S., "Reflector Design as an Initial-Value Problem," IEEE Transactions on Antennas and Propagation, (Communication), Vol. AP-24, July 1976, pp. 531-533.
30. Westcott, B. S., and Norris, A. P., "Reflector Synthesis for Generalized Far Fields," Journal of Physics: A, Mathematics, Nuclear, and General, Vol. 8, 1975, pp. 521-532.
31. Jenkins, F. A. and White, H. E., Fundamentals of Optics, McGraw-Hill, New York, 1957.
32. Conrady, A. E., Applied Optics and Optical Design, Part 1, Dover Publications, Inc., New York, 1957.
33. Longhurst, R. S., Geometrical and Physical Optics, John Wiley & Sons, Inc., New York, 1967.
34. Holt, F. S., "Application of Geometric Optics to the Design and Analysis of Microwave Antennas," AFCRL, Bedford, MA., AFCRL-67-0501, September 1967.
35. Fry, G. A., Geometrical Optics, Chilton Book Co., Philadelphia, 1969.
36. Cornbleet, S., Microwave Optics, Academic Press, New York, 1976.

37. Collins, G. W., "Shaping Subreflectors in Cassegrainian Antennas for Maximum Aperture Efficiency," IEEE Transactions on Antennas and Propagation, Vol. AP-21, May 1973, pp. 309-313.
38. Williams, W. F., "High Efficiency Antenna Reflector," Microwave Journal, Vol. 8, July 1965, pp. 79-82.
39. Green, K. A., "Modified Cassegrain Antenna for Arbitrary Aperture Illumination," IRE Transactions on Antennas and Propagation, (Communication), Vol. AP-11, September 1963, pp. 589-590.
40. Kitsuregawa, T. and Mizusawa, M., "Design of the Shaped Reflector Cassegrainian Antenna in Consideration of the Scattering Pattern of the Subreflector," IEEE Group; Antennas and Propagation, International Symposium Digest, September 9-11, 1968, pp. 391-396.
41. Rouffy, F., "Design of Dual Reflector Antennas," U.R.S.I. 1968 Fall Meeting Digest, September 10-12, 1968, p. 88.
42. Von Hoerner, S., "The Design of Correcting Secondary Reflectors," IEEE Transactions on Antennas and Propagation, Vol. AP-24, May 1976, pp. 336-340.

43. Millner, M. O., and Bates, R. H. T., "Design of Subreflectors to Compensate for Cassegrain Main Reflector Deformations," Proceedings of the IEE, Microwaves, Optics and Antennas, to be published.
44. Morgan, S. P., "Some Examples of Generalized Cassegrainian and Gregorian Antennas," IEEE Transactions on Antennas and Propagation, Vol. AP-12, November 1964, pp. 685-691.
45. Qian Ji-zen, "Equivalent Phase Center of the Subreflector in the Shaped Cassegrain Antenna," IEE 2nd International Conference on Antennas and Propagation, April 1981, York, U.K., pp. 204-206.
46. Buchmeyer, S. K., "An Electrically Small Cassegrain Antenna with Optically Shaped Reflectors," IEEE Transactions on Antennas and Propagation, Vol. AP-25, May 1977, pp. 346-351.
47. James, G. L., "Analysis of Radiation Pattern and G/T_A for Shaped Dual Reflector Antennas," Proceedings of the IEE, Microwaves, Optics and Antennas, Vol. 127, No. 1, February 1980, pp. 52-60.
48. Tanaka, M. and Mizusawa, M., "Elimination of Cross Polarization in Offset Dual-Reflector Antennas," Electronics and Communications in Japan, Vol. 58-B, No. 12, 1975, pp. 71-78.

49. Akagawa, M., "Application of Offset Dual Reflectors of Spacecraft Antennas," COMSAT Technical Memorandum CL-42-78, September 26, 1978.
50. Mizuguchi, T., Akagawa, M., and Yokoi, H., "Offset Gregorian Antenna," Electronics and Communications in Japan, Vol. 61-B, No. 3, 1978, pp. 58-66.
51. Galindo-Israel, V., Mittra, R., and Cha, A., "Aperture Amplitude and Phase Control of Offset Dual Reflectors," IEEE Transactions on Antennas and Propagation, Vol. AP-27, March 1979, pp. 159-164.
52. Lee, J. J., Parad, L. I., and Chu, R. S., "Shaped Offset-Fed Dual Reflector Antenna," IEEE Transactions on Antennas and Propagation, Vol. AP-27, March 1979, pp. 165-171.
53. Mittra, R., and Galindo-Israel, V., "Shaped Dual Reflector Synthesis," IEEE Antennas and Propagation Newsletter, August 1980, pp. 5-9.
54. Bjontegaard, G., and Pettersen, T., "A Shaped Offset Dual Reflector Antenna with High Gain and Low Sidelobe Levels," IEE 2nd International Conference on Antennas and Propagation, April 1981, York, U.K., pp. 163-167.
55. Westcott, B. S., Stevens, F. A., and Brickell, F., "GO Synthesis of Offset Dual Reflectors," IEE Proceedings, Vol. 128, February 1981, pp. 11-18.

56. Ingerson, P. G., and Wong, W. C., "Focal Region Characteristics of Offset Fed Reflectors," 1974 International IEEE/AP-S Symposium Program and Digest, June 10-12, 1974, pp. 121-123.
57. Rudge, A. W., and Adatia, N. A., "Offset-Parabolic-Reflector Antennas: A Review," Proceedings of the IEEE, Vol. 66, December 1978, pp. 1592-1618.
58. Adatia, N. A., and Rudge, A. W., "Beam Squint in Circularly Polarized Offset-Reflector Antennas," Electronic Letters, Vol. 11, No. 21, October 16, 1975, pp. 513-515.
59. Woo, K., "Array-Fed Reflector Antenna Design and Applications," IEE 2nd International Conference on Antennas and Propagation, April 1981, York, U.K., pp. 209-213.
60. Bird, T. S., Boomars, J. L., and Clarricoats, P. J. B., "Multiple-Beam-Dual-Offset Reflector Antenna with an Array Feed," Electronic Letters, Vol. 14, No. 14, July 6, 1978, pp. 439-440.
61. Ohm, E. A., "A Proposed Multiple-Beam Microwave Antenna for Earth Stations and Satellites," Bell System Technical Journal, Vol. 53, October 1974, pp. 1657-1665.

62. Ohm, E. A. and Gans, M. J., "Numerical Analysis of Multiple-Beam Offset Cassegrainian Antennas," AIAA/CASI 6th Communications Satellite Conference, April 5-8, 1976.
63. Ohm, E. A., "System Aspects of a Multibeam Antenna for Full U.S. Coverage," International Conference on Communications, June 10-14, 1979, pp. 49.2.1-49.2.5.
64. Chang, D. C., and Rusch, W. V. T., "Transverse Beam Scanning for an Offset Dual Reflector System with Symmetric Main Reflector," IEE 2nd International Conference on Antennas and Propagation, April 1981, York, U.K., pp. 207-208.
65. Krichevsky, V., "Optimized Feed Locations in the Offset Cassegrainian Antenna," COMSAT Technical Memorandum CL-47-79, November 20, 1979.
66. Li, T., "A Study of Spherical Reflectors as Wide-Angle Scanning Antennas," IRE Transactions on Antennas and Propagation, Vol. 47, July 1959.
67. Holz, F. S. and Bouche, E. L., "A Gregorian Corrector for a Spherical Reflector," IEEE Transactions on Antennas and Propagation, Vol. AP-12, January 1964, pp. 44-47.

68. Tong, G., Clarricoats, P. J. B., and James, G. L., "Evaluation of Beam-Scanning Dual Reflector Antennas," Proceedings of the IEE, Vol. 124, No. 12, December 1977, pp. 1111-1113.
69. Fitzgerald, W. D., "Limited Electronic Scanning with an Offset Feed Near-Field Gregorian System," M.I.T. Lincoln Laboratory, Technical Report 486, September 1971, DDC AP-736029.
70. White, W. D., and DeSize, L. K., "Scanning Characteristics of Two-Reflector Systems," 1962 IRE Convention Record, Part I, pp. 44-70.
71. Claydon, B., "The Schwarzschild Reflector Antenna with Multiple or Scanned Beams," The Marconi Review, First Quarter, 1975, pp. 14-43.
72. Ponomarev, N. G., "Graphical Method for the Design of Profile of Aplanatic Antennas," Radio Engineering and Electronic Physics, Vol. 6, 1961, p. 42.
73. Galinov, G. K., "A Two-Mirror Antenna with Polar Diagram Scanning Through Ninety Degrees," Telecommunications and Radio Engineering, Vol. 28, March 1973, pp. 95-99.
74. van de Sande, J. H. A. W., Herbeu, M. H. A. J., and Maanders, E. J., "Designing Schwarzschild Antenna Systems," IEE 2nd International Conference on Antennas and Propagation, April 1981, York, U.K., pp. 153-157.

75. Roberts, G. E., "Parametric Solution of the Equations of the Schwarzschild Two-Reflector Optical System," Journal of the Optical Society of America, Vol. 54, No. 9, September 1964, pp. 1111-1114.
76. Rao, B. L. J., "Bifocal Dual Reflector Antenna," X-750-73-263, NASA Goddard Space Flight Center, Greenbelt, Md., September 1973.
77. Rao, B. L. J., "Bifocal Dual Reflector Antenna," IEEE Transactions on Antennas and Propagation, Vol. AP-22, September 1974, pp. 711-714.
78. Kumazawa, M. and Karikomi, M., "Multiple-Beam Antenna for Domestic Communication Satellites," IEEE Transactions on Antennas and Propagation, Vol. AP-21, November 1973, pp. 876-877.
79. Karikomi, M., "A Limited Steerable Dual Reflector Antenna," Electronics and Communications in Japan, Vol. 55-B, No. 10, 1972, pp. 62-68.
80. Holt, F. S., and Mayer, A., "A Design Procedure for Dielectric Microwave Lenses of Large Aperture Ratio and Large Scanning Angle," IRE Transactions on Antennas and Propagation, January 1957, pp. 25-30.
81. Brown, R. M., "Dielectric Bifocal Lenses," IRE National Convention Record, 1956, pp. 180-187.

82. Claydon, B. A., "The Scanning Corrected Cassegrain Reflector Antenna," *The Marconi Review*, Second Quarter, 1975, pp. 77-94.
83. Chang, D. C. D. and Lang, K. C., "A Scan-Corrected Offset Dual Reflector Antenna System," P-GAP, 1980, pp. 557-559.
84. Hildebrand, F. B., Advanced Calculus for Applications, Prentice-Hall, Inc., Englewood Cliffs, N.J., 1976.
85. Sommerfeld, A., Partial Differential Equations in Physics, Academic Press, New York, 1949.
86. Hay, G. E., Vector and Tensor Analysis, Dover Paperback, New York, 1953.
87. Pizer, S. M., Numerical Computing and Mathematical Analysis, Science Research Associates, Inc., Chicago 1975.
88. Abramowitz, M., and Stegun, I., Handbook of Mathematical Functions, Dover Publications, Inc., New York, 1965.
89. Cook, W., "A General Purpose Antenna Program," COMSAT Technical Memorandum CL-2-74, January 8, 1974.
90. Mrstik, A. V., "Scan Limits of Off-Axis Fed Parabolic Reflectors," IEEE Transactions on Antennas and Propagation, Vol. AP-27, September 1979, pp. 647-651.

91. Lo, Y. T., "On the Beam Deviation Factor of a Parabolic Reflector," IRE Transactions on Antennas and Propagation, Vol. AP-8, May 1960, pp. 347-349.
92. Ruze, J., "Antenna Tolerance Theory--A Review," Proceedings of the IEEE, Vol. 54, April 1966, pp. 633-640.
93. King, A. P., "The Radiation Characteristics of Conical Horn Antennas," Proceedings of the IRE, March 1950, Vol. 38, pp. 249-251.
94. Dell-Imagine, R. A., "A Comparison of Experimental and Theoretical Properties of Wide Angle Beam Scanning Paraboloids," IEEE P-GAP, 1975, pp. 137-140.
95. Semplak, R. A., "100-GHz Measurements on a Multiple-Beam Offset Antenna," Bell System Technical Journal, March 1977, pp. 385-398.
96. Gruner, R., Williams, A., and Frey, F., "Calculated and Measured Data for the Phase Corrected Toroidal Antenna System," COMSAT Technical Memorandum CL-38-75, April 22, 1975.
97. Shelton, P., "Multiple Feed Systems for Objectives," IEEE Transactions on Antennas and Propagation, Vol. AP-13, November 1965, pp. 992-994.

98. Oliver, R. E., "Large Spacecraft Antennas: New Geometric Configuration Design Concepts," Jet Propulsion Laboratory Technical Review, Vol. 1, No. 1, April 1971, pp. 78-85.
99. Dragone, C., "Offset Multireflector Antennas with Perfect Pattern Symmetry and Polarization Discrimination," Bell System Technical Journal, September 1978, pp. 2663-2684.
100. Dragone, C., and Gans, M. J., "Imaging Reflector Arrangements to Form a Scanning Beam Using a Small Array," Bell System Technical Journal, February 1979, pp. 501-515.
101. Takano, T., Ogawa, E., Betsudan, S., and Sato, S., "High Efficiency and Low Sidelobe Design for a Large Aperture Offset Reflector Antenna," IEEE Transactions on Antennas and Propagation, Vol. AP-28, July 1980, pp. 460-465.
102. Korsch, D., "Design and Optimization Techniques for Three Mirror Telescopes," Applied Optics, Vol. 19, No. 2C, November 1980, pp. 3640-3645.